UNIVERSITÀ
DEGLI STUDI
DI PADOVA

Head Office: Università degli Studi di Padova

Department of Industrial Engineering

Ph.D. COURSE IN INDUSTRIAL ENGINEERING
CURRICULUM: MECHANICAL ENGINEERING
SERIES XXX

INDUSTRIAL X-RAY COMPUTED TOMOGRAPHY: ACCURACY ENHANCEMENT AND ERRORS EVALUATION TOWARDS TRACEABILITY OF COORDINATE MEASUREMENTS

Coordinator: Ch.mo Prof. Paolo Colombo
Supervisor: Ch.mo Prof. Simone Carmignato
Co-Supervisor: Ch.mo Prof. Enrico Savio

Ph.D. student: Valentina Aloisi

A mio Padre e a mia Madre

Preface

This thesis has been prepared as one of the requirements of the Ph.D. degree.
The Ph.D. program was carried out at the Ph.D. School of Industrial Engineering, curriculum of Mechanical Engineering, of University of Padova, under the supervision of Prof. Simone Carmignato and co-supervision of Prof. Enrico Savio.

I would like to thank my Ph.D. supervisor Prof. Simone Carmignato, for his experience, the discussions and for the accurate suggestions to my work. I also want to thank Prof. Enrico Savio for his positivity, experience and fruitful suggestions. Furthermore, I want to thank North Star Imaging Inc. for having made available the equipment used in Chapter 4 and 5 of this thesis. In particular, I would like to thank Dr. Joe Schlecht and Dr. Eric Ferley from North Star Imaging Inc., for their passion, availability and valuable contributions and collaboration to the work presented in Chapter 4 and 5 of this thesis. I also thank Tec Eurolab S.r.l. for the availability and collaboration provided.

I express my gratitude to my Parents to who I dedicate this PhD thesis, and to my Brother. Thank you for being always my biggest support, and for your passion, determination and enthusiasm that have always driven me.
I want to thank my whole Family who has always supported me.

October 2017

Valentina Aloisi

Abstract

In the recent years, X-ray computed tomography (CT) has been increasingly used in the field of coordinate metrology for performing dimensional verifications on industrial parts. X-ray CT provides significant advantages compared to traditional coordinate measuring machines, which have made this technology one of the most promising and innovative non-contact measuring techniques in the field of dimensional metrology. With a CT scan of the component to be inspected, it is possible to obtain, in a relatively short time and in a non-contact way, its volumetric model fully describing its internal and external geometries. On this three-dimensional model a multitude of measuring tasks can be performed, which often are not possible with conventional measuring technologies; these include the measurement of inner and non-accessible complex geometrical features without any need to cut or destroy the part.

CT, therefore, has acquired a primary role in the field of dimensional metrology, enabling also the inspection and analysis of new and innovative products. However, despite the advantages that X-ray CT provides there are some current challenges that need to be addressed in order for CT systems to be widely accepted in the field of coordinate metrology. As for all coordinate measuring systems, CT measurements must be traceable to the unit of length, the meter, and CT measurement uncertainty must be adequate for the measuring tasks performed. The establishment of measurements traceability and the study and enhancement of CT measurement accuracy however are complex tasks, mainly due to the several influence factors that affect CT measurement chain. At the state of the art, no internationally accepted standards are available for testing CT metrological performances and for determining the uncertainty of CT measurements – which is a fundamental requirement for establishing metrological traceability.

This PhD thesis contributes with research on these topics. The effects of relevant influence factors affecting CT measurements are studied and modelled with the aims of characterizing the measurement errors produced by each influence factor and to determine the sensitivity of measurement results to these error sources. This is a primary fundamental step for the establishment of measurement traceability and for the enhancement of CT measurement accuracy. The effects of CT system geometrical errors are studied and quantitatively determined. Different experimental campaigns were designed in order to determine the measurement errors caused by geometric errors of the X-ray detector and of the rotary table. The sensitivity of the measurement results to each of the investigated geometrical errors is provided, moreover the influence of the measurement direction and object positioning in the CT volume is determined.

The analysis and mapping of geometrical errors is fundamental in coordinate metrology, and the system geometry influences the whole measurement chain. A thorough experimental description of the effects produced by CT system geometrical errors still lacks in literature.

Measurement errors due to the cone-beam artifact – which is an inherent influence factor in circular cone-beam trajectories – are studied and mapped by means of experimental investigations. An advanced solution in the field of CT metrology, the use of helical scanning trajectories, is studied in order to exploit all the benefits that CT can offer in terms of measurement accuracy, scan resolution and image quality. CT helical scanning metrological performances are investigated, as well as the effects of the main helical scanning parameters on the measurement accuracy.

Being a multi-purpose measuring technique, X-ray CT offers the possibility to scan a wide variety of industrial parts, which in some cases are characterized by high surface roughness. It is thus of significant importance to quantify the effects of the workpiece surface roughness on CT dimensional measurements. For this purpose, different reference objects were designed in order to experimentally map the effects of surface roughness on CT dimensional measurements performed on periodic roughness profiles. Numerical simulation campaigns were also designed and performed in order to analyze difficult to produce profiles. The measurement errors caused by surface roughness with respect to conventional tactile coordinate measurements are reported and a model for roughness error correction is provided. Measurement uncertainty is calculated according to the substitution method and it is demonstrated how the correction of roughness effects is fundamental for a proper determination of CT measurement uncertainty and for a significant enhancement of measurement accuracy.

Sommario

Negli ultimi anni, la tomografia computerizzata a raggi X (*X-ray computed tomography,* CT) è sempre più utilizzata nel campo della metrologia a coordinate per effettuare verifiche dimensionali di componenti industriali. La tomografia computerizzata a raggi X fornisce vantaggi significativi rispetto alle tradizionali macchine di misura a coordinate, i quali hanno reso questa tecnologia una delle tecniche di misura non a contatto più promettenti ed innovative nel campo della metrologia dimensionale. Dalla scansione tomografica del componente da ispezionare è possibile ottenere, in un tempo relativamente ridotto e senza alcuna forma di contatto, il suo modello volumetrico il quale descrive le geometrie interne ed esterne di tale componente. Su questo modello tridimensionale è possibile eseguire una moltitudine di *task* di misura, spesso non possibili con le tecniche di misura tradizionali, come ad esempio la misurazione di caratteristiche geometriche interne e non accessibili ed estremamente complesse, senza alcuna esigenza di sezionare o alterare il componente.

La tomografia a raggi X pertanto ha acquisito un ruolo primario nel campo della metrologia dimensionale, consentendo inoltre l'ispezione e l'analisi di prodotti nuovi ed innovativi. Tuttavia, nonostante i vantaggi che la tomografia computerizzata consente, ci sono varie sfide che devono essere indirizzate per far sì che i sistemi CT vengano ampiamente accettati nel campo della metrologia a coordinate. Come per tutti i sistemi di misura a coordinate, le misure CT devono essere riferibili all'unità di misura di lunghezza, il metro, e l'incertezza di misura deve essere adeguata per il *task* di misura da effettuare. L'ottenimento della riferibilità metrologica e lo studio ed il miglioramento dell'accuratezza di misura CT tuttavia sono compiti molto complessi, principalmente a causa dei numerosi fattori di influenza che intervengono nella catena di misura tomografica. Allo stato dell'arte non sono disponibili norme accettate a livello internazionale per la caratterizzazione delle prestazioni metrologiche dei sistemi CT e per la determinazione dell'incertezza di misura – che è un requisito fondamentale per stabilire la riferibilità metrologica.

Questa tesi di dottorato contribuisce alla ricerca su questi argomenti. Gli effetti di rilevanti fattori di influenza che affliggono la catena di misura CT sono studiati e modellati, con gli obiettivi di caratterizzare gli errori di misura prodotti da ogni fattore di influenza e di determinare la sensitività dei risultati di misura rispetto a queste fonti di errore. Questo è un passo fondamentale per stabilire la riferibilità metrologica delle misure CT e per il miglioramento dell'accuratezza di misura.

In questa tesi, gli effetti degli errori geometrici di un sistema CT sono studiati e determinati quantitativamente. Diverse campagne sperimentali sono state progettate e condotte allo scopo di determinare gli errori di misura causati dagli errori geometrici del *detector* e della tavola rotante. La sensitività dei risultati di misura rispetto agli errori geometrici investigati è analizzata e discussa, inoltre l'influenza della direzione di misura e del posizionamento del campione nel volume CT è determinata.

L'analisi e la determinazione degli errori geometrici è fondamentale nella metrologia a coordinate, e la geometria del sistema influenza tutta la catena di misura. Una descrizione

sperimentale dettagliata degli effetti prodotti dagli errori geometrici di un sistema CT non è ancora presente in letteratura.

Gli errori di misura causati dal *cone-beam artifact* – un fattore di influenza inerente alle scansioni con traiettoria circolare a fascio conico – sono studiati e mappati tramite investigazioni sperimentali. Una soluzione avanzata nel campo della tomografia per la metrologia, l'utilizzo di traiettorie di scansione elicoidali, è studiata in questa tesi allo scopo di sfruttare tutti i benefici che la tomografia può offrire in termini di accuratezza di misura, risoluzione e qualità di immagine. Le prestazioni metrologiche delle scansioni elicoidali sono investigate, ed anche gli effetti dei principali parametri di scansione elicoidali sull'accuratezza di misura.

Essendo una tecnica di misura estremamente polivalente, la tomografia computerizzata a raggi X offre la possibilità di scansionare una grande vastità di componenti industriali, i quali in alcuni casi sono caratterizzati da un'alta rugosità superficiale. È quindi di fondamentale importanza quantificare gli effetti della rugosità superficiale del componente scansionato sulle misure tomografiche dimensionali. A questo fine, diversi campioni di riferimento sono stati sviluppati in questo lavoro con lo scopo di mappare sperimentalmente gli effetti della rugosità sulle misure dimensionali tomografiche effettuate su profili di rugosità periodici. Delle campagne di simulazione numeriche sono inoltre state progettate ed eseguite per analizzare profili complessi da produrre sperimentalmente. Gli errori di misura causati dalla rugosità superficiale rispetto alle tradizionali misure a coordinate a contatto sono riportati e discussi, ed è presentato il modello sviluppato per la correzione degli errori causati dalla rugosità superficiale. L'incertezza di misura è calcolata secondo il metodo di sostituzione, e viene dimostrato come la correzione degli errori dovuti alla rugosità superficiale è fondamentale per una determinazione appropriata dell'incertezza di misura e per un significativo miglioramento dell'accuratezza di misura.

Table of contents

Chapter 1

Introduction

This Chapter provides an introduction to the role of CT in coordinate metrology and to the industrial state of the art. The challenges in order to use CT systems for dimensional quality control are presented and the aim of the PhD research work is discussed. A description of the PhD thesis structure is provided.

1.1. Computed tomography in industrial metrology

In industry, X-ray Computed Tomography (CT) has recently established its potential as an innovative non-contact coordinate measuring technique [1]. Thanks to its high capabilities and the benefits it provides, it has become an attractive alternative to conventional measuring techniques (e.g. traditional tactile and optical coordinate measuring machines (CMMs)) producing rapid developments [2].

In the field of precision engineering, the requirements of dimensional quality control are becoming more complex. The actual trends call for highly complex components, for example produced with the newly additive manufacturing (AM) technologies that enable the production of complex internal features with no material removal, or the quality control of parts produced by micro-injection molding and in general precision micro-manufacturing technologies. New measurement tasks, therefore, have become necessary in order to perform the quality control of such parts, providing accurate and reliable measurements [2].

To this extent, X-ray CT systems have shown their valuable application as new generation non-contact and multi-purpose coordinate measuring systems (CMSs) which enable to perform a wide variety of measurement tasks [3].

Although the well-known application of X-ray computed tomography in the medical imaging dates back to 1970s, and its subsequent use for Non-Destructive Testing (NDT) started from the 1980s, the most recent application of X-ray CT as non-contact measuring technique for coordinate metrology is recent and started in the first decade of this century [1, 4].

The use of X-ray CT for dimensional quality control has made a substantial transition from the NDT applications (e.g. defect/failure analysis, crack detection, etc.) moving from qualitative to quantitative analyses. In dimensional metrology, the field of application of CT is extremely wide, and includes a high number of sectors such as automotive, castings, electronics, traditional manufacturing techniques, additive manufacturing, etc [2].

The working principle of X-ray CT systems is based on X-rays propagation through the work-piece to be inspected and the recording of several radiographic projections containing information on the X-rays attenuation through the object by mean of specific hardware components [5]. By using dedicated reconstruction algorithms, the collected radiographic projections of the object are processed in order to obtain the volumetric model of the component under investigation, characterizing its whole internal and external features. By means of other specific algorithms which are used in order to determine the surface of the scanned object it is possible to determine the coordinates of the points of the object and thus to perform dimensional measurements on the CT volume [1].

On the CT generated volume, which is characterized by dense volumetric data, holistic measurements of the entire workpiece can be performed without any form of contact and need to cut or destroy the part. Among this measuring tasks, there are dimensional and geometrical measurements on inner and outer geometrical features, measurements on micro components and difficult to access geometries, CAD comparisons etc., which can be performed with micrometer accuracy [3, 6]. It comes that CT not only is a valid alternative to traditional tactile and optical CMMs, but also enables to perform measuring tasks which are not possible with conventional measuring techniques, thanks to its flexibility and the intrinsic characteristics of its measuring principle.

The application of computed tomography in the field of coordinate metrology is a field in continuous improvement and it is not limited to use of conventional CT circular trajectories, but includes the study of new solutions and innovations. To these extents, the use of innovative CT scanning trajectories in the coordinate metrology field, such as helical scanning, enables to enhance the flexibility of application of CT and to overcome some of the intrinsic limits of the conventional CT circular trajectories [2].

In all these contexts, CT capabilities are relevant in the whole product cycle. It can be used not only for industrial quality control and tolerance verification, but also for process and product development, production process optimization, design optimization, etc. Thanks to these advantages, the industrial environment is investing in the development and use of metrological CT systems for industrial metrology applications.

Even though CT has been applied for several decades in the medical field and for non-destructive testing (NDT), the use of CT systems as CMSs for dimensional metrology applications has introduced new fundamental requirements and the need of a deep understanding of the effects of the error sources affecting CT measurement chain on the measurement results. In order for CT systems to be recognized as CMSs capable of providing reliable and comparable measurements, the metrological traceability of CT measurements to the unit of length, the meter, has to be established [1]. This is a fundamental requirement for the use of CT systems in dimensional quality control, as prescribed e.g. by internationally accepted standards on quality systems management [7] and verification of Geometrical Product Specification (GPS) [8]. One necessary step in order to achieve CT measurements traceability is to determine the uncertainty of CT measurements. CT measurement accuracy moreover has become an important requirement with the use of CT systems for dimensional metrology. The enhancement of CT measurement accuracy by mean of error modelling and correction and development of new CT scanning solutions is a target in CT metrology. This in order to be able to provide accurate measurements especially in relation to high accuracy requirements in industry and verification of strict tolerances.

1.2. Aim of PhD project

CT systems are complex multi-purpose measuring instruments, for which the establishment of measurement traceability is a complex and challenging task. This is mainly related to the presence of several influence quantities in the CT measurement chain, that complexly interact and strongly affect CT measurement accuracy and because of which the determination of CT measurement uncertainty is a difficult task. Up to now, no internationally accepted standards for performance verification and measurement uncertainty determination are available for CT systems.

The identification of these error sources and the quantitative investigation of the effects they produce on the measurement results is a fundamental step in order to achieve CT measurement traceability. The understanding of the effects of error sources and the implementation of methods for error corrections in fact enable to improve CT systems metrological performance and to enhance CT measurement accuracy, e.g. by correcting known systematic errors, to properly determine CT measurement uncertainty by identifying the uncertainty contributions and taking into account the relevant uncertainty component in a suitable way, and thus to achieve CT measurements traceability. This PhD project dealt with these topics with the final aim of contributing to the research for traceability establishment and accuracy enhancement in industrial X-ray CT for coordinate metrology. In particular, the PhD research covered the following main aspects of CT measurement errors evaluation and accuracy enhancement: CT system geometrical errors determination, investigation on CT helical scanning for coordinate metrology and evaluation of the effects of cone-beam artifacts in conventional circular scanning trajectories, and finally determination of the effects of surface roughness in CT dimensional measurements.

The influence of CT system geometrical errors, including detector and rotary table geometrical errors, is studied by mean of experimental investigations, and the measurement errors as well as the sensitivity of CT measurements to various amplitudes of geometrical misalignments and to measurement direction and object positioning is determined for several CT system misaligned configurations. Geometrical errors are one of the most relevant influence quantity for coordinate measuring systems, and the whole CT measurement chain relies on the information needed to describe the geometry of data acquisition.

One fundamental information describing the CT scanning set-up is the scanning trajectory used. In this work, the use of helical scanning trajectories is investigated. Helical trajectories are an innovative scanning method in the CT metrology field, which, however, is not widely implemented due to its further complexity and the introduction of additional influence factors. The metrological performances of helical scanning are studied and compared to those of conventional circular scans. The significant advantages provided by helical scanning are demonstrated and discussed, together with the limits of conventional circular trajectories caused by specific influence factors which are experimentally determined. Moreover, the influence of the additional helical scanning parameters on the measurement results are determined and their optimization is provided. Helical trajectories constitute one of the possible advancements of CT coordinate metrology and strongly contribute to perform measurement tasks which cannot be performed with conventional circular cone-beam trajectories and to widen CT applications.

Among the various applications of CT in the metrology field, often workpieces characterized by high surface roughness are scanned. The scanned workpiece itself is an error source, and in particular the workpiece surface roughness can have a relevant impact on CT measurement accuracy and on the uncertainty of CT measurements. Detailed experimental and simulation analyses were designed and performed in order to study the effects of surface roughness on CT dimensional measurements on periodic roughness profiles. The understating of the effects of these influence factors is fundamental for measurement traceability establishment, and for accuracy enhancement. It is here demonstrated how the correction of the determined errors caused by surface roughness enables a substantial decrease of CT measurement uncertainty and a significant enhancement of CT measurement accuracy.

1.3. Thesis structure

The structure of the PhD thesis is here presented with an overview of the contents for each Chapter.

Chapter 2 provides an overview of industrial CT systems and their main components and X-ray CT measuring principles. The CT measurement chain and its steps, and the most relevant applications of computed tomography in the industrial metrology field are presented and discussed. The advantages provided by CT with respect to other coordinate measuring techniques are discussed.

Chapter 3 discusses the main concepts of measurement traceability and the role it has in coordinate metrology together with the requirements in order to obtain traceable dimensional measurements and a measurement uncertainty adequate for the specific task. An overview of the state of the art of CT standardization and its framework in the field of CT metrology is provided. Metrological performance verification and methods for measurement uncertainty determination are discussed. The main influence quantities affecting CT measurement chain and an overview of reference objects available in literature are presented and analyzed.

Chapter 4 investigates the influence of CT system geometrical errors on CT measurement results. The importance of CT system geometry in the whole CT measurement chain is first presented and discussed. The possible geometrical errors affecting CT system geometry are then theoretically analyzed (also by using the concepts of classical coordinate metrology), discussed and reviewed. Then various physically induced misalignments are studied by means of experimental investigations which were conducted in collaboration with North Star Imaging Inc., Minnesota, USA. Specifically, three different experimental campaigns are presented, each involving various misalignments and misalignment magnitudes. Detector angular misalignments (pitch, yaw and roll) are studied using two tactile CMM calibrated reference objects, a ball bar and a ball plate, in order to experimentally determine and quantify the effects of the mechanically induced detector angular misalignments on CT measurements and the dependency of measurement errors with the amplitudes of the misalignments, the measurement direction and object position in the CT volume. The effects of rotary table misalignments are investigated by means of a CMM calibrated ball plate; hence, the measurement errors and sensitivity of CT measurements to the experimentally induced misalignments are presented and discussed.

Chapter 5 deals with the use of an innovative and high potential alternative scanning method in CT metrology, CT helical scanning. The work was carried in collaboration with North Star Imaging Inc., Minnesota, USA. This Chapter focuses on the study and determination of the metrological performance and the measurement errors that affect CT helical scans and the advantages that helical scanning can provide for industrial applications, especially in relation to image quality and enhancement of CT measurement accuracy. The inherent limits of traditional circular scanning trajectories and the measurement errors due to cone-beam artifacts are experimentally studied and demonstrated by mean of a specifically designed experimental investigation using different cone-angles. Then the measurement errors and metrological performance in CT helical scanning are determined, and the investigation of the sensitivity of measurement results to the main helical scanning parameters is provided. CT helical scans are compared to conventional circular trajectories and the significant improvements that helical scanning can provide are experimentally shown. Finally, an optimization of helical scanning parameters is given in order to enhance CT measurement accuracy.

Chapter 6 studies the influence of surface roughness on CT dimensional measurements. First, CT dimensional measurements are compared to tactile CMM measurements and the different measuring principles are analyzed and discussed. Three reference objects, featuring different periodic roughness profiles, were specifically designed and manufactured in order to experimentally investigate the influence of surface roughness on CT dimensional measurements. Different sets of experimental analyses were performed in order to investigate the effects of surface roughness on CT dimensional measurements of periodic roughness profiles for varying surface morphologies and CT surface filtering characteristics. CT measurement uncertainty is calculated according to ISO 15530-3 and the effects of roughness errors correction on CT measurement uncertainty determination and CT measurement accuracy are discussed. An investigation on the influence of post-processing parameters on CT dimensional measurements performed on periodic roughness profiles is also provided. The specifically designed numerical simulation analyses conducted on a wide set of periodic roughness profiles and for various resolutions are discussed and the measurement results are reported and compared to the experimental results.

The model developed for surface roughness error determination in function of different periodic roughness profiles and CT surface filtering characteristics is presented and discussed.

Chapter 7 provides the main conclusions of the PhD research presented throughout the thesis and discusses the importance of the obtained results for the achievement of CT measurement traceability and the enhancement of the measurement accuracy.

Chapter 2

X-ray Computed Tomography for coordinate metrology

This chapter provides an overview on industrial CT systems and their applications for coordinate metrology purposes. First, the different types of industrial CT systems and their characteristics are presented as well as the fundamentals of X-ray CT working principle. A description of X-ray CT systems components and CT measurement chain is provided. Finally, the main industrial metrological applications of computed tomography are presented together with the main advantages that CT provides compared to traditional measuring techniques, and its current limits and challenges.

2.1. Industrial X-ray CT

A typical industrial CT system is constituted of three main components i.e. an X-ray source, a rotary table and kinematic system, and a detector. Visualization and computation units are also needed in order to serve as interface and set the scanning parameters needed to perform the CT scans, and to process and analyze CT acquired data. CT systems can be classified, as represented in Figure 2.1, based on their configuration and thus hardware components, and based on their scanning trajectories [1, 2]. A primary classification distinguishes between 2D systems (e.g. fan-beam systems) and 3D systems also known as cone-beam systems.

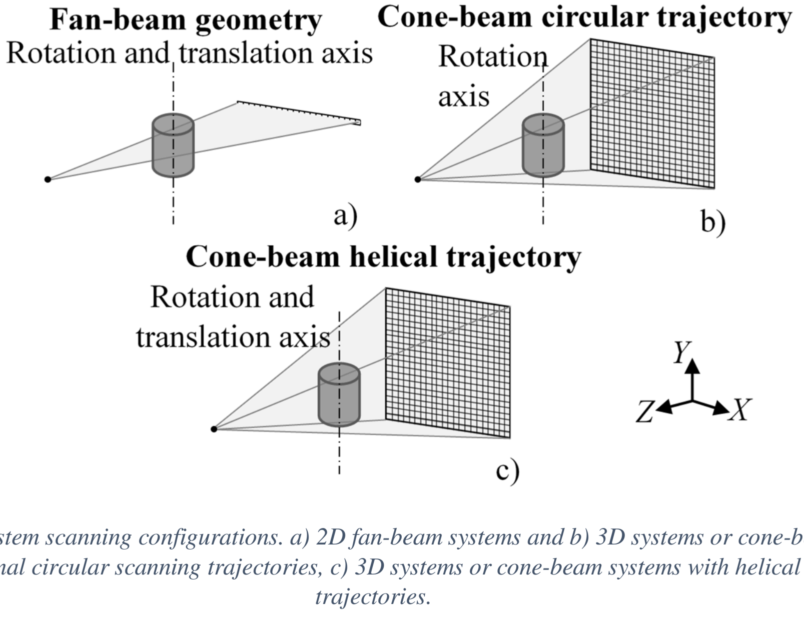

Figure 2.1: CT system scanning configurations. a) 2D fan-beam systems and b) 3D systems or cone-beam systems with conventional circular scanning trajectories, c) 3D systems or cone-beam systems with helical scanning trajectories.

Fan-beam systems make use of a fan shaped X-ray beam and a linear array detector constituted of a single row of pixels. With this scanning configuration the complete 3D model of the scanned object is obtained by translating typically the object along the vertical axis of Figure 2.1 a). At each of the selected *y* coordinates the object undergoes a rotational movement in order to collect 1D radiographic projections at multiple angular positions which will be combined into a slice of the object. The acquired CT slices at each y coordinate are then reconstructed into a volumetric model of the component. This kind of systems are thus called 2D systems because the object is CT scanned slice by slice and the information contained in each slice is bi-dimensional i.e. on the *xz* plane.

3D systems instead are characterized by a cone-beam shaped X-ray beam and a flat-panel detector. The use of a conical beam combined with a bi-dimensional detector constituted of several rows and columns of pixels enables to acquire for each angular step bi-dimensional X-ray projections and thus to obtain the 3D volume of the entire object without the need to translate the part vertically. This provides a significant reduction of scanning time compared to fan-beam systems. For example, if considering a flat-panel detector composed of 2000 rows of pixels, in order to acquire the same amount of information with a linear array detector it might take 2000 times more time [1]. However, fan-beam systems also have advantages over cone-beam systems. These include the reduction of X-ray scattering thanks to the presence of a single row of pixels, and the absence of cone-beam artifacts which typically affect cone-beam geometries [1,9,10]. Cone-beam artifacts will be further discussed in Chapter 5.

3D cone-beam systems can also be classified based on their scanning trajectory (see Figure 2.1) and can be divided mainly into: cone-beam systems with conventional circular trajectories (Figure 2.1 b)) and cone-beam systems with helical scanning trajectories (Figure 2.1 c)).

Cone-beam systems using conventional circular scanning trajectories are the most used ones in industrial practice [1,2], and their scanning trajectory basically consists of a rotation of 360° of the workpiece in order to acquire the volumetric information of the object. No translation of the object in the vertical direction is required. As introduced before however this kind of scanning trajectory in cone-beam systems is affected by the so called cone-beam artifacts also known as Feldkamp artifacts which are inherently present and cannot be eliminated but just reduced [9,10]. The larger is the cone-beam angle and the larger is the distance of the feature of interest from the central plane of the detector the more pronounced are the cone-beam artifacts [11].

Helical scanning trajectory instead is an alternative scanning strategy which, as represented in Figure 2.1 c) consists of a combined rotational and translational movement of the object along the rotation axis direction (i.e. the vertical axis of Figure 2.1 c)) [10,12]. Helical scanning trajectory is an innovative and powerful tool for CT industrial and metrological applications that enables to not only reduce and in theory eliminate the cone-beam artifacts but also other major advantages for CT applications such as scanning long objects exceeding the dimension of the detector in one single scan [2,13]. Chapter 5 will deal with the application of helical scanning trajectories for coordinate metrology and will provide detailed experimental investigations on the benefits that this technology (currently underutilized at the state of the art due to its further complexity) provides for metrological applications.

An additional distinction is made by dividing CT systems based on the characteristics of the X-ray focal spot [2]. The X-ray focal spot size in fact is related to the spatial resolution and image quality that a CT system can provide. In particular, three categories can be identified: nano-focus CT systems, micro-focus CT systems, and macro-focus CT systems [2]. While the first ones are characterized by a sub-micrometer focal spot size [14], the micro-focus and macro-focus CT systems are typically characterized respectively by spot sizes ranging from one to some tens of microns, and over 100 µm in the case of macro-focus X-ray CT systems [2]. Synchroctron CT systems also exists, in this case the resolutions that can be obtained can be in the order of 0.2 µm [2,15–17]. In general, the higher are the X-ray scanning powers that can be achieved, the larger are the dimensions of the components that can be scanned [1].

Independently from the type of CT system utilized, all X-ray CT systems measuring principle is based on the acquisition of a multitude of radiographic projections of the scanned object. In particular, these radiographs are acquired exploiting geometrical magnification concepts.
As visible in Figure 2.2 in fact, the scanned part is magnified by a factor *M*, depending on the distance between the X-ray source and the detector also called *SDD,* and the distance between the X-ray source and the object or *SOD*.

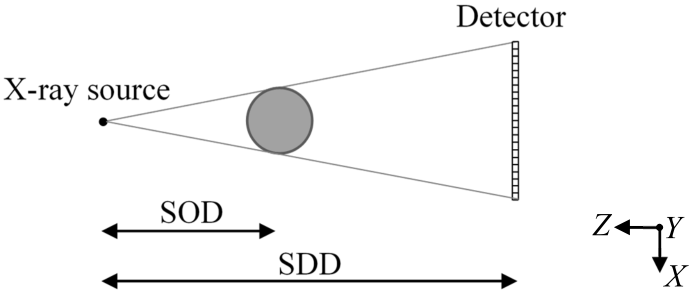

Figure 2.2: Schematic representation of the geometrical magnification of the sample.

The geometrical magnification used for the CT scan affects the resulting resolution, and thus the quality of the scan as it will be discussed in the following of the Chapter.
The projection acquisition step is just the first phase of the CT process chain, which comprises also the phases of volume reconstruction, surface determination and metrological analyses and it will be described in section 2.4. Together with geometrical magnification concepts, CT technology is based on the generation and interaction of X-rays with matter, the basic concepts of which are provided in the following.

2.2. Principles of X-rays physics

X-rays are electromagnetic waves that were discovered by the German physician W.C. Röntgen in 1895. They are characterized by a wavelength in the range of 0.01 nm to 10 nm [12]. The energy *E* associated to each photon is described by Planck’s law:

$$E = h \cdot \mathrm{f} = \frac{h \cdot c}{\lambda} \tag{2.1}$$

where h is Planck's constant ($6.626 \cdot 10^{-34}$ Js), c is the speed of light ($2.998 \cdot 10^{8}$ ms^{-1}), f is the frequency (Hz), and λ is the wavelength (m). Therefore, the smaller is the wavelength the higher is the energy of each photon.
In radiology the parameters that characterize an X-ray beam are [5]:

- Intensity: it is measured in A and describes the flux or amount of incident radiation flowing in the unit of time;
- Quantity: it is measured in kV and describes the energetic distribution of X-rays.

X-ray beams can be monochromatic this is the case for example of synchrotron radiation [2], or in most of the cases polychromatic i.e. the energy spectrum has different energy contents. In polychromatic X-ray beams, according to Equation 2.1, when λ decreases E increases.

In the energy spectrum of Figure 2.3 the intensity represents the vertical axis, whereas the quantity is represented by the horizontal axis and describes the penetration power of X-rays [1, 3].

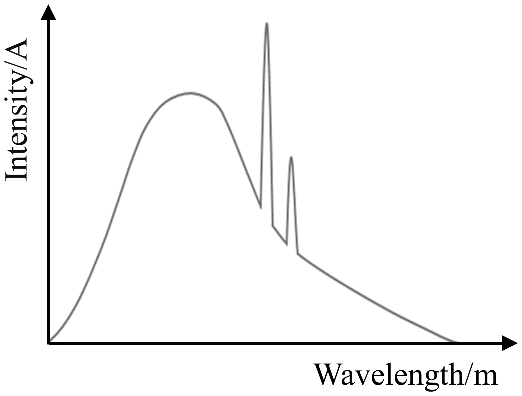

Figure 2.3: Schematic example of the representation of the X-rays energy spectrum in function of λ. Adapted from [3].

2.2.1. X-rays production

The X-rays production takes place in the X-ray source (see section 2.3) where the electrons emitted by the cathode, typically a tungsten wire, are accelerated by mean of the electric potential towards the anode acquiring a high kinetic energy. At the anode, the electrons hit the metal target where they are strongly decelerated, and their kinetic energy is converted into heat (99%) and X-rays (1%) [5]. It comes that the X-rays generation is a highly inefficient process which generates a significant amount of heat which has to be dissipated.

When the electrons hit the target two kinds of interactions can take place, both of them leading to X-rays production: "Bremsstrahlung radiation" or continuous radiation, and characteristic radiation [1,5,10,12].

Bremsstrahlung radiation or continuous radiation

The Bremsstrahlung radiation is the predominant X-rays production process. When the electrons reach the target with high kinetic energy they are strongly attracted by the positive nuclei of the atoms and are suddenly decelerated. The lost energy is emitted as X-rays with the same energy. The higher is the atomic number of the target material and the kinetic energy of the electrons the higher is the probability of this interaction. The Bremsstrahlung radiation produces a continuous spectrum as described in Figure 2.4 [1,10,12].

Characteristic radiation

When an electron with a sufficient energy hits one of the electrons of the inner shells of the target atoms this electron is ejected leaving a vacancy and an electron of an outer shell with a higher energy level occupy this vacancy. A photon with an energy equal to the difference of the energy levels of the two shells is thus released [10,12].
Each element has characteristic boundary energies therefore the characteristic radiation depends on the atomic number of the target material. The characteristic radiation thus produces some specific peaks that in the X-rays energy spectrum are superimposed to the energy spectrum produced by the Bremsstrahlung radiation, see Figure 2.4 [1,10,12].

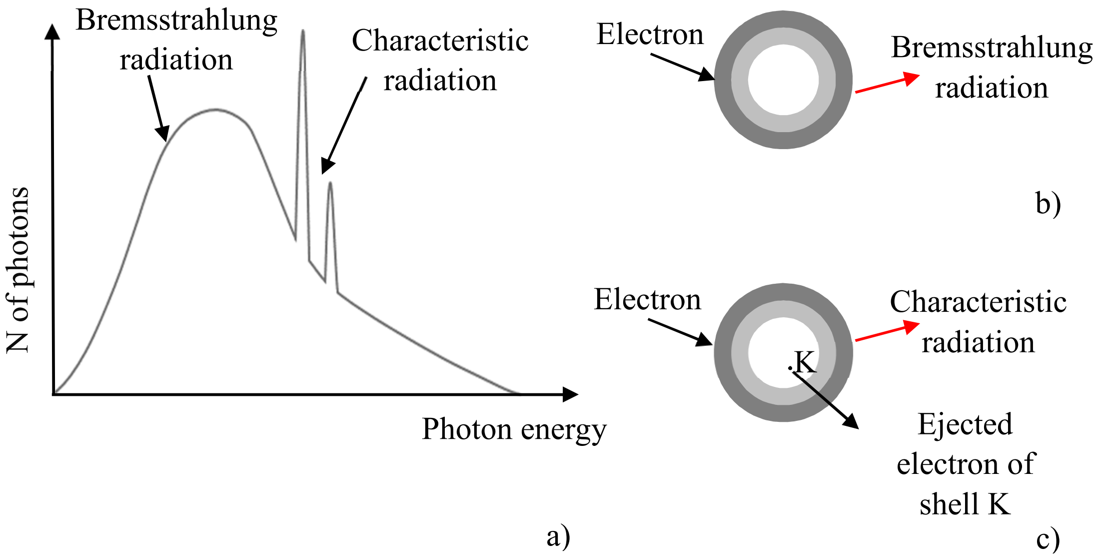

Figure 2.4:a) X-rays energy spectrum, b) Bremsstrahlung radiation, c) continuous radiation, an electron from e.g. shell K is ejected. Adapted from [12].

The X-rays energy spectrum is affected by the current, the voltage and physical filtering of the beam used in order to harden the beam (see section 2.4.1) [1,19]. The number of electrons flowing from the cathode to the anode is related to the current of the circuit whereas the energy content of the spectrum is determined by the electric potential between the cathode and the anode [1,12]. However, while the current affects only the intensity without modifying the quality of the energy spectrum and thus the penetration power of X-rays, the voltage influences both the quality and intensity of the beam. When increasing the tube voltage in fact, the X-rays spectrum is shifted towards higher energies and also the intensity of radiation is increased [1].

2.2.2. Interaction of X-rays with matter

When the X-rays impact with the component to be scanned, an interaction between the X-rays and matter occurs. This interaction can take place in different ways depending on the part of matter involved [10,12,16,17]. The result can be:

- A complete or partial loss of energy of the emitted photons, i.e. absorption;
- A change in the trajectory i.e. scattering. Scattering can be:
  - Elastic scattering, without loss of energy
  - Inelastic scattering, with a loss of energy.

There are 12 possible types of interaction between photons and matter which include the photoelectric effect, the Compton effect, Rayleigh scattering and pair production [18]. The interactions of major interest in the range of micro-focus X-ray CT systems industrial applications are the photoelectric effect and Compton effect which are discussed in the following [1].

Photoelectric effect

An X-ray photon with a sufficient energy interacts with an electron of the inner shells of the atom and is completely absorbed. This causes the ionization of the atom due to the ejection of the electron which acquires a kinetic energy equal to photon energy which exceeds the boundary energy [12,17]. The vacancy which is thus created is filled by one of the electrons of the outer shells with higher energy level as described in Figure 2.5 a). A photon of characteristic radiation is thus emitted (see section 2.2.1). The photoelectric effect is the predominant mechanism at low energies. The probability that the photoelectric effect occurs between a photon with energy E and a material with atomic number Z increases for materials with high atomic number and for low energies and thus high wavelengths [10,12].

Compton effect

A photon with a higher energy than the boundary energy interacts with one of the outer shells electrons of the atom causing the ejection of the electron and the deviation of the photon from its original trajectory [1,12,17]. The photons with higher energy are mainly deviated with an angle smaller than 90 ° [12]. The probability that the Compton effect takes place is directly proportional to the atomic number Z and indirectly proportional to the photon energy E. The Compton effect is thus predominant at high energies [17].

For the imaging the Compton effect produces negative influences in fact, the photons which are scattered with small angles can reach the detector and contribute to increase the noise [12].

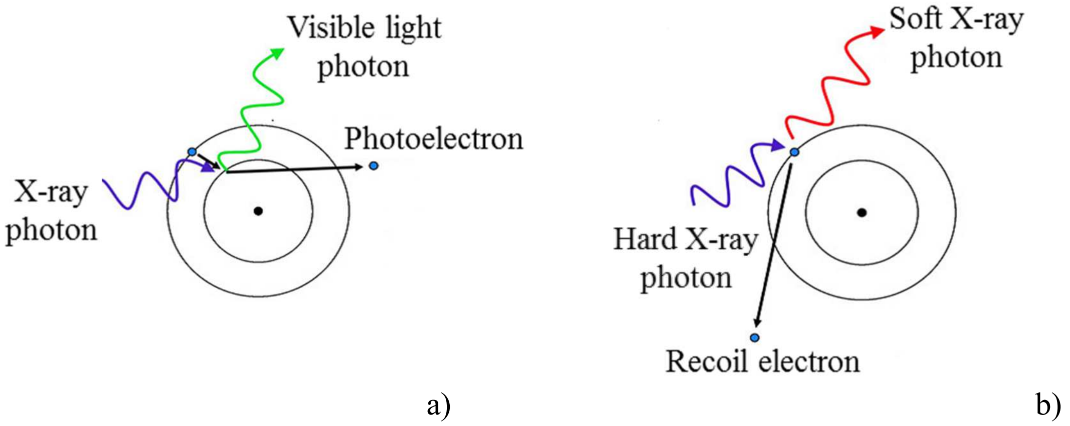

Figure 2.5: a) Schematic representation of photoelectric effect, b) schematic representation of Compton effect [1].

The above mentioned mechanisms are energy dependent, therefore, when the X-rays of the beam interact with the scanned object material, the processes described above can take place simultaneously each of them being caused by specific photons of the beam. This results in a decrease of the X-rays intensity which is called attenuation [10,16,19].
The Lambert-Beer's law describes the attenuation of the X-rays intensity in the case of a monochromatic beam and homogenous material:

$$I = I_0 \cdot e^{-\mu ds} \tag{2.2}$$

Where I_0 is the initial intensity of radiation, I is the intensity transmitted through a material with a thickness s, and μ is the linear attenuation coefficient. The X-rays intensity is thus exponentially attenuated according to Equation 2.2 when passing through the material.
In the case of non-homogeneous material and polychromatic radiation (i.e. composed of more energy levels) Equation 2.2 is rewritten as follows:

$$I = \int I_0(E) \cdot e^{-\int \mu(s,E)ds}\, dE \tag{2.3}$$

The number of photons which is transmitted through the object therefore depends on the energy level, the material thickness, and the type of material (density and atomic number). The linear attenuation coefficient $\mu(s,E)$ it also function of the photon energy. Typically, materials with low atomic number have a lower attenuation coefficient than materials with high atomic number. A high atomic number in fact means that the atoms contain more electrons and thus the probability of interaction with photons is higher and consequently also the attenuation [20].
Materials with lower density are also characterized, theoretically, by a lower probability of interaction and thus also a lower attenuation. These considerations are valid from a theoretical point of view, in fact as discussed above it has to be taken into account that the attenuation coefficient is dependent on the energy level [20].

In the energy range in which micro-focus industrial CT systems operate, that is dominated by photoelectric effect and Compton effect, the linear attenuation coefficient can be decomposed into two components:

$$\mu(E) = \mu_{ph}(E) + \mu_C(E) \tag{2.4}$$

Where μ_{ph} is the linear attenuation coefficient due to photoelectric effect, and μ_c is the linear attenuation coefficient due to Compton effect.

2.3. Components of a CT system

As introduced in section 2.1 a CT system typically consists of three major components, the X-ray source, the rotary table and kinematic system, and the detector.
The X-ray source produces the X-ray beam according to the physical principles described in section 2.2.1. The object to be scanned is positioned by mean of a kinematic system and is rotated typically 360 °. The emitted X-rays interact with the object material due to photoelectric effect and Compton effect (in the energy range of micro focus CT systems), and they are attenuated according to Equation 2.3. At each angular step of rotation an X-ray radiographic projection, containing information on the transmitted X-rays intensity, is recorder by mean of the detector. Subsequently, all the radiographic projections are processed by mean of specific algorithms in order to obtain the 3D model of the component.

In the following the main components of industrial CT systems are presented.

2.3.1 X-ray Source

The X-ray source typically consists of an X-ray tube which is composed mainly of two electrodes i.e. the cathode and the anode, the target, a system of optics and devices for collimation of the beam, and a window generally made of aluminum or beryllium in order to keep the vacuum inside the tube. Several other auxiliary components are also present in order for example to dissipate the heat produced at the target (see section 2.2.1). A schematic representation of an X-ray tube is given in Figure 2.6.

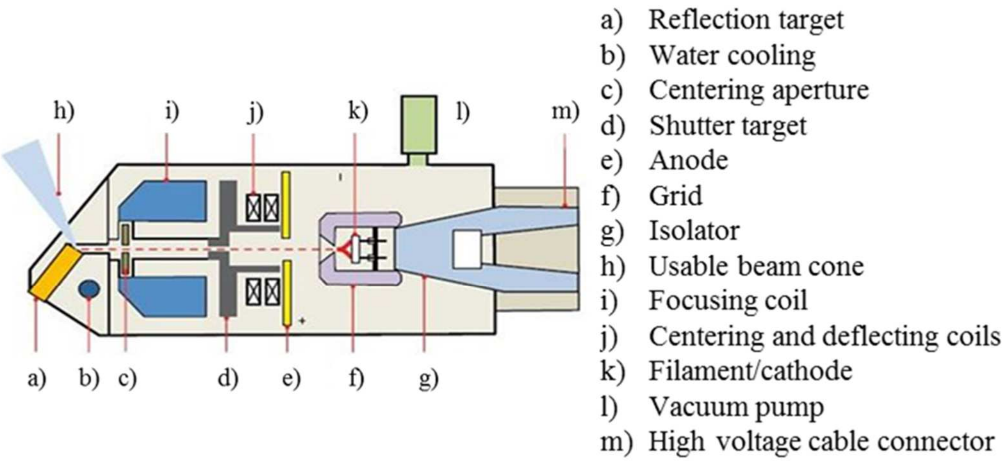

(Source: Viscom AG, Hannover, Germay)

Figure 2.6: Schematic representation of an X-ray tube [21].

The cathode is typically made from a tungsten wire whereas the anode generally consists of a metal part in which is embedded a metal target made from e.g. tungsten or molybdenum [1, 21].

There are configurations with fixed anode or rotating anode in order to facilitate the heat dissipation not only by mean of thermal conductivity but also by mean of thermal convection [1].

The target is the portion of material that is hit by the electrons coming from the cathode and from which the X-rays generation takes place. For the reasons discussed in section 2.2.1 it is typically made by high atomic number materials. Each material produces different X-rays spectra, and the higher is the atomic number of the target material the higher is the penetration power of the X-rays [5]. The portion of the target where the X-rays impact determines the focal spot dimensions. Ideally the X-ray focal spot is a point however in practice this is not possible due to the high amount of heat produced at the target [5]. In general, the higher is the X-ray power used the higher the dimensions of the X-ray focal spot. The X-ray focal spot dimension is an important characteristic as it affects the image quality and CT resolution [1]. The bigger is the focal spot the blurrier the X-ray images will be [1,14,20,22]. When using CT systems for performing metrological analyses the focal spot dimensions and in general CT resolution are important factors that affect the accuracy of the measurements [1,23]. The target can be a reflective target or a transmitting target. In reflective targets the X-rays are reflected by the target and are typically used for higher X-ray energies thanks to the easier heat dissipation [1,21]. In transmission targets instead the X-rays are transmitted by the target and lead to smaller focal spot dimensions, however they are not used for high energies due to the lower resistance to high temperatures [1,21].

Multi-material targets also exist in order to produce multiple X-rays spectra.

The X-ray tube current, voltage and physical philtering of the beam are important parameters that affect the X-ray spectrum as discussed in section 2.2.1 and that are selected by the user in the projection acquisition phase (see section 2.4.1).

2.3.2 X-ray Detector

The X-ray detector has the function to collect the transmitted X-ray radiation and to transform the acquired information into an electric output signal. This electric output signal is converted into grey levels that are stored in each radiographic projection acquired.

As introduced in section 2.2. X-ray detectors can be classified in line sensors and area sensor (flat-panel detectors).

Line sensors

Line detectors can be straight or curved and are composed by a mono-dimensional array of ideally uniform pixels. The acquired radiographic projections thus consist of a 1D grey level profile. At each full rotation of the sample they enable to acquire one single slice of the scanned object. In order to obtain the CT volume of the entire object it is thus required a translation of the component along the rotation axis direction.
Although the long scanning times required due to the possibility to acquire just one slice for each complete rotation, the use of line sensor presents some advantages [1]:

- Elimination of cone-beam artifacts;
- Higher accuracy: due to the presence of a mono-dimensional array of pixels the scattering is highly reduced;
- Resistance to higher energies;
- They enable to obtain a better Signal to Noise Ratio (SNR) thanks to the presence of thicker scintillators.

Area sensors

The area sensors are made from a bi-dimensional array of ideally uniform pixels and are used in combination with conical X-ray beams. This enables to collect 2D radiographic projections at each angular step. In this case indeed, with a full rotation of the object, the 3D volume of the component can be acquired. The scanning time is significantly reduced compared to line sensors. However, a significant drawback is the presence of cone-beam artifacts or Feldkamp artifacts which occur while moving away from the central plane of the detector.

The X-ray detectors are also classified based on their working principles [1]:

- Counting-type detectors or direct detectors: the output is proportional to the number of incident photons;
- Ionization detectors: the output is proportional to the energy for unit of mass;
- Scintillation type detectors or indirect detectors: the output is proportional to the total incident energy. They are called indirect detectors because the X-rays are converted into electromagnetic wavelengths in the range of visible light which then are transformed into an electric output signal by a photo diode.

Indirect detectors are widely used and are often based on amorphous silicon transistor/photodiode arrays positioned behind X-ray scintillators [1,24].

The X-ray detector characteristics impact on the CT scan. For example, the pixel size of the detector influences the resolution of the CT scan and its dimensions determine the maximum dimensions of the sample to be scanned (see chapter 5 on helical scans). Moreover, the properties resulting from its manufacturing process can impact on image quality. For example, detector pixels have to be uniform in size, and efficiency.

2.3.3 Kinematic systems

The kinematic system of a CT scanner mainly consists of:

1. Rotary table: enables the rotation of the sample at different angular steps. The rotation can be continuous or stepwise;
2. A horizontal translation axis namely the z axis or magnification axis which allows for the positioning of the rotary table with the object along the z direction (see Figure 2.2). The rotary table position determines the source to object distance *SOD* according to Figure 2.2 and thus the geometrical magnification of the object. The closer is the object to the X-ray source the bigger is the geometrical magnification;
3. A vertical translation axis namely the *y* axis: it enables the positioning of the rotary table with the object along the y direction (see Figure 2.2). In the case of fan-beam systems the translation along the rotation axis direction is necessary to acquire the different slices of the object whereas for cone-beam helical trajectories it is a necessary movement in order to perform the helical scan. For conventional circular cone-beam trajectories the y axis is needed just for the positioning of the part within the field of view;
4. A horizontal translation axis namely the *x* axis, in order to position the sample within the field of view (see Figure 2.2).

Additional translation axes may also be present.

The hardware components of a metrological CT system have to be characterized by high accuracy and geometrical and thermal stability. Encoders are also used in order to monitor the position of the rotary table along the axes.

The accurate determination of the geometry of a CT system is a fundamental influence factor that occur in CT process chain and that affect all the following phases [25]. The determination of the effect of CT system geometrical errors and misalignments is a necessary step towards traceability of CT measurements [25,26,27]. Chapter 4 deals with the effect of CT system geometrical errors on CT measurements.

Finally, metrological CT systems are characterized by temperature controlled cabinets or in general are positioned into temperature controlled environments in order to maintain the temperature at 20°C which is the reference metrological temperature [28].

2.4. X-ray CT process chain

The main steps of the X-ray CT process chain are summarized in Figure 2.7.

Figure 2.7: Main steps of X-ray CT process chain.

2.4.1. X-ray radiographic projections acquisition

The first phase consists of the CT scan of the component. Before starting the scanning process, the sample has to be positioned on the rotary table by mean of a proper fixture. Typically foam and low absorbing materials such as carbon-fiber reinforced polymers are used for creating the fixtures thanks to their almost transparency to X-rays. The sample fixing is an important step especially when metrological tasks have to be performed. The fixture in fact has to guarantee a stable positioning of the component in order to avoid any unwanted movement during the rotation. Moreover, thermally stable materials should be preferred when creating the fixture in order to avoid deformation or expansions/shrinkage of the fixture. Typically, once the proper fixture has been created the sample is let stabilize for an appropriate time (inside the temperature controlled cabinet of the system or in the temperature controlled environment at 20 °C in the case of metrological systems) in order to achieve thermal and mechanical stability.

When positioning the object on the rotary table and when creating the object fixture, it is fundamental to choose the object orientation in the proper way. The length travelled by the X-rays and e.g. the presence of cone-beam artifact is dependent on the object orientation and affect CT measurement accuracy and image quality [29–31].

In order to perform the CT scan, the operator then has to select the scanning parameters. The most relevant scanning parameters include, the magnification, the X-ray voltage and current, the exposure time, the X-rays physical filtering and the number of projections.

As described in section 2.1 the magnification is the term used to express the geometrical magnification of the object during the CT scan. The magnification factor *M* is calculated according to Equation 2.5 as the ratio between the source-to-detector distance *SDD* and the source-to-object distance *SOD:*

$$M = \frac{SDD}{SOD} \tag{2.5}$$

The smaller is the *SOD* the bigger is the magnification. The magnification is related to the resolution of the CT scan. In fact, when the magnification increases the voxels size of which the CT volume is composed decreases:

$$Voxel\ size = \frac{p}{M} \qquad (2.6)$$

Where p is the pixel pitch of the detector.
The voxel, whose term stands for volumetric pixel, is the equivalent in 3D of the pixel. These concepts will be clarified when discussing the CT volume reconstruction step.
When the magnification increases however also the blurring due to the finite focal spot dimensions increases [1,32]. This influences negatively the CT scan resolution.

The maximum magnification that can be used is determined by the dimensions of the sample and of the X-ray detector. When using helical trajectories however the vertical dimensions of the detector are not a constraint as it will be discussed in chapter 5.

Once the geometrical magnification has been defined also the remaining scanning parameters have to be set. The X-rays voltage and current have to be carefully selected by the user within the operating range of the machine taking into account the material of the object, its dimensions and geometries and the required task and accuracy. The X-ray power, given by the product of current and voltage has to be sufficient in order to penetrate the object otherwise artifact will occur in the reconstructed volume [1,12]. In metrological applications, one of the aims is also to use a low scanning power. High scanning powers in fact increase the focal spot dimensions and thus the blurring. Physical filtering is also typically used in order to harden the beam i.e. the remove the soft X-rays. This reduces the beam hardening effects [20,33,34].
The number of projections is also defined by the user and determines the number of angular step in correspondence of which an X-ray radiographic projection is acquired. The bigger the number of projections the higher the amount of information contained on the CT scan. However, the used of a high number of projections significantly increase the scanning time. The number of projections acquired may vary between several hundreds to more than 3000 projections depending on the measurement task to be performed.

At the end of the X-ray projections acquisition phase therefore, a set of several radiographic images have been recorder, each of them containing different grey levels which are a measure of the X-rays attenuation trough the component for each angular step (typically from 0 ° to 360 °).

2.4.2 Volumetric model reconstruction

In this phase the recorded radiographic projections are reconstructed into a 3D volume of the object by mean of specific software and algorithms.
The 3D model of the object is composed by voxels, the three-dimensional equivalent of the pixel, each of them being characterized by a singular grey value which corresponds to the local attenuation in the given position. For each X-ray projection in fact, the recorded grey level represents the sum of the attenuation coefficient along the path followed by the X-rays [1,10,12]. All this information contained in each projection are processed by specific algorithms in order to assign to each voxel one single and representative grey value.

The most widely implemented approximate reconstruction algorithm for cone-beam geometries is the FDK algorithm developed by Feldkamp, Davis and Kress in 1984 [9]. This algorithm is based on the filtered back projection algorithm (FBP) [10,12]. Figure 2.8 gives an overview of an object reconstruction obtained with different number of projections using the FBP algorithm.

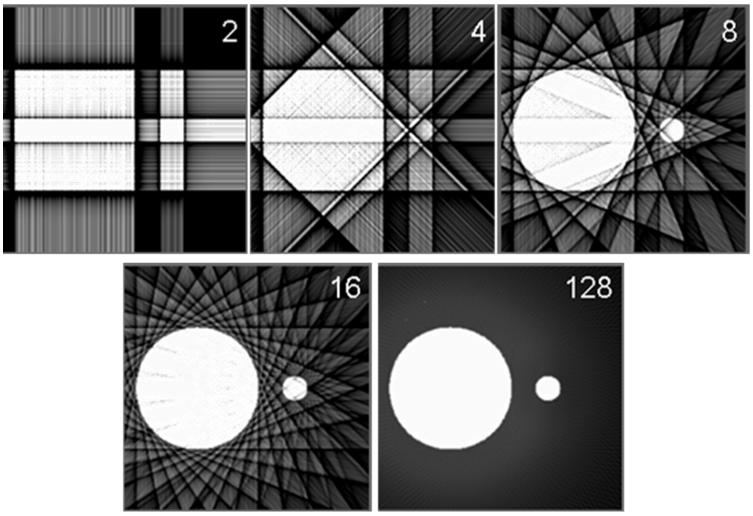

Figure 2.8: Schematic representation of and object reconstruction by mean of the filter-back-projection algorithm, using different number of projections i.e. 2-4-8-16-128 projections [source http://www.impactscan.org/slides/impactcourse/basic_principles_of_ct/img15.gif, accessed on September 30, 2017].

During the reconstruction phase it is possible to correct via software some of the artifact which may be generated in the CT scan such as beam hardening.

2.4.3 Surface determination

The surface determination step is essential in order to perform the metrological analyses on the reconstructed volume. It is one of the most critical phases in CT process chain and strongly affects CT measurements accuracy [15,35–38].

After the reconstruction the 3D CT model consists of several voxels containing grey levels information related to different attenuations of X-rays. In order to perform the metrological analyses, it is necessary to use this information to determine the surface of the component.

The surface detection is operated by mean of a thresholding process in which the threshold value between the object material and the background (e.g. air) is determined [1,14,20].

A simple method in order to perform the surface determination is the so called ISO-50 [1] (Figure 2.9).

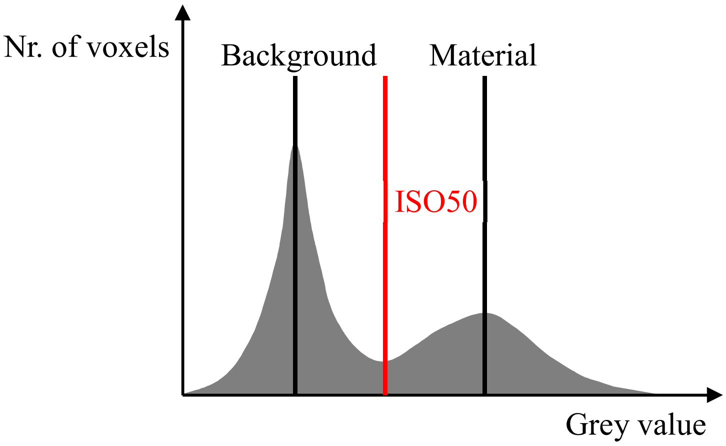

Figure 2.9: Determination of ISO-50 threshold value in a mono-material object. Adapted from [3].

By analyzing the histogram containing in the horizontal axis the grey values and in the vertical axis the number of voxels, in the case of a mono material component there will be two peaks, one corresponding to the object material and one to the background (in the case of multi-material objects more peaks will be present).

The threshold value (red line in Figure 2.9) is identified as the average grey value between the two peaks. Therefore, all the voxels with a grey value bigger that he ISO-50 will be considered material, whereas all voxels with a grey value smaller that the ISO-50 will be considered background. The threshold determined in this way is applied to the whole dataset, for this reason the ISO-50 method is a global method [1].

As visible in Figure 2.9 some intermediate grey values between the background and material peaks exist. This is because of the partial volume effect [1,39] which causes the transition between the background and the object to be characterized by voxels with intermediate grey values. In fact, due to CT acquisition principles, the voxels close to the surface are just partially covered by material and thus have an intermediate grey level. The surface determination software performs an intra-voxel interpolation in order to obtain a sub-voxel accuracy [39]. The partial volume effect and related concepts are analyzed in detail in chapter 6.

The ISO-50 method can be used in the case of homogenous and mono material objects assuming that no artifacts are present. In real CT scans however, due to non-homogenous objects and e.g. beam hardening and scattering effects this method is not accurate enough being a global method and could lead to the presence of additional artifacts or errors due to an erroneous surface determination [40].

For a more accurate surface determination a local adaptive method is typically used [39,41]. In this case the ISO-50 value can be used as a starting point and subsequently a more refined method based on the grey values gradient is used to locally search for the surface within a user determined search distance [39].

The surface determination step strongly influences CT measurement accuracy [1,3,35]. For example, the use of a too high threshold causes an underestimation of external dimensions and an overestimation of the internal dimensions. The opposite in the case of a too low threshold.

As it will be discussed in section 3.7 some features are influenced by the threshold [3,35].

2.4.4 Metrological analyses

Once the surface of the object has been determined the metrological analyses can be performed.

These analyses can be performed directly on the voxel volume by mean of specific software, in this case however the computation effort needed in order to handle the measurements on the CT volume (which might consist of several GB) is highly relevant. Another possibility is to export the point cloud of the voxel model or the STL model and then perform the measurements of interest. In the latter two cases it is not necessary to use CT dedicated software and also the computation effort is definitely smaller, however the creation of the mesh introduces additional errors which can be of significant relevance.

In general CT dimensional analyses can involve:

- The fitting of primitive geometrical elements on the voxel model or e.g. on the extracted point cloud or STL model;
- Nominal/actual comparisons between for example the CT volume and the CAD model of the part.

2.5. Industrial metrological applications of X-ray computed tomography

In the recent years, industrial X-ray computed tomography has successfully entered the field of coordinate metrology thanks to its broad range of applications and unique advantages offered [2,6].

In the ‘80s X-ray CT started to be use in industrial practice typically for classical NDT applications providing visual and qualitative information on the scanned object. NDT applications include material characterization and defect analyses such as crack detection, porosity analysis etc [2]. These kind of testing however do not provide quantitative information on the scanned part, and can be performed directly on the CT volume without the need to perform the surface determination step.

With the advent of X-ray CT in the field of coordinate metrology another substantial and major advantage offered by CT has started to be exploited, the possibility to obtain quantitative information from the CT three-dimensional volume of the scanned object [1,42,43]. With the opening of these new horizons, a wide variety of new and complex measurement tasks have become possible on several industrial applications, combining material characterization and quality control in one single scan.

One of the key aspects of the use of CT in the modern industry is the possibility to perform quantitative analyses on a lot of different applications in a variety of markets, ranging e.g. to micro-injection molding components to turbine blades, and at several stages of the different products cycles enabling optimization of products and processes [2, 42–44].

This is a high relevant factor, in a market which is evolving towards miniaturization of parts and high complex geometries produced with additive manufacturing technologies [38,45].

In the following an overview of the main categories of industrial CT metrological applications is provided.

Tolerance verification

By fitting primitive geometrical elements such as circles, planes, cylinders, etc. on the CT volumetric model (or point cloud or STL model) after the surface determination step has been performed, it is possible to calculate dimensions, distances, form errors etc. of the fitted geometrical elements and thus to perform geometrical product specification (GPS) verification tasks. In order to perform these tasks, the definition of a reference system is required, following the classical principles of coordinate metrology. Measurands have to be well defined, and for each of them it is necessary to specify the number of fit points, the evaluation criterion, etc. Figure 2.10 shows an example of tolerance verification on the CT volume of a scanned parted obtained by micro-machining.

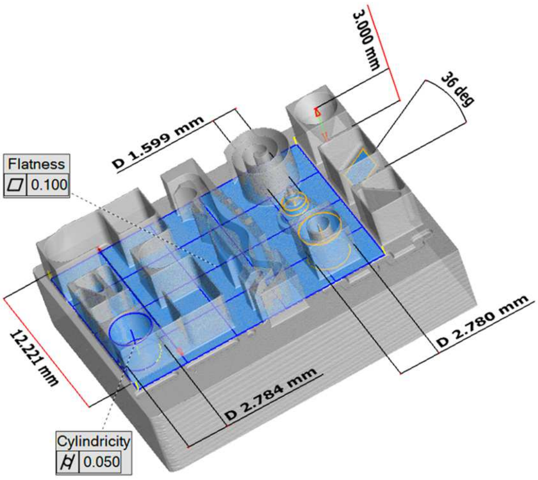

Figure 2.10: Example of various measurements performed in the CT volume. Courtesy of University of Padova. – Lab. TE.SI.

Dedicated software for performing metrological analyses on CT volumes are available. Being a non-contact measuring technique CT allows for the verification of GPS on both internal and external features of the part without the need to cut or destroy it. This is one fundamental advantage provided by CT as it will be described in section 2.6.

Nominal/actual comparison

In this case the CT volume (or surface model) is compared with a reference model for example the CAD model of the part which is used thus used as the nominal model. A fundamental requirement in order to perform an accurate nominal/actual comparison is the alignment of the CT volume and the reference model, which can significantly influence the results.

The output of the analysis consists of a colored map providing quantitative information on the local deviations from the nominal model as shown in Figure 2.11.

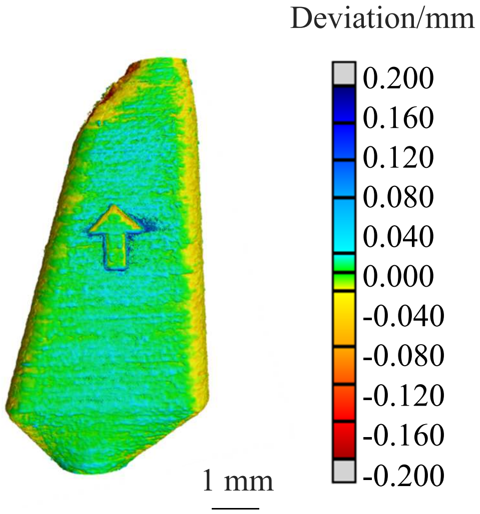

Figure 2.11: Example of nominal/actual comparison with colored map providing the local deviation from the CT volume and CAD model of the part. In this case a micro valve produced by additive manufacturing is reported. Courtesy of University of Padova. – Lab. TE.SI.

As visible this kind of comparison enables to obtain not only a visual and qualitative information on the deviations, but also to determine the quantitative value of the particular deviation in the specific point and the point coordinates on the measurement volume. Besides using the CAD model of the part it is also possible to use models obtained from different measuring systems, e.g. tactile and optical coordinate measuring machines (CMMs), or to compare CT volumes of the same component scanned in different stages, for example in the case of a micro-milling tool before and after the machining process.

Other analyses: porosity analysis, wall thickness analysis and fiber orientation analysis

From a CT scan it is also possible to perform other quantitative analyses, such as porosity analysis. As visible in Figure 2.12, CT enables to provide qualitative and quantitative information on the location of pores, their volumes (e.g. assuming a spherical shape of pores) and their equivalent diameter. The output of the analysis consists e.g. on colored maps reporting these pieces of information.

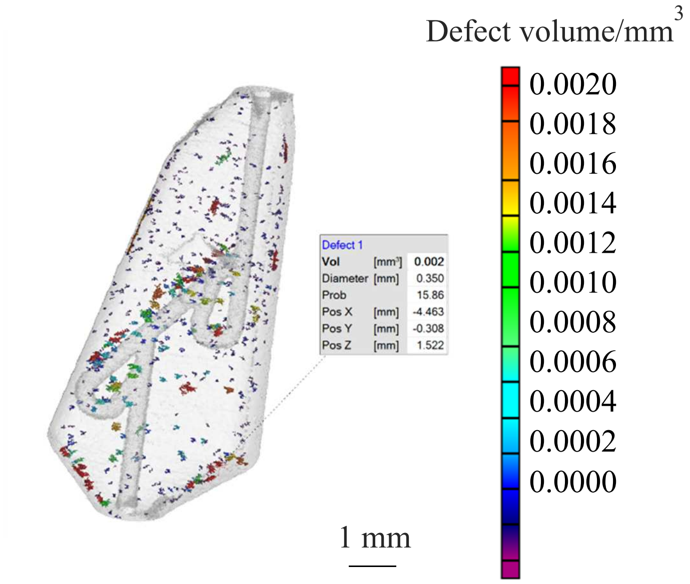

Figure 2.12: Example of porosity analysis in a micro valve produced by additive manufacturing. Courtesy of University of Padova. – Lab. TE.SI.

CT enables to perform also other kinds of analyses including wall thickness analyses, and fiber orientation analyses e.g. on fiber reinforced materials. In the first case the output of the CT scan is a colored map reporting quantitative information on the wall-thickness of the component, in the second case the output of the scan is a colored map reporting information on the fiber orientation and density as reported in Figure 2.13.

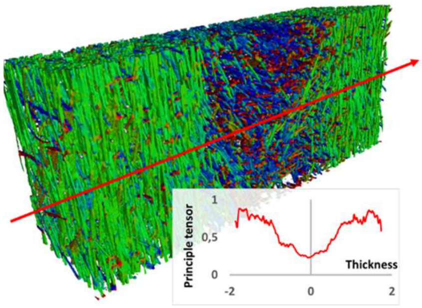

Figure 2.13: Example of fiber orientation analysis. Courtesy of University of Padova. – Lab. TE.SI.

2.6. Comparison of X-ray CT and other coordinate measuring systems

X-ray computed tomography is a powerful and innovative technology that enables the possibility to solve a wide variety of measurement tasks.

In particular, by comparing X-ray CT with traditional tactile CMMs that currently provide the reference in industrial practice [46–48] and with other state of the art equipment such as optical measuring systems, CT is a very flexible technology which allows to solve more measuring tasks that often are not possible with the above mentioned measuring techniques.

Moreover, CT measurements can be performed on several steps of products life cycle and on extremely different components including micro components, automotive and aerospace parts, complex parts produced by additive manufacturing (AM), biomedical applications etc. CT systems can thus be defined as new generation multi-purpose measuring systems [3].

.

The advantages that CT offers are unique. In the following a summary of the advantages provided by CT over traditional measuring techniques is reported:

- ✓ Dimensional analysis in a non-destructive way on internal or non-accessible features;
- ✓ Measurements on deformable components;
- ✓ Measurements on any kind of surface regardless of color and reflectivity;
- ✓ Holistic measurements on the entire workpiece and material analysis in a single scan;
- ✓ Acquisition of dense volumetric information;
- ✓ Analysis of assemblies (i.e. components in the assembled state);
- ✓ Reverse engineering;
- ✓ Quantitative defect analyses.

As discussed CT allows to obtain a complete 3D model of the object with highly-dense information in a relatively short amount of time. Being based on X-rays attenuation principles as described in section 2.2 X-ray CT is a non-contact measuring technique which thus does not require any form of contact with the scanned workpiece. It comes that one of the major advantages provided by CT is the possibility to measure inner geometrical features or in general non accessible geometrical features without any need to cut or destroy the part. This is a serious issue when using tactile and optical coordinate systems. In the first case in fact, a mechanical contact between the probe stylus tip and the feature of interest is always required, whereas when using optical systems the surface needs to be accessible to the optical sensor. It comes that in both cases it is not possible to measure internal non accessible features; the only way is to cut the part. However, it is well known that the sectioning of the part always alters its original characteristics. In the case of tactile systems, it is also worth noting that the smallest feature which can be measured is limited by the minimum dimensions of the probe (which in general cannot go down than 0.2 mm). When using CT, depending on the resolution and on the part characteristics, it is also possible to measure smaller features.

All these tasks can be performed also on soft components which typically are difficult to accurately measure with tactile CMMs.

Another advantage provided by CT is the possibility to measure any kind of surface regardless its shape, color and reflectivity. This is often a serious issue for optical systems.

CT also allows to analyze components in the assembled state. This task is usually not possible to perform with traditional measuring instruments. Typically, in fact, the various components of the assembly are analyzed singularly however, the compliance to the specifications of the single component in the disassembled state does not necessarily mean the proper functioning of the whole assembly.

Moreover, it is possible to exploit CT dense volumetric data in order to perform reverse engineering, CAD comparisons etc.
It follows that no competitive measuring systems exist in many cases.

With the advent of CT into the coordinate metrology field however, new challenges have been set in order to obtain traceable CT measurements. A summary of CT disadvantages is given:

- ↓ Several influence quantities affect CT process chain and need to be studied;
- ↓ Possible presence of artifacts in the CT scans;
- ↓ Lack of standardization;
- ↓ Traceability to the unit of length is not well defined yet;
- ↓ Limits on sample dimensions due to penetrability of material.

Full metrological traceability needs to be established to allow CT measurements to be traced back to the unit of length, the meter. This is still a challenge in CT measurements due to the interaction of multiple and complex error sources that affect CT process chain. Due to the complexity of the technology, and its recent application in the field of coordinate metrology, internationally accepted standards for verifying CT systems metrological performances and to determine CT measurement uncertainty still lack.
In the following chapter traceability of CT measurement is discussed.

Chapter 3

Traceability of X-ray CT measurements

The chapter discusses the concepts of measurement traceability in CT measurements and its requirements. An overview on the state of the art of standardization for computed tomography for dimensional metrology is provided; furthermore, the current limitations and challenges for establishing CT measurement traceability and enhancing CT measurement accuracy are studied and analyzed. The current testing procedures for metrological performance verification of CT systems and the different methods applicable for CT measurement uncertainty determination are also reviewed and discussed. Then an overview of the reference objects available in the literature for the testing of CT systems is presented, and the identification and classification of the influence factors affecting CT measurements is discussed.

3.1. Metrological traceability of measurements

Metrological traceability is the property of a measurement result whereby the result can be related to a reference through a documented unbroken chain of calibrations, each contributing to the measurement uncertainty [49].

Traceability is thus the property of a measurement result and it is obtained through an unbroken chain of calibrations performed in different stages. In each of these stages, a reference workpiece or a measuring instrument, whose metrological characteristics have already been determined in a previous stage, are used to calibrate the measuring instrument or measuring object of the following stage. In each of these calibrations, performed under controlled and documented environmental conditions, the relationship between the value of the quantity given by the measuring object and the corresponding indications provided by the measuring instrument is established [49]. In each of these steps, the measurement uncertainty is calculated and is called calibration uncertainty. The uncertainty for each step is influenced by the uncertainties of all the previous steps.

By mean of this documented unbroken chain of calibrations a traceability chain is realized as described in Figure 3.1.

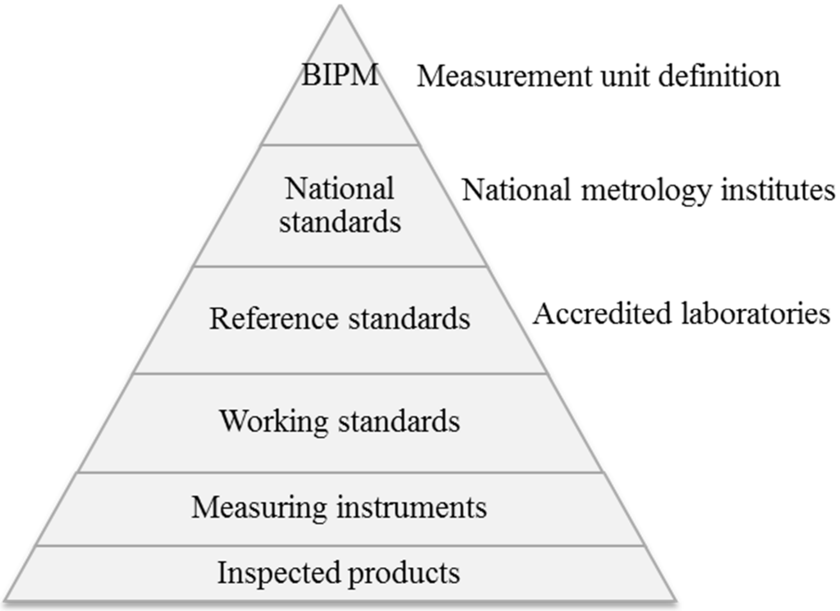

Figure 3.1: Traceability chain. At the bottom of the chain there is the part which has to be inspected.

At the bottom of the chain there is the product to be inspected. By going back in the traceability chain each stage is linked to the previous one by documented calibrations until reaching the definition of the unit in the international system (SI) which in the case of dimensional measurements is the meter. In this way, it is possible to link, by mean of these following steps, the measurement results of the products to be inspected to the unit of length.

As stated in the Guide to the expression of Uncertainty in Measurements (GUM) [28] the result of a measurement is only an approximation or estimate of the value of the measurand and thus is complete only when accompanied by a statement of the uncertainty of that estimate.

Therefore, a complete description of the measurement result is given by:

$$Y = y \pm U \tag{3.1}$$

where y is the measurement value and U is the expanded uncertainty.

With reference to Equation 3.1 the closeness of agreement between a measured quantity value and a true quantity value of a measurand defines the measurement accuracy, as reported in the International Vocabulary of Metrology (VIM) [49].

3.1.1. The role of traceability in dimensional quality control

Measurement results cannot be compared, neither between them, nor with reference values provided in the specifications it they are not traceable to the unit of length by mean of an unbroken chain of comparisons with stated measurement uncertainties [50].

The need to guarantee reliable and comparable measurements, and thus the possibility of parts interchangeability and the requirement to be able to prove technically and legally

the quality of products, are some of the reasons for which it is necessary that the measurement results are traceable to the unit of length.
Traceability is a requirement of the following international standards:

- ISO 9001: *Quality management systems – Requirements* [7];
- ISO 17025: *General requirements for the competence of testing and calibration laboratories* [51];
- ISO 14253-1: *Geometrical Product Specifications (GPS)-Inspection by measurement of workpieces and measuring equipment – Decision rules for proving conformance or non-conformance with specifications* [8].

3.1.2. Decisional rules for proving conformance or non-conformance with specifications

ISO 14253-1: *Geometrical Product Specifications (GPS)-Inspection by measurement of workpieces and measuring equipment – Decision rules for proving conformance or non-conformance with specifications* defines the decisional rules for proving conformity or non-conformity to specifications. These rules are valid in the case in which the conformance of a manufactured product to specifications expressed under the form of tolerances in the technical drawing has to be proven, and also in the case of measuring equipment for which specifications are expressed in the form of maximum permissible errors (MPE).
In both cases the standard states that it is necessary to take into account the measurement uncertainty in order to prove conformance or non-conformance to these specifications.

In the design phase, the component or measuring equipment is compliant to specifications if the metrological characteristics for which the compliance has to be determined are within the lower specification limit (LSL) and upper specification limit (USL), see Figure 3.2.
In the verification phase, the measurement uncertainty reduces the amplitude of the conformity and non-conformity zones as shown in Figure 3.2.

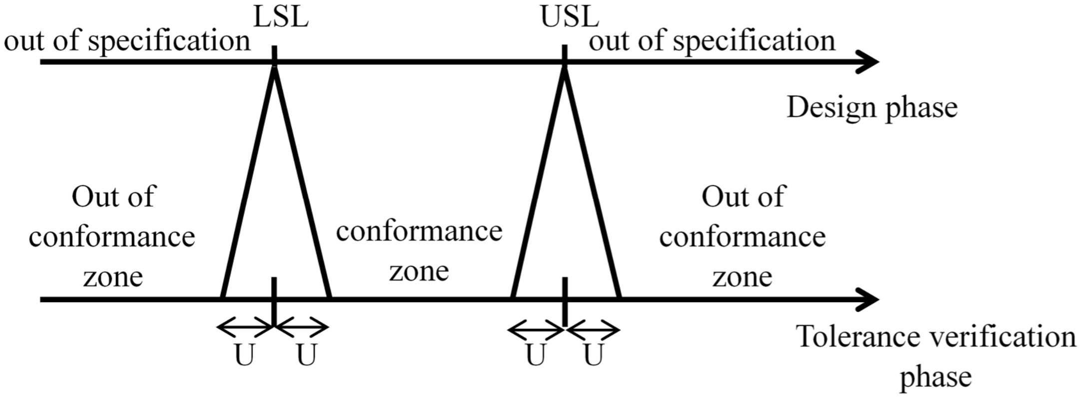

Figure 3. 2: Decisional rules for proving conformance or non-conformance to specifications according to ISO 14253-1.

Therefore, the bigger is the measurement uncertainty the smaller the conformance zone will be.
According to ISO 14253-1 a component is compliant to specifications if Equation 3.2 is respected:

$$LSL + U < y < USL - U \tag{3.2}$$

where y is the measurement value U is the expanded uncertainty calculated assuming a coverage factor of k=2 if not otherwise specified.
In the same way a component is non-compliant with specifications if:

$$y < LSL - U \; or \; USL + U < y \tag{3.3}$$

It might be the case that the conformity or non-conformity cannot be proved. This happens when the measurement result is in proximity of the upper or lower specification limits and thus $y \pm U$ includes one of the specification limits. In this case the measurement result is in the so called ambiguity zone.

A high measurement uncertainty thus significantly reduces the amplitude of the conformance zone and enhances the probability that the measurement results are in the ambiguity zone or outside the specifications. This means that the measurement uncertainty has to be correlated to the specification limits. The smaller is the specification zone the smaller has to be the uncertainty of measurement. A good compromise between the costs generated by the measurements and the costs generated by the non-acceptance of a component due to the too high measurement uncertainty has to be found.

3.2. Introduction to CT measurements traceability

With the introduction of CT systems in the field of dimensional metrology and thus their use as coordinate measuring systems (CMSs) the traceability of CT measurements has become a fundament requirement in order to perform dimensional quality control and to guarantee the comparability of products [1,15,18,42,48,52].
As discussed in chapter 2 CT systems are new generation multi-purpose coordinate measuring systems [3] which enable solving a wide variety of measuring tasks. However, being complex measuring systems there are a multitude of influence quantities affecting CT measurement results [30]. These quantities arise throughout the entire CT process chain, which includes several steps i.e. the CT scanning of the part, volume reconstruction, surface determination and dimensional analyses. These influence quantities complexly interact in a non-linear way, this makes extremely difficult to develop a function expressing the relationship between the measurement result and the influence quantities.
At an international level, the basic idea in order to obtain traceable CT measurements is to make use of the knowledge on coordinate measuring machines (CMMs) and to apply it and adapt it to CT. CMMs in fact are typically used to determine reference measurements and widely accepted international ISO standards are present (e.g. ISO

10360 series [53]. The use of the same concepts which are applied for traditional CMMs moreover enable the comparability between different coordinate measuring systems (CMS) [48].

Besides the various influence quantities affecting CMM measurements however several additional influence quantities arise in CT process chain and affect CT measurement results. The study of the effects of these influence quantities and the determination of the measurement errors caused on CT measurements is fundamental to obtain CT measurements traceability as it will be discussed in section 3.7. Moreover, the knowledge on the specific error sources and their effects enables the possibility to enhance CT measurement accuracy.

The steps which are needed in order to study and determine the accuracy of CT measurements and CT measurements traceability include:

- Metrological performance verification of CT systems;
- Determination of the influence quantities and analyses of their effects on the measurement results;
- Determination of task specific measurement uncertainty.

In order to perform these steps typically reference objects are used as it will be discussed in section 3.6.

3.3. State of the art of CT standardization and guidelines in dimensional metrology

As discussed in the previous section, CT is an extremely complex measurement technology which is affected by several influence quantities complexly interacting. Significant effort therefore is needed in order to develop and establish procedures and standards suitable for CT coordinate measuring systems [54].

Being a well-known NDT technique from the ‘80s international and European standards as well as national guidelines not related to the use of X-ray CT in dimensional metrology are available and include ISO 15708 series [18], EN 16016 series [55], ASTM E1441[56], ASTM E1570 [57], ASTM E1672 [58], ASTM E1695 [59], ASTM E1935 [60].

For the above mentioned reasons however currently no internal standard is available for CMS using CT principles. At the international level, the ISO Technical Committee (TC) 213 Working Group (WG) 10, responsible for creating international standards for the acceptance testing of CMSs, is currently working on creating a future part of ISO 10360 for CMSs using computed tomography [54,61,62]. The future standard on CT in the ISO 10360 series is assumed to get the identification ISO 10360-11 [61].

At a national level the German VDI/VDE has developed a series of guidelines for the use of CT systems for dimensional metrology. Table 3.1 provides the description of the VDI/VDE published guidelines.

Standard/Guideline	Title	Status
VDI/VDE 2630-Part 1.1	Computed Tomography in dimensional measurement - Basics and definitions.	Published
VDI/VDE 2630-Part 1.2	Computed Tomography in dimensional measurement - Influencing variables on measurement results and recommendations for computed tomography dimensional measurements.	Published
VDI/VDE 2630-Part 1.3 (VDI/VDE 2617-Part 13)	Computed tomography in dimensional measurement - Guideline for the application of DIN EN ISO 10360 for coordinate measuring machines with CT sensors.	Published
VDI/VDE 2630-Part 1.4	Computed Tomography in dimensional measurement - Measurements procedure and comparability.	Published
VDI/VDE 2630-Part 2.1	Computed Tomography in dimensional measurement - Determination of the uncertainty of measurement and the test process suitability of coordinate measurement systems with CT sensors.	Published

Table 3.1: Overview of the VDI/VDE guidelines available on Computed Tomography for dimensional metrology.

While part 1.1 and 1.2 of the VDI/VDE 2630 [63,64] series deal respectively with the basics and definitions and with the influencing variables on measurement results for CT in dimensional metrology, VDI/VDE 2630-Part 1.3 (VDI/VDE 2617-Part 13) [65] deals with acceptance and reverification tests of CMMs with CT sensors, whereas VDI/VDE 2630-Part 2.1 [66] concerns the measurement uncertainty determination and test process suitability of CMSs with CT sensors.

In particular, due to the lack of internationally accepted standards on CMSs using CT measuring principles, VDI/VDE 2630-Part 1.3 is currently used in industry [62].

As it is visible VDI/VDE 2630-Part 1.3 provides the guidelines for the application of ISO 10360 [53] for coordinate measuring machines with CT sensors. As discussed before in fact the aim in the CT standardization framework is to enable the comparison of different CMSs (as well as between different CT systems) [54]. These principles are taken into account in the standardization and research environment dealing with CT for dimensional metrology.

Significant work is currently performed by national and international organizations for standardizations and in the research environment in the field of CT for coordinate metrology. International inter-comparisons related to various aspects of CT metrology have also been performed enabling a broad overview of CT current status for coordinate metrology [47,67].

The development of widely accepted procedures for metrological performance verification of CT systems and CT measurement uncertainty determination and the understanding and determination of the effects caused by the influence factors affecting CT dimensional measurements are fundamental steps towards the achievement of CT measurements traceability and measurement accuracy enhancements. The following sections will deal with the discussion of these topics.

3.4. Performance verification of CT systems

At the international level the ISO 10360 series [53] provides the reference for CMS testing. The aim of the acceptance and reverification testing procedures established in ISO 10360 series is:

- to specify the acceptance tests for verifying the performance of a CMM as stated by the manufacturer;
- to specify reverification tests that enable the user to periodically reverify the performance of the CMM.

In the first case, acceptance testing is performed in order to verify if the metrological characteristics of the CMM are within the Maximum Permissible Errors (MPE) stated by the manufacturer. In the second case the user periodically reverifies the metrological characteristics of the CMM. In this second case however the user defines the boundaries i.e. the MPE which is suitable for its own range of applications. In acceptance testing instead the MPE stated by the manufactured is the specification and if the machine does not perform within this MPE in the acceptance testing procedure the machine is out of specification and thus can be rejected.

The basic idea in acceptance and reverification testing is to establish procedures constituted by a series of measurements which are representative of the CMS performance under specific boundary conditions. These kind of testing at the same time must be economic but also provide reliable information on the CMS metrological performance [52]. However, it is not in the scope of acceptance and reverification testing procedures to investigate on specific individual error sources in CT measurements. Due to the simplified nature of these testing the measurement errors might be smaller than when measuring real workpieces. This is because, for complex CMSs as CT the complexity of the measurement tasks might differ significantly and thus the effects of specific error sources on CT measurements [1,2,22,29,30]. As it will be discussed later for CT systems as for CMMs the measurement uncertainty varies with the specific task [46,68,69].

At the state of the art, as described before, the reference for acceptance and reverification testing is provided by the German guideline VDI/VDE 2630 – Part 1.3 (2011-12) which is discussed in the following.

In close reliance to ISO 10360-2 [70] and ISO 10360-5 [71] VDI/VDE defines the metrological characteristics Probing Errors and Length measurement errors.
The basic idea is to look at the CMS as an integrated system and to test the global and the local error behaviors of the CMS.

In order to perform these kind of tests, calibrated reference objects are typically used. An overview of the main reference objects available at the state of the art for performance verification testing is given in section 3.6.

Probing Errors

Probing errors describe the local error behavior of the CT system and typically are obtained by measuring calibrated reference objects such as spheres, spherical calottes, or objects containing combinations of spheres. In all cases the reference objects used for assessing probing errors must be characterized by negligible form errors and surface roughness.

It is recommended to perform the test at two different magnifications and to measure the probing errors in six positions in the measuring volume.

Probing errors are divided into Probing errors of form (PF) and Probing errors of Size (PS).

The Probing error of form is calculated as the difference between the maximum and minimum distance of the measured points from the center of the regression sphere computed by mean of Gaussian Least-squares fitting, as expressed in Equation 3.4

$$PF = R_{max} - R_{min} \tag{3.4}$$

where R_{max} and R_{min} are respectively the maximum and minimum distances from the center of the regression sphere.

The Probing error of size is defined as the difference between the measured sphere diameter D_a and the calibrated sphere diameter D_r:

$$PS = D_a - D_r \tag{3.5}$$

Length measurement errors

Length measurement errors are used in order to test the global behavior of the CT system. In this case the calibrated samples used for testing the length measurement errors include ball bars, gauge blocks, ball plates hole plates etc. It is worth noting that the use of e.g. gauge blocks or hole plates for the testing of CT systems might involve the penetration of a relevant thickness of material. The influence of material thickness is a research topic of high interest in CT metrology and is currently a subject of ISO test surveys [61,72,73].

In close reliance with ISO 10360-2 the test prescribes to measure 5 different bi-directional lengths in 7 different spatial positions. Each measurement must be repeated 3 times for a total of 105 measurements.

The length measurement error E_L is defined as:

$$E_L = L_a - L_r \tag{3.6}$$

Where L_a is the measured length and L_r the calibrated length.
The E_L test therefore prescribes the measurement of bi-directional lengths. In coordinate metrology, bi-directional measurements involve the probing of a single point on each end of e.g. a step gauge by approaching these probing points by diametrically opposite directions. Uni-directional measurements instead involve the probing of a single point on each end of the gauge by approaching the points by the same direction. The difference between bi-directional and uni-directional lengths is reported in Figure 3.3.

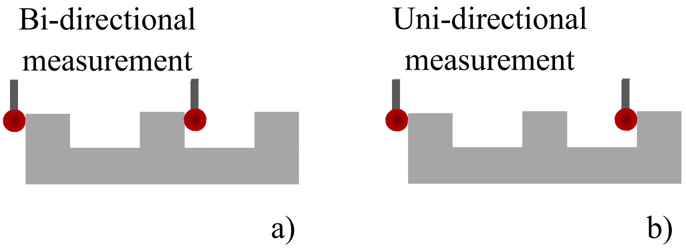

Figure 3.3: a) example of bidirectional measurement on a step gauge, b) example of unidirectional measurement on a step gauge.

However as introduced before, often when testing the metrological performance of CT systems calibrated reference objects characterized by the combination of several spheres are used. One of the reason is because when measuring sphere center-to-center distances and in general unidirectional length [35] there is no significant influence of the threshold (see section 3.7). When performing bidirectional lengths instead the measurement results can be significantly affected by the surface determination step [3].

In the case of spheres center-to-center measurements VDI/VDE 2630 part 1.3 defines the metrological characteristic *SD* sphere distance error calculated as the difference between the measured sphere center-to-center distance and the calibrated sphere center-to-center distance. In this case however, the probing errors of form are not fully taking into account due to the averaging effects which are present when computing the spheres centers. The VDI/VDE part 1.3 therefore suggests to take the probing errors into account separately and suggests two procedures. One of them includes the scanning of an additional gauge block for each length, the second one is a more simplified procedure and consists of adding the calculated probing errors to the *SD* obtaining in this way a worst case scenario. It is worth noting that if applying this second method in presence of big probing errors also the length measurement errors will present relevant values.

After having performed the tests the system is compliant to the specifications if:

$$\begin{gathered} PF < MPE_{PF} \\ PS < MPE_{PS} \\ EL < MPE_{EL} \end{gathered} \tag{3.7}$$

The test uncertainty according to ISO/TS 23165 [74] has to be taken into account as described in section 3.1.2.

Structural resolution

In addition to the above mentioned tests, the VDI/VDE 2630 part 1.3 suggests also possible methods for testing the structural resolution of CT measurements. According to VDI/VDE 2630 part 1.3 the structural resolution describes the size of the smallest structure that can still be measured dimensionally and must be distinguished from the structural resolution in the grey scale range of the voxels. In fact, the structural resolution encompasses the complete dimensional measurement chain (e.g. it includes the thresholding process).

The structural resolution is an important characteristic to be tested, as it provides additional information to those acquired when testing length measurements errors and probing errors. For example, increasing low-pass filtering improves the probing errors of form however at the same time worsens the structural resolution for dimensional measurements. Research studies on the structural resolution as well as proposed methods for its testing are discussed in [62,75–80].

3.5. Measurement uncertainty determination

As discussed in section 3.1 the determination of measurement uncertainty is a fundamental requirement in order to achieve CT measurement traceability. According to the international vocabulary of metrology (VIM), the measurement uncertainty is defined as the non-negative parameter characterizing the dispersion of the quantity values being attributed to a measurand, based on the information used [49]. As stated in the GUM, the measurement uncertainty is necessary in order to provide complete information on the measurement result. The measurement results therefore have to always provide information on the measurement uncertainty in order to enable the achievement of measurement traceability.

The determination of measurement uncertainty for CT systems is currently studied by many authors in the research field [48,81–84].

CT measurement uncertainty determination is a difficult and challenging task, mainly due to the complex and multiple influence quantities that interact in CT process chain, the study of which is thus fundamental [27]. For complex coordinate measuring systems like CT systems the complexity of the measurement tasks to be performed can be extremely different. For example, a state of the art micro-focus CT system can be used for measuring e.g. polymeric parts produced by injection molding and characterized by geometrical features in the order of some hundreds of microns, as well as for measuring e.g. metal automotive parts with dimensions in the order of several tens of millimeters. It is clear that in the two cases the measurement accuracy and measurement uncertainty can be significantly different. CT measurement uncertainty therefore has to be related to the task, and therefore is referred to as task specific measurement uncertainty [68].

It comes that the performance verification procedures and tests described in section 3.4, which aim at testing the metrological performance of the CMSs under specific and controlled boundary conditions are not enough to guarantee the metrological traceability of CT measurements [52,54]. In industrial practice in fact CT systems are rarely used to measure regular geometries of selected materials and sizes, and as previously discussed cover a wide range of applications [2]. Measurement traceability can thus be obtained only if the task specific measurement uncertainty is determined.

Due to the above mentioned reasons CT measurement uncertainty determination is a difficult task for CT users. This has been also demonstrated in the results of the CT Audit an inter-comparison organized by University of Padova [47], and the InteraqCT comparison on assemblies organized by the Technical University of Denmark [67].

At the state of the art, there are no international standards available for CT measurement uncertainty determination. The German guideline VDI/VDE 2630 part 2.1 has been published in 2015 and currently it is the only published document specifically drafted for CT measurement uncertainty determination. As reported in the guideline several methods could be options for CT measurement uncertainty evaluation, which are [66]:

- Uncertainty budget according to ISO/IEC Guide 98-3;
- Uncertainty budget using the simulation approach, Monte Carlo method (see GUM Supplement 1);
- Uncertainty budget using calibrated workpieces (ISO 15530-3 approach).

The first method is the method proposed by the GUM [28] which is based on the development of an analytical model for the determination of measurement uncertainty. The model has to express the relationship between the influence quantities affecting the measurement process and the measurand, as well as the effects that the variations of these influence quantities produce on the measurand. However, in the case of complex CMS as CT systems, the development of such a model is extremely difficult due to the numerous and often unknown influence quantities affecting the measurement chain. All the influence quantities have to be taken into account in order to have a representative model, however this is not always possible; the identification of the influence quantities themselves might be a challenging task. Moreover, the development of such model also implies the knowledge of the single uncertainty components, this however it is not always practically possible due to the complex interaction of several influence quantities. For all these reasons, up to now just a few simplified studies have been performed on this method [29].

The second method is based on the use of simulation, in particular the Monte Carlo method [85], in order to calculate CT measurement uncertainty. In this case the measurement uncertainty is determined by mean of several simulations in a similar way as for the "*virtual* CMM" [86]. Some studies on CT measurement uncertainty determination by mean of simulation are reported in [22,84]. Also in this case however, the knowledge of all the influencing factors is needed as well as the set-up of an analytical model describing the relationship between the influence quantities and the measurand and its sensitivity to the influence quantities.

The last method is regarded by many authors in literature and in the research field as the most practical one, and has been proposed and discussed in several research studies [82,87,88]. The VDI/VDE 2630 part 2.1 guideline focuses on this method, as the suitable one for CMMs equipped with CT sensors, and describes its application when dealing with CT measurement uncertainty determination.

The procedure proposed in the VDI/VDE Guideline consists on the application of the approach described in ISO 15530-3 "*Geometrical Product specifications (GPS)– Coordinate measuring machines (CMM): Technique for determining the uncertainty of measurement – Part 3: Use of calibrated workpieces or measurement standards*" [89] to CT sensors.

In order to apply the method a workpiece similar in dimensions and geometry to the one for which the measurement uncertainty has to be evaluated (which in the following will be referred to as real workpiece) has to be calibrated (e.g. by a CMM) and used as masterpiece for the uncertainty determination procedure [89]. This is done in order to achieve traceability for the specific task.

On the masterpiece, several repeated CT scans will be performed under the same conditions that will be used when measuring the real workpiece and with the same CT system that will be used when performing the measurements on the real workpiece. The same conditions include same measurement procedure, environmental conditions, positioning and orientation of the workpiece. In particular, the positioning and orientation of the workpiece, and the environmental conditions should vary within the limits accepted in the real measurement process in order to take into account the variability that could occur in the real measurements. However, as specifically expressed in the VDI/VDE 2630 part 2.1 document, it is strongly recommended to perform the measurements on workpieces identical to the real workpiece to be tested (i.e. it is recommended that the masterpiece and the real workpiece are identical). In fact, it is well known that, when dealing with CT measurements, even a small change in the penetration length or on the workpiece orientation could cause the presence of artifacts or significant variations on the measurements [61].

By knowing the calibrated values for each measurand and the repeated measurements performed on the masterpiece it is possible to determine the measurement uncertainty for each measurand. The estimated measurement uncertainty will be referred to the specific task, as each measurand will have a calibrated value and its own estimated measurement uncertainty. After this process, when real measurements will be performed on the real workpiece, it will be possible to associate to these measurements the corresponding measurement uncertainty calculated before.

The application of the method on CT measurements is described in Figure 3.4.

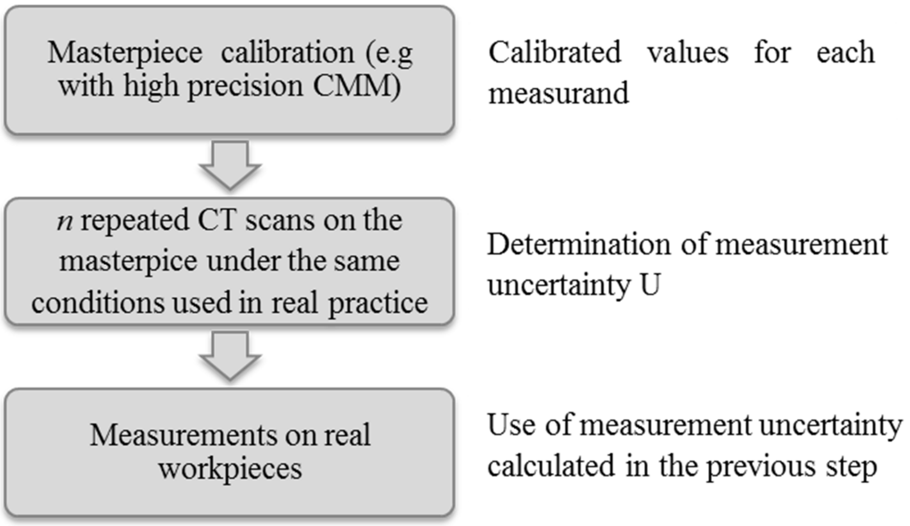

Figure 3.4: Application of ISO 15530-3 approach to CT measurements.

In order to have statistically significant data, it is recommended to perform at least 20 measurements. The measurement cycle shall contain all the actions which will be performed in the real measurement cycle to guarantee the same conditions. Moreover, it is recommended to perform these measurements under varying conditions raging within the limits accepted in the real measurements (e.g. different operator, mounting and remounting of the workpiece etc.)
The uncertainty budget takes into account the following uncertainty components and is performed according to Equation 3.8:

$$U = k \cdot \sqrt{u_{CAL}^2 + u_P^2 + u_W^2 + {u_b}^2} \tag{3.8}$$

Where

- u_{CAL} is the standard calibration uncertainty;
- u_p is the standard uncertainty of the measurement procedure;
- u_w is the standard uncertainty due to variations in material and production;
- u_b is the standard uncertainty due to the correction of systematic errors;
- b is the systematic error.
- k is the coverage factor (equal to 2, assuming a normal distribution, for a confidence level of 95%).

The measurement result thus will be expressed as reported in Equation 3.9:

$$Y = (\mathrm{y} - b) \pm U \tag{3.9}$$

Where y is the measured value, U is the expanded uncertainty calculated according to Equation 3.8 and b is the systematic error calculated as follows:

$$b = \bar{y} - x_{CAL} \tag{3.10}$$

Where x_{CAL} is the calibrated value and $\bar{y}$ is the average value of the n repeated measurements.

Equation 3.8 is in accordance with the GUM which, when dealing with the presence of known systematic errors, prescribes to compensate for these errors by applying a correction.

The correct treatment of systematic errors is an important issue when dealing with CT measurements and especially when comparing CT and tactile CMM measurements which rely on different acquisition principles. In chapter 6, which deals with the influence of surface roughness on CT dimensional measurements, this topic is discussed in detail and the effects of surface roughness on CT dimensional measurements and CT uncertainty are described.

An overview of the advantages and disadvantages of the method is reported in the following:

Advantages of the method:

- ✓ If properly applied it provides a realistic estimate of measurement uncertainty with no need of establishing a mathematical model describing the function that relates the input quantities and the measurand;
- ✓ The global variability is taken into account and, therefore, it is not required to know all the single uncertainty components that occur in the measurement;
- ✓ The experimental approach enables to take into account all the effects that influence the measurement. When using the simulation approach or the analytical approach this is more difficult because in these cases all the influence quantities should be input in the model;

Disadvantages of the method:

- ↓ Calibrated workpieces similar (strongly recommended identical) to the ones for which measurement uncertainty has to be estimated have to be available;
- ↓ The time to perform the procedure is relevant;
- ↓ When several different workpieces have to be inspected, more calibrated workpieces are required. This increases time and costs.

3.6. Reference objects

As discussed above reference objects, typically calibrated by mean of accurate and high-precision tactile CMMs, are used for the testing of CT systems. In general, reference objects can be used for assessing CT systems metrological characteristics and thus for performance verification, in order to study and determine CT specific error sources, and

for task specific measurement uncertainty determination. The design of reference objects developed for CT systems often is based on similar concepts of the reference objects typically used for coordinate measuring machines, taking into account constraints given by CT specific effects (e.g. CT physics depends on X-rays penetration of the material and not on mechanical or optical measurements).
An overview of different reference objects available in literature, and used for different purposes is given in Figure 3.5.

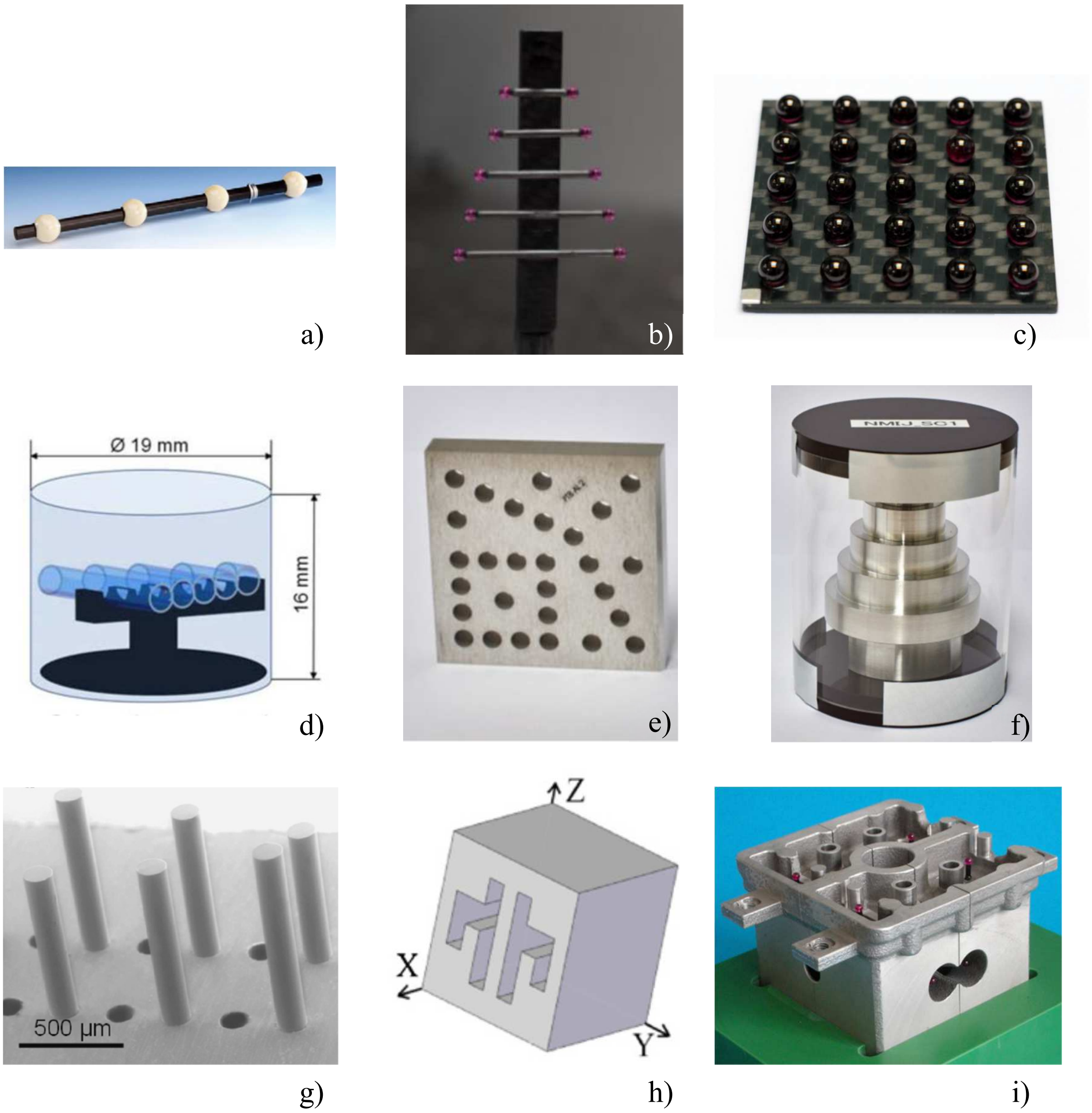

Figure 3.5: Overview of different reference objects available in literature. a) ball bar [90], *b) CT tree* [3], *c) ball plate* [3], *d) Panflute gauge* [47], *e) hole plate* [61], *f) step cylinder* [61], *g) fiber gauge* [15], *h) test object with parallel groves [35], i) workpiece-near reference standard* [91].

Often CT dedicated reference objects comprise the combination of two or more spheres made of ruby or ceramic and glued on a carbon-fiber reinforced polymer frame, as in Figure 3.5 a), b) and c). Carbon-fiber is used for its thermal stability and for its low attenuation coefficient. Ruby and ceramic spheres are often used since they are typically characterized by accurate production processes leading to extremely small surface roughness and form errors. During the design of the reference objects, especially when using high density materials, it is essential to take into consideration the spheres diameters in order to achieve a sufficient X-rays penetration.

Figure 3.5 a) shows an example of a calibrated ball bar providing one sphere center-to-center measurement along one direction. In Figure 3.5 b) it is represented the CT tree a reference object developed by DTU [3], which can be used for performance verification of CT systems and for scale errors correction (see section 3.7). Also in this case the object has calibrated sphere center-to-center distances, however in this case multiple lengths (5 as required by ISO 10360-2) can be tested in one single scan. Figure 3.5 c) shows a ball plate with calibrated sphere center-to-center distances, which provides information on multiple directions in one single scan.

While the above mentioned objects typically provide information on sphere center-to center measurements, reference objects specifically designed in order to perform bi-directional measurements are present in literature (it should be noted that in the case that a point-to-point bi-directional length between two spheres is calibrated also samples composed by several arrangements of spheres can provide bi-directional measurements). Figure 3.5 d) provides a description of the PanFlute gauge a reference object developed at Univeristy of Padova and consisting of five tubes with nominal inner diameter of 1.5 mm, nominal outer diameter of 1.9 mm, but different lengths (ranging from 2.5 to 12.5 mm) supported by a carbon-fiber reinforced polymer frame. The measurands of interest on the PanFlute gauge are inner and outer diameters ad tubes lengths. Therefore, it allows evaluating bi-directional measurements (tube lengths) but it is not suitable for testing probing errors.

The above mentioned reference objects do not provide information on the influence of material thickness on CT measurements. In industrial practice, often objects with complex geometries, denser materials and higher thickness are scanned.

In [61] it is reported how in a recent ISO test survey on material influence in dimensional computed tomography, calibrated reference objects made of aluminum alloys, two hole plates (Figure 3.5 e)) provided by Physikalisch Technische Bundesanstalt (PTB) Germany, and two step cylinders (Figure 3.5 f)) provided by the National Metrology Institute of Japan NMIJ, AIST and with calibrated bi-directional lengths were used in order to study how to include material thickness influence in acceptance testing.

Dedicated reference objects were also developed in literature in order to test specific influence quantities. Figure 3.5 g) reports the fiber gauge a sample designed at University of Padova and consisting of 12 fibers and 12 holes with nominal diameters equal to 125 μm and fiber lengths ranging from 350 μm to 700 μm, which can be used in order to determine the correct threshold value [15]. In [35] it is discussed how to use a test object with parallel grooves and cactus-shaped groves (Figure 3.25 h)) in order to test the accuracy of CT measurements.

Finally, in [91] a workpiece-near reference object (Figure 3.25 i)), a miniaturized dismountable cylinder head whose segments can be registered by mean of reference elements, is presented. As discussed above the accuracy and measurement uncertainty of CT measurements strongly depend on the specific task. This reference object allows to assess the dimensional measurement performance of industrial CT for the specific task.

3.7. Influence quantities

CT measurements are affected by a multitude of error sources, which make the traceability of CT dimensional measurements to the unit of length, the meter, an extremely complex task [1,27]. The study of the influence quantities and the analysis and determination of the effects and errors that the specific influence quantity causes on CT measurements is one fundamental step in order to achieve CT measurement traceability. The identification of the error sources and the determination of their effects in fact enable to improve CT systems metrological performance and to enhance CT measurement accuracy, e.g. by correcting known systematic errors, to properly determine CT measurement uncertainty by taking into account all the relevant uncertainty components in a suitable way, and thus to achieve CT measurements traceability. The investigation of the influence quantities thus is crucial for the use of CT systems in coordinate metrology. As discussed in section 3.5 CT measurement uncertainty is task specific, this is because the various influence quantities and their effects vary with the specific task performed.

The German guideline VDI/VDE 2630-part 1.2 [63]: *Computed Tomography in dimensional measurement - Influencing variables on measurement results and recommendations for computed tomography dimensional measurements*, provides an overview of the influence factors affecting CT dimensional measurements.

Category	Error sources
Hardware	X-ray source: geometrical errors, focal spot size and drift, spectrum, cone-angle X-ray detector: geometrical errors, quantum efficiency, noise, internal scattering Rotary table: repeatability, geometrical errors Axes: geometrical errors
Workpiece	Geometry, dimensions Material Surface roughness
Scanning parameters	Current, voltage, filtering, exposure time, number of projections Voxel size Orientation and positioning Fixturing
Software/data processing	Reconstruction Surface determination Filtering Artifacts (e.g. beam hardening, noise, ring artifact etc.)
Environment	Temperature Vibrations Humidity

Table 3. 2: Main influence factors affecting CT dimensional measurements.

Table 3.2 reports the main influence factors that affect CT process chain, grouped into five main categories: hardware (e.g. X-ray source, detector, rotary table and kinematic axes), workpiece related influence factors, scanning parameters, software and data processing and environmental conditions.

Hardware geometrical errors, are an extremely important influence quantity for CT measurements [25,26,92-94]. The effect of CT system geometrical errors will be covered in chapter 4. The effect of scanning parameters is investigated in chapter 5 for a new promising scanning method for CT metrology: CT cone-beam helical scanning. The influence of workpiece specific effects due to surface roughness is analyzed in detail in chapter 6.

Research studies are present in literature on the influence of scanning parameters for conventional circular trajectories (e.g. object orientation and positioning, CT scanning time etc.) on CT dimensional measurements [95], and on the negative effects of beam hardening for example as reported in [33,34].

In the following, two of the influence factors affecting CT measurements that have been studied in literature are described: scaling errors and thresholding errors.

Scaling errors

Scaling errors strongly affects CT dimensional measurements; their effects have been studied in literature and different correction methods have been proposed [3,95,96].

Scaling errors basically consist of an incorrect determination of the voxel size, i.e. the actual voxel size differs from the determined voxel size, which leads to a linearly increasing measurement error (with respect to reference measurements) with increasing dimensions of the characteristics to be measured or distance between two features (e.g. sphere center-to-center distance) [3]. This can be caused for example by a wrong determination of the *SOD* and *SDD* parameters (see section 2.1). The correction of scaling errors is performed by correcting the voxel size dimension, thus it is also called voxel size correction.

The voxel size can be corrected by multiplying the originally determined voxel size by a correction factor CF as reported in Equation 3.11:

$$Voxel\ size_{corrected} = Voxel\ size_{\ original} \cdot CF \tag{3.11}$$

The correction factor CF is typically calculated by measuring a calibrated reference object composed of two or multiple spheres (e.g. a ball bar). This is done in order to eliminate the influence of the threshold as it will be discussed in the next section. The reference object has to be scanned with the same scanning parameters and magnification which are used to scan the actual workpiece as discussed in several research studies [96].

The correction factor *CF* can be calculated according to Equation 3.12 as the ratio between the calibrated value and the CT measured value [3]:

$$CF = \frac{L_{calibrated}}{L_{CT}} \tag{3.12}$$

In some research studies [36,48] some methods are also proposed in order to perform the scaling errors correction by using features not dependent on the threshold and belonging to the actual workpiece. This approach provides the advantage of not requiring reference objects to be scanned before/after or in combination with the scanned workpiece, however it does require the calibration of the actual workpiece by mean of a more accurate measuring instrument e.g. a tactile CMM. Moreover, the features used in order to perform the scaling errors correction have to be carefully selected.

Thresholding errors

The surface determination step is a fundamental and critical step necessary in order to perform CT dimensional measurements and that strongly affects CT measurement accuracy [15, 35].

A classification can be made, distinguishing between:

- Measurements dependent on the threshold, Figure 3.6 a);
- Measurements non-dependent on the threshold, Figure 3.6 b).

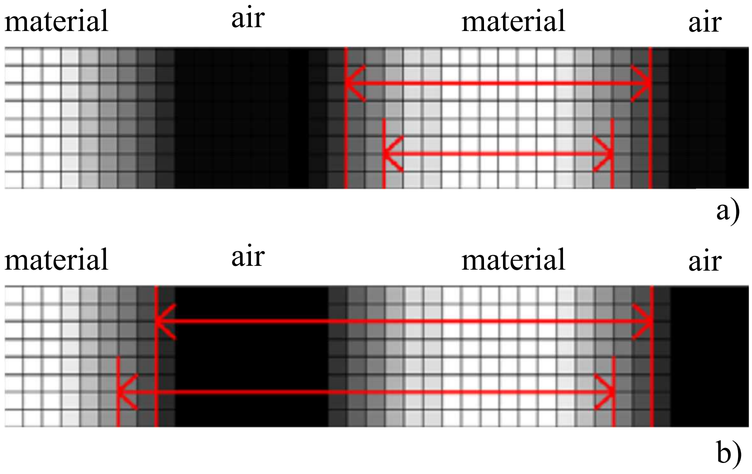

Figure 3.6: a) Measurements dependent on the threshold, b) measurements non-dependent on the threshold [35].

The measurements non-dependent on the threshold are e.g. sphere center-to-center measurements, and in general all the distances which are measured within a transition of the same type e.g. material and air and material and air, as reported in Figure 3.6 b). These kind of measurements are suitable for scaling errors correction because they do not introduce additional errors caused by a wrong threshold that could compromise the voxel size correction.

Measurements which include different transitions e.g. between air and material and material and air, see Figure 3.6 a), are instead dependent on the threshold. This kind of measurements are for example diameter measurements, and bi-directional measurements in general. The wrong determination of the threshold causes the presence of systematic errors in the dimensional measurements and thus reduces CT measurement accuracy.

In particular, the use of a too high threshold or a too low threshold produces opposite effects in inner and outer dimensions, as visible in Figure 3.7.

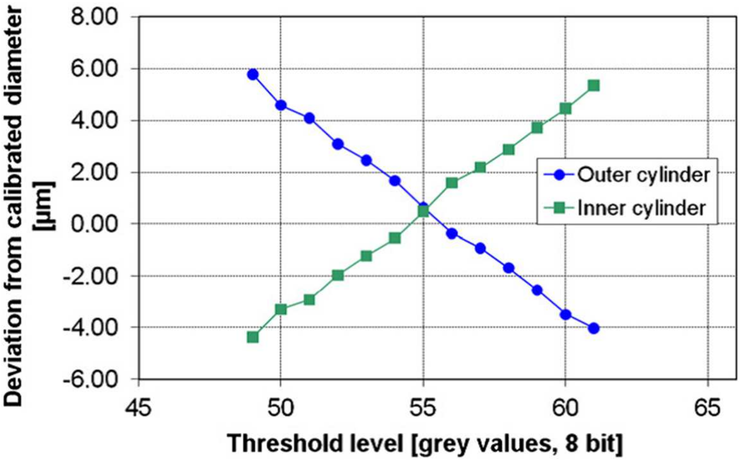

Figure 3.7: Inner and outer diameters expressed as a function of the used threshold [15].

In [15] it is proposed to determine the correct threshold as the value which at the same time minimizes the dimensional errors for the outer and inner dimensions (i.e. the point of intersection of Figure 3.7).

In the following chapters, the traceability of CT measurements and their accuracy enhancement is studied. The influence of specific influence quantities that strongly affect CT measurements the understanding of which is fundamental for achieving CT measurement traceability is studied. In chapter 4 the influence of CT systems geometrical errors is investigated by means of different set of experimental investigations. Chapter 5 deals with the study of an innovative technology in the field of CT metrology that present several advantages, cone-beam helical scanning. The metrological performances of CT helical scanning are analyzed and the influence of the main CT helical scanning parameters and CT measurement accuracy are studied. The influence of cone-angle on conventional circular cone-beam trajectories is also investigated and the measurement results are compared to those obtained with helical trajectories. Finally, chapter 6 concerns the investigations performed in order to determine the influence of a workpiece dependent error source, surface roughness. The obtained results are used to improve CT measurement accuracy and to reduce CT measurement uncertainty.

As described in the previous sections, performance verification is a necessary step in order to determine CT systems metrological characteristics, and the understanding and determination of the effects caused by the different influence quantities is fundamental in order to enable CT measurements traceability. The different influence quantities in fact play significant roles in measurement uncertainty determination, traceability establishment and accuracy enhancement of CT measurements.

Chapter 4

Influence of CT system geometrical errors

As introduced in chapter 3 the study and analysis of CT system geometrical errors is of primary importance towards CT measurement traceability. This chapter investigates the influence of CT system geometrical errors on CT measurement results. In the first part of the chapter a theoretical analysis of the possible geometrical errors affecting CT system geometry is presented and discussed. The second part of the chapter deals with the experimental investigations of the effects of CT system geometrical misalignments on CT measurement results. Specifically, in sections 4.3 and 4.4 detector angular misalignments are studied using two reference objects calibrated by means of tactile CMM measurements, a ball bar and a ball plate. The effects of the mechanically induced detector angular misalignments on CT measurements are experimentally determined and quantified. Moreover, the dependency of the measurement errors by the magnitude of the misalignments and the measurement direction and object position in the CT volume is investigated. Finally, in section 4.5 the experimental results obtained when studying the lateral shift of the rotary table are presented and discussed.

4.1. Introduction

As discussed in chapter 3, fundamental requirements for using CT systems as coordinate measuring systems (CMSs) for traceable coordinate metrology are the study of measurement accuracy and the establishment of traceability to the unit of length, the meter.

Due to their complex nature, CT scanning technology and thus CT measurements are affected by multiple error sources that complexly interact in the measurement chain. The German guideline VDI/VDE 2630-part 1.2 [63] provides a detailed description of the factors influencing CT dimensional measurements. Examples of these influence factors are CT scanning parameters, work-piece properties (e.g. material, size, surface roughness), geometrical errors, software and data processing etc. (see Sect. 3.7 for more details). Because of the multitude of these influencing quantities and the complexity and non-linearity of their interaction, CT measurements traceability is a major challenge for metrological applications. In particular, the assessment of measurement uncertainty (see Sect. 3.5), which is essential for traceability establishment, is one of the more critical tasks.

Among the influence factors affecting CT measurement chain, the study and analysis of CT system geometrical errors is of primary importance [25,52,92,93,94]. As for most precision measuring instruments, the design of a CT system involves the assembly of several components, the most important of which are the X-ray source, the rotary table and the detector. These components need to be carefully aligned to obtain accurate measurements. Moreover, in the majority of the systems, at least one of these components, i.e. the rotary stage, is moved e.g. on linear guideways to reach the desired configuration or set-up to perform the CT scan. The physical structure of a CT system is therefore itself a source of measurement uncertainty. Different configurations and designs of CT systems exist, and also different CT scanning methods (see Sect. 2.1). Each of the different scanning methods will be affected by CT system geometrical errors, and will include also new influence quantities compared to the ones of cone-beam circular scans. This contributes to make the analysis of CT system geometrical errors even a more complicated task.

The determination of the CT system geometry is a crucial step on which all the following steps in the measurement chain rely on. In fact, the system geometry provides the necessary information to fully describe the geometry of data acquisition and performing the tomographic reconstruction on which all the dimensional analyses are based. An error in the determination of the CT system geometry (i.e. geometric set-up) or the presence of geometrical errors not accounted for during the reconstruction affect all the subsequent steps in the measurement chain and could lead to artifacts, distortions and measurement errors in the reconstructed volume [25]. It is evident therefore that it is extremely important to investigate and quantify the influence of CT system geometrical errors on CT measurements.

4.2. Cone-beam CT system geometry

Typically, when dealing with the application of CT systems for coordinate metrology purposes, they are often compared to traditional CMMs. The basic idea in the international framework for CT metrology standardization is to use the knowledge and the well-established standards available for coordinate measuring machines and adapt them to CT. In fact, CT systems can be seen as coordinate measuring machines with CT sensors [65]. This concept is valid also when dealing with the study of geometrical errors on CT systems.

X-ray computed tomography is a non-destructive technique based on the attenuation of the X-rays when they pass through a matter and the subsequent tomographic reconstruction of the radiographic projections recorded by the detector. It is therefore an imaging technique. However, the machine frame of a CT system is typically composed of three ideally orthogonal linear axes which generate the geometry of a Cartesian coordinate system and allow for motion in X, Y and Z directions (see chapter 2). Moreover, a rotary axis enables for sample rotation and the recording of the radiographic projections at the different angular steps. Therefore, the principles used to describe CMMs geometrical errors are also applicable to CT systems.

Figure 4.1 describes a typical industrial cone-beam CT system geometry. As reported in Sect. 2.1 also other designs exist; however, for the purpose of this thesis the design reported in Figure 4.1 is considered as it is the one mostly used in industrial settings. In Figure 4.1 the line passing through the X-ray cone vertex (i.e. the X-ray focal spot, which as described in Sect. 2.3 ideally is a point), and the center of the detector is defined as the *z* axis, also the magnification axis. The axis which is parallel to the rotation axis of the object is called *y* axis, finally the *x* axis is perpendicular to both the *y* and *z* axis. The *x*, *y*, and *z* axis form therefore a Cartesian coordinate system.

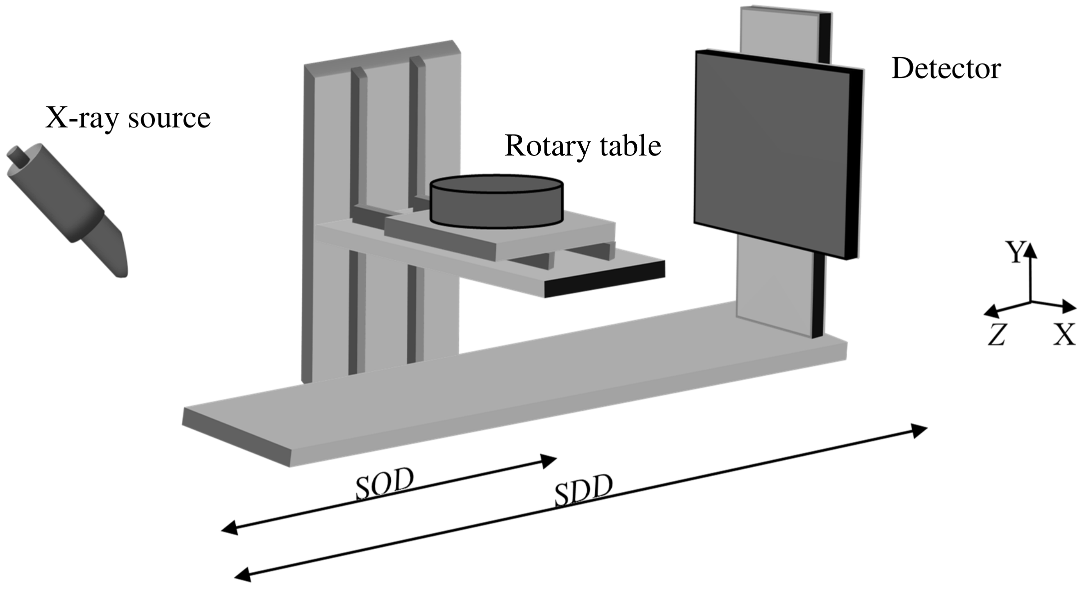

Figure 4.1: Typical cone-beam system geometry.

The distance between the X-ray source and the center of the detector is defined as the source-to-detector-distance *SDD*, whereas the distance between the X-ray source and the intersection between the rotation axis and the magnification axis is referred to as source-to-object distance *SOD* (or also *SRD*: source-to-rotation axis distance). The ratio between the *SDD* and the *SOD* distances gives the magnification factor *M* which describes the geometrical magnification and thus the voxel size used for the CT scan (see Sect. 2.4.1).

In general, no coordinate measuring system is constructed and aligned perfectly. In real practice, in fact, the components constituting the system are characterized by deviations from ideal geometries and shapes due to the manufacturing processes. Moreover, only ideally the components are perfectly aligned. In general, the major error sources that affect the geometry and thus the accuracy of the measurements performed with a coordinate measuring system include: deviations of the components from the ideal alignment (i.e. geometrical misalignments), kinematic errors, thermo-mechanical errors (e.g. expansion of guideways resulting from changes in the environmental temperature), loads, dynamic forces, motion control and control software [98]. The study of all these error sources is extremely complex, and many times their effects are difficult to predict. When dealing with CT systems, moreover, other specific error sources must be taken into account. For example, the focal spot drift can affect the geometry of the system and therefore the resulting measurement accuracy.

In the following two extremely relevant error sources, geometrical misalignments and kinematic errors are reviewed. The study of these two geometrical error sources in fact enable to provide the systematic of the geometrical error description; the presence of thermo-mechanical errors for example will affect the actual geometry of the system however it does not change the systematic of the geometrical error description [98]. The same considerations are valid for loads (quasi-rigid body behaviors). Moreover, precision measurements are usually carried out at small speeds, therefore the focus is not on dynamic forces [99].

4.2.1. Alignment of a CT system

In a perfectly aligned CT system (see Figure 4.2), the X-ray focal spot center (the vertex of X-ray cone), the center of rotation and the detector center are positioned on a straight line. This line is perpendicular to the detector surface on its center and coincides with the central ray (i.e. the X-ray path on the central plane of the cone which goes perpendicularly from the vertex of the cone to the center of the detector). Moreover, the rotation axis is perpendicular to the line containing the center of rotation, the X-ray focal spot and the detector center, while its projection is parallel to the detector columns [25].

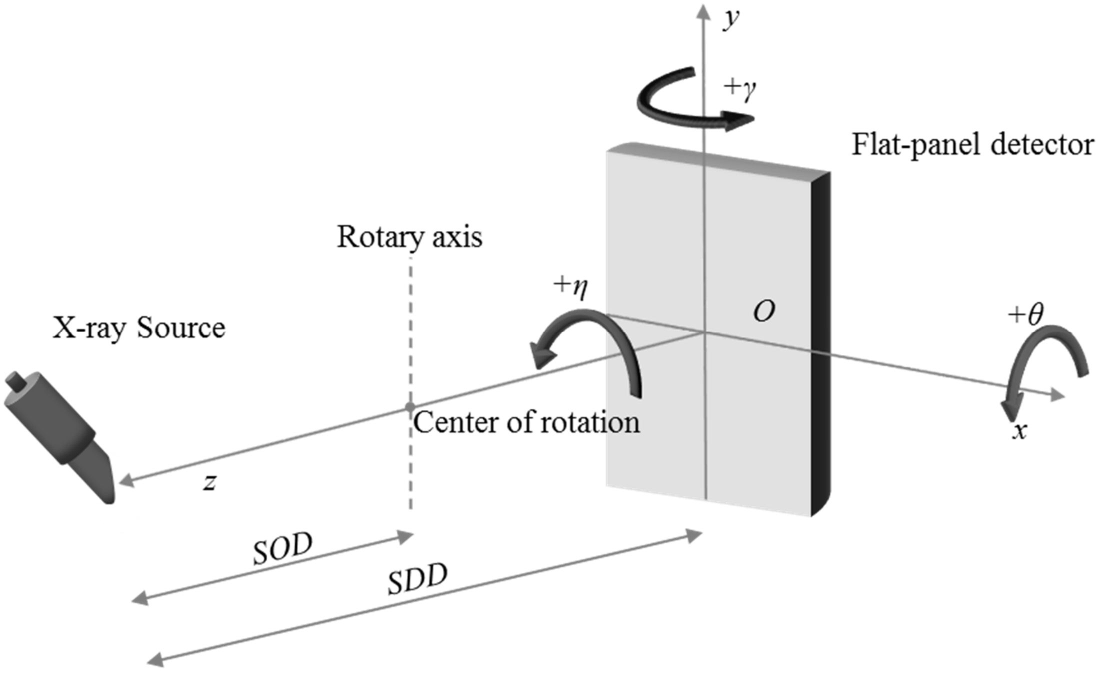

Figure 4.2: Ideal alignment of a cone-beam CT system. The origin of the coordinate system is placed on the detector center. The three rotations θ, γ, η describe the detector angular misalignments.

In real practice, however, it is not possible to reach the perfect alignment conditions represented in Figure 4.2 and some residual errors between the three components will be present in the system geometry [25].

To describe the geometry of a CT system the right-handed Cartesian coordinate system with origin on the detector surface and depicted in Figure 4.2 is used. The positive *z* direction points towards the X-ray source, the positive *y* axis direction is in the opposite direction of gravity and the *x* direction is defined by the right hand rule. A rotation about the *x* axis is described by the angle θ, whereas rotations about the *y* and *z* axis are described respectively by the angles γ and η. Positive rotations are also defined by the right hand rule. The origin *O* of the reference system is located at the intersection between the central column and the central row of the detector.

A CT system can suffer mainly of three different categories of misalignments, which can be attributed to the three main components of the system: misalignments of the detector, misalignments of the X-ray source and the misalignments of the rotary table. These misalignments are described in the following.

Detector misalignments

Assuming a perfect alignment of the X-ray source and of the rotary table the detector can be affected by three angular misalignments and three positional misalignments.

Detector pitch

Detector pitch (θ) is an out-of-plane rotation of the detector which occurs about the detector horizontal axis.

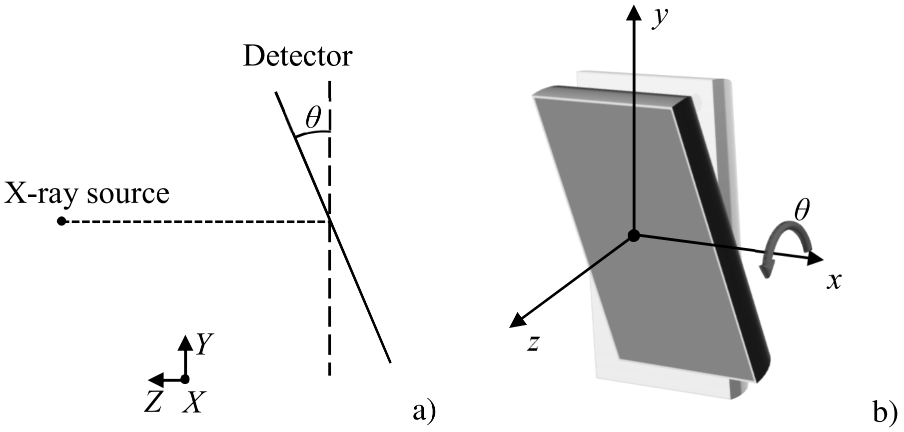

Figure 4.3: Schematic representation of a detector pitch about the central horizontal axis of the detector x. a) Representation of detector pitch in the z-y plane. The detector in the aligned configuration is described by the dashed line, the detector in the misaligned configuration is represented with a solid line. b) Perspective view of a positive detector pitch of θ about the x axis of the detector.

Figure 4.3 represents a detector pitch about the *x* axis, which is the horizontal axis passing through the detector center. In this case, the condition of perpendicularity of the straight line (containing the X-ray source focal spot center, the center of rotation and the detector center) to the detector surface on its center is not respected.

As it is visible, in Figure 4.3, due to this kind of misalignment, the upper and lower regions of the detector are respectively closer and further away from the center of the X-ray source.

In the presence of a detector pitch about the *x* axis of Figure 4.3, from the X-ray source perspective the height of the detector becomes smaller.

Detector yaw

A detector yaw (γ) occurs when the detector is tilted around its vertical axis. Detector yaw, as detector pitch, also describes an out-of-plane rotation.

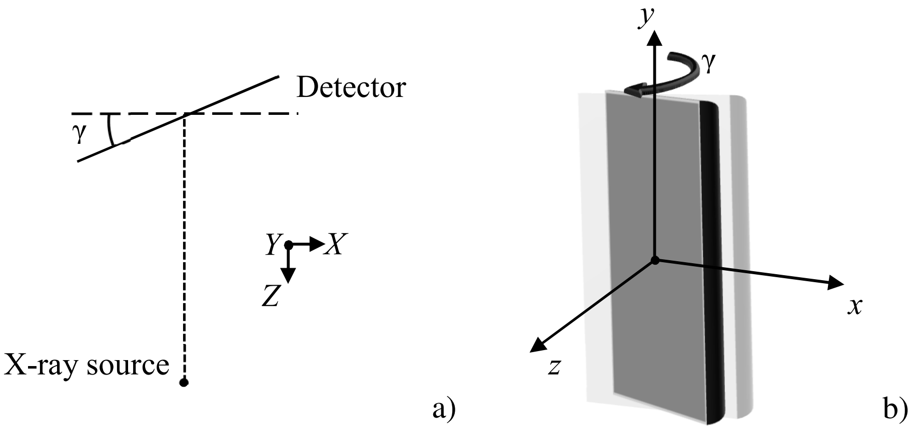

Figure 4.4: Schematic representation of a detector yaw about the central vertical axis of the detector y. a) Representation of a positive detector yaw in the x-z plane. The detector in the aligned configuration is described by the dashed line, the detector in the misaligned configuration is represented with a solid line. b) Perspective view of a negative detector yaw of γ about the y axis of the detector. A negative rotation is shown for better visibility.

Figure 4.4 describes a detector yaw about its central vertical axis, *y*. Also in this case due to the detector misalignment some regions of the detector are closer of further from the X-ray source. In Figure 4.4 a) the left-hand side of the detector is closer to the X-ray source whereas the right-hand side is further away from the X-ray source. Also here the condition of perpendicularity between the straight line and the detector surface on its center is not respected.

In the presence of a detector yaw about the *y* axis of Figure 4.4, from the X-ray source perspective the width of the detector becomes smaller.

Detector roll

Detector roll (η) describes an in-plane rotation of the detector. Figure 4.5 represents a detector in presence of a detector roll about the *z* axis.

When in presence of a detector roll the condition requiring the projection of the rotation axis to be parallel to the detector columns is not respected.

Due to a detector roll about the *z* axis, the effective width and height of the detector viewed from the X-ray source are altered.

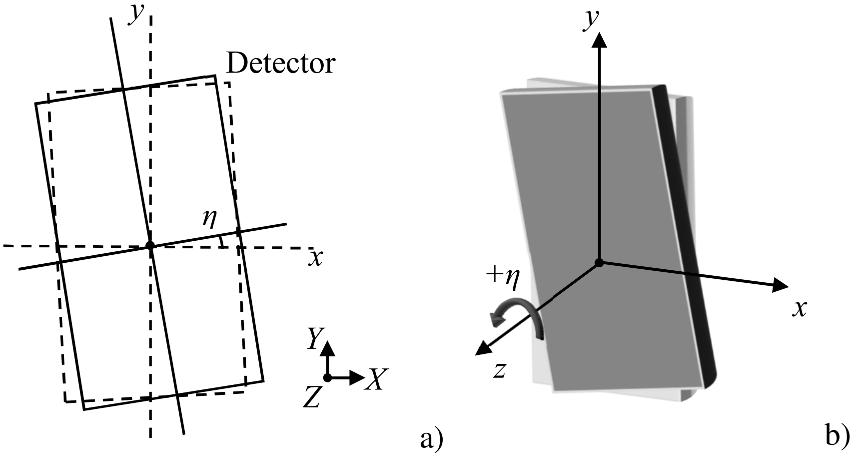

Figure 4.5: Schematic representation of a detector roll about the magnification axis z. a) Representation of a positive detector roll η in the x-y plane. The detector in the aligned configuration is described by the dashed line, the detector in the misaligned configuration is represented with a solid line. b) Perspective view of a +η detector roll about the z axis.

Longitudinal shift along the direction of the magnification axis

The longitudinal shift of the detector along the magnification axis is described by an offset of Δz_D.

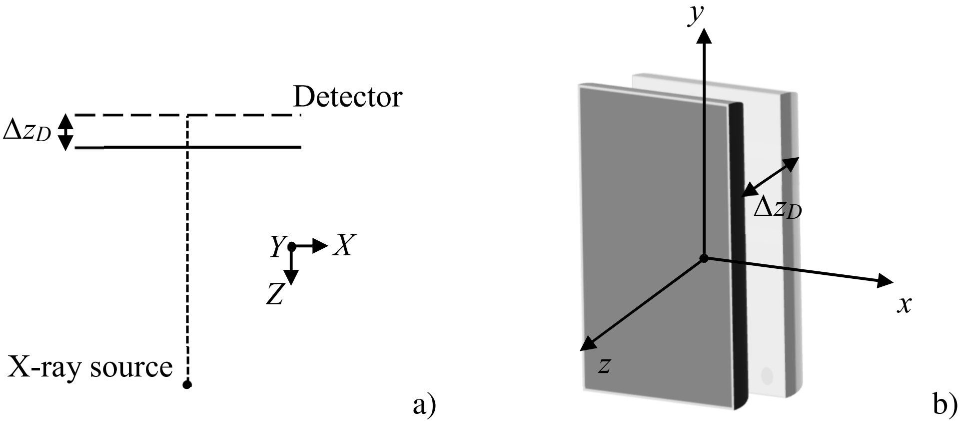

Figure 4.6: Detector longitudinal shift along the magnification axis. a) Representation of a Δz_D shift in the x-z plane. The detector in the aligned configuration is described by the dashed line, the detector in the misaligned configuration is represented with a solid line. b) Perspective view of a Δz_D shift of the detector along the magnification axis.

Figure 4.6 describes a Δz_D offset of the detector along the magnification axis. In presence of this kind of positional misalignment the effective source-to-detector distance *SDD* becomes bigger or smaller than the *SDD* in the aligned configuration depending on the sign of the offset. An error in *SDD* affects the geometrical magnification *M* and thus the actual voxel size (see Sect. 3.7).

Horizontal shift along the direction of the *x* axis

The horizontal shift of the detector along the *x* axis is described by an offset of Δx_D. In this case the alignment condition requiring the center of the detector, center of rotation and the X-ray focal spot to be positioned on a straight line is not respected.

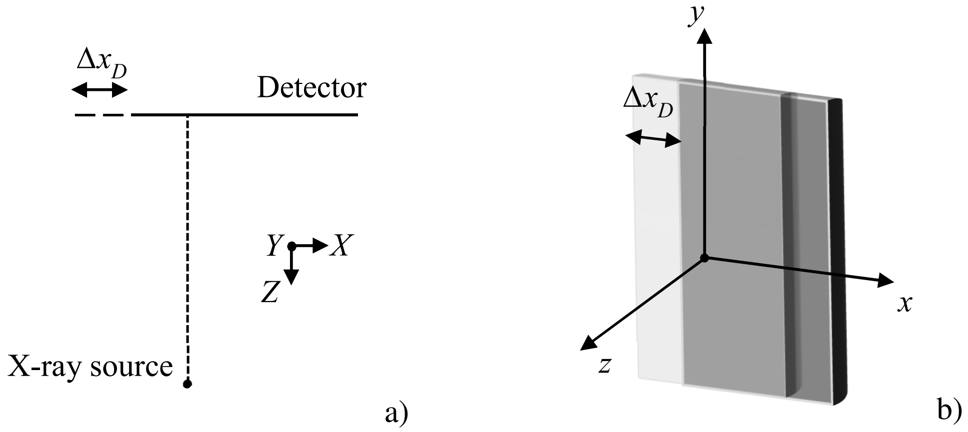

Figure 4.7: Detector horizontal shift along the x axis. a) Representation of a Δx_D shift in the x-z plane. The detector in the aligned configuration is described by the dashed line, whereas the overlapping solid line represents the detector in the misaligned configuration. b) Perspective view of a Δx_D shift of the detector along the x axis.

Figure 4.7 describes a Δx_D offset of the detector along the *x* axis. Compared to a longitudinal shift along the magnification axis direction this misalignment implies the deviation from the ideal alignment condition of the straight line containing the X-ray focal spot, center of rotation and detector center. Moreover, also the other requirement of perpendicularity between the straight line and the detector surface on its center is not respected. The longitudinal positional misalignment and the horizontal positional misalignment have therefore different effects. While the first one leads to a positional error in the *z* direction which affects *SDD* and leads to the presence of errors in the determined geometrical magnification, a horizontal shift along the *x* axis direction may also affect the image quality.

Vertical shift along the direction of the *y* axis

The vertical shift of the detector along the *y* axis is described by an offset of Δy_D.
Figure 4.8 describes a Δy_D offset of the detector along the *y* axis. As for a horizontal shift of the detector, when the detector is affected by a positional misalignment in the *y* direction, the requirement of the straight line containing the X-ray focal spot, center of rotation and detector center, and the requirement of perpendicularity between this straight line and the detector surface on its center are not respected.

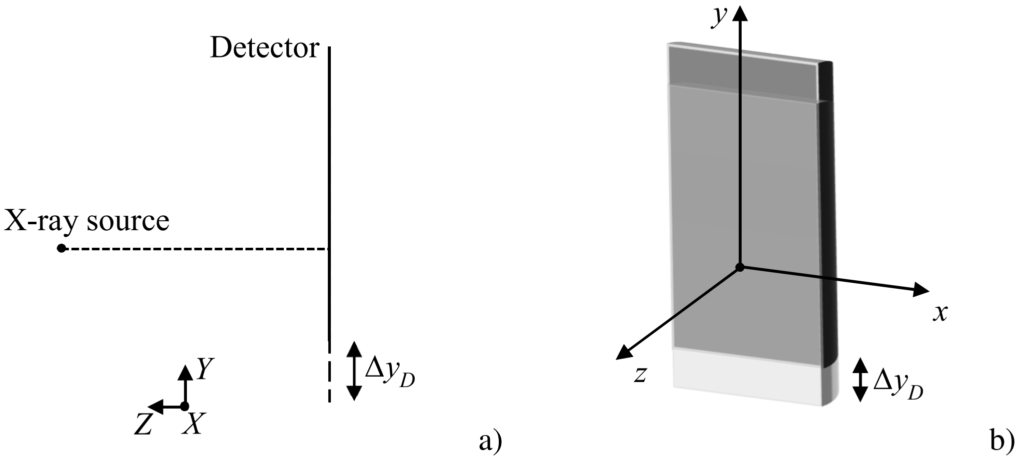

Figure 4.8: Detector vertical shift along the y axis. a) Representation of a Δy_D shift in the y-z plane. The detector in the aligned configuration is described by the dashed line. The overlapping solid line represents the detector in the misaligned configuration. b) Perspective view of a Δy_D shift of the detector along the y axis.

Detector misalignments can occur also about axes different than the detector central axes represented in Figure 4.2. For example, detector angular misalignments can occur about any row and column of the detector. Moreover, the misalignments described in Figure 4.3 to Figure 4.8 can be combined together and happen simultaneously as in Figure 4.9. These types of misalignments can be decomposed and expressed as functions of the parameters which describe the detector misalignments about its central axes [26,94].

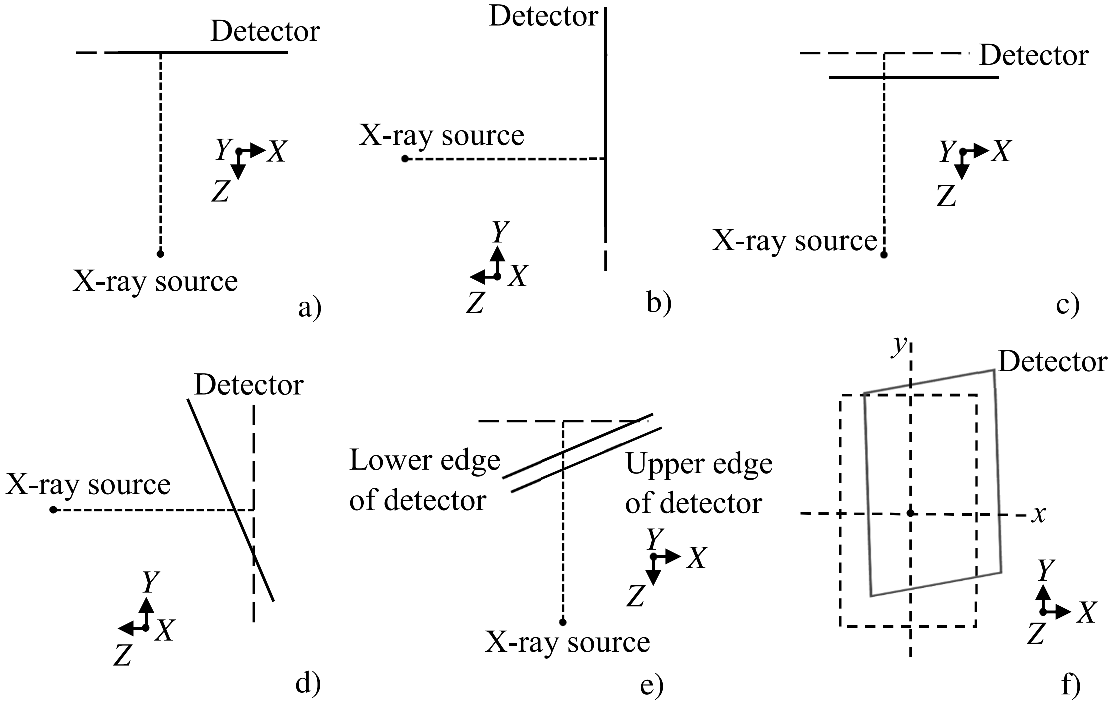

Figure 4. 9: Superimposition of different detector misalignments about any row and column of the detector. Each of the six images shows the superimposition of the described detector misalignment to the ones represented in the previous images. Figure f) represents the superimposition of all the misalignments described in images from a) to e). a) The ideally aligned detector is affected by a horizontal shift, b) vertical shift of the detector, c) longitudinal shift of the detector, d) out of plane rotation of the detector about an axis parallel to the x axis, e) out of plane rotation of the detector about an axis parallel to the y axis, f) in plane rotation of the detector about an axis parallel to the z axis.

This enables to convert detector misalignments about any axes to the special cases of detector misalignments about its central axes by considering them as a superimposition of detector rotations about its central axes and detector translations [94].

X-ray source misalignments

Assuming a perfect alignment of the rotary table and of the detector the X-ray source can be affected by the following misalignments.

Longitudinal shift along the direction of the magnification axis

The longitudinal shift of the X-ray source along a direction parallel to the magnification axis is described by an offset of Δz_S.
Figure 4.10 describes a Δz_S offset of the X-ray source along the magnification axis.

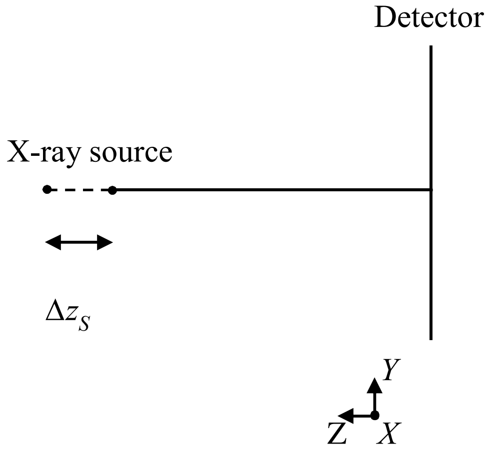

Figure 4. 10: X-ray source longitudinal shift along the magnification axis. The X-ray source position in the aligned configuration is described by the dashed line. The overlapping solid line represents the X-ray source position in the misaligned configuration.

As for a longitudinal shift of the detector along the magnification axis, the presence of this kind of positional misalignment causes an error in the source-to-detector distance *SDD* which becomes bigger or smaller than the *SDD* in the aligned configuration depending on the sign of the offset. However, in this case, also the source-to-object distance *SOD* is affected by the misalignment. This produces an error in the magnification factor *M*.

Horizontal shift along the direction of the *x* axis

The horizontal shift of the X-ray source along a direction parallel to the *x* axis is described by an offset of Δx_S. The alignment condition requiring the center of the detector, center of rotation and the X-ray focal spot to be positioned on a straight line is not respected. It follows that, also the other requirement of perpendicularity between the straight line and the detector surface on its center is not respected.

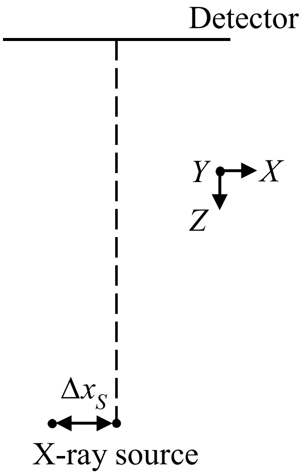

Figure 4.11: X-ray source horizontal shift along the x axis. The X-ray source position in the aligned configuration is described by the dashed line, the X-ray source position in the misaligned configuration is described by the Δx_S shift.

Figure 4.11 describes a Δx_S offset of the X-ray source along the *x* axis. As for the detector, if we compare the effects of a longitudinal shift of the X-ray source along the magnification axis direction, and the effect of an X-ray source horizontal shift, the misalignment due to a horizontal shift of the source implies the deviation from the ideal alignment conditions reported above, therefore, the longitudinal position misalignment and the horizontal position misalignment produce different effects.

Vertical shift along the direction of the *y* axis

The vertical shift of the X-ray source along a direction parallel to the *y* axis is described by an offset of Δy_S.

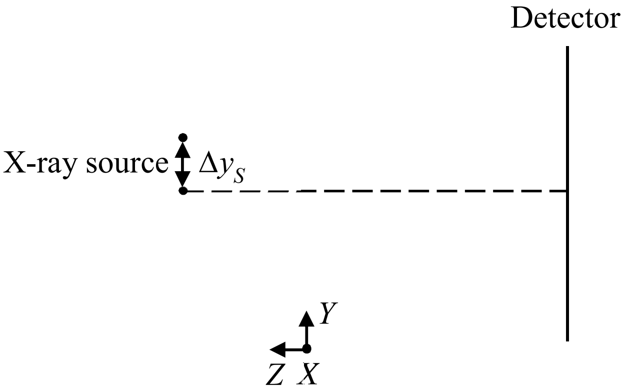

Figure 4. 12: X-ray source vertical shift along the y axis. The X-ray source position in the aligned configuration is described by the dashed line, the X-ray source position in the misaligned configuration is described by the Δy_S shift.

Figure 4.12 describes a Δy_S offset of the X-ray source along the *y* axis. As for a vertical shift of the detector, when the X-ray source is affected by a positional misalignment in the *y* direction, the requirement of the straight line containing the X-ray focal spot, center of rotation and detector center, and the requirement of perpendicularity between the straight line and the detector surface on its center are not respected.

Besides the positional misalignments, the X-ray source may also suffer from angular misalignments. In particular X-ray source tilts about axes parallel to the *x* axis of Figure 4.2 and X-ray source yaws about axes parallel to the *y* axis of Figure 4.2 will produce a deviation from the ideal alignment condition requiring the central ray to be coincident with the straight line containing the X-ray source focal spot, the center of rotation and the center of the detector. These angular misalignments will cause a non-symmetric covering of the X-ray beam on the detector (e.g. the X-ray cone may point towards the positive *y* axis).

Also it is worth pointing out that, drifts of the X-ray source due to the heating of the target can occur in the *x*, *y* and *z* direction and can cause changes in the position of the X-ray focal spot. These changes are difficult to predict since they depend on a wide variety of factors such as the type of X-ray source (i.e. reflection target or transmission target), target material, cooling conditions, X-ray parameters etc.

Rotary table misalignments

In addition to the detector and X-ray source misalignments also the rotary table can exhibit deviations from the ideal geometrical alignment.

Longitudinal shift along the direction of the magnification axis

The longitudinal shift of the rotary table along a direction parallel to the magnification axis is described by an offset of Δz_R and depicted in Figure 4.13.

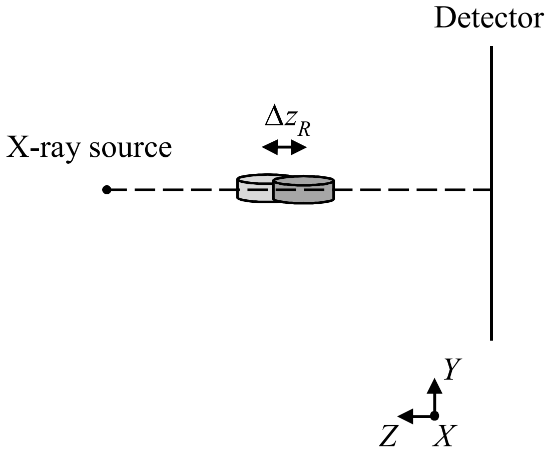

Figure 4.13: Rotary table longitudinal shift of Δz_R along the magnification axis. The aligned position of the rotary table is represented in light grey color, whereas the misaligned position is represented in dark grey.

This kind of positional misalignment causes an error in the source-to-object distance *SOD* which becomes bigger or smaller than the *SOD* in the aligned configuration depending on the sign of the offset. This produces an error in the magnification factor *M*.

Horizontal shift along the direction of the *x* axis

The horizontal shift of the rotary table along a direction parallel to the *x* axis is described by an offset of Δx_R. In this case, the center of rotation, the center of the detector, and the X-ray focal spot are not positioned on a straight line.

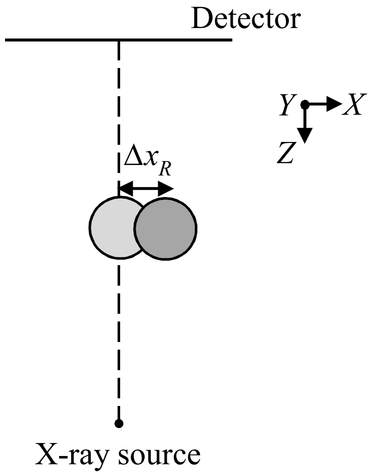

Figure 4.14: Rotary table horizontal shift of Δx_R along the x axis. The aligned position of the rotary table is represented in light grey color, whereas the misaligned position is represented in dark grey.

Figure 4.14 describes a Δx_R offset of the rotary table along the *x* axis. As for the detector, if we compare the effects of a longitudinal shift of the rotary table along the magnification axis direction, and the effects of a rotary table horizontal shift, the misalignment due to a horizontal shift of the rotary table causes the deviation from the ideal alignment conditions reported above, therefore, the longitudinal positional misalignment and the horizontal positional misalignment produce different effects.

Vertical shift along the direction of the *y* axis

The vertical shift of the rotary table along a direction parallel to the *y* axis is described by an offset of Δy_R.

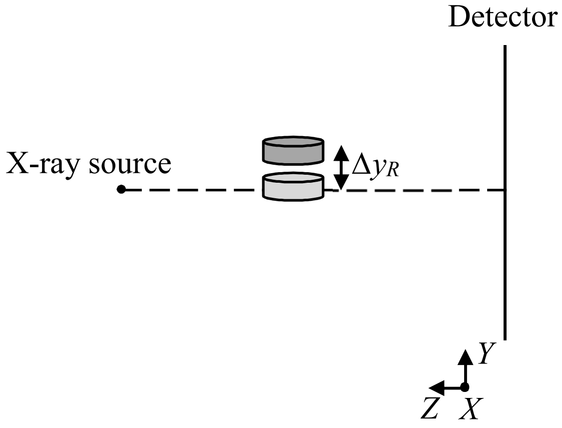

Figure 4.15: Rotary table vertical shift of Δy_R along the x axis. The aligned position of the rotary table is represented in light grey color, whereas the misaligned position is represented in dark grey.

Figure 4.15 describes a Δy_R offset of the rotary table along the *y* axis. This vertical shift positional misalignment is relevant in case of scanning methods that require a movement in the *y* direction, for example cone-beam helical scanning, or in 2D systems with fan-beam geometries (see Sect. 2.1).

Rotary table pitch

Besides the linear shifts from the ideal position, the rotary axis can exhibit also angular misalignments. A tilt of the rotation axis θ_R about an axis parallel to the *x* axis and passing through the center of rotation is described in Figure 4.16.

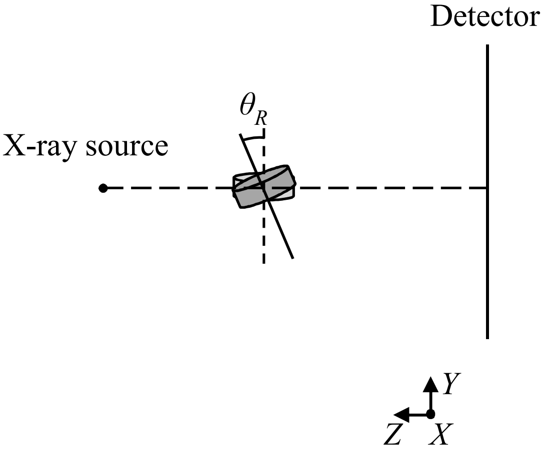

Figure 4.16: Rotary table pitch about an axis parallel to the x axis and passing through the center of rotation. The ideal aligned configuration of the rotary table is represented in light grey color and the rotation axis is described by a dashed line. The misaligned configuration is represented in dark grey and the misaligned rotary axis is described by a solid line.

In this case, the conditions for ideal alignment requiring the perpendicularity between the straight line (containing the X-ray focal spot center, the center of rotation and detector center) and the rotary axis is not respected, moreover also the requirement of parallelism of the rotary axis to the detector columns is not respected.

Rotary table roll

The rotary axis of the rotary table can also be affected by angular misalignments about the *z* axis (η_R), as described in Figure 4.17.
Also in this case, the rotary axis is not parallel to the detector columns.

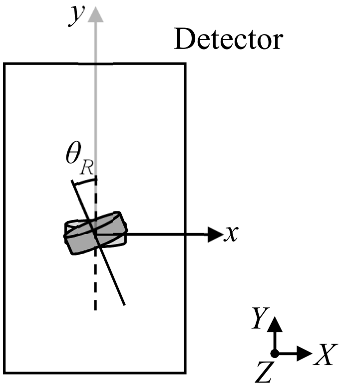

Figure 4.17: Rotary table roll about the z axis. The ideal aligned configuration of the rotary table is represented in light grey color and the rotation axis is described by a dashed line. The misaligned configuration is represented in dark grey and the misaligned rotary axis is described by a solid line.

The X-ray source misalignments (longitudinal, horizontal and vertical shifts) and the rotary axis misalignments can be described, by applying mathematical and trigonometrical concepts, as functions of the parameters defined to describe the detector misalignments [27,100].

In presence of the misalignments described in this section therefore, for the given set-up, the geometry of the cone-beam CT system can be fully described by the following parameters: *SOD*, *SDD*, Δx_D, Δy_D, Δz_D, θ, γ, η.

However, as reported before, the majority of CT systems is characterized by the possibility to move the rotary stage on linear guideways (in *x*, *y* and *z* directions of Figure 4.2) to reach the desired configuration to perform the CT scan. Moreover, a CT scan always requires a rotational movement to acquire the projections at the different angular steps. These motions may cause the presence of kinematic errors, which are function of the position in space.
The above mentioned parameters which can be used to uniquely describe the geometry of a CT system in fact, do not take into account the presence of error motions, and are valid only for the particular CT system scanning configuration. When the rotary table is moved, for example along the *z* axis to perform a scan with a different voxel size, kinematic errors can occur, and the parameters need to be calculated again. In real practice however, the presence of kinematic errors is unavoidable.

As described before, the machine frame of a CT system is composed of three ideally orthogonal linear axes, which generate the geometry of a Cartesian coordinate system and allow for motion in *x*, *y* and *z* directions. Moreover, the rotary axis enables the sample rotation and the recording of the radiographic projections at the different angular steps. Therefore, the same principles used to describe the kinematic errors of CMMs equipped with a rotary table can be used also for CT systems, and are reported in the following.

4.2.2. Kinematic errors

Kinematic errors are typically studied by the rigid-body theory. Each movement of a machine axis can then be described by its six degrees of freedom: three translational motions and three rotational motions (roll, pitch, and yaw). Typically, only one of the six degrees of freedom is the desired nominal movement. A typical CMM thus is characterized by twenty-one sources of geometrical errors: six errors per axis which include three translational errors (one positioning error, and two straightness error motions) and three rotation errors, and three squareness errors which describe the orthogonality errors between any two pairs of axes [101,102].

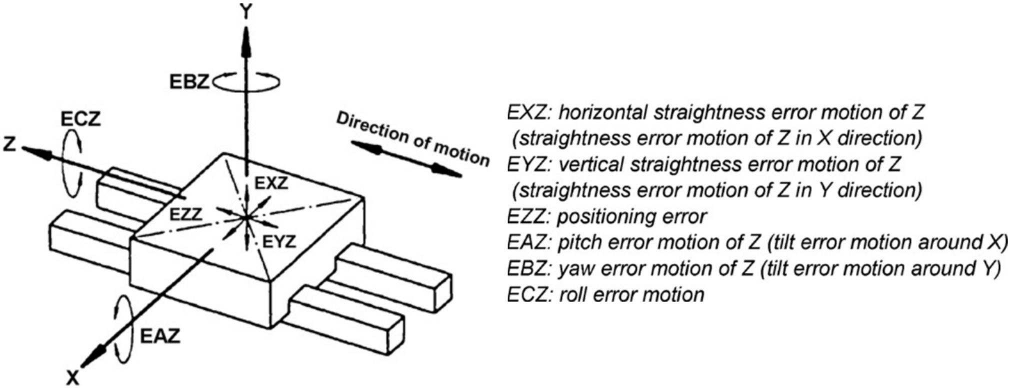

Figure 4.18: Geometrical error motions of a linear axis [98].

When dealing with CT systems each of these errors affect the actual geometry of the system. For example, a horizontal straightness error motion of *z* in the *x* direction *EXZ* will cause a horizontal offset of the rotary table along the *x* direction. A squareness error of the *y* axis with respect to *z* axis will cause an error in the source-to-object distance *SOD* and thus an error in the magnification factor *M*. These are just two examples out of 21 of how the kinematic errors affect CT system geometry.

For CMMs equipped with a rotary table, the rotary axis is also described by a similar set of six parametric errors. Three translational errors, namely an axial error motion and two radial error motions, and three angular errors (an angular position error, and two tilt error motions) [98,102].

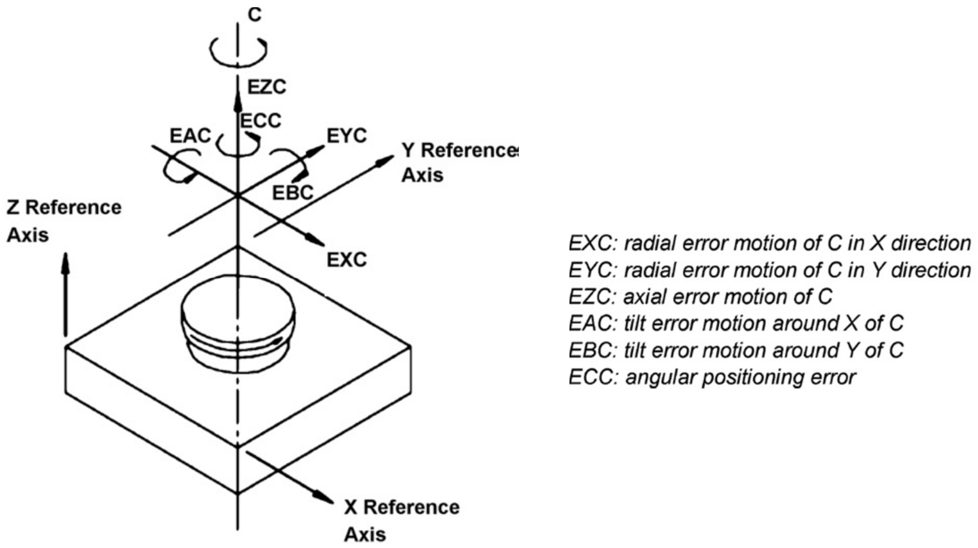

Figure 4.19: : Geometrical error motions of a rotary axis [98].

For example, in CT systems an angular positioning error *ECC* will cause an error in the actual angular step in which the projections are acquired.
Moreover, most of the rotary axes, for example the ones of rotary tables, have to be perpendicular to CMMs tables, which give other two additional squareness errors [102]. Therefore, for a CMM equipped with a rotary axis, the total number of geometrical errors is 29 (21 originating from the axis X, Y, Z and 8 originating from the rotary axis). The same concepts can be applied also to CT systems.

Error motions can be minimized physically, i.e. manufacturing components with stricter tolerances and accurate mechanical assembly, and by mechanical adjustment. This physical approach however can be extremely costly and time consuming: the mechanical adjustment needed to correct one geometrical error in fact can influence the other geometrical errors leading to iterative adjustments [102].
Another approach is geometrical error mapping, and the subsequent software correction of geometrical errors, which is a well-established method in coordinate metrology [98,101,102]. In this approach, each of the rigid-body error is measured. There are several ways to measure these errors which can be divided into direct methods (in which single errors are measured) and indirect (in which superimposed errors are measured) [98]. In general, the methods available make use of one of the following techniques [101]:

- measuring instruments such as straight edges, autocollimators and levels;
- laser interferometer system and associated optics;
- calibrated reference objects (e.g. hole plates);
- tracking laser interferometer.

The measured errors are then used together with the mathematical model which describes the machine behavior, in order to compensate for these errors. This can be done by active compensation (moving for example the CMM stylus to the correct position) which is done real-time, or by passive compensation (a correction of the measurement coordinates which is done after the collection of measurement points) [102]. Of course, only systematic errors can be compensated which means that the errors should be significantly greater than the random errors. Other requirements also apply which can be found in [99].

Whether active or passive, geometrical errors compensation means calibrating the CMM and thus mapping the systematic errors of the CMM so that they can be compensated for. If all the steps in the calibration procedure are traceable (i.e. the error mapping process is traceable) the basis for measurement uncertainty determination and traceability are established. In fact, it is important to note that geometrical calibration itself is not sufficient to obtain traceable measurements. Other influence quantities, such as workpiece related effects, affect the measurements.

The presence of kinematic errors therefore leads to CT system misalignments. In fact, for each position of the axes, the alignment of the CT system will be influenced by the effects of kinematic errors. It is therefore essential to deeply study the effects of CT system geometrical misalignments.

4.2.3. Actual CT system geometry

In a real system, the actual CT system geometry therefore will be affected by the presence of geometrical misalignments. Misalignments will origin from the alignment procedure of the CT system (which will always lead to a certain extent of residual errors with respect to the ideally and perfect aligned configuration) or from kinematic errors. Of course the more accurate is the alignment procedure and the smaller is the presence of kinematic errors, the smaller will be the geometrical misalignments and therefore the more accurate will be the measurements.

In CT process chain, the accurate knowledge of the actual system geometry is a fundamental information. In fact, the CT system geometry describes the geometry of the data acquisition which is essential to perform the tomographic reconstruction. Any discrepancy between the actual system geometry and the geometry used in the reconstruction phase (i.e. the use of an incorrect CT system geometry for reconstruction) will lead to the presence of artifacts, distortion and measurement errors. The CT system geometry input to the reconstruction algorithm may be incorrect for two reasons which can be described with two different scenarios [25].

In the first case the actual CT system geometry is affected by the presence of hardware physical misalignments (e.g. an angular misalignment of the detector, the presence of a straightness error motion in the x direction, etc.). In this scenario, if the misalignments present in the actual geometry are not accounted for during reconstruction, the reconstructed volume will be affected by errors, distortions and artifacts. It is important to underline that the errors in the reconstructed volume are generated due to the reconstruction with an incorrect system geometry which differs from the actual one. The presence of a physical misalignment itself, does not necessarily constitute a problem as long as it is accounted for properly during reconstruction.

In the second scenario, the geometry of the CT system is estimated directly from images. For example, several studies are available in which different methods based on the acquisition of single or multiple projections images of test phantoms, generally composed

of high density point-like objects (e.g. spheres), are proposed for estimating cone-beam CT systems geometries [100,103,104]. In this case, the presence of a physical misalignment is not necessarily a problem. If the geometry is misestimated however, the reconstructed volume will be affected by errors.
Therefore, the presence of geometrical misalignments and/or the wrong estimation of the system geometry could have a strong impact on the reconstructed volume leading to artifacts and distortions, and to measurement errors for metrological applications [94].
In [92] Kumar et al. investigated the influence of specific geometrical errors on simulated ball bars showing that they can have significant impact on CT data. In [93] different simulated detector angular misalignments of 1°, 2°, 5° and 10° are studied showing that, depending on the kind of misalignments, significant distortions might be present in the CT volume.

Thus it is of fundamental importance to study the effects of geometrical misalignments on CT measurements and to determine the sensitivity of measurements to the different misalignments. The detailed comprehension and quantification of the effects of geometrical misalignments is an essential step to achieve the development of calibration procedures for CT systems and to obtain traceable CT measurements which is the final aim of CT metrology. Knowing which effects are produced by each misalignment, and which is the sensitivity of CT measurements to the particular misalignment enables also to identify which are the most critical geometrical errors and to enhance CT measurement accuracy.

The following sections of this chapter focus on the investigation of the effects of cone-beam CT system geometrical misalignments on the measurement results obtained using circular scanning trajectories. Different sets of experimental investigations performed with calibrated reference objects were specifically designed to investigate the effects of CT system geometrical misalignments on measurement results and to determine the sensitivity of measurements to the particular type of misalignment. This is of primary importance to obtain traceable CT measurements and enhance CT measurement accuracy. Specifically, section 4.3 and 4.4 will deal with detector misalignments whereas in section 4.5 the results of rotary table misalignments will be presented.

4.3. Experimental investigation on the effects of detector pitch, yaw and roll on vertical measurements

As reported in Sect. 4.2.1, the geometrical misalignments of the X-ray source and the rotary table can be expressed as function of the parameters that describe the detector misalignments, namely Δx, Δy, Δz, θ, γ, η (see Figure 4.9). Therefore, the study of detector misalignments is of major importance. The work reported in this section was performed in collaboration with North Star Imaging Inc. In particular, in this section detector angular misalignments are investigated, that is θ, γ, η. Vertical and longitudinal misalignments i.e. Δy and Δz will not be addressed since vertical misalignments can be relevant in case of movements along the y direction (e.g. fan-beam systems or different scanning trajectories) which do not occur during traditional cone-beam circular scans, whereas Δz shifts along the magnification axis lead to errors in *SDD* and therefore in the magnification factor *M*. These errors have already been study in literature and their effects are analyzed for example in [96,97].

4.3.1. Experimental set-up

In order to study the influence of detector angular misalignments on CT measurements dedicated experimental campaigns were specifically designed [25,94]. For this purpose, a calibrated ball bar containing 7 equally spaced ceramic spheres with nominal diameter of 1.59 mm and center-to-center nominal distances ranging between 5 mm and 30 mm was used (Figure 4.20). The calibrated ball bar was provided by North Star Imaging Inc. A carbon-fiber reinforced rod was used as frame of the object in order to enable for thermal and mechanical stability.

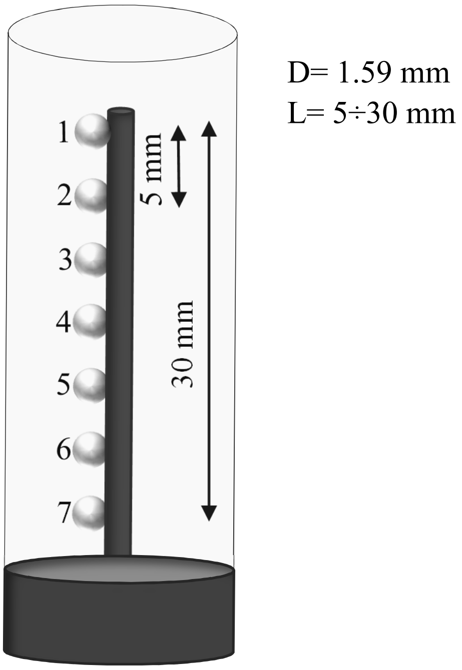

Figure 4.20: Schematic representation of the calibrated ball bar used for the experimental investigation.

Reference measurements of sphere diameters, sphere center-to-center distances (including the distances between non-adjacent pairs of spheres) and form errors were acquired with a tactile CMM.

A ball bar was chosen for the experimental investigations because it is a well-established object used in the testing of CT systems that allows for excellent thermal stability, consistent and solid CMM calibration, and do not introduces additional influence quantities in CT measurements. In fact, the measurement of center-to-center distances are not threshold dependent (see Sect. 3.7) and therefore allow for measurements that are not affected by the selected threshold and particular surface extraction algorithm used. Moreover, the ceramic spheres being of simple geometry and relatively easy to penetrate with the X-rays do not introduce geometry and material effects [61,73]. These characteristics are essential to isolate different influence quantities. Since the interest of this work is on the effects of detector angular misalignments it was necessary to use an object that do not cause the superimposition of the above mentioned influence quantities. All the CT scans were performed with a metrology CT system, a NSI CXMM 50 featuring a 225kV micro-focus reflection X-ray source, a 2D flat panel detector with a 127 µm pixel size, and an air-cooled cabinet.

In the first step of the investigation, after having aligned the system according to manufacturer's procedures, repeated CT scans of the ball bar were performed with the system properly aligned in order to investigate the residual errors of CT measurements performed with the system properly aligned. The ball bar was positioned in the measurement volume oriented in the vertical direction (i.e. parallel to the *y* axis of Figure 4.2) and off-center from the center of rotation. This was done to reveal the errors on measurements performed in the vertical direction. Sphere number 4 was centered on the middle plane of the detector, sphere 1 was positioned close to the upper edge of the detector and sphere 7 was positioned close to the lower edge of the detector as described in Figure 4.21 in order to obtain a completely symmetric positioning of the spheres on the detector.

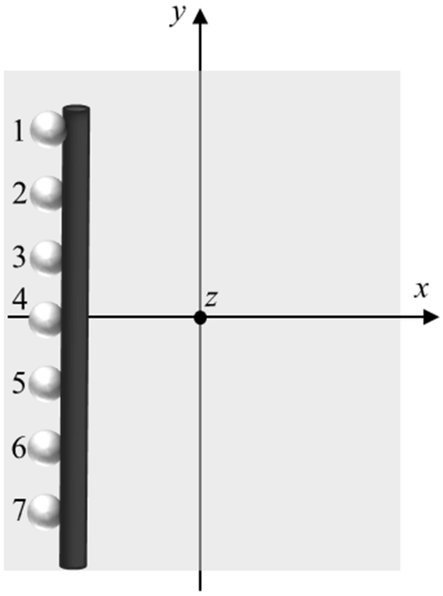

Figure 4.21: Positioning and orientation of the ball bar in the CT volume. The ball bar was oriented in the vertical direction and positioned off-center from the center of rotation. Sphere 4 was positioned in the central plane of the detector, whereas sphere 1 and sphere 7 were positioned respectively close to upper and lower edges of the detector.

CT scans were performed using the scanning parameters reported in Table 4.1.

Voltage	110 kV
Current	150 µA
Exposure time	1.5 fps
Frame averaging	2
Filtering	none
Voxel size	20 µm

Table 4. 1: Scanning parameters used for the experimental investigation.

The use of a *SDD* of nominally 1300 mm enabled to minimize the effects of cone-beam artifacts in the upper and lower regions of the detector.

After that the flat-panel detector was purposefully physically misaligned in order to study the influence of detector out of plane rotations about the *x* and *y* axis and detector in plane rotations about the *z* axis on the measurement results. Three different sets of misalignments (i.e. detector pitch, detector yaw and detector roll) were carried out separately in order to study the effects of the single type of misalignment individually. For each set of misalignments three angular misalignments of nominally 0.5°, 1° and 1.5° were induced to investigate the influence of the misalignment with varying angles, for a total of 9 different misaligned configurations. CT scans in each of the 9 misaligned configurations were performed with the sample oriented in the same way as for the scans performed with the system properly aligned and with the scanning parameters of Table 4.1.
Minimum misalignments of 0.5° were chosen in order to be able to isolate the effects of detector angular misalignments on the measurement results. The use of smaller angles in fact, could have caused the effects of detector misalignments to be of the same order of magnitude of other influence quantities making the analysis of the effects of detector angular misalignments not possible. The use of a minimum misalignment of 0.5° degrees guarantees that detector misalignments are the preponderant influence quantity. The presence of misalignments bigger than 1.5° instead is unlikely for industrial systems in which an alignment procedure has been carried out and with a certain degree of accuracy in the mechanical assembly.
The misalignments were produced by physically acting on the detector hardware. First the parameters needed to obtain the specific misalignments were mathematically calculated using the detector hardware specifications. Then the detector was physically adjusted accordingly in order to obtain the desired configurations. The misalignments were also measured using an electronic digital level with a 0.01° resolution (only for misalignments were the use of the level was possible) that provided excellent consistency of the results with mathematical calculations.
After each set of misalignments, the system was re-aligned by re-performing the alignment procedures in order to guarantee the system was in the aligned configuration before starting the next set of misalignments, and to avoid therefore the superimposition of the effects of different misalignments. After each re-alignment a CT scan of the ball bar was also performed in order to check the consistency of the measurement results. Of course in real practice misalignments of the detector can occur simultaneously however the purpose of this study is to investigate the effects of the misalignments separately in order to quantify the effects that each misalignment produces on the measurement results.

With reference to the coordinate system defined in Figure 4.2, the investigated misalignments are: three angular misalignments in the negative θ rotation, three misalignments in the positive γ rotation and three misalignments in the negative η rotation (see Figure 4.22).

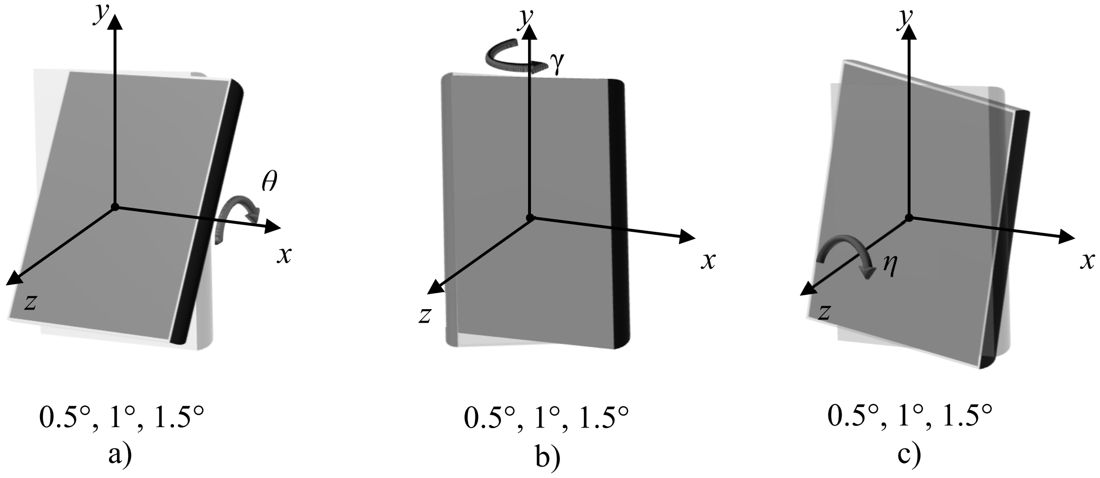

Figure 4.22: Angular misalignments studied in the experimental investigation. a) Three angular misalignments of 0.5°,1°,1.5° investigated in the negative θ rotation, b) three angular misalignments of 0.5°,1°,1.5° investigated in the positive γ rotation, c) three angular misalignments of 0.5°,1°,1.5° investigated in the negative η rotation.

For each scan a procedure to estimate the geometry of the system was applied as per the system manufacturer's guide. In this procedure, out of plane rotations of the detector were disabled from the geometry estimation. Therefore, the detector misalignments about the *x* and *y* axis were not accounted for during reconstruction, whereas magnification errors at the center of the detector were taken into account. For misalignments about the *z* axis also in plane rotation of the detector was disabled from the geometry estimation. The acquired information was then used to perform the reconstruction.

4.3.2. Data analysis

All CT data were reconstructed by means of the manufacturer's reconstruction software NSI efX-ct, using a conventional FDK based algorithm. CT volumes were subsequently imported and analyzed using VGStudio MAX 2.2. A local adaptive surface determination algorithm was used for all CT scans [105]. First, the ISO 50 value, i.e. the average gray value between the peaks of the material and the peaks of the background, was determined, then the more refined surface determination algorithm which locally searches for the maximum gradient of gray values was applied [105].
In order to avoid inaccuracies in measurements due to the part of the spheres glued to the carbon-fiber reinforced rod the region of interest consisting of the top hemispheres was considered. Sphere diameters, sphere center-to-center distances and spheres form errors were then calculated for each of the CT scans using Gaussian least-squares fitting.
Sphere distance errors, probing errors of size and probing errors of form were then computed according to VDI/VDE 2630 part 1.3.

4.3.3. Results and discussions

In this section the results obtained from CT measurements performed with the system aligned according to manufacturer's guidelines, and in presence of the three different set of detector angular misalignments are presented and discussed. The section is divided into four subsections that analyze the results obtained respectively in the aligned configuration (section 4.3.3.1), in presence of detector pitch (section 4.3.3.2), detector yaw (section 4.3.3.3) and detector roll (section 4.3.3.4).

4.3.3.1. Aligned configuration

The measurement results obtained for the repeated CT scans performed with the system in the aligned configuration are compared to the calibrated values obtained from tactile CMM measurements [25,94]. Figure 4.23 reports the errors, calculated as (CT measurements − CMM measurements), for the 21 sphere center-to-center measurements of the ball bar.

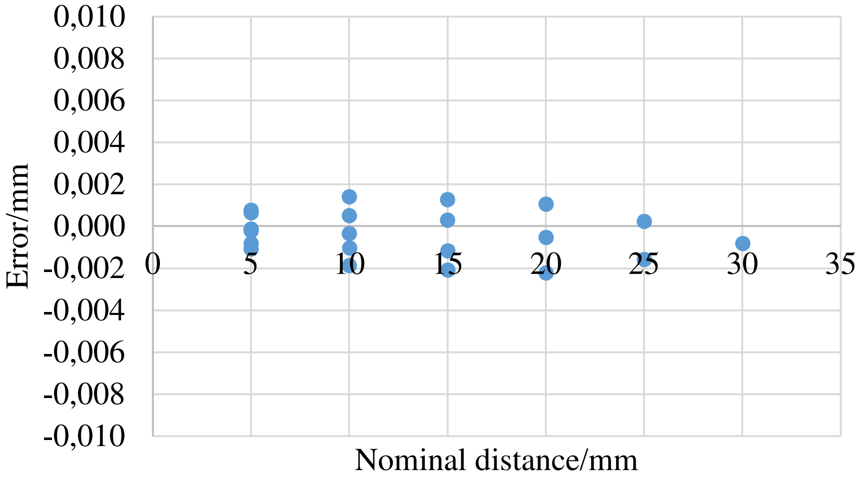

Figure 4.23: Sphere distance errors obtained for the CT scans of the ball bar with the system in the aligned configuration. The horizontal axis of the diagram reports the nominal distance between the sphere centers. The vertical axis gives the measurement errors calculated as (CT measurements - CMM measurements) for the series of three repeated CT scans.

In Figure 4.23 CT measurements are the average of three repeated CT scans. Standard deviations smaller than 0.4 µm were found.
As it is visible in Figure 4.23, when the system is aligned according to manufacturer's guidelines the sphere distance errors are always within ± 2 µm and do not exhibit any trend.

Figure 4.24 a) and b) report the results obtained for diameter measurements and form measurements of the 7 spheres of the ball bar. In both figures, in the vertical axis the errors between CT measurements and reference CMM measurements are reported whereas in the horizontal axis the sphere numbers are present. Also in this case the measurements in the charts are obtained as the average of three repeated CT scans.

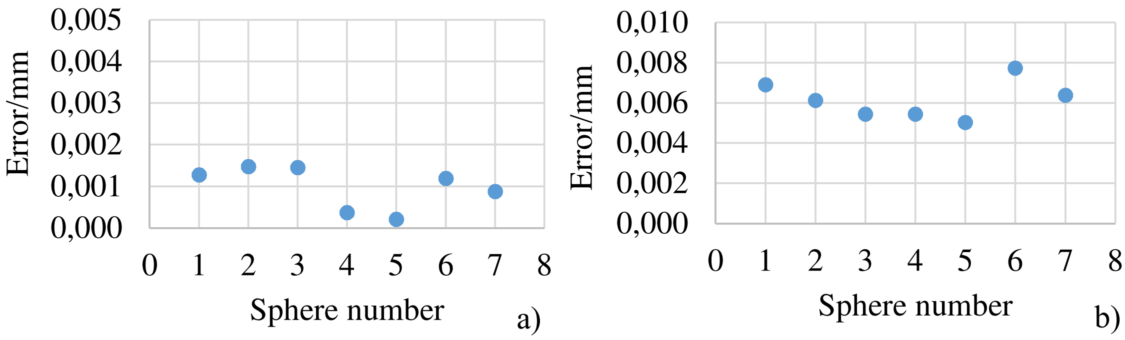

Figure 4.24: a) Sphere diameter errors and b) Sphere form errors obtained for the CT scans of the ball bar performed with the system in the aligned configuration. The horizontal axis of the diagram reports the sphere numbers. The vertical axis of figure a) gives the measurement errors calculated as (CT measurements - CMM measurements) for the series of three repeated CT scans. The vertical axis of figure b) gives the sphere form errors for the series of three repeated CT scans.

As visible in Figure 4.24 sphere diameter errors smaller than 2 µm and sphere form errors smaller than 8 µm were found. It is important to underline that, when computing the sphere form errors, no filtering was applied to the measurements.

The obtained results confirm the proper operation of the CT system before the misalignment processes, and these results can be used as reference results showing the residual errors which are present when measuring the ball bar with that scanning strategy with a properly aligned CT system.

4.3.3.2. Detector pitch

In this section the results obtained for the different misaligned configurations, characterized by different amplitudes of the detector pitch about the *x* axis (see Figure 4.22) are reported [25,94]. In this case, CT measurement results in the misaligned configurations are compared to the CT measurements obtained with the system in the aligned configuration. The measurement results reported in section 4.3.3.1 in fact provide the errors between measurements of the ball bar performed with the system properly aligned and the CMM calibrated values. This gives the description of the residual errors present when the system is in the aligned status. These residual errors cannot be primarily attributed to the presence of CT system geometrical errors which, when the system is in the aligned configuration, are not the predominant influence quantity. The residual errors obtained are smaller than 2 µm and are likely to be caused by the superimposition of other influence quantities which typically affect CT process chain. Therefore, it was decided to compare CT measurements in the misaligned configuration to CT measurements in the aligned configuration in order to have consistent comparison between CT measurements performed with the same scanning parameters and investigate just the errors which can be primarily attributed to geometrical misalignments.

For each CT scan performed with a misaligned detector, the measurement errors with respect to CMM calibrated data were also calculated and showed and optimal agreement with the results obtained using the CT scans acquired with the system in the aligned configuration as reference measurements.

In Figure 4.25 sphere center-to-center measurement errors, calculated as the difference between CT measured values in the misaligned configurations and CT measured values in the aligned configuration, are plotted for each of the six nominal lengths of the ball bar.

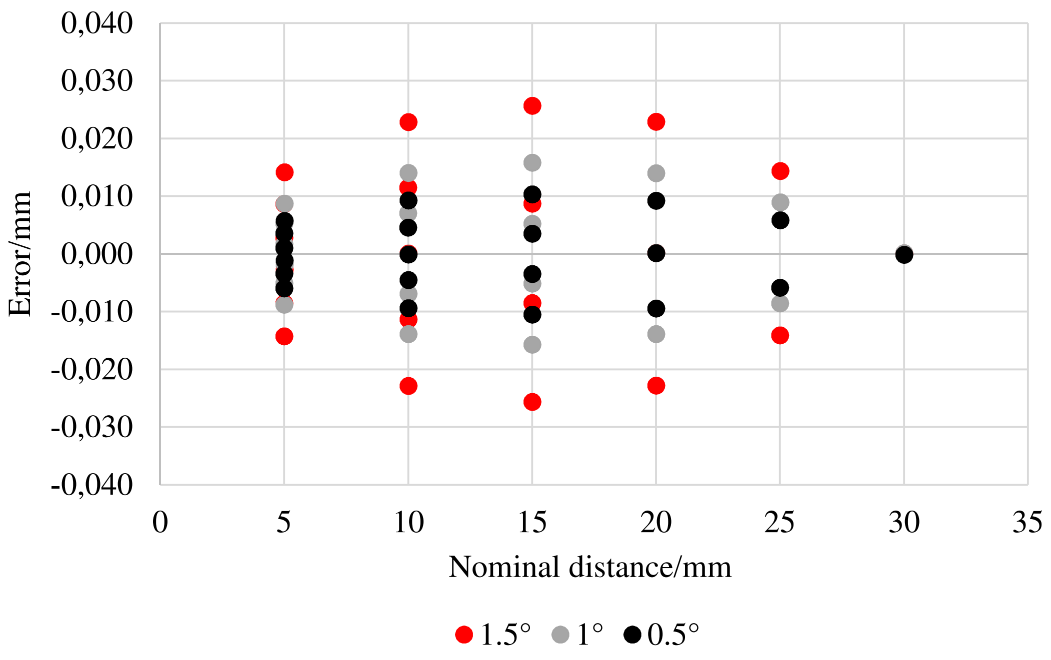

Figure 4.25: Sphere center-to-center distance errors for all the six nominal distances of the ball bar. The horizontal axis of the diagram reports the nominal distance between the sphere centers. The vertical axis gives the measurement errors calculated as (CT values misaligned – CT values aligned) for all the angular detector pitch investigated.

From Figure 4.25 it is evident how the amplitude of angular misalignment has a strong influence on the measured results. With a detector pitch of 0.5° about the *x* axis sphere center-to-center errors up to 10 µm are present. When increasing the amplitude to 1° the sphere center-to-center errors increase and they reach 16 µm. The worst case is represented by the 1.5° misalignment which leads to sphere distance errors close to 26 µm. As expected by increasing the detector angular misalignment, the sphere distance errors increase and reach values significantly larger than the ones obtained with the system aligned. Already with a 0.5° pitch, the maximum sphere center-to-center error found is 10 µm which is significantly larger than the errors obtained with an aligned system. Therefore, for the presented experimental results, it can be concluded that a detector misalignment about the *x* axis has a significant effect on center-to-center measurements performed in the vertical direction (*y* direction represented in Figure 4.2). It is interesting to notice from Figure 4.25 that for all the three detector pitch investigated up to 1.5°, the sphere center-to-center errors present a symmetrical behavior about the *x* axis (i.e. for example the error between sphere 1 and 2 is similar to the error between sphere 6 and 7 but with the opposite sign) [25,94]. This is more visible in Figure 4.26 which reports the sphere center-to-center errors in function of each specific sphere distance.

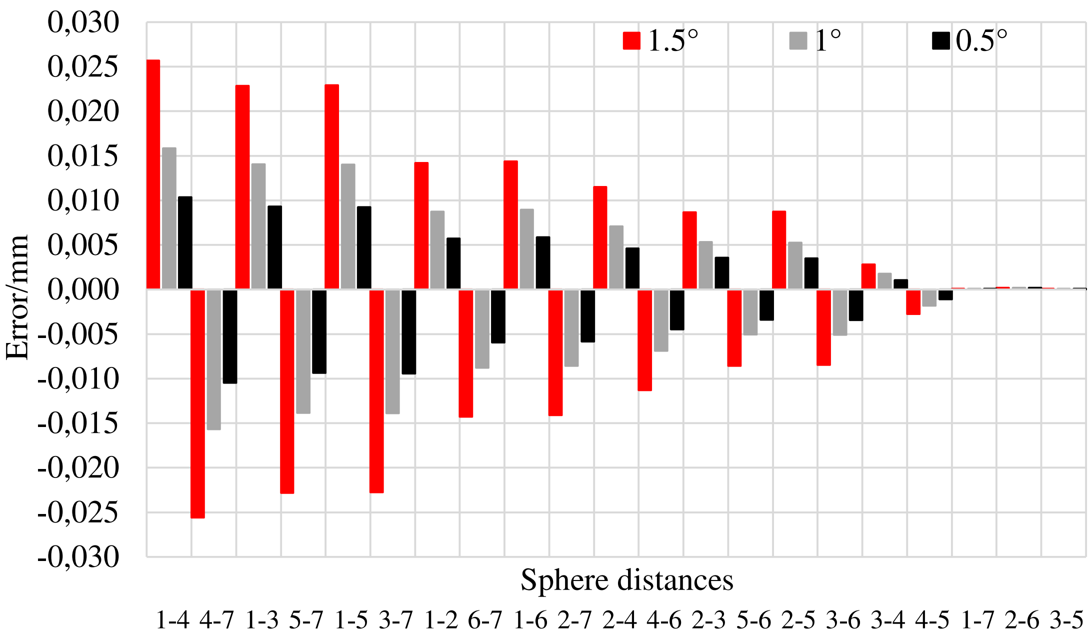

Figure 4.26: Sphere center-to-center distance errors between the seven spheres of the ball bar. The horizontal axis of the diagram reports the names of sphere distances. The vertical axis gives the measurement errors calculated as (CT values misaligned – CT values aligned) for all the detector pitch investigated.

Distances between spheres positioned above the central plane of the detector in the aligned configuration present positive errors, whereas distances between spheres positioned below the central plane present negative errors. For example, the error between sphere 1 and 4 is similar to the one between sphere 4 and 7 but with the opposite sign. The magnification, in fact, is established at the center of the detector and the angle introduced as shown in Figure 4.22 affects the magnification symmetrically about the detector center [25,94]. In particular, the source to detector distance (*SDD*) is affected in opposite directions (Figure 4.23).

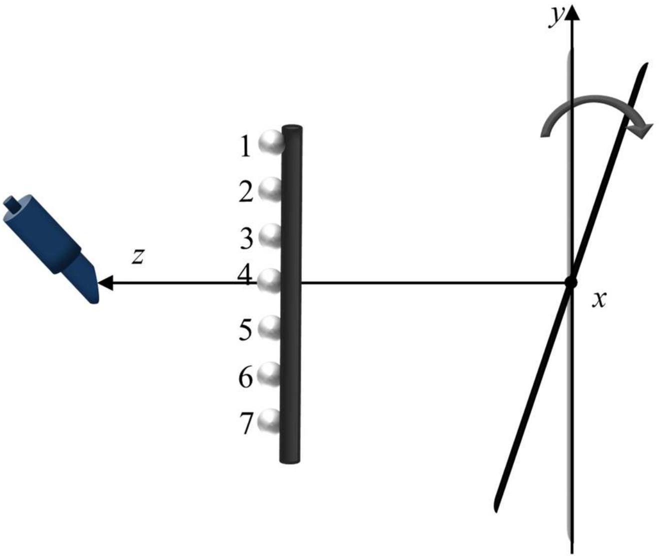

Figure 4.27: Schematic representation of the effects of the studied misalignments. The ideally aligned detector is represented in light grey color, the misaligned detector is represented in dark grey color. Due to the detector misalignment the source to detector distance SDD is affected in opposite directions at top and bottom of the detector.

With respect to the aligned configuration, for the induced misalignments, *SDD* increases for spheres above the central plane of the detector and it decreases for spheres below. This means that for spheres positioned above the central plane of the detector the actual *SDD*, and as a consequence the actual magnification, are bigger. This means that in the upper part of the detector the voxel size of the reconstructed volume is overestimated with respect to the actual voxel size. This over estimation leads to positive measurement errors. In the regions of the detector below the central plane instead, the actual *SDD*, and as a consequence the actual magnification, are smaller. This means that in that regions the voxel size of the reconstructed volume is underestimated with respect to the actual voxel size, which gives negative measurement errors.

Magnification errors therefore are present in the whole detector and increase for spheres far away from the center of the detector in the aligned configuration [25,94]. For example, the distance between spheres 2 and 4 is smaller than the distance between spheres 1-4 (and with opposite sign of distance 4-6). Moreover, as visible in Figure 4.26, the lengths which comprise points symmetric about the *x* axis are characterized by a smaller error because they have opposite errors that cancel out; for example, this happens for sphere distance 1-7.

Figure 4.28 describes the effects of the different angles, on the diameter errors of the spheres of the ball bar. It is visible how in this case the spheres which occupy similar regions on the detector (but at opposite sides vertically) in the aligned configuration, show diameter errors with opposite sign.

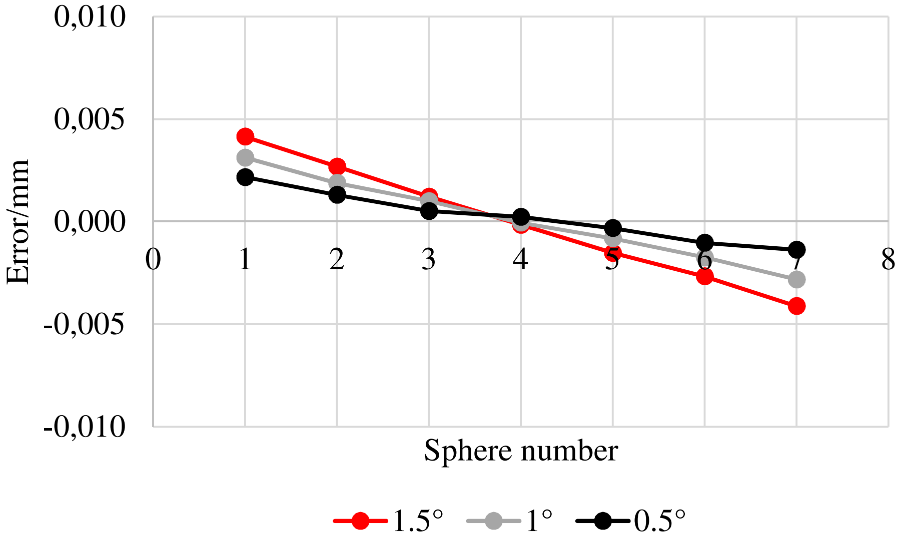

Figure 4.28: Diameter errors for all of the seven spheres of the ball bar. The horizontal axis of the graph reports the sphere numbers. The vertical axis gives the measurement errors calculated as (CT values misaligned – CT values aligned) for all the angular misalignments considered in the study.

Also in this case, when increasing the angular misalignment, the measured diameter errors increase. For a 1.5° misalignment they reach 4 µm for sphere number 1. It is interesting to note that sphere 4, which is approximately in the center of the detector, is nearly unaffected by the misalignments.

In the aligned configuration, no trend in the diameter error was visible and all the errors were randomly ranging from zero to 2 µm. Therefore, it can be concluded that the particular trend visible in Figure 4.28 is caused by the angular misalignment about the *x* axis (see Figure 4.22).

The form errors were also compared, and are reported in Figure 4.29.

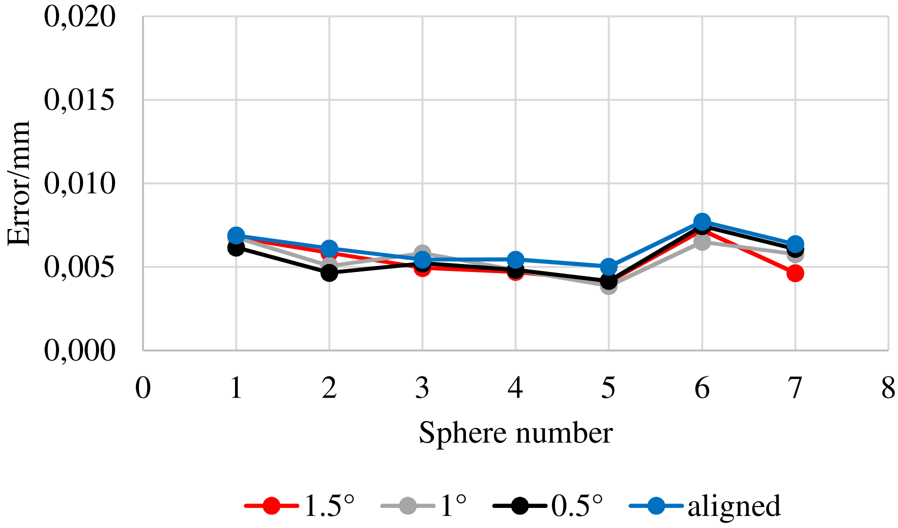

Figure 4.29: Form errors obtained for the aligned configuration and for detector pitch misalignments. The horizontal axis of the graph reports the sphere numbers. The vertical axis gives the spheres form errors.

In this case, no significant difference between the aligned and misaligned configurations was found.

This is likely due to the relatively small change in magnification over the extent of a single sphere which is dominated by other factors contributing to the form error, such as detector noise.

The experimental results therefore show that a pitch about the *x* axis of the detector has significant effects when measuring sphere center-to-center errors and diameter errors of a ball bar positioned in the vertical direction. Moreover, for the *x* tilts of the detector up to 1.5° considered in this study, magnifications errors are present which increase for spheres far away from the center of the detector. These magnification errors are also characterized by opposite sign, depending whether the sphere is positioned in the upper or lower part of the detector [25,94].

4.3.3.3. Detector yaw

The effects caused by detector yaw of 0.5°, 1° and 1.5° about the *y* axis were also investigated.

Figure 4.30 reports the errors between CT measurements performed in the three misaligned configurations and CT measurements with the system properly aligned.

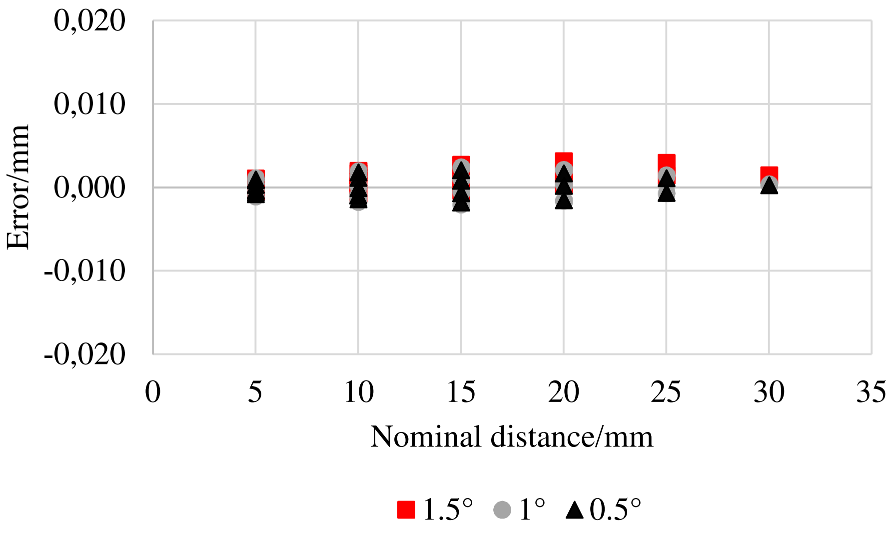

Figure 4.30: Sphere center-to-center distances errors for all the six nominal distances of the ball bar. The horizontal axis of the diagram reports the nominal distance between the sphere centers. The vertical axis gives the measurement errors calculated as (CT values misaligned – CT values aligned) for all the angular detector yaw investigated. For a better visibility the measurement results obtained for a 0.5°detector yaw are represented as triangles, whereas the measurement results obtained for a 1° and 1.5° detector yaw are represented respectively as dots and squares.

In case of detector yaw up to 1.5°, the sphere center-to-center distances of the ball bar positioned in the vertical direction are not affected by significant measurement errors. As visible in Figure 4.30 in fact, the errors are comprised within +3µm and -2µm and do not exhibit any particular trend. For all the three misalignments, namely 0.5°,1° and 1.5° no significant difference is observed for the measured sphere center-to-center distance errors. Therefore, it can be concluded that the detector yaw investigated and up to 1.5° do not affect the measurements performed in the vertical direction. This holds true for different amplitudes of the misalignment (i.e. 0.5°, 1°, 1.5°).

The explanation for this behavior is reported in the following. When the detector is affected by a yaw about the *y* axis the spheres of the ball bar, which for all the experimental investigations was placed vertically and off-center from the center of rotation, are characterized by a change in magnification during the rotation. In fact, the magnification is established at the center of the detector; however, in presence of a detector yaw in the positive *y* axis rotation the right side of the detector will be further away from the X-ray source, whereas the left hand side will be closer to the source (see Figure 4.31). This causes a change in the actual magnification, which varies with the horizontal distance from the center of the detector and is constant along the detector columns. During its 360° rotation the ball bar oriented vertically, pass through zones with equal and opposite magnifications. This causes spheres center-to-center distances measured in the vertical direction that do not present measurement errors.

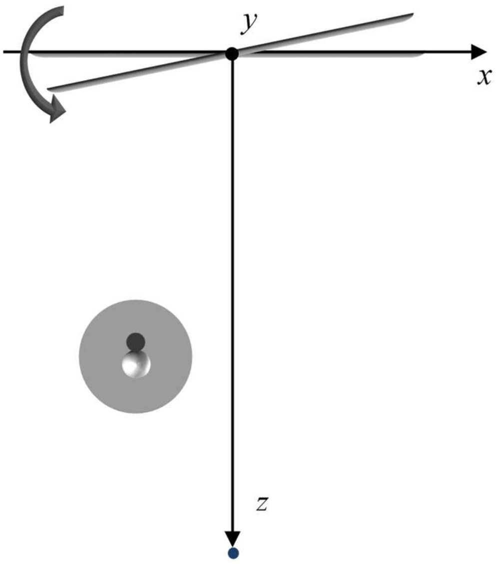

Figure 4.31: Schematic representation of the effects of detector yaw about the y axis. The ideally aligned detector is represented in light grey color, the misaligned detector is represented in dark grey color. Due to the detector misalignment the left hand side of the detector is closer to the source whereas the right hand side of the detector is further away from the source. During its rotation therefore the object passes through zones with different magnifications.

In Figure 4.32 the effects of detector yaw on the diameter errors are represented. For all the three investigated detector yaw the sphere diameter errors are smaller than 2.5 µm.

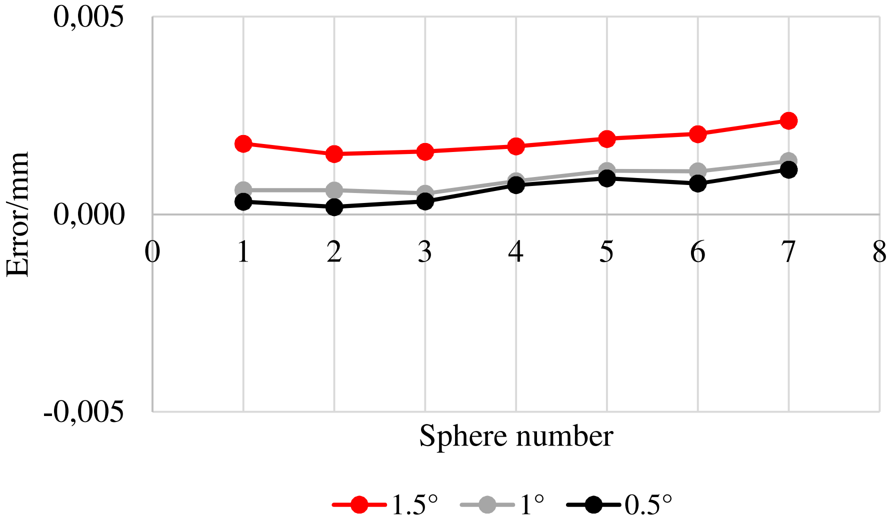

Figure 4.32: Diameter errors for all of the seven spheres of the ball bar. The horizontal axis of the diagram reports the sphere numbers. The vertical axis gives the measurement errors calculated as (CT values misaligned – CT values aligned) for all the angular yaw investigated.

As for the sphere center-to-center distances, in this case as well the sphere diameters measurements obtained from CT scan of the ball bar oriented vertically and placed off-center from the center of rotation in the measurement volume do not present significant measurement errors for detector yaw up to 1.5°. From Figure 4.32 it is also visible how, for all the three different amplitude of detector yaw investigated, the sphere diameter errors exhibit a horizontal trend. This means that the spheres diameters are not affected by the position of the spheres in the vertical direction.

Although the small errors obtained for the sphere diameters measurements of the ball bar scanned in the vertical direction and off center from the rotary center do not reveal significant influence of detector yaw up to 1.5°, by analyzing the sections of the spheres in VGStudio MAX it was observed that artifacts occur due to the induced detector yaw (Figure 4.33).

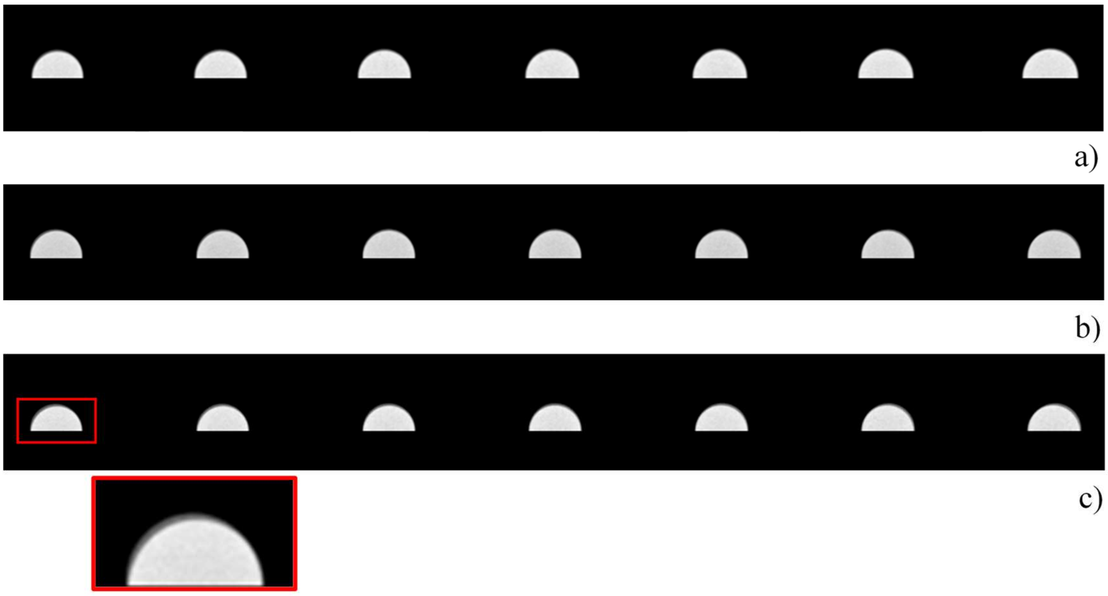

Figure 4.33:Central sections in the xy plane of the three different CT volumes. a) 0.5° detector yaw, b) 1° detector yaw, c) 1.5°detector yaw. In all the images sphere 1 is positioned on the left hand side.

Figure 4.33 shows how, due to the detector yaw experimentally investigated, the reconstructed volume if affected by the presence of artifacts which increase with the amplitude of the misalignment. In particular, the edges of the spheres are not sharp anymore and appear doubled. This behavior becomes stronger as the amplitude of the induced misalignments increases.

When measuring the form errors of the spheres instead the presence of those artifacts in the reconstructed volume affects the measurements. Figure 4.34 reports the form errors obtained for the 7 spheres of the ball bar for the three detector yaw investigated and for the CT scans acquired with the system in the aligned configuration.

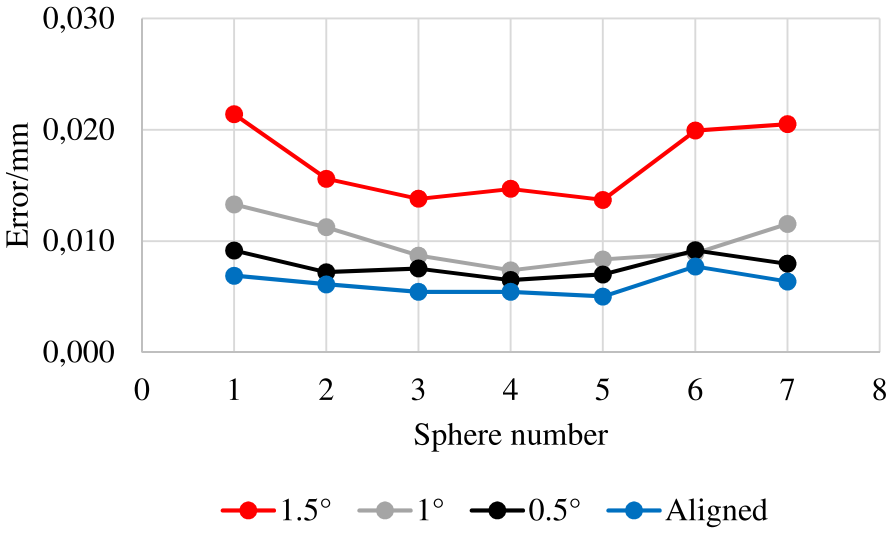

Figure 4.34: Form errors obtained for the aligned configuration and for detector yaw misalignments. The horizontal axis of the diagram reports the sphere numbers. The vertical axis gives the form errors.

With a 0.5° yaw of the detector sphere form errors are slightly affected by the artifacts depicted in Figure 4.33, and reach 9 µm. When increasing the amplitude of the detector yaw the spheres form errors become more affected by the presence of the artifacts. In particular, with a 1° yaw form errors reach 13 µm whereas for a 1.5° yaw form errors reach 21 µm.

From the he experimental results it can be concluded therefore, that detector yaw about the *y* axis of the detector up to 1.5° do not show significant effects when measuring sphere center-to-center errors and diameter errors of a ball bar positioned in the vertical direction and placed off-center from the center of rotation. Such kind of misalignment however causes the presence of artifacts in the reconstructed volume because of which the edges of the spheres appear to be doubled. These artifacts affect the form errors which increase with the amplitude of the detector yaw.

4.3.3.4. Detector roll

Detector roll describes an in plane rotation of the detector. In this section the measurement result obtained after inducing detector roll of 0.5°, 1° and 1.5° are reported.
In the case of detector roll, before reporting the results obtained for sphere center-to-center distances, diameter errors and form errors, it is interesting to analyze before the effects that this kind of misalignment produces on the reconstructed volume. Figure 4.34 and Figure 4.35 describe the effects of the three investigated detector roll respectively on the 3D view of the ball bar and on sections on the middle plane of the sphere.

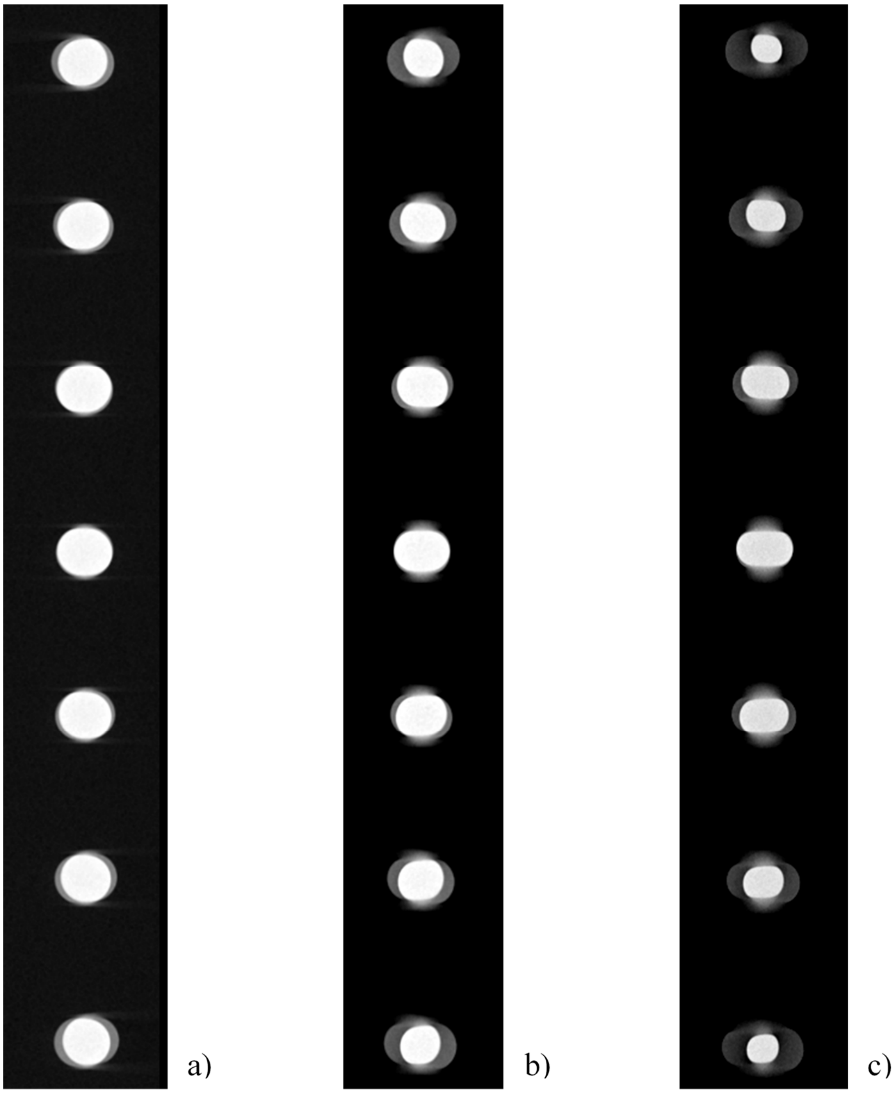

Figure 4.35: Effects of the experimentally investigated detector roll on of the central sections in the yz plane of the ball bar. a) 0.5° detector roll, b) 1° detector roll, c) 1.5° detector roll. In all the images sphere 1 is positioned on the top of the image.

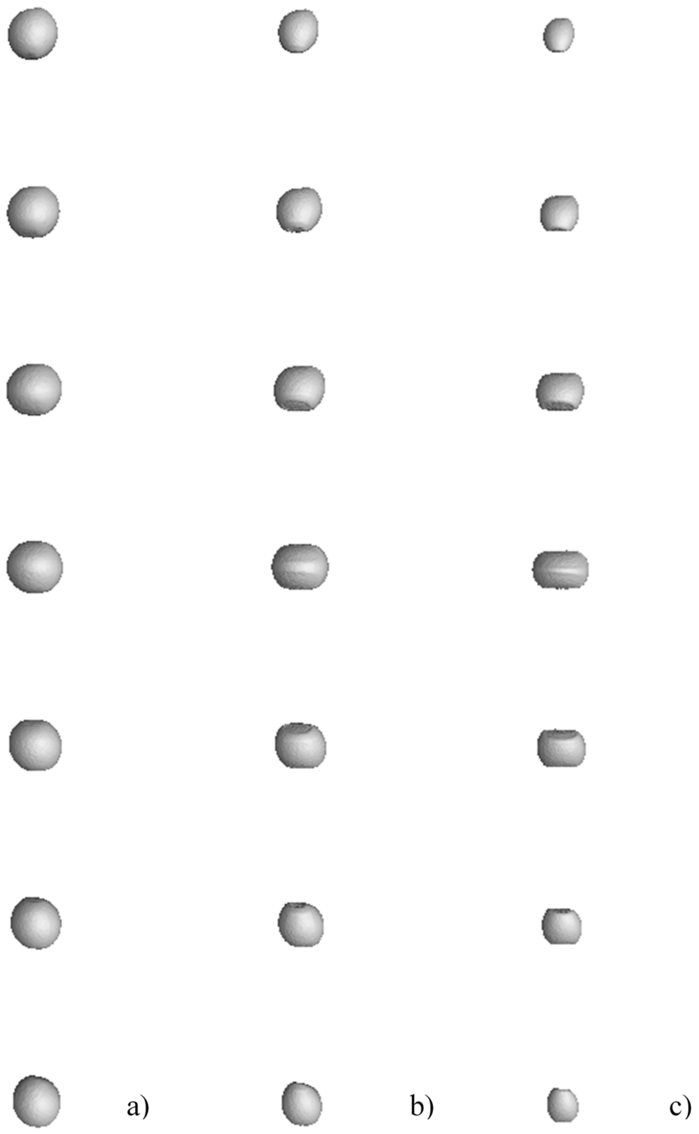

Figure 4.36 Effect of the experimentally investigated detector roll on the 3D views of the ball bar. a) 0.5° detector roll, b) 1° detector roll, c) 1.5° detector roll. In all the images sphere 1 is positioned on the top of the image.

It is immediately visible that this kind of angular misalignment produces extremely severe artifacts. In presence of a detector roll of 0.5°, which is the smallest roll investigated in this study, severe artifacts are already present in the reconstructed volume. By looking at the central sections of the ball bar (Figure 4.35) it is visible how the spheres appear doubled and are characterized by higher and lower gray values, as they were composed of two different spheres overlapping. These overlapping portions are characterized by gray values similar to the ones that characterizes the spheres in the CT scans acquired in the aligned configuration. By performing the surface determination process using the local advanced algorithm in VGStudio MAX 3.0 with starting contour the edges of these zones in which the spheres are overlapping, it is possible to generate the surface for the overlapping regions of the spheres as represented in the 3D view of (Figure 4.36). Here it is visible how the balls of the rod are not characterized by a spherical shape anymore.

This behavior become significantly more accentuated when increasing the amplitude of the detector roll. With a 1.5° detector roll the balls completely loose the spherical shape. For all the investigated detector roll the experimental results show how the artifacts become more severe for the spheres which are further away from the center of the detector.

In the following the measurement results obtained for the misaligned configurations investigated and characterized by the presence of detector roll of different amplitudes are presented. In all cases the measurements are performed after the surface determination step as described above. For each misalignment moreover, the measurement results obtained after applying a software correction for detector roll are also reported.

Figure 4.37 a) describes the sphere center-to-center distance errors calculated in presence of a detector roll. For detector roll of 0.5° and 1° the sphere center-to-center measurement errors reach respectively 3 µm and 5µm. In this case, the sphere centers are just relatively affected by the misalignment. In fact, if we consider the severe artifacts to which are subject the spheres, errors of 5 µm are relatively small compared to the distortion of the spheres surfaces. When increasing the amplitude of the misalignment, also the sphere center to center distances increase and for a 1.5° misalignment they reach absolute values of 29 µm which is significantly bigger than the maximum errors obtained for the 0.5° and 1° misalignments. However, again the magnitude of the errors is relatively small compared to the amount of distortion of the spheres.
Figure 4.37 b) reports the sphere center-to-center distance errors obtained after applying a software correction for detector roll to the same dataset acquired with a physically induced detector roll. In this case it is visible how the measurement results for all the three amplitudes investigated are within ± 2µm. This confirms the effectiveness of the detector roll software correction, moreover it also confirms that the detector roll was the predominant influence quantity and that after its correction the measurement errors are really small, as if the physical roll of the detector was not present.

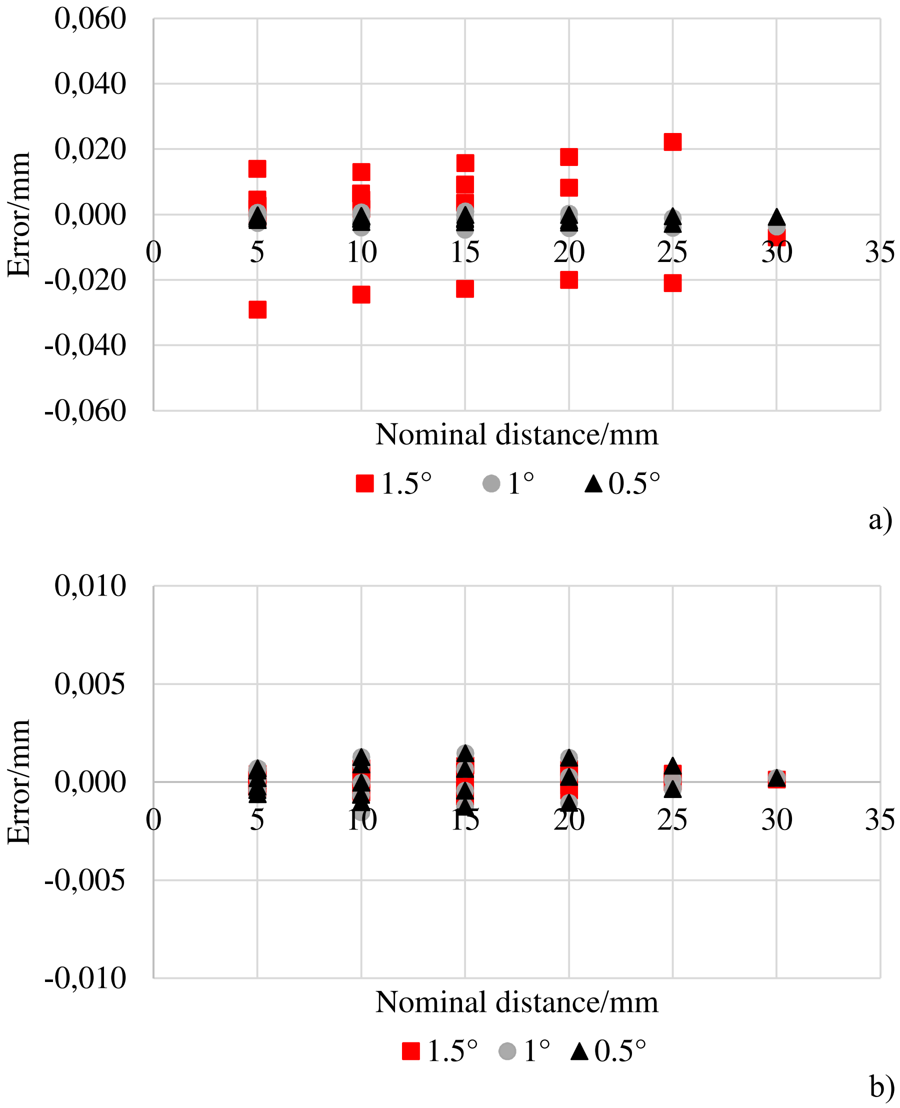

Figure 4.37: Sphere center-to-center distance errors in presence of the three investigated detector roll. The horizontal axis of the diagram reports the nominal distance between the sphere centers. The vertical axis gives the measurement errors calculated as (CT values misaligned – CT values aligned). Figure a) measurement results in presence of detector roll, b) measurement results obtained from the same scans but after software correction for detector roll. For a better visibility the measurement results obtained for a 0.5°detector roll are represented as triangles, whereas the measurement results obtained for a 1° and 1.5° detector roll are represented respectively as dots and squares.

In Figure 4.38 a) the sphere diameter errors are represented. In this case, as expected from Figure 4.35, the CT measured diameters in presence of a detector roll are significantly affected by the misalignment. When the detector is misaligned due to a detector roll the measured diameters are consistently smaller than the ones obtained with the system in the aligned configuration. The measurement errors therefore present negative values. When increasing the amplitude of the misalignment, the errors become significantly bigger. For a detector roll of 0.5° the maximum sphere diameter error reaches 212 µm. For detector roll of 1° and 1.5° the measured errors reach respectively 430 µm and 723 µm. Moreover, Figure 4.38 a) shows also that this misalignment causes a particular trend in the sphere diameter errors. In fact, for all the three amplitudes of the misalignment, the sphere in the center detector (i.e. sphere 4) present the smallest error, whereas the errors increase symmetrically with increasing distance from the center of the detector vertically. For example, sphere 1 and sphere 7 present similar errors for the three amplitudes investigated.

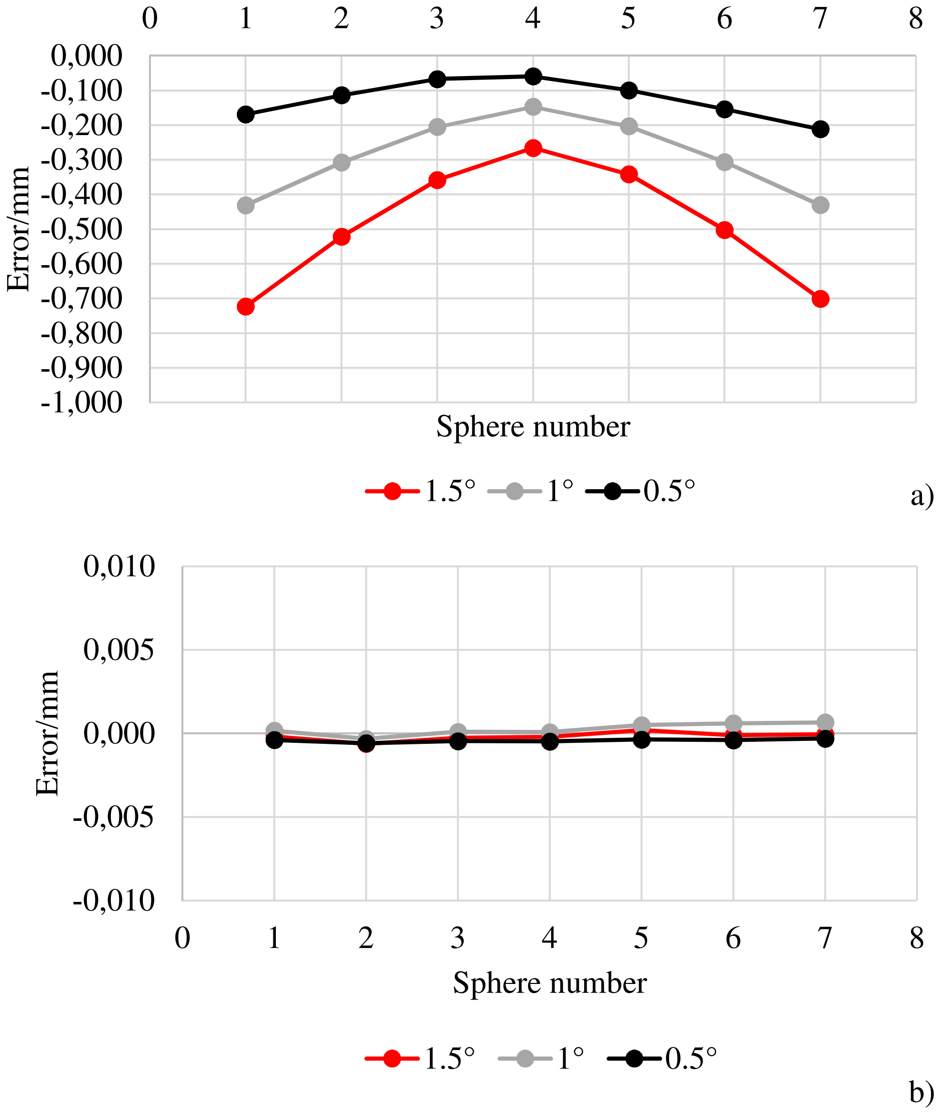

Figure 4.38: Diameter errors in presence of the three investigated detector roll values. The horizontal axis of the graph reports the sphere numbers. The vertical axis gives the measurement errors calculated as (CT measurements in the misaligned configuration - CT measurements in the aligned configuration). Figure a) measurement results in presence of detector roll, b) measurement results obtained from the same scans but after software correction for detector roll.

Sphere center-to-center distance errors in presence of the three investigated detector roll. The horizontal axis of the diagram reports the nominal distance between the sphere centers. The vertical axis gives the measurement errors calculated as (CT values misaligned – CT values aligned). Figure a) measurement results in presence of detector roll, b) measurement results obtained from the same scans but after software correction for detector roll. For a better visibility the measurement results obtained for a 0.5°detector roll are represented as triangles, whereas the measurement results obtained for a 1° and 1.5° detector roll are represented respectively as squares and dots.

When analyzing the sphere diameter errors (see Figure 4.38 b)) after having applied a software correction to the CT scan performed with a physically misaligned detector, it is visible also in this case that errors obtained are extremely small and that the correction is effective.

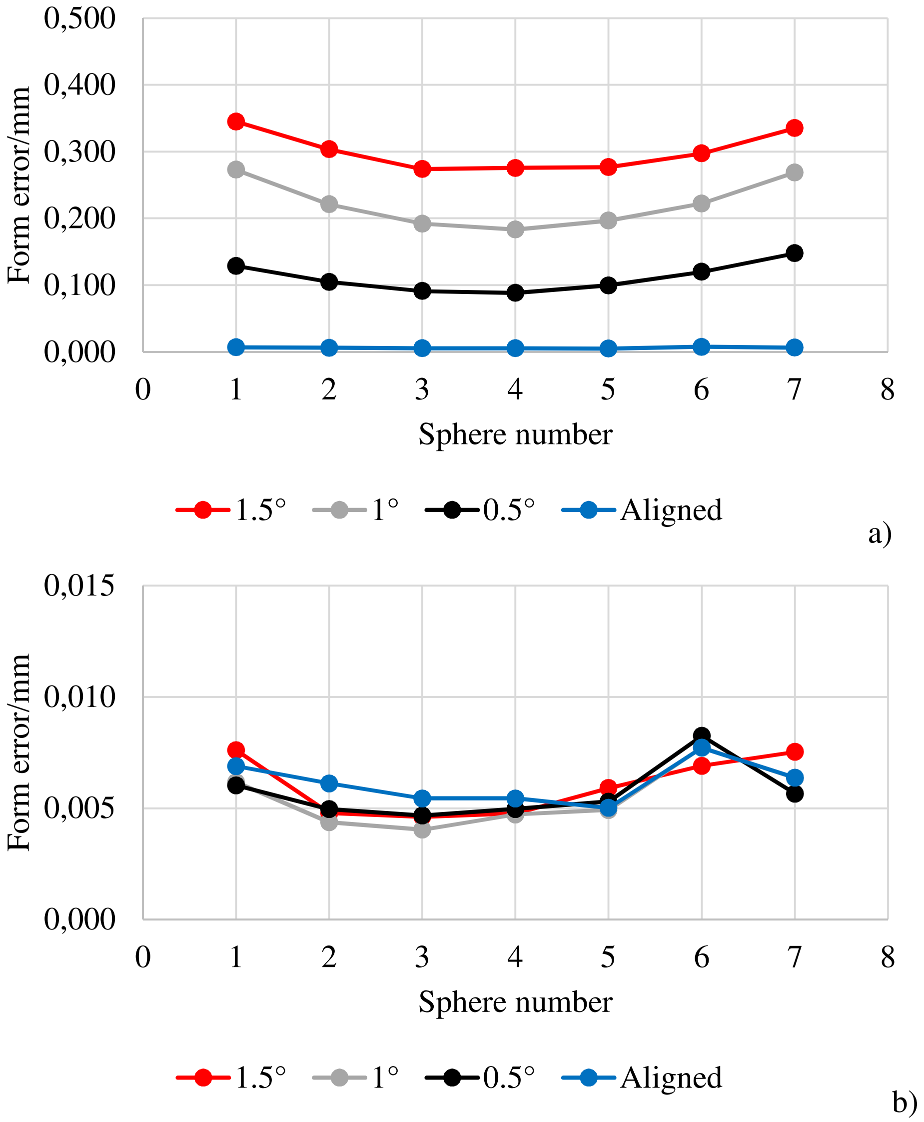

Figure 4.39: Form errors in presence of the three investigated detector roll values. The horizontal axis of the diagram reports the sphere numbers. The vertical axis gives the spheres form errors. Figure a) measurement results in presence of the detector roll, b) measurement results obtained from the same scans but after software correction for detector roll.

Figure 4.39 a) reports the measured form errors obtained in presence of a detector roll. Here, it is visible how the form errors are significantly affected by the in plane rotation, and when increasing the amplitude of the misalignment the form errors consistently increase. For a 0.5° roll form errors up to 148 µm are present. For 1° and 1.5°

misalignments they reach respectively 273 µm and 345 µm. Also for form errors the particular trend found for the diameter errors is visible. Sphere 4 which was positioned at the center of the detector, is characterized by the smaller form error, whereas the form error increase symmetrically while vertically moving away from the central plane of the detector (e.g. sphere 3 and 5 have similar errors, sphere 2 and 6 etc.).
Also in the case of form errors the software correction for detector roll is effective. In fact, as visible in Figure 4.39 b), after applying a software correction for detector roll the obtained form errors present the same values which were obtained for the CT scan acquired with the system in the aligned configuration.

It can be concluded that detector roll significantly affects the measurement results of a ball bar oriented in the vertical direction and placed off-center from the center of rotation. In particular, diameter measurements and form measurement are significantly affected by this kind of misalignment. Sphere center-to-center measurements performed in the vertical direction are also influenced by the presence of a detector roll, however, considering the deformation to which the spheres surfaces are subject the effects of the detector roll experimentally investigated on center-to-center measurements are relatively small.

4.3.4. Conclusions

In section 4.3 the effects of detector pitch, yaw and roll on CT measurements performed on a tactile CMM calibrated ball bar oriented vertically in the measurement volume and positioned off center from the center of rotation were experimentally investigated. The flat-panel detector was purposefully physically misaligned in order to study detector angular misalignments about the x, y and z axis. For each set of misalignments (pitch, yaw and roll), three angular misalignments of nominally 0.5°, 1° and 1.5° were physically induced on the detector, in order to study the sensitivity to different amplitudes of misalignments. The use of the same amplitude of misalignments for detector pitch, yaw and roll enabled also to investigate the sensitivity of CT measurements to each kind of misalignment and compare the magnitude of the obtained errors.
The designed experimental campaigns led to 3 different set of misalignments, namely detector pitch, yaw and roll, and a total of 9 misaligned configurations. Each set of misalignment was studied separately in order to investigate the effects of each single misalignment on the measurement results (i.e. detector pitch, yaw and roll were not combined together but were studied singularly). In between each set of misalignment, a re-alignment of the CT system was performed in order to assure the proper alignment of the system before moving ahead to the next set of misalignment and avoiding the superimposition of different and unwanted misalignments.
The experimental results showed that a detector pitch about the x axis of the detector has significant effects on sphere center-to-center measurements performed in the vertical direction. For a 1.5° detector pitch measurement errors reach 26 µm. In particular, detector pitch produces a specific symmetric behavior of sphere center-to-center distance errors, caused by magnifications errors. For all the investigated detector pitch up to 1.5°, magnification errors symmetric about the x axis were found, which increase for spheres

far away from the center of the detector. When increasing the angular misalignment, the measurement errors consistently increase. For diameter errors, it was also found that spheres which occupy similar regions on the detector but at opposite sides vertically, show diameter errors with opposite signs. With a detector pitch of 1.5° maximum diameter errors of 4 µm were found. The effects on form errors were found to be negligible for detector pitch up to 1.5°.

Detector yaw about the *y* axis of the detector up to 1.5° do not show significant effects when measuring sphere center-to-center distance errors and diameter errors of a ball bar positioned in the vertical direction and placed off-center from the center of rotation. In both cases, in presence of a detector yaw of 1.5° measurement errors smaller than 3 µm were found. This kind of misalignment however causes the presence of artifacts in the reconstructed volume because of which the edges of the spheres appear to be doubled. Form measurements are affected by the presence of the artifacts, and the form errors increase with the amplitude of the detector yaw. For a 1.5° detector yaw the maximum form error reaches 21 µm which is consistently bigger than the form errors obtained with the system in the aligned configuration.

When dealing with a detector roll it can be concluded that it significantly affects the measurements of a ball bar oriented in the vertical direction and placed off-center from the center of rotation. In particular, the spheres of the ball bar do not present a spherical shape anymore. This behavior becomes stronger with increasing vertical distance from the center of the detector. Diameter measurements and form measurements are significantly affected by this kind of misalignment and for a 1.5° roll they reach respectively 723 µm and 345 µm. Sphere center-to-center measurements performed in the vertical direction are not significantly affected by detector roll up to 1°. For a 1.5° roll maximum errors of 29 µm are present. However, considering the deformation to which the spheres are subject the effects of the detector roll experimentally investigated on center-to-center measurements are relatively small.

By comparing the effects caused by the three set of misalignments experimentally investigated therefore, it can be concluded that a pitch of the detector is more problematic when the interest is on the measurement of dimensions (e.g. distances between spheres centers, diameters, etc.) due to the presence of magnifications errors, whereas detector pitch up to 1.5° do not affect form measurements. On the other hand instead, detector yaw affects form measurements, whereas measurement of sphere center-to-center distances and diameter measurements of the ball bar positioned vertically and off-center from the center of rotation are almost unchanged for yaw up to 1.5°. In plane rotations of detector (roll) affect all the measurands investigated in this study, in particular diameter measurements and form measurements, and produces errors with order of magnitude significantly bigger than the ones produced by out of plane rotations of the detector (i.e. pitch and yaw). In fact, for example, when comparing the effects of a 0.5° detector pitch and 0.5° detector yaw to the effects caused by a 0.5° detector roll the distortions caused by detector roll in the measurement volume are significantly evident and measurement errors reach relevant values. Therefore, it can be concluded that detector roll is a more critical factor than detector pitch and detector yaw in the alignment of the detector and that angles smaller than 0.5° might produce relevant measurement errors. However, it was demonstrated that effective software corrections can compensate for the presence of detector roll which therefore can be corrected.

4.4. Experimental investigation on the influence of measurement directions and object positioning on the errors caused by a misaligned detector

The experimental results presented and discussed in section 4.3 are of fundamental importance to study and quantify the effects of detector pitch, yaw and roll on CT measurements. In particular, they enabled to determine the specific effects caused by each different misalignment (i.e. pitch, yaw and roll) on the measurement results of a ball bar oriented vertically and positioned off-center form the center of rotation, and to calculate the measurement errors for each misaligned configuration experimentally investigated. Moreover, they allowed for the quantification of the impact of the amplitude of the misalignments on CT measurements. However, in practice the CT scanned objects can be oriented and positioned in different ways in the CT volume. This means that, measurements within the objects can be performed on different directions with respect to the CT coordinate system of Figure 4.2 (e.g. horizontally, vertically, etc.), and that the object features can also be positioned at different coordinates with respect to the CT coordinate system. Therefore, to fully quantify the CT measurement errors caused by the presence of a misaligned detector, it is essential to investigate the influence of the measurement direction and object positioning. The work presented in the following section was performed in collaboration with North Star Imaging Inc.

4.4.1. Experimental set-up

In order to investigate the influence of measurement direction and object positioning on the measurement errors caused by a misaligned detector a new set of dedicated experimental campaigns were specifically designed. A ball plate containing 25 equally spaced ruby spheres with nominal sphere diameter of 5 mm, glued on a carbon-fiber reinforced polymer plate was used for the experimental investigation (Figure 4.40). The ball plate was developed, manufactured and calibrated by DTU [3].

Figure 4.40: Calibrated ball plate used for the experimental investigation.

Calibrated measurements of sphere diameters, sphere center-to-center distances (including the distances between non-adjacent pairs of spheres) and form errors were acquired with a tactile CMM.

The ball plate of Figure 4.40 was chosen for the experimental investigations because, with respect to the coordinate system represented in Figure 4.1, it allows for multiple measurements between spheres centers in different directions and different locations on the CT volume. More specifically the array of 5x5 spheres enables the measurements of 50 center-to-center distances along the horizontal direction (i.e. *x* axis), and 50 center-to-center distances along the vertical direction (i.e. *y* axis). Moreover, the horizontal and vertical measurements are homogeneously distributed in 5 equally spaced rows and 5 equally spaced columns which therefore homogeneously cover the surface a 2D flat-panel detector. This enables to fully investigate, with the use of one reference object, the influence of measurement direction and feature location on the errors caused by a misaligned detector.

Also in this case, as for ball bars, ball plates made from a carbon-fiber reinforced plate and ruby spheres are well-established objects used in the testing of CT systems, and allow for consistent and solid CMM calibration, as well as the measurement of center-to-center distances which are not threshold dependent.

CT scans of the ball plate were performed with a metrology CT system, a NSI CXMM 50 featuring a 225kV micro-focus reflection X-ray source, a 2D flat panel detector with a 127 µm pixel size, and an air-cooled cabinet.

As described in section 4.3 also in this case after having aligned the system according to manufacturer’s procedures, repeated CT scans of the ball plate were performed with the system properly aligned in order to investigate the residual errors of CT measurements performed with the system in the aligned configuration.

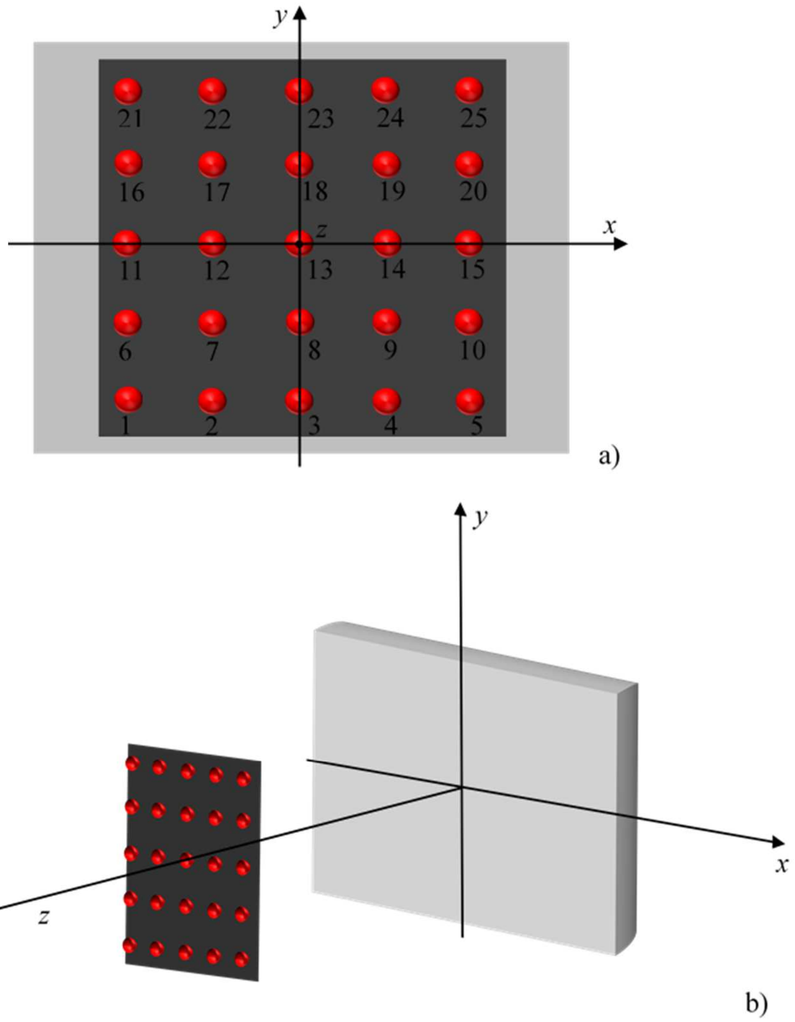

Figure 4.41: Positioning and orientation of the ball plate in the measurement volume. a) schematic representation of the sphere positioning with respect to the detector surface, b) orientation of the ball plane in the measurement volume.

The ball plate was manually positioned in the CT system measurement volume so that it was oriented in the vertical direction (i.e. line through sphere 1 to 21 nominally parallel to the *y* axis of Figure 4.2) and with row number 3 nominally positioned in the central plane of the detector (see Figure 4.41). In this way, two rows of the ball plate, namely row 4 and row 5 are positioned in the upper part of the detector and respectively at increasing distance from the central plane of the detector. Whereas two rows, namely row 1 and row 2 are positioned in the lower part of the detector at nominally symmetric position with respect to row 5 and 4. In the same way two columns of the ball plate, namely column 1 and column 2 are positioned in the left side of the detector and respectively at increasing distance from the detector vertical axis passing through its center. Columns 4 and column 5 are positioned at nominally symmetric position with respect to column 2 and 1 but on the right side of the detector.

In this way the flat-panel detector is homogeneously covered by the ball plate. This enables to reveal the sensitivity of measurement errors caused by detector pitch, yaw and roll on measurements performed in the horizontal, vertical and tilted directions and for different positioning of the spheres.

After a set of preliminary tests the CT scanning parameters reported in Table 4.2 were selected for performing the experimental investigations.

Voltage	165 kV
Current	140 µA
Exposure time	1 fps
Frame averaging	3
Filtering	Copper
Voxel size	40 µm

Table 4.2: Scanning parameters used for the experimental investigation.

The use of a *SDD* of nominally 1200 mm enabled to minimize the effects of cone-beam artifacts in the upper and lower regions of the detector.

After performing the CT scans with the system properly aligned, the same approach described in section 4.3.1 was used for purposefully inducing physical misalignments on the flat-panel detector by physically acting on the detector hardware. First the parameters needed to obtain the specific misalignments were mathematically calculated using the detector hardware specifications. Then the detector was physically adjusted accordingly in order to obtain the desired configurations. The misalignments were also measured using an electronic digital level with a 0.01° resolution (only for misalignments were the use of the level was possible) that provided excellent consistency of the results with mathematical calculations.

The flat-panel detector was physically misaligned in order to study the effects of detector pitch about the x axis, detector yaw about the y axis and detector roll about the z axis. With reference to the coordinate system defined in Figure 4.2, the investigated misalignments are: three angular misalignments in the positive θ rotation, three misalignments in the positive γ rotation and three misalignments in the negative η rotation (see Figure 4.42). Each misalignment was induced separately in order to analyze the effects of the single type misalignment individually (no superimposition of detector pitch, yaw and roll). Of course in real practice misalignments of the detector can occur simultaneously however the purpose of this study is to investigate the effects of the misalignments separately in order to quantify the effects that each misalignment produces on the measurement results.

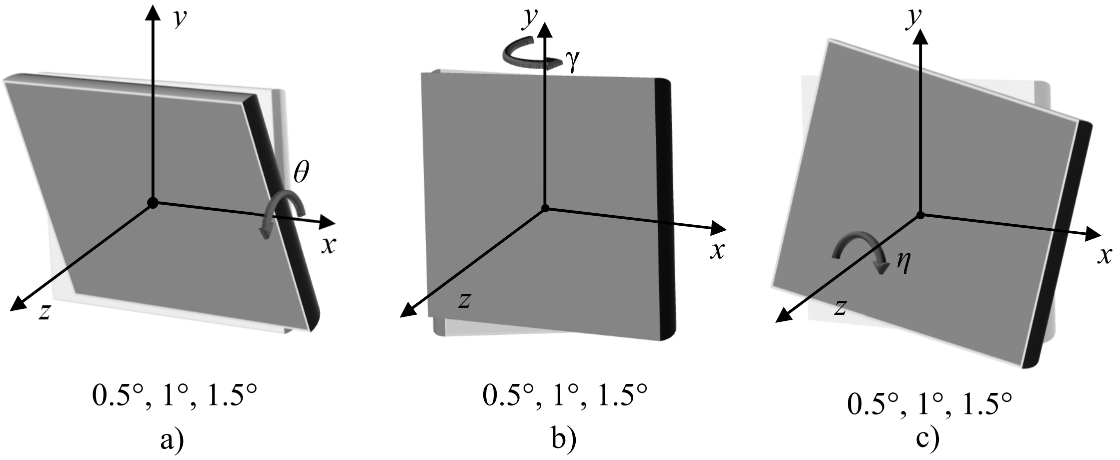

Figure 4.42: Angular misalignments studied in the experimental investigation. a) Three angular misalignments of 0.5°,1°,1.5° investigated in the positive θ rotation, b) three angular misalignments of 0.5°,1°,1.5° investigated in the positive γ rotation, c) three angular misalignments of 0.5°,1°,1.5° investigated in the negative η rotation

For each set of misalignments three angular misalignments of nominally 0.5°, 1° and 1.5° were induced to study the sensitivity of the errors caused by the misalignments to the varying angles, for a total of 9 different misaligned configurations. Three repeated CT scans were performed in each of the 9 misaligned configurations with the sample oriented in the same way as for the scans performed with the aligned system and with the scanning parameters of Table 4.2, for a total of 27 CT scans.

After each set of misalignments, the system was re-aligned by re-performing the alignment procedures in order to guarantee the system was in the aligned configuration before starting the next set of misalignments, and to avoid therefore the superimposition of the effects of different misalignments. After each re-alignment a CT scan of the ball plate was also performed in order to check the consistency of the measurement results. A schematic describing the workflow of the experimental campaign is reported in Figure 4.43.

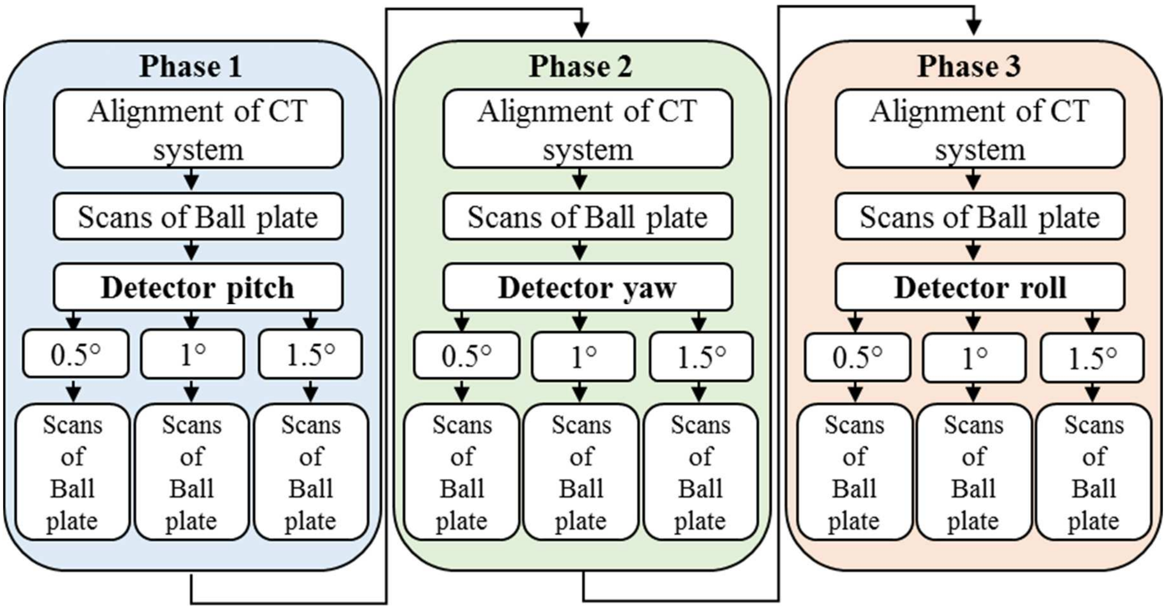

Figure 4.43: Schematic of the workflow of the experimental campaign. In Phase 1 the effects of detector pitch were investigated. Phase 2 and Phase 3 deal respectively with the investigation of detector yaw and detector roll. In between each phase the alignment procedures of the system were performed.

Minimum misalignments of 0.5° were chosen in order to be able to isolate the effects of detector angular misalignments on the measurement results and avoiding the interference of other influence quantities producing effects of the same order of magnitude of the ones produced by the investigated misalignment. In fact, the results obtained in section 4.3.3 confirmed that the use of minimum misalignments of 0.5° degrees guarantees that detector misalignments are the preponderant influence quantity. On the other hand, the presence of misalignments bigger than 1.5° instead is unlikely for industrial systems in which an alignment procedure has been carried out and with a certain degree of accuracy in the mechanical assembly.

For each scan a procedure to estimate the geometry of the system was applied as per the system manufacturer's guide. In this procedure, out of plane rotations of the detector were disabled from the geometry estimation. Therefore, the detector misalignments about the x and y axis were not accounted for during reconstruction, whereas magnification errors at the center of the detector were taken into account. For misalignments about the z axis also in plane rotation of the detector was disabled from the geometry estimation. The acquired information was then used to perform the reconstruction.

4.4.2. Data analysis

All CT data were reconstructed by means of the manufacturer's reconstruction software NSI efX-ct. After reconstruction the CT volumes were imported and analyzed using VGStudio MAX 3.0. The local adaptive surface determination algorithm described in section 4.3.2 was used for surface determination.

For each sphere of the plate a region of interest, consisting of the top hemisphere, was taken into account in order to remove the part of the spheres glued to the carbon-fiber reinforced plate, which could lead to inaccuracies in measurements.

Sphere diameters, sphere center-to-center distances and spheres form errors were then calculated for each of the CT scans in the aligned and misaligned configurations using Gaussian least square fitting.

4.4.3. Results and discussions

This section presents and discusses the measurement results obtained from the CT scans of the ball plate in all the 9 misaligned configurations experimentally studied and for all the 27 CT scans performed. More specifically section 4.4.3.1 presents the experimental results obtained when studying a detector pitch about the *x* axis, section 4.4.3.2 deals with the effects on measurement results of detector yaw about the *y* axis, and section 4.4.3.3 addresses the measurement errors caused by the presence of detector roll about the *z* axis.

As described in section 4.4.1 CT scans were performed with the system in the aligned configuration and the obtained measurement results were compared to the calibrated CMM data in order to study the residual measurement errors which are present when scanning the ball plate with the CT scanning strategy of Table 4.2. For the three repeated CT scans of the ball plate performed with the system properly aligned, the measurement errors calculated as CT measurements − CMM measurements showed sphere center-to-distance errors smaller than 3.5 µm, diameter errors smaller than 3.1 µm and standard deviations smaller than 0.5 µm.
These measurement errors obtained from the comparison to the calibrated CMM data provide a quantification of the residual errors, which cannot be primarily attributed to CT system geometrical misalignments, but that are likely to be the result of the superimposition of influence quantities that typically interact in CT measurement chain. Given the order of magnitude of these residual errors it can be concluded that the CT scanning strategy chosen for the CT scans of the ball plate is suitable for the purpose of the study as it does not cause the presence of measurement errors due to the interaction of other predominant influence quantities.

In all the following sections CT measurement results in the misaligned configurations are compared to the CT measurements obtained with the system in the aligned configuration and described above. This was done because the comparison between CT scans performed with an aligned system and the calibrated CMM measurements confirmed the proper operation of the system, and that the residual CT measurement errors are smaller than 3.5 µm in the case of center-to-center measurements and 3.1 µm in the case of diameter measurements. It was therefore decided to compare CT measurements in the misaligned configuration with CT measurements in the aligned configuration in order to have consistent comparison between CT measurements performed under the same scanning conditions and to investigate the errors which can be primarily attributed to geometrical misalignments.

4.4.3.1. Detector pitch

Figure 4.44 reports the measurement errors for the sphere center-to-center measurements of the ball plate along the horizontal and vertical directions. Each dot represents the average of three repeated measurements.
As it was demonstrated in section 4.3.3.2 detector pitch strongly affects sphere center-to-center measurements. In this case, for a detector pitch of 1.5° sphere distance errors reach maximum values of 56 µm. Maximum errors of 36 µm and 18 µm are present respectively for 1° and 0.5° detector pitch. It is therefore confirmed, that the amplitude of the misalignments significantly affects the measurement results and for increasing misalignments also the measurement error increases.

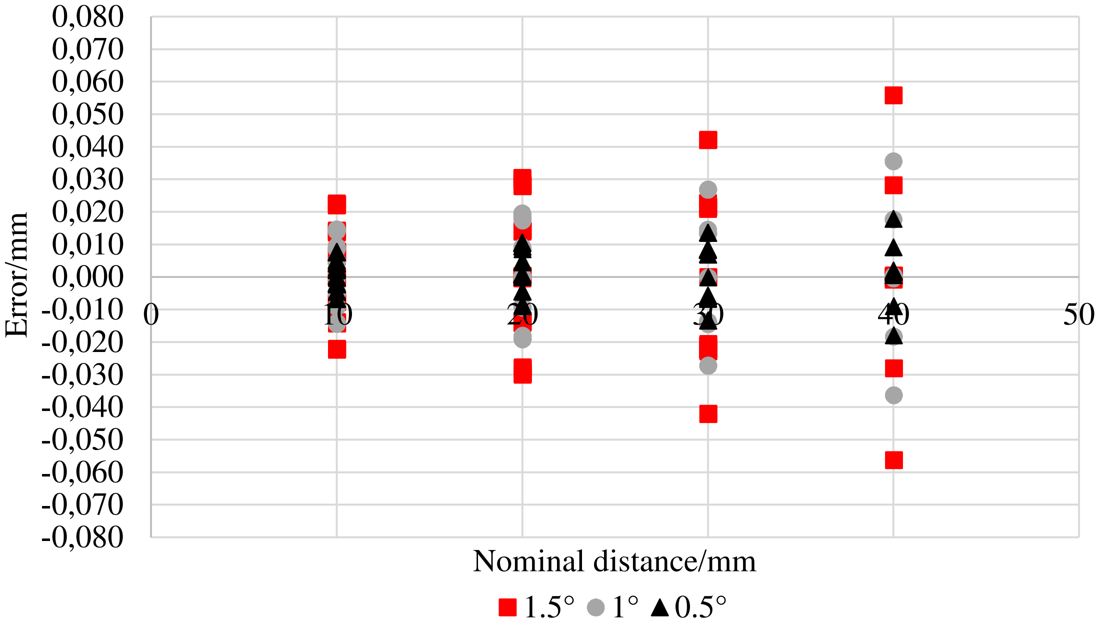

Figure 4.44: Sphere center-to-center distance errors for the 100 center-to-center measurements of the ball plate in presence of the three investigated detector pitch values. The horizontal axis of the diagram reports the nominal distances between the sphere centers. The vertical axis gives the measurement errors calculated as (CT measurements in the misaligned configuration - CT measurements in the aligned configuration).

In order to study the effects produced by detector pitch on measurements performed along the vertical and horizontal direction, the sphere center-to-center distance errors obtained for vertical and horizontal measurements of the ball plate are represented respectively in Figure 4.45 and 4.46.

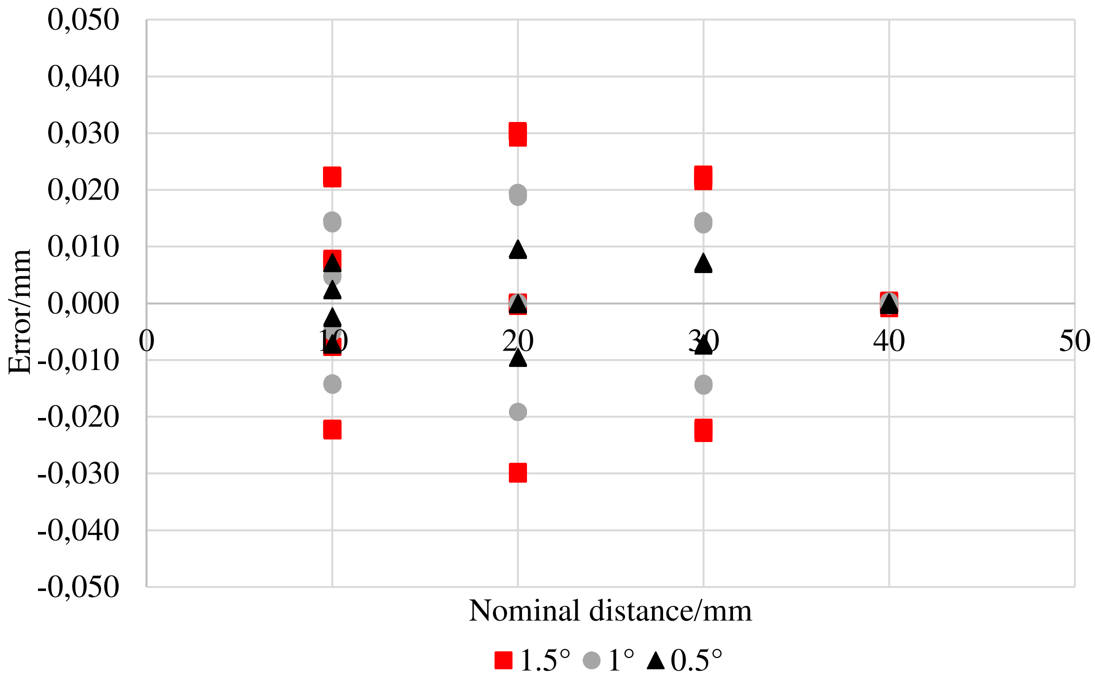

Figure 4.45: Sphere center-to-center distance errors for the 50 vertical measurements of the ball plate in presence of the three investigated detector pitch values. The horizontal axis of the diagram reports the nominal distances between the sphere centers. The vertical axis gives the measurement errors calculated as (CT measurements in the misaligned configuration - CT measurements in the aligned configuration).

Figure 4.45 reports the measurement results obtained for the 50 vertical measurements performed on the ball plate, namely measurements between spheres belonging to the same column of the ball plate (10 measurements for each of the 5 columns). It is evident how, for vertical measurements, it is present the same behavior found in Figure 4.25 and 4.26 for the ball bar. Also in this case in fact, vertical measurements show a symmetric behavior about the *x* axis. For example, the error between sphere 1 and 6 is similar to the error between sphere 16 and 21 (that belong to the same column of sphere 1 and 6) but with the opposite sign.

Distances between spheres positioned below the central plane of the detector present positive errors, whereas distances between spheres positioned above the central plane present negative errors. The magnification, in fact, is established at the center of the detector and the angle introduced as shown in Figure 4.42 affects the *SDD* symmetrically about the detector center.

With respect to the aligned configuration, for the induced misalignments, *SDD* is affected in opposite directions and it decreases for spheres above the central plane of the detector and it increases for spheres below. As a consequence, for spheres positioned below the central plane of the detector the actual *SDD*, and therefore the actual magnification, are bigger. This means that in the upper part of the detector the voxel size of the reconstructed volume is overestimated with respect to the actual voxel size. This over estimation leads to positive measurement errors. In the regions of the detector above the central plane instead, the actual *SDD*, and as a consequence the actual magnification, are smaller than the one used for reconstruction. This means that in that regions the voxel size of the

reconstructed volume is underestimated with respect to the actual voxel size, which gives negative measurement errors.
As it was found for vertical measurements of the ball bar, also in this case magnification errors are present which increase for spheres far away from the center of the detector. For example, the distance between spheres 10 and 15 is smaller than the distance between spheres 5-15. Moreover, the lengths which comprise points symmetric about the x axis are characterized by a smaller error because they have opposite errors that cancel out; for example, this happens for sphere distance 5-25 and 10-20.

By using a ball plate moreover more information is available. In fact, the 5 columns of the ball plate used for the experimental investigation uniformly cover the detector surface. The obtained results show how the vertical measurements performed on the ball plate are not affected by the column horizontal position. In fact, the measurement results obtained for column 1,2,3,4 and 5 present the same behavior and really close measurement results. It can therefore be concluded that for detector pitch experimentally investigated and up to 1.5° vertical measurements are strongly affected and do not significantly depend on the horizontal position of the columns of the ball plate.

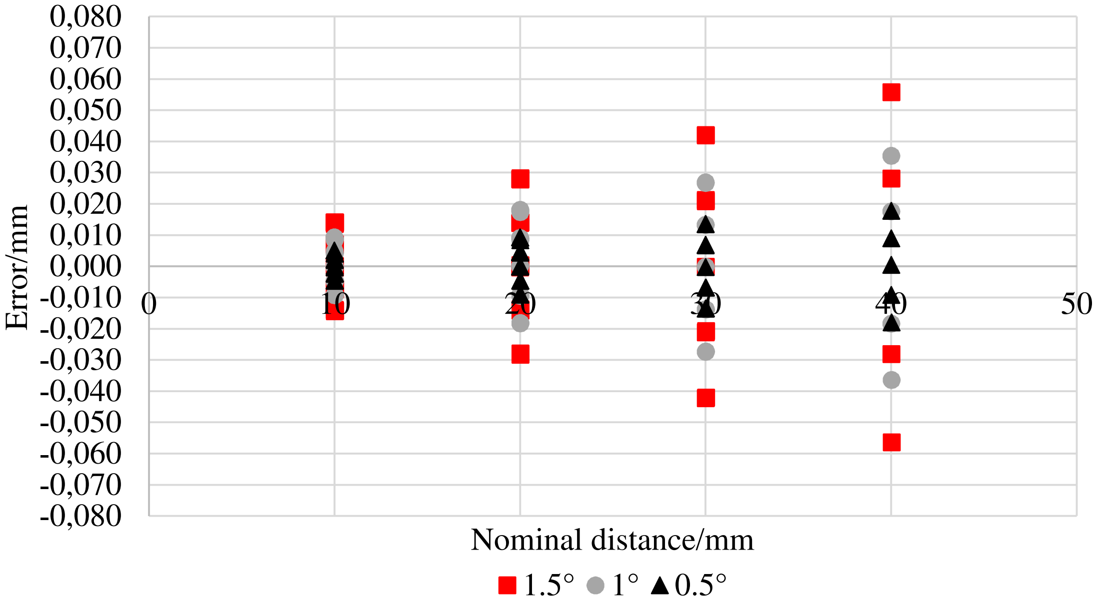

Figure 4.46: Sphere center-to-center distance errors for the 50 horizontal measurements of the ball plate in presence of the three investigated detector pitch values. The horizontal axis of the diagram reports the nominal distances between the sphere centers. The vertical axis gives the measurement errors calculated as (CT measurements in the misaligned configuration - CT measurements in the aligned configuration).

Figure 4.46 reports the measurement results obtained for the 50 horizontal measurements of the ball plate, namely measurements between spheres that belong to the same row (10 measurements for each of the 5 rows). As visible also horizontal measurements are affected by the presence of a detector pitch with a specific symmetrical behavior.
Row 3 which nominally is positioned in the middle plane of the detector (see Figure 4.41), present small measurement errors which are close to zero for all the three amplitudes of detector pitch investigated. In Figure 4.46 the measurement results obtained for row 3 are

characterized by errors close to zero for all the sphere center-to-center distances. For rows at increasing vertical distance from the middle plane of the detector instead the sphere distance errors are affected by scaling errors. This is visible in the graph from the measurement errors that almost linearly increase with increasing sphere center-to-center distances between the spheres of the ball plate. For example, in the case of 1.5° detector pitch, row 5 which is positioned close to the upper edge of the detector is characterized by the bigger scaling error with a maximum error of 56 µm for a 40 mm center-to-center nominal length. Row 4 which is positioned at a vertical position on the detector in between row 3 and row 5 (see Figure 4.41) is characterized by a maximum error of 28 µm for the 40 mm center-to-center nominal length. Row 1 (at nominally opposite position of row 5 on the detector vertically) was found to have a similar behavior to row 5 but with errors characterized by the opposite sign, and in the same way row 2 was found to have a similar behavior to row 4 but again with errors characterized by the opposite sign. This behavior holds true for all the three investigated amplitudes of detector pitch, and the bigger is the amplitude the stronger is the presence of this behavior.

The explanation for this particular behavior of horizontal measurements of the ball plate is presented in the following. With respect to the aligned configuration, due to the angles introduced up to 1.5° (Figure 4.42), the magnification is affected symmetrically about the detector center and magnification errors are present which increase for spheres far away from the center of the detector vertically. As a consequence of the magnification errors, the actual voxel size differs from the voxel size of the reconstructed volume. Errors in the dimension of the voxel size produce scaling errors when measuring increasing length because more voxels are comprised in the measurements.

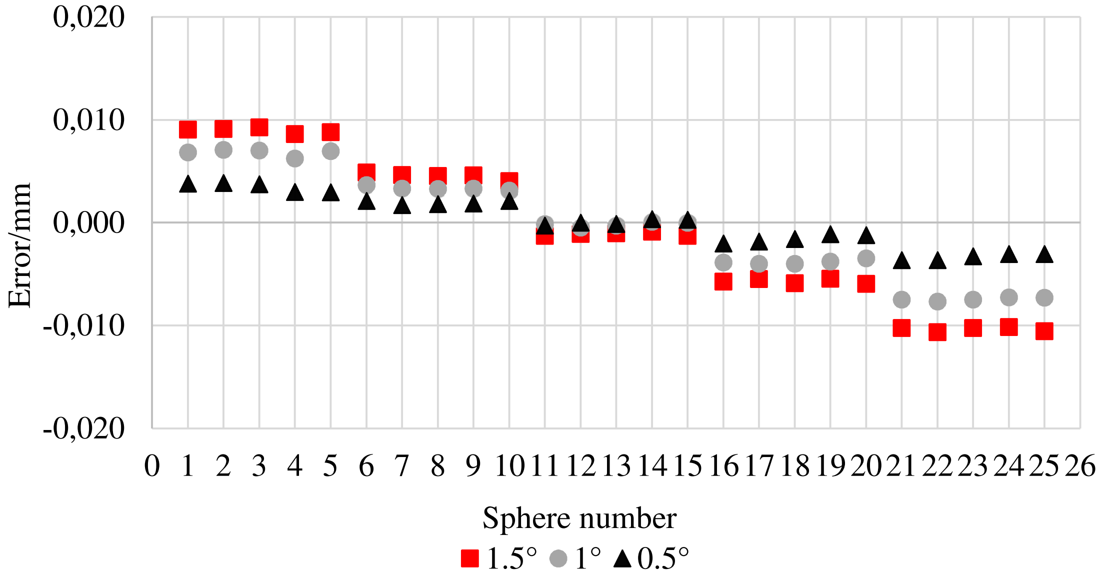

Figure 4.47: Sphere diameter errors for the 25 spheres of the ball plate for the three investigated detector pitch values. The horizontal axis of the diagram reports the sphere numbers. The vertical axis gives the measurement errors calculated as (CT measurements in the misaligned configuration - CT measurements in the aligned configuration).

Figure 4.47 describes the effects of the different angles, on the diameter errors of the spheres of the ball plate. Also for diameter measurements, when increasing the angular misalignment, the measured diameter errors increase. In particular Figure 4.47 shows how spheres which occupy similar regions on the detector but at opposite sides vertically (e.g. sphere 1 and sphere 21) show diameter errors with opposite sign. This confirm what it was found in the case of the ball bar measurements reported in section 4.3.3. The use of a ball plate moreover enables to demonstrate also that the spheres belonging to the same row present similar diameter errors. It is interesting to note that row 3, which is nominally positioned in the center of the detector, is nearly unaffected by the misalignments and present diameter errors close to zero. With increasing vertical distance of the rows from the central plane of the detector diameter errors increase. Row 5 and row present the highest diameter errors (with opposite signs).

Form errors were also investigated and as in the case of the ball bar measurements reported in section 4.3.3, also when measuring form errors of the ball plate in presence of detector pitch up to 1.5° no significant differences between the aligned and misaligned configurations were found. For the ball plate measurement as well, it is likely that the relatively small change in magnification over the extent of a single sphere is dominated by other factors contributing to the form error, such as detector noise.

4.4.3.2. Detector yaw

As in the case of detector pitch, also for detector yaw three angular misalignments of 0.5°, 1°, and 1.5° were investigated (see Figure 4.42).
Figure 4.48 reports the experimental results obtained when comparing the sphere center-to-center measurements for each of the three amplitudes of detector yaw investigated to the measurement results obtained with the system in the aligned configuration.

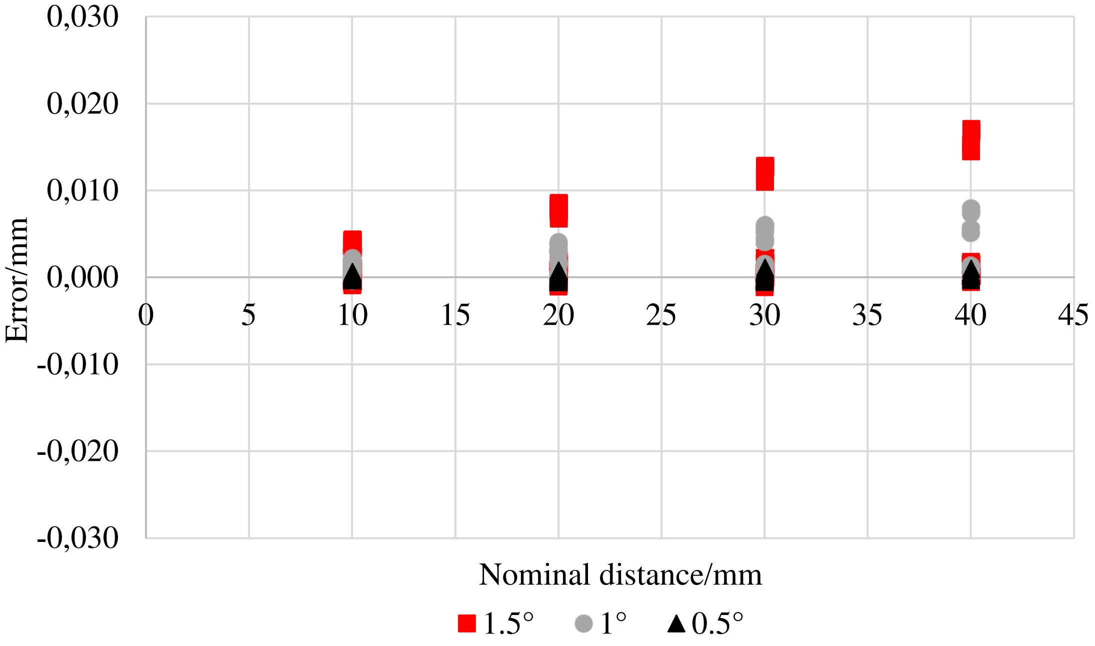

Figure 4.48: Sphere center-to-center errors for the 100 measurements of the ball plate for the three investigated detector yaw values. The horizontal axis of the diagram reports the nominal distance between the sphere centers. The vertical axis gives the measurement errors calculated as (CT measurements in the misaligned configuration - CT measurements in the aligned configuration).

It is visible how, for a detector yaw of 0.5° the measurement errors are small and are not significantly affected by the presence of the misalignment. This is true for all the rows and columns of the ball plate. For a 1° and 1.5° detector yaw instead the measurement errors present a different behavior. The measurements performed along the columns of the ball plate (i.e. the nominally vertical measurements) are not affected by the presence of the misalignment and the sphere center-to-center distance errors are within 1.6 µm and 2.5 µm respectively for 1° and 1.5° detector yaw. This is visible in the graph as the series of dots, from the nominally 10 mm center-to-center distance to the 40 mm nominal center-to-center distance, almost overlapping close to the zero error.

For the 1° and 1.5° detector yaw, the nominally horizontal measurements instead (measurements performed along each of the rows of the ball plate) are characterized by scaling errors. The experimentally obtained results in fact show that the horizontal measurements between the spheres belonging to the same row are characterized by a scaling error which causes the measurement errors to increase with increasing sphere center-to-center distances. In particular, it was observed that the rows of the ball plate exhibit similar scaling errors as it can be seen in the graph with the measurement errors almost linearly increasing with increasing sphere center-to-center distances.

The detector yaw investigated in fact, as depicted in Figure 4.42, affects the magnification symmetrically about the y axis. This means that, in presence of a yaw of the detector, during the rotation the object will be subject to these magnification changes. This causes vertical measurements (between spheres belonging to the same columns of the ball plate) not to be affected by this particular misalignment. The horizontal measurements instead are sensitive to the position of the object in the measurement volume. The scaling errors reported in Figure 4.48 are likely to be caused by the manual positioning of the ball plate in the measurement volume. In this case the central column of the ball plate (column 3) was slightly offset from the center of the detector, and this caused the presence of the scaling errors for horizontal measurements. This is because, due to the manual positioning, the spheres were subject to magnification changes through their rotation that did not globally cancel out.

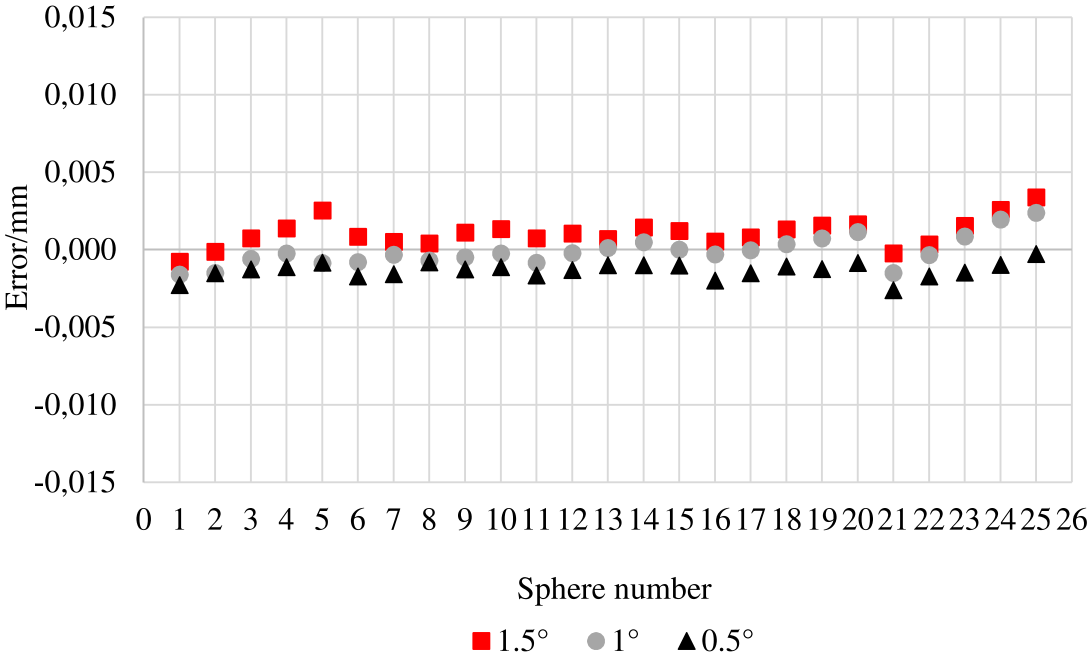

Figure 4.49: Diameter errors for the 25 spheres of the ball plate in presence of the three investigated detector yaw values. The horizontal axis of the diagram reports the sphere number. The vertical axis gives the measurement errors calculated as (CT measurements in the misaligned configuration - CT measurements in the aligned configuration).

Figure 4.49 reports the experimentally obtained measurement errors for the sphere diameters of the ball plate. As it was found in the case of spheres diameter measurements of the ball bar reported in section 4.3.3, the sphere diameters of the ball plate are not strongly affected by the presence of the detector yaw experimentally investigated. Maximum errors of 3.5 µm were found in the case of a 1.5° yaw of the detector about the *y* axis. The ball plate measurements however enable to obtain additional information on the effects of the yaw of the detector about the *y* axis on the sphere diameters. From Figure 4.49, it is visible how for all the three amplitudes investigated the diameter errors of the spheres positioned on the same row present a monotonic trend. In particular, for each row, the spheres that belong to the two most outer columns of the ball plate are positioned at the top and bottom of each monotonic trend.

Figure 4.50 reports the sphere form errors for the experimentally investigated detector yaw. Form errors are affected by detector yaw and increase with an increasing amplitude of the misalignment. It is observed that higher form errors are present for increasing distance horizontally from the center of the detector. For example, column 1 and 5 are characterized by higher form errors than column 3,2 and 4. Spheres belonging to column 3 are not significantly affected by the misalignment.

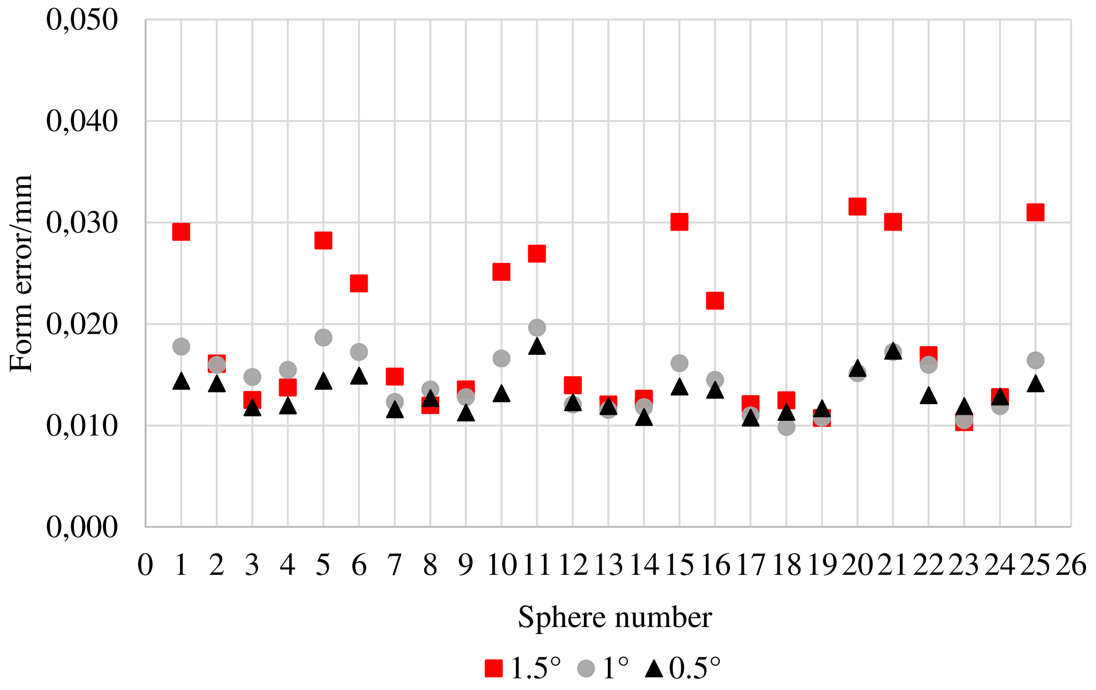

Figure 4.50: Sphere form errors for the 25 spheres of the ball plate in presence of the three investigated detector yaw values. The vertical axis of the diagram gives the sphere form errors. The horizontal axis reports the sphere numbers.

4.4.3.3. Detector roll

In this section the results obtained for the experimentally investigated detector roll are presented. Figure 4.51 provides a visual overview of the effects of detector roll about the *z* axis described in Figure 4.42 on the central section of the ball plate. Respectively Figure 4.51 shows the effects of a 0.5° detector roll, Figure 4.52 the effects of a 1° roll and Figure 4.53 the effects of a 1.5° detector roll.

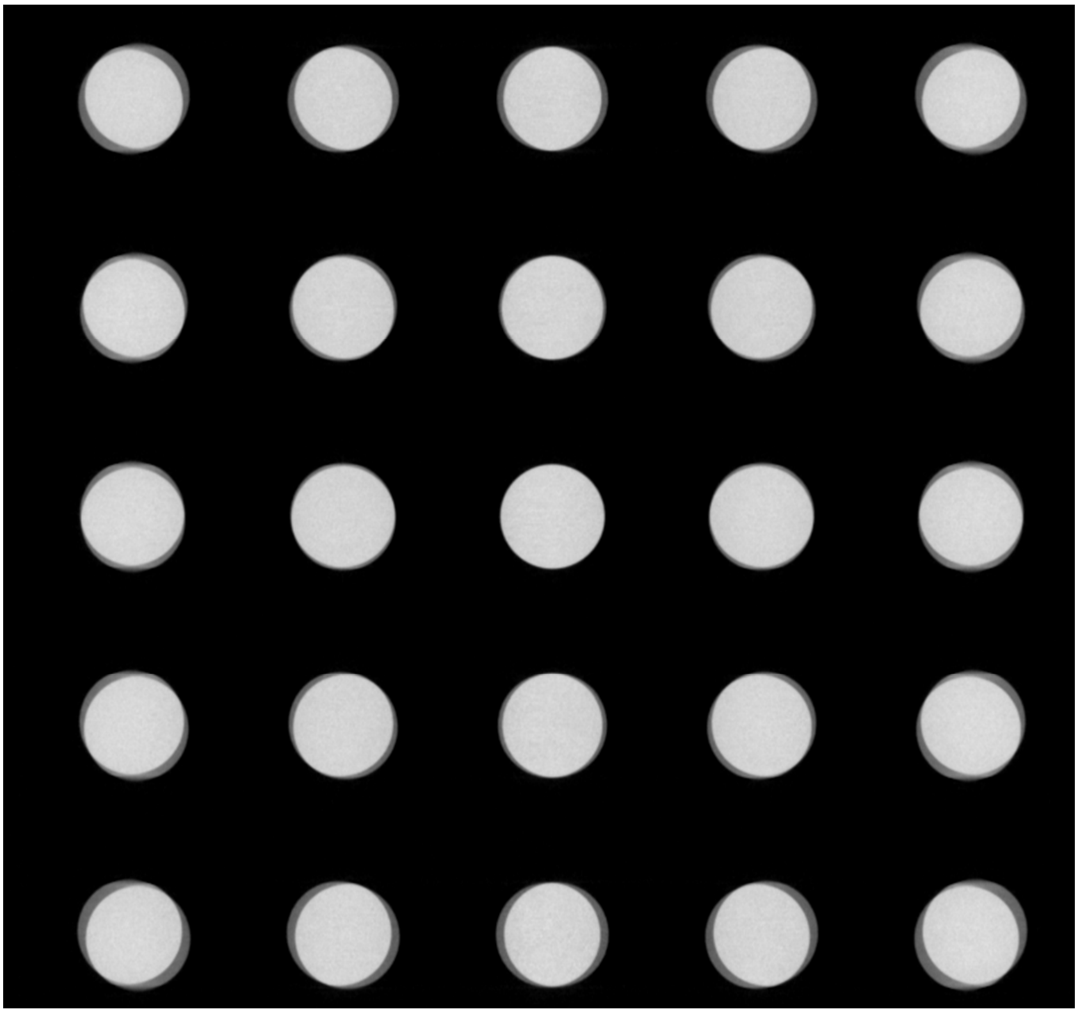

Figure 4.51: Effects of the investigated detector roll. The central section of the ball plate in the xy plane is represented. for a 0.5° detector roll.

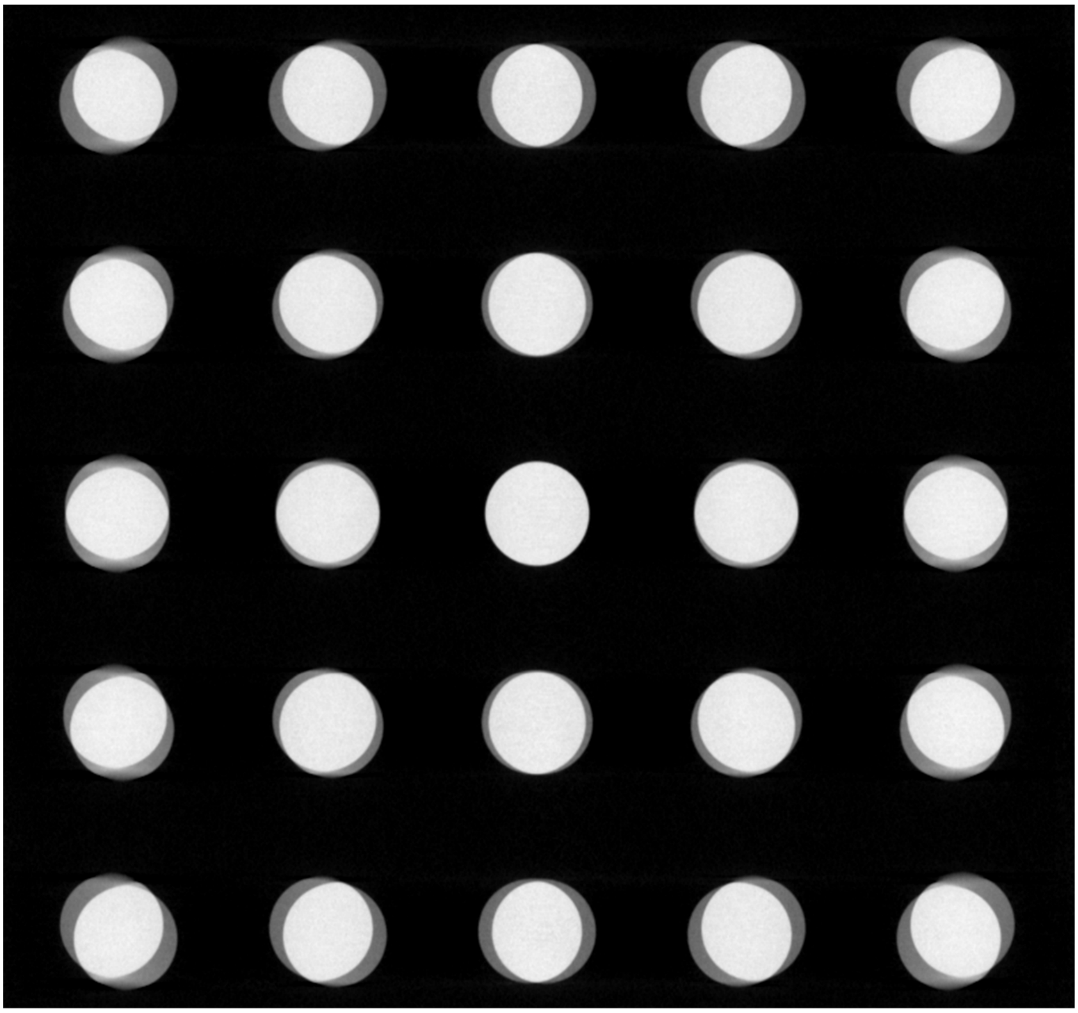

Figure 4.52: Effects of the investigated detector roll. The central section of the ball plate in the xy plane is represented. for a 1° detector roll.

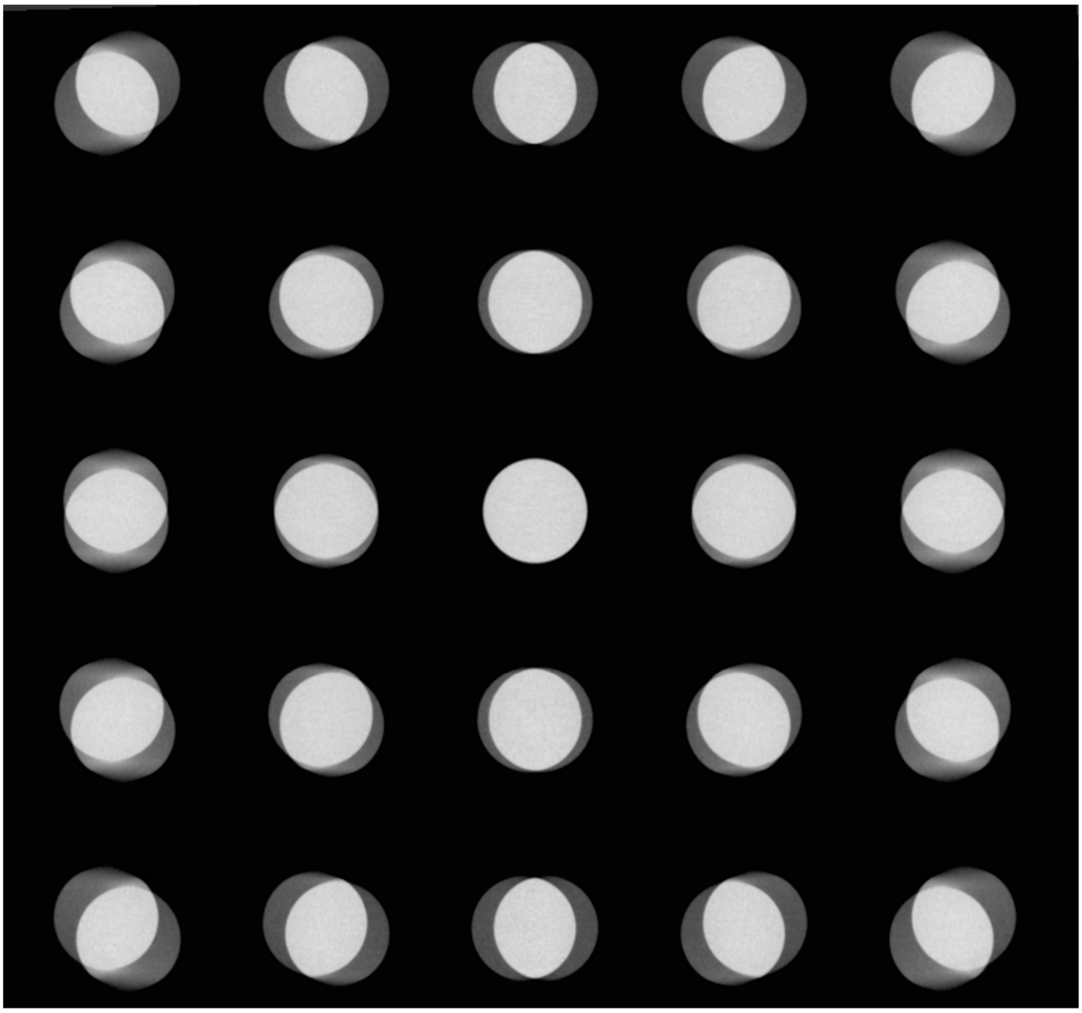

Figure 4. 53: Effects of the investigated detector roll. The central sections of the ball plate in the xy plane is represented. for a 1.5° detector roll.

It is clearly visible that detector roll produces strong effects on the reconstructed volume. All the spheres of the ball plate are severely affected by artifacts, just sphere 13 which is positioned at the center of the detector does not suffer of severe artifacts that affect the other spheres of the ball plate. The behavior that was found in section 4.3.3 for the ball bar is confirmed also here. Due to the presence of detector roll the edges of the spheres appear as doubled, as if two spheres were overlapping. As a consequence, each of the balls of the plate, that originally had a spherical shape, is described by a region with a higher gray value created by the two overlapping spheres described before, and by regions with lower gray values, as visible in Figures 4.51, 4.52 and 4.53. The overlapping portions are characterized by gray values similar to the ones that characterizes the spheres in the CT scans acquired in the aligned configuration By performing the surface determination process in VGStudio MAX 3.0 using as starting contour the edges of these zones with higher intensity and then applying the more refined algorithm which locally searches for the maximum gradient of grey values it is possible to perform dimensional and form measurements between the spheres of the plate. Figure 4.54, 4.55 and 4.56 describe the 3D views obtained after the surface determination step.

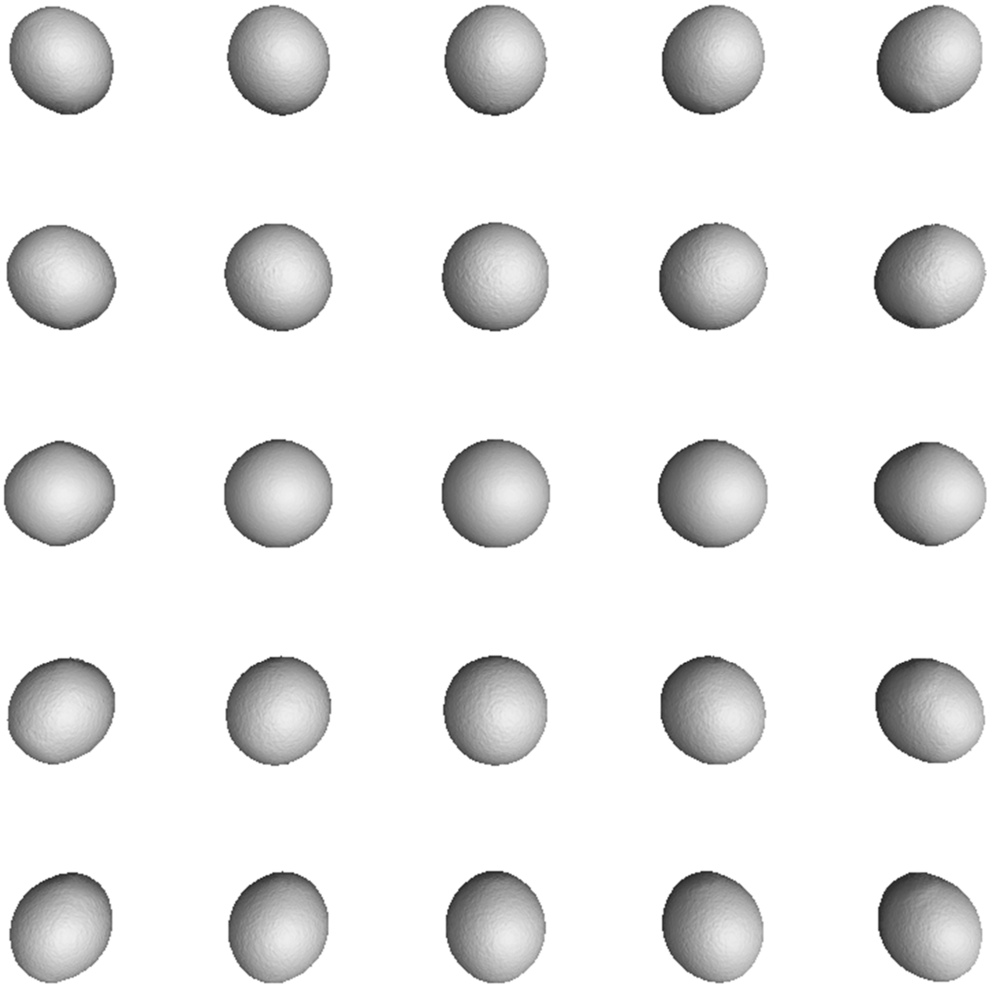

Figure 4. 54: 3D view of the ball plate in presence of the investigated detector roll of 0.5°.

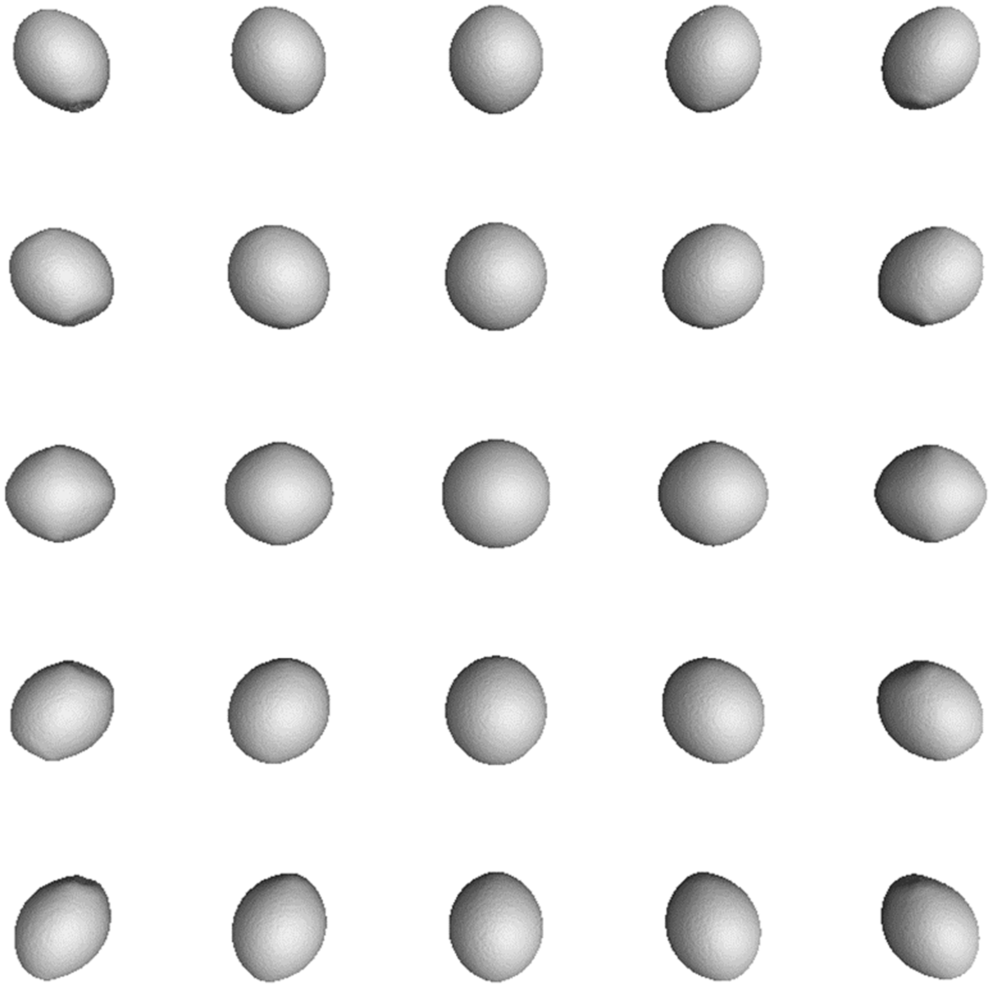

Figure 4. 55: 3D view of the ball plate in presence of the investigated detector roll of 1°.

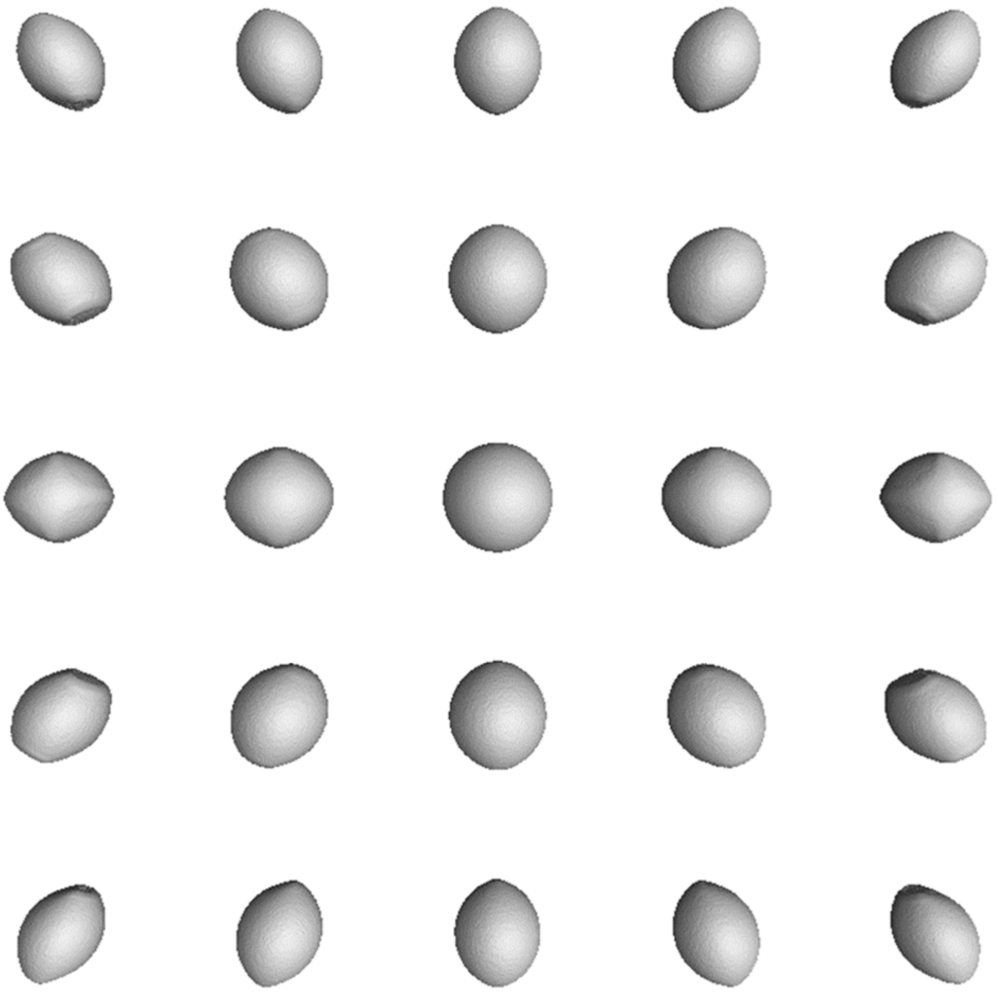

Figure 4.56: 3D view of the ball plate in presence of the investigated detector roll of 1.5°.

It is visible also here how all the balls of the plate except sphere 13 do not have any more a spherical shape. In particular, the deviation from the spherical shape increase with increasing vertical and horizontal distance from the center of the detector. Moreover, as it will be quantitatively shown in the following, from Figure 4.5, 4.55 and 4.56 it is also visible how spheres which are at symmetrically opposite positions are characterized by extremely similar deviations from the spherical shape. For example, spheres 3 and 23 show really similar deviations. This is valid for all spheres at radially opposite position from the detector center.

Figure 4.57 reports the sphere center-to-center errors for the vertical and horizontal measurements of the ball plate.

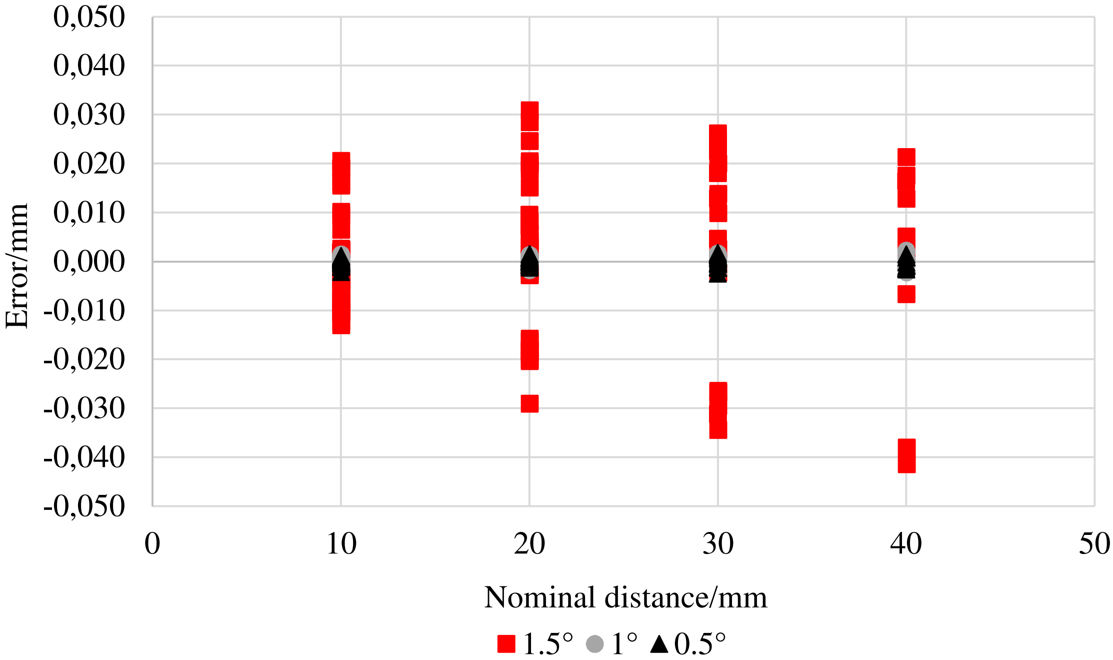

Figure 4.57: Sphere center-to-center errors for the 100 measurements of the ball plate for the three investigated detector roll values. The horizontal axis of the diagram gives the nominal distance between the centers of the spheres. The vertical axis reports the measurement errors calculated as (CT measurements in the misaligned configuration - CT measurements in the aligned configuration).

As discussed in the case of the ball bar in section 4.3.3, the sphere center-to-center measurements are not significantly affected by detector roll of 0.5° and 1° even if visible deformations of the spheres are present. With a detector roll of 1.5° instead, also center-to-center measurements are affected by the misalignment and maximum errors of 40 µm are present. Therefore, it can be concluded that the amount of error present for sphere center-to-center distances do not fully reflect the distortion of the spheres surface caused by detector roll.

In Figure 4.58 the measurement errors obtained for the sphere diameters are shown. Sphere diameters are affected by significant measurement errors, and they are always smaller than diameters calculated from CT scans performed with the system in the aligned configuration. As visible in Figure 4.51 to Figure 4.53 in fact, the region with higher gray value used as starting contour for the more refined local adaptive surface determination algorithm is smaller than the sphere diameters measured with the aligned system.

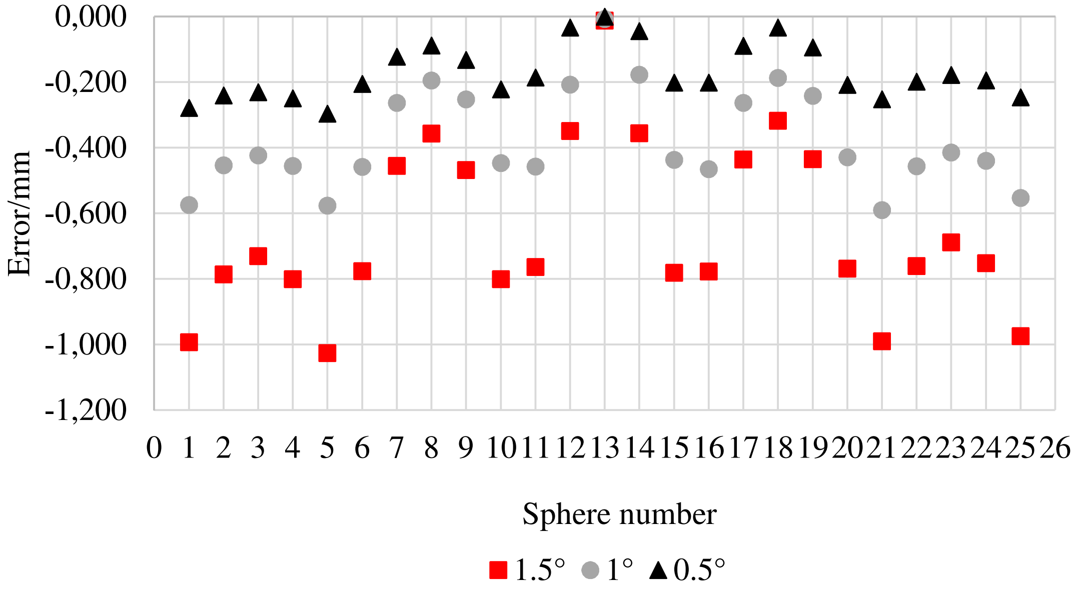

Figure 4.58: Sphere diameter errors for the 25 spheres of the ball plate for the three investigated detector roll values. The horizontal axis of the diagram reports the sphere number. The vertical axis gives the measurement errors calculated as (CT measurements in the misaligned configuration - CT measurements in the aligned configuration).

By analyzing the diagram it is visible that, as described in Figure 4.54 to Figure 4.56, sphere 13 which is nominally positioned at the center of the detector is not affected by severe artifacts. By radially moving away from the center of the detector measurement error increase. Measurement errors in fact present a symmetrical behavior about the *x* and *y* axis. For example, sphere 7,9,17 and 19 show similar diameter errors. Another example is given by sphere 3, 11, 15, 23 that also show similar diameter errors but bigger than the spheres mentioned above. For all the three amplitudes investigated the bigger diameter errors are obtained for spheres 1,5,21, 25 that are positioned at maximum distance from the center of the detector. For a 1.5° roll, maximum errors of 1.026 mm are present.

Figure 4.59 reports the measurement results obtained for the form errors for all the three amplitudes of misalignment investigated. The same behavior found for diameter measurements is present also for form measurements. In this case as well, form errors increase with radial distance from the center of the detector, and with the amplitude of the misalignment. For the 1.5° configuration maximum errors of 647 µm are present.

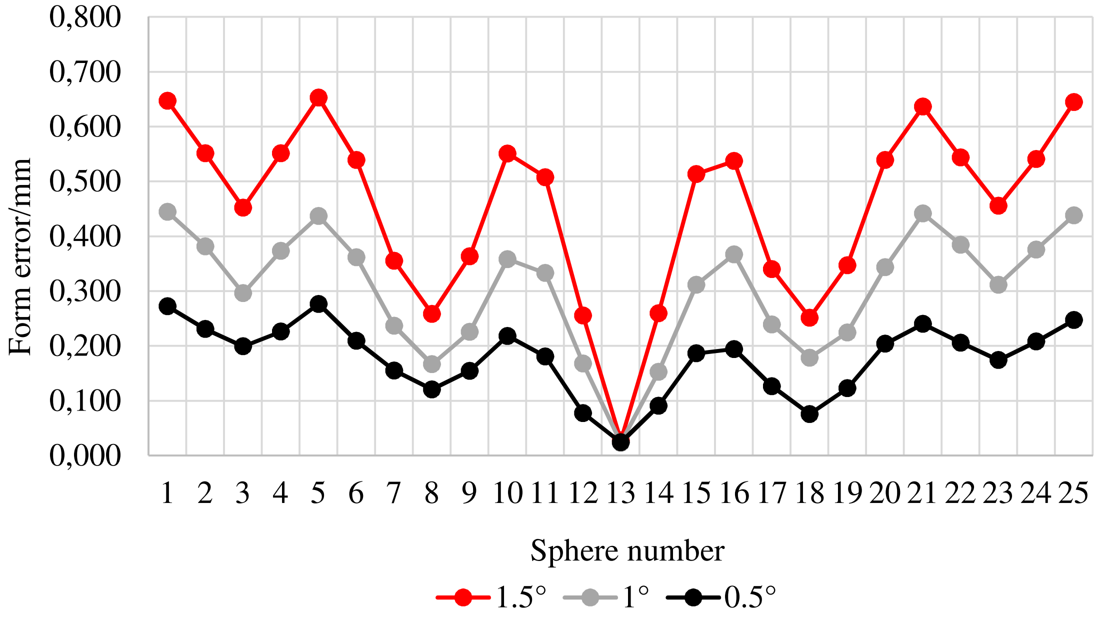

Figure 4.59: Sphere form errors for the 25 spheres of the ball plate for the three investigated detector roll values. The horizontal axis of the diagram gives the sphere number. The vertical axis reports the experimentally obtained form errors.

As described in section 4.3.3 also in this case a software correction was applied to correct for the detector roll experimentally investigated. The application of software correction to the CT data acquired in the misaligned configuration is extremely effective and gives measurement errors as for the scans acquired with the system in the aligned configuration.

4.4.4. Conclusions

In section 4.4 the influence of measurement direction and object position on the errors caused by a misaligned detector was investigated. For this purpose, a tactile CMM calibrated ball plate consisting of an array of 5x5 equally spaced ruby spheres glued on a carbon-fiber reinforced plate was used for the experimental investigation. The ball plate was positioned in the vertical orientation in the CT volume (i.e. with the carbon fiber plate nominally parallel to the detector surface) so that it homogenously covered the detector surface. The central column and central row of the ball plate were nominally positioned on the detector center, two rows occupied the upper part of the detector and the other two rows occupied the nominally symmetrical position on the lower part of the detector. In the same way, two columns were positioned in the left-hand side of the detector, and the remaining two columns were positioned at nominally symmetrical positions on the right side of the detector. This was done in order to map the measurement errors caused by a misaligned detector with regards to the measurement direction and object positioning in the measurement volume. An experimental campaign was designed to investigate the influence of detector pitch about the x axis, detector yaw about the y axis and detector roll about the z axis. For this purpose, the flat-panel detector was purposefully mechanically misaligned and three different amplitudes, i.e. 0.5°, 1° and 1.5°, for each of the misalignment described above was physically performed. The use of three different amplitudes of misalignment enabled to investigate the sensitivity of the errors with the amplitude of the induced misalignments. The resulting experimental set-up therefore led to the investigation of three detector pitch about the horizontal central axis of the detector and in the positive rotation direction, three detector yaw about the vertical central axis of the detector and in the positive rotation direction, and three detector roll about the longitudinal central axis of the detector and in the negative rotation direction. Each CT scan was repeated three time, leading to a total of 27 CT scans in the misaligned configurations (9 misalignments x 3CT scans for each misalignment). Detector pitch, yaw and roll were investigated separately in order to isolate the effects caused by each angular misalignment. For this purpose, a realignment of the CT system was performed in between each set of misalignment in order to avoid the superimposition of other unwanted geometrical misalignments.

The obtained results showed that detector pitch strongly affects the measurements of sphere center-to-center distances in the experimentally tested conditions. It was found that, for detector pitch up to 1.5°, the sphere center-to-center distance errors present a symmetric behavior about the x axis of the detector. The investigated misalignments, with respect to the aligned configuration, affect the source-to-detector distance symmetrically about the detector center. As a consequence, magnification errors are present which increase for spheres far away from the center of the detector. The experimental results enabled also the prove that, in the tested conditions, the 50 vertical measurements performed on the ball plate (i.e. measurements between spheres belonging to the same column) cause the symmetric behavior about the x axis, and this behavior does not vary with the detector columns, i.e. the horizontal position of the column do not affect the measurement errors. In this case maximum errors of 30 µm were found for the 1.5° detector pitch. The 50 horizontal measurements, i.e. measurements between spheres belonging to the same raw, are affected by scaling errors which increase with increasing vertical distance of the rows from the central plane of the detector (and with increasing amplitude of the misalignment). These scaling errors are caused by the magnification errors that are present by vertically moving away from the central plane of the detector. In fact, errors in the voxel size dimension are the cause of scaling errors which determine the center-to-center measurement errors to increase with increasing distance between the center of the spheres: more voxels are comprised for longer lengths. In this case for a 1.5° pitch, maximum errors of 56 µm were found. Diameter errors were also found to have a symmetrical behavior about the x axis. Spheres which occupy similar regions on the detector but at opposite sides vertically showed diameter errors with opposite sign. Moreover, it was observed that spheres belonging to the same row present similar diameter errors and that with increasing vertical distance of the rows from the central plane of the detector diameter errors increase. Form errors do not show significant differences between the aligned and misaligned configurations for detector pitch up to 1.5°.

The experimentally investigated detector yaw also exhibit sphere center-to-center measurements affected by the misalignment. More specifically vertical measurements are nearly unaffected by the presence of the yaw of the detector, whereas horizontal measurements present similar scaling errors which increase for increasing amplitude of the misalignment. These scaling errors are attributed to the manual positioning of the object in the measurement volume because of which the central column of the detector was not perfectly positioned on the vertical central axis of the detector. In presence of a detector yaw, the spheres of the ball plate are affected by a magnification change through their rotation and, due to the not perfect positioning the spheres are subject to magnification changes that do not globally cancel out. In the case of diameter measurements maximum errors of 3.5 μm were found for a 1.5° yaw of the detector about the *y* axis. The experimental results enable also to obtain additional information. The presence of detector yaw also affects image quality. In fact, due to this kind of misalignment the edges of the spheres of the ball plate appear as doubled. The presence of these artifacts increases with increasing distance from the central horizontal and vertical planes of the detector. For all the three amplitudes investigated the diameter errors of the spheres positioned on the same row present a monotonic trend. In particular, for each row, the spheres that belong to the two most outer columns of the ball plate are positioned at the top and bottom of each monotonic trend. Maximum absolute errors of 3 μm were found the 1.5° misalignment. The presence of the artifacts therefore, in the experimentally tested conditions, do not significantly affects the diameter measurements. However, they affect form measurements. When analyzing form errors, it was found that detector yaw affect form measurements. In particular, higher form errors were observed for increasing distance horizontally from the center of the detector. Maximum errors of 32 μm were found for a 1.5° yaw.

The presence of a detector roll causes strong artifacts on the reconstructed volumes. This misalignment in fact strongly affects the balls of the plate and already with a 0.5° misalignment the balls do not present anymore a spherical shape. For the experimentally investigated detector roll it was found that mostly diameter errors and form errors are affected by this kind of misalignment which is the one among the investigated ones (i.e. pitch and yaw and roll) that produces the biggest and most visible artifacts and errors. In particular, both diameter errors and form errors exhibit a trend with errors increasing with increasing radial distance from the center of the detector. The spheres located at the edges of the ball plate presents the higher diameter and form errors which in the case of a 1.5° misalignment reach respectively absolute values of 1.026 mm and 647 μm. It is therefore evident that it is extremely important to accurately align the system to avoid in plane rotation and/or depending on the accuracy obtained to correct for it via software. It was here demonstrated that the software correction of the experimental data acquired in the misaligned configuration is extremely effective and gives measurement errors as for the scans acquired with the system in the aligned configuration.

In conclusion, the results experimentally obtained and here reported enabled to map the influence of the measurement direction and the object positioning on the measurement volume with regards to the measurement errors obtained in presence of a misaligned detector. Measurement direction and object positioning strongly affect the measurement results and cause the presence of particular behavior and trends. The detailed comprehension and quantification of the effects caused by CT system geometrical misalignment is of extreme importance and it is an essential step to achieve the development of calibration procedures for CT systems and to obtain traceable CT measurement. The experimentally found results are extremely useful also in industrial practice in fact, they enable to identify which are the possible misalignments that affect flat-panel detectors in real practice based on actual CT measurements, and also provide a quantitative description of which are the most critical misalignments.

4.5. Errors induced by a rotary table offset

As described in section 4.2.1 also the rotary table of a CT system can be affected by geometrical errors which cause the CT system geometry to differ from the ideal alignment conditions. Rotary table geometrical errors can be angular geometrical errors or positional geometrical errors. Positional geometrical errors can occur due to offsets in the magnification axis direction, in the *y* direction and in the horizontal direction (*x* axis). As introduced in section 4.2.1 rotary table offsets along the magnification axis direction lead to errors in the *SOD* and therefore to the presence of errors in the determination of the magnification factor *M*. References [3,96,97] discuss the effects of scaling errors on the measurement results. An offset of the rotary table in the *y* direction is relevant in the case that the CT scanning method requires movement along the vertical direction, this is the case for example for fan beam systems.

In this section the effects of a rotary table offset along the *x* axis direction are investigated for CT circular scans and the experimental results are presented. The work was performed in collaboration with North Star Imaging Inc.

4.5.1. Experimental set-up

In order to study the effects of a rotary table offset along the *x* axis direction of Figure 4.2 a dedicated experimental campaign was designed. The calibrated ball plate [3] described in section 4.4 was used for the experimental investigation, and was CT scanned with the same positioning and orientation described in Figure 4.41 and with the scanning parameters of Table 4.2. The ball plate in fact, as discussed in the previous sections allows for multiple measurements in different directions and different locations on the CT volume, and for a homogeneous mapping of the effects of the induced geometrical misalignments thanks to it symmetric design and to the rotational symmetry of CT scans. Moreover, the use of the same CT scanning parameters and the same positioning and orientation in the CT volume used for investigating the detector misalignments enable to compare the results and therefore the impact they have on the measurement results.

Three positional misalignments of the rotary table along the ***x*** axis were experimentally investigated. First the CT system alignment procedures were performed according to manufacturer’s guidelines in order to guarantee the system was in the aligned status and avoid the presence of other unwanted misalignments. CT scans of the ball plate were then acquired with the system in the aligned configuration in order to establish the baseline for comparison with the scans acquired with a misaligned rotary table.

After that, CT scans of the ball plate were acquired with the three rotary table offsets reported in Figure 4.60. Table offsets of respectively 1, 2 and 3 times the voxel size, which for the experimentally tested conditions was 40 µm, were physically induced on the rotary table as reported in Table 4.3.

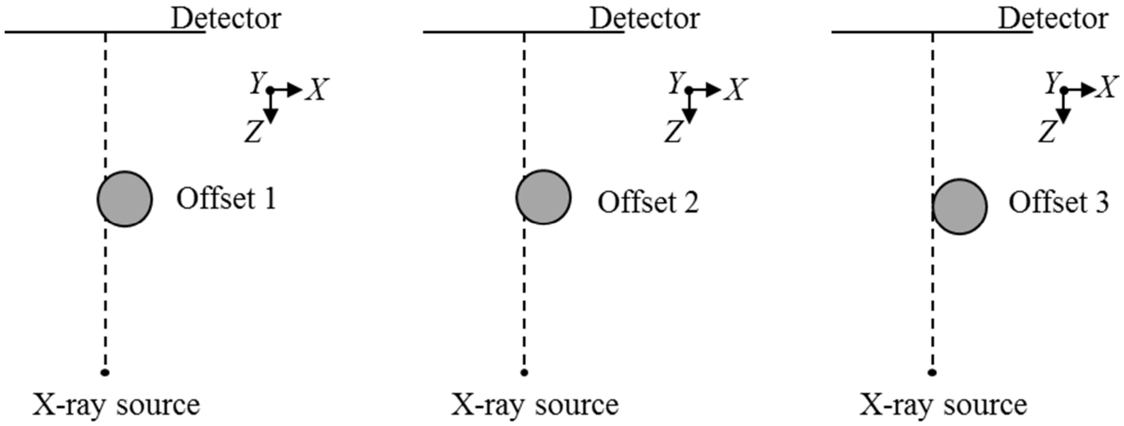

Figure 4.60:Schematic representation of the rotary table offsets experimentally investigated.

	Displacement
Offset 1	0.040 mm
Offset 2	0.080 mm
Offset 3	0.120 mm

Table 4.3: Offsets physically induced on the rotary table.

Offsets of 1,2 and 3 times the voxel size dimension were chosen in order to study the impact of a table offset along the *x* axis on the measurement results for varying amplitudes of the offset and to study the sensitivity of the measurement results to this kind of misalignment.

4.5.2. Data analysis

CT acquired data were reconstructed using the reconstruction software NSI efX-ct. Subsequently the reconstructed volumes were analyzed using VGStudio MAX 3.0. The first step of the analysis consisted on the surface determination which was carried out using the local adaptive surface determination algorithm. More specifically, the ISO 50 value was first determined and after that, in order to have a more refined surface determination, the local search for the maximum gradient of gray values was applied.
In order to avoid inaccuracies in measurements due to the part of the spheres glued to the carbon-fiber reinforced plate, the region of interest consisting of the top hemispheres was considered. Sphere diameters, sphere center-to-center distances and spheres form errors were then calculated using Gaussian least square fitting for all CT scans.

4.5.3. Results and discussion

In this section the experimentally obtained results are presented and discussed for all the three offsets along the *x* direction.
Figure 4.61, Figure 4.62 and Figure 4.63 report the effects of the three rotary table offsets investigated on the central section of the ball plate.

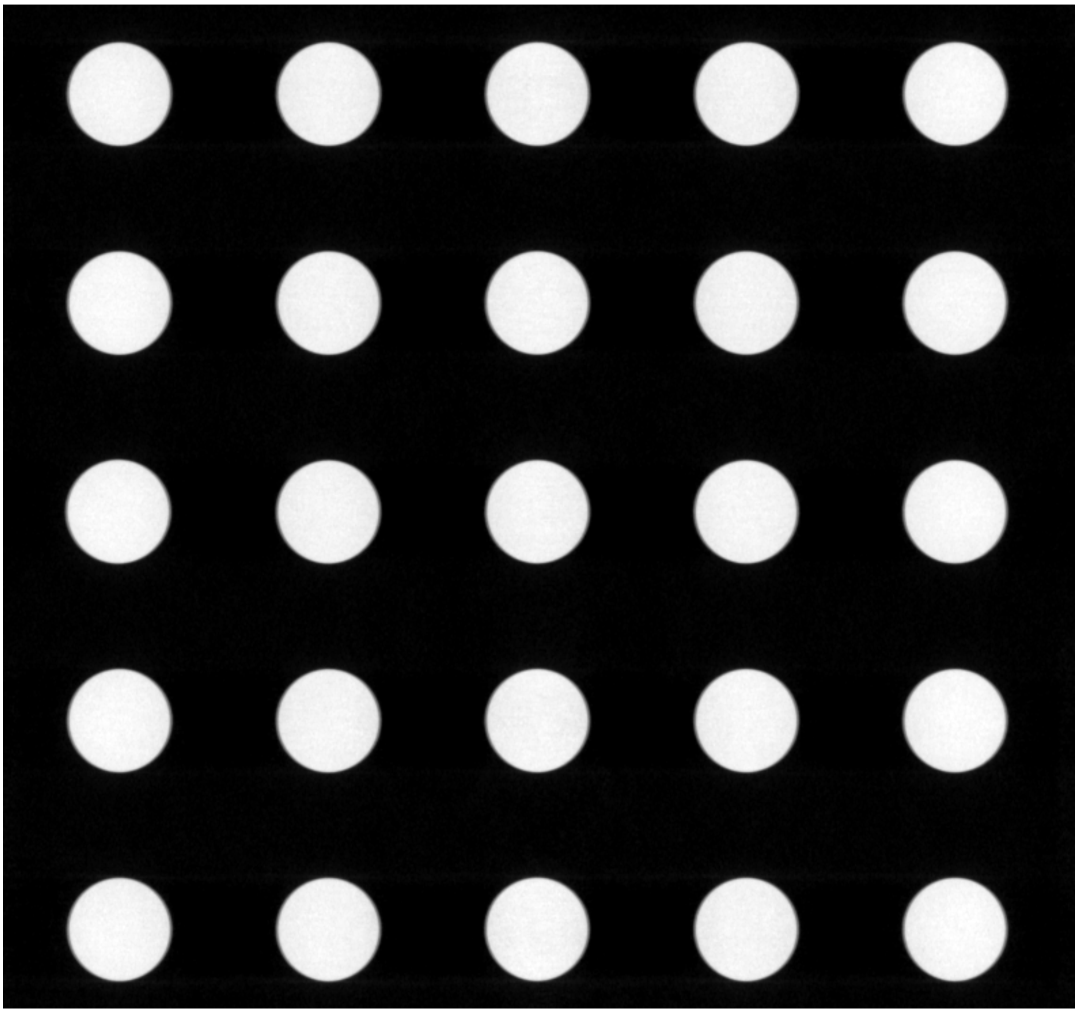

Figure 4. 61: Effects of a rotary table offset of 1 time the voxel size dimension. The central section of the ball plate in the xy plane is represented.

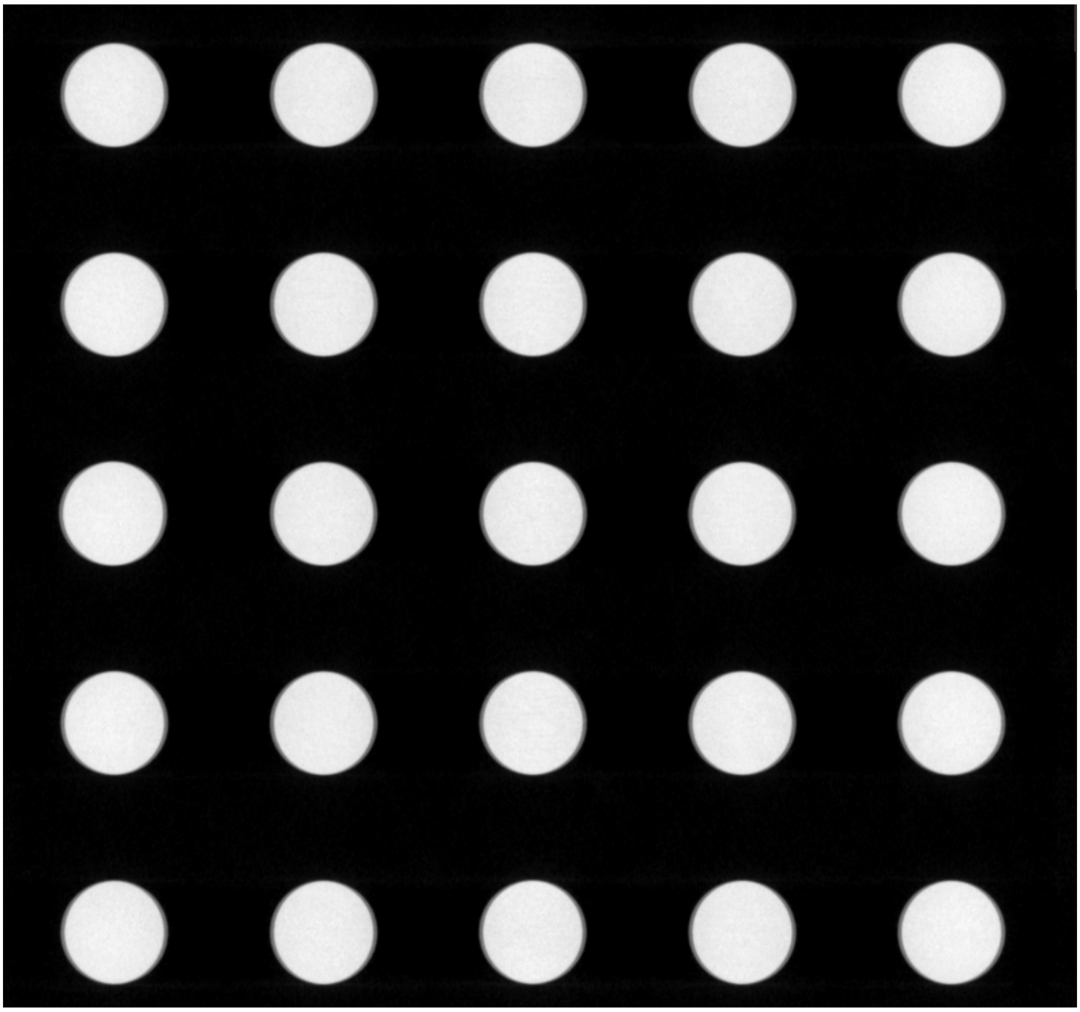

Figure 4. 62: Effects of a rotary table offset of 2 times the voxel size dimension. The central section of the ball plate in the xy plane is represented.

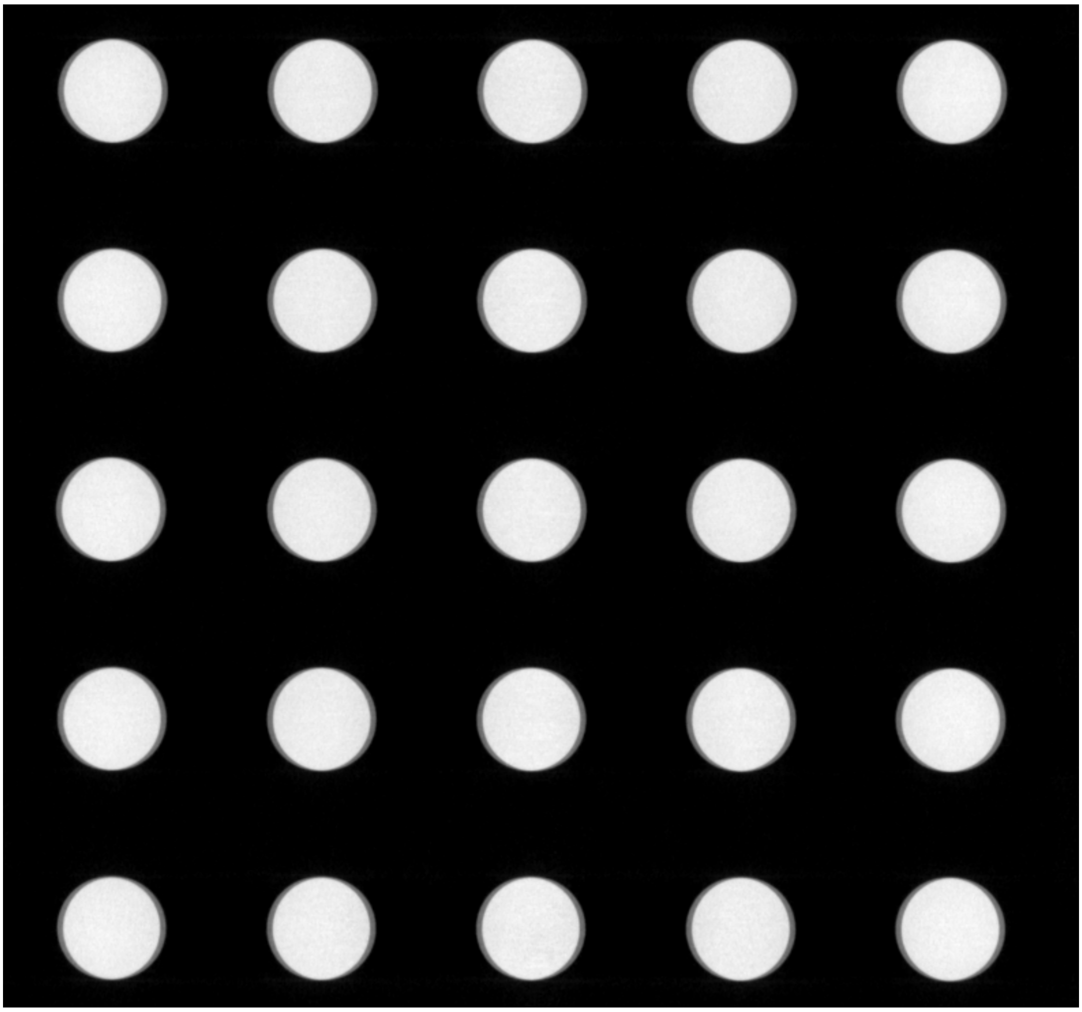

Figure 4.63: Effects of a rotary table offset of 3 times the voxel size dimension. The central section of the ball plate in the xy plane is represented.

From the analysis of Figure 4.61 to Figure 4.63, rotary table offset has a strong impact on image quality. It causes the presence of blurry edges which increase with increasing shift of the table. In particular, the effect of table offset on image quality is homogeneous for all the spheres of the ball plate in the considered misaligned configuration.

The experimental results enable also to investigate the effects of rotary table offset along the x axis from a quantitative point of view. In the following the measurement errors obtained by comparing the experimental results obtained in the three misaligned configurations with the CT scans acquired in the aligned configuration are presented. CT measurements obtained from the three misaligned configurations were compared with measurement results obtained from CT scans in the aligned configuration in order to study the effects that can be attributed just to a table offset. In fact, all the CT scans in the aligned and misaligned configurations were acquired with the same scanning parameters (other than table offset) and the same scanning strategy. In order to quantify the residual errors which were present for the measurements on performed on CT scans acquired with the system in the aligned configuration, they were also compared to CMM calibrated data. The obtained measurement errors show the proper operation of the CT system with sphere center-to-center distance errors smaller than 3.5 µm and diameter errors smaller than 3 µm.

Figure 4.64 shows the measurement errors obtained for sphere center-to-center distances in the presence of the three experimentally investigated misalignments.

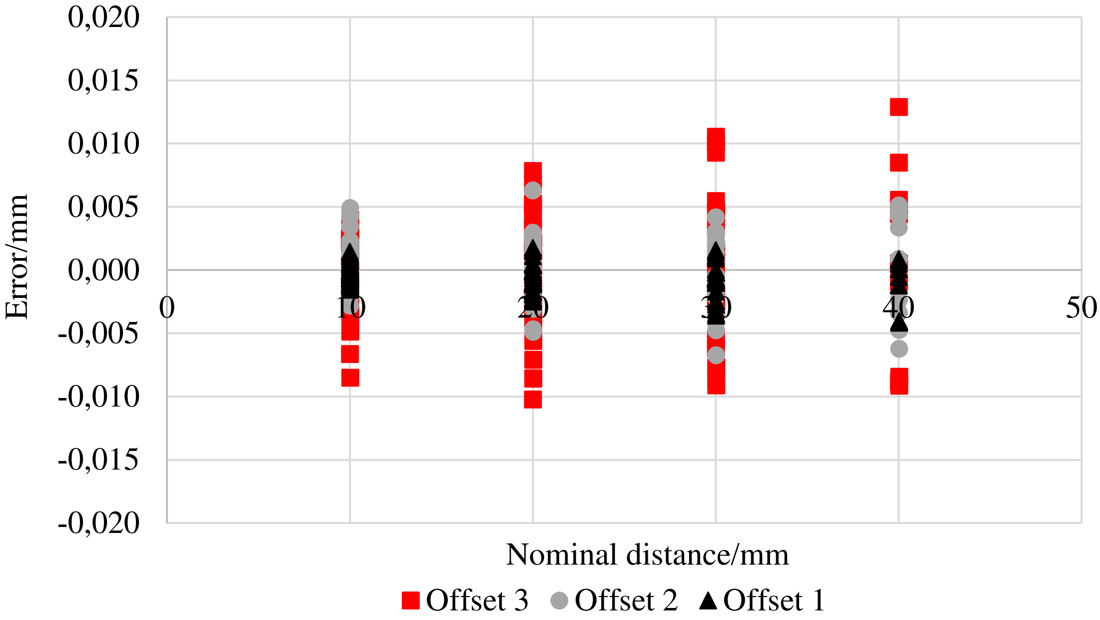

Figure 4.64: Sphere center-to-center distance errors for the three investigated rotary table offset values. The horizontal axis of the diagram reports the nominal distance between the spheres centers. The vertical axis gives the measurement errors calculated as (CT measurements in the misaligned configuration - CT measurements in the aligned configuration).

From the analysis of the graph it is visible how for an offset of 40 µm sphere center-to-center distances are just slightly affected by the misalignment and the maximum errors reach 4 µm. When increasing the table offset to 80 µm instead the measurement errors increase and reach maximum absolute values of 7 µm. For the maximum table offset investigated of 120 µm measurement errors significantly increase and reach 13 µm. In all the three cases however it can be observed how the behavior is similar with the measurement errors dispersion increasing with increasing sphere center-to-center distance.

The measurement errors obtained for sphere diameters are reported in Figure 4.65. In this case, for a 40 µm offset sphere diameters present a homogenous behavior, i.e. all the spheres have similar errors, and maximum errors of 8 µm are present. With increasing offset the maximum errors also increase and reach respectively 23 µm and 60 µm for a 80 µm and 120 µm offset.

It can be noted how with increasing misalignment the sphere diameter errors present a certain level of variability. This is attributed to the blurring caused by the misalignment that affects the surface determination process and thus the diameter measurements.

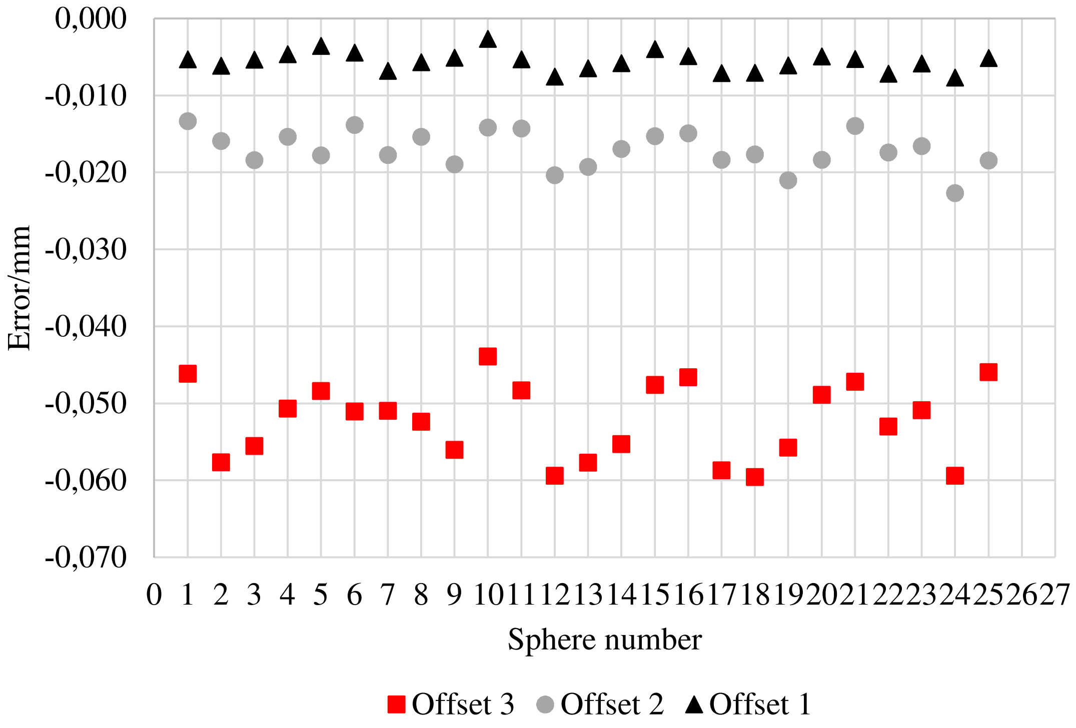

Figure 4.65: Diameter errors for the 25 spheres of the ball plate for the three investigated rotary table offset values. The horizontal axis of the graph reports the sphere number. The vertical axis gives the measurement errors calculated as (CT measurements in the misaligned configuration - CT measurements in the aligned configuration).

Form errors are also affected by the presence of a rotary table offset along the *x* axis. The measurement results obtained from the experimental investigations are reported in Figure 4.66.

For an offset of 40 µm form errors reach 46 µm and show a homogeneous behavior for all the spheres. With a 80 µm offset maximum form errors of 90 µm are present whereas 178 µm of maximum form error were obtained for a 120 µm offset. For form errors too it can be observed than with an increasing amplitude of the misalignment the variability between the form errors of the spheres of the ball plate tend to increase.

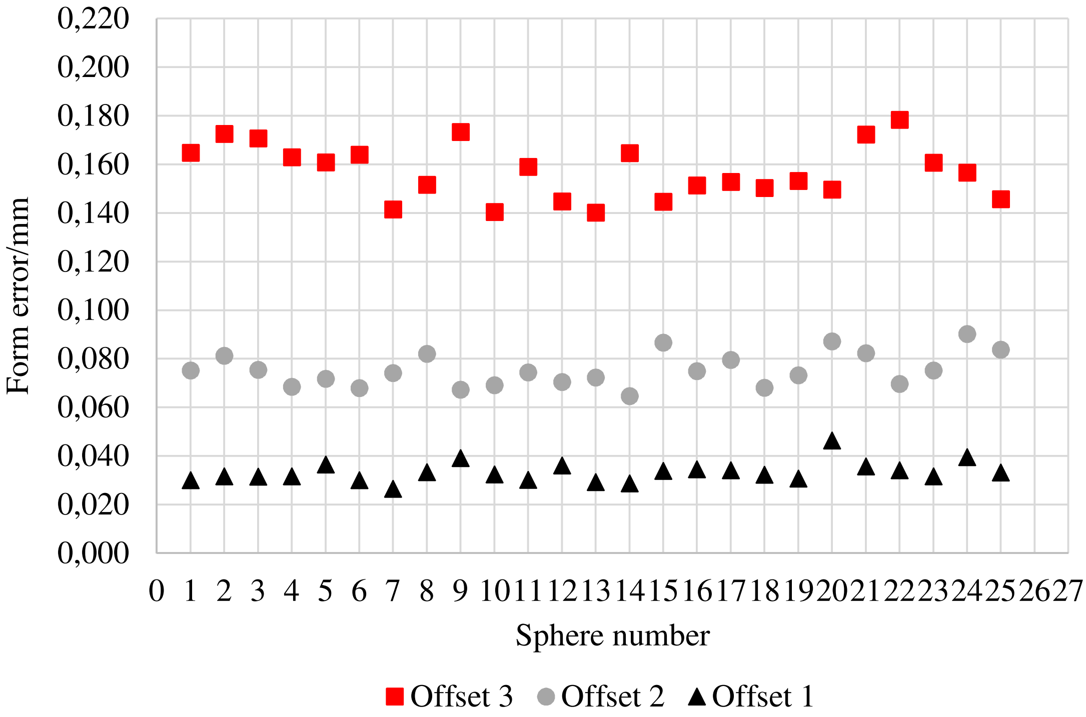

Figure 4.66: Sphere form errors for the 25 spheres of the ball bar. In the horizontal axis of the graph the sphere number is reported. The vertical axis reports the form errors for the three investigated rotary table offsets values.

4.5.4. Conclusions

In this section, the effects of a rotary table lateral shift along the *x* axis were studied. An experimental investigation was designed and performed using a tactile CMM calibrated ball plate which allowed for multiple measurements in different directions and locations on the CT volume, and for a homogeneous mapping of the effects of the induced geometrical misalignments thanks to it symmetric design.

In the first part of the study, the CT system alignment procedures were performed according to manufacturer's guidelines in order to guarantee the system was in the aligned status and avoid the presence of other unwanted misalignments. CT scans of the ball plate were then acquired with the system in the aligned configuration in order to establish the baseline for comparison with the scans acquired with a misaligned rotary table. The comparison of CT measurement results with the tactile CMM calibrated data enabled to determine residual measurement errors with the system properly aligned which were found to be smaller than 3.5 µm for sphere center-to-center distances and smaller than 3 µm for diameter errors.

Three different rotary table offsets where then mechanically induced in the CT system, respectively of 40 µm (one time the voxel size), 80 µm (two times the voxel size) and 120 µm (three times the voxel size) and CT scans were performed in each of the misaligned configurations. This enabled to study the impact of a table offset along the *x* axis on the measurement results for varying amplitudes of the offset and to study the sensitivity of the measurement results to this kind of misalignment in relation to the voxel size. The obtained measurement results show that a shift of the rotary table causes strong effects on image quality. All the spheres of the ball plate were affected by the presence of blurry edges. The bigger is the shift the bigger is the blurring caused in the CT volume.

Sphere distance errors, diameter errors and form errors were computed for all the three misaligned configurations in order to quantitatively determine the effects caused by a rotary table offset along the *x* axis.

Sphere center-to-center distances were found to be affected by the misalignment, and measurement errors increased with an increasing shift of the table. For an offset of 40 µm, sphere center-to-center distances are just slightly affected by the misalignment and the maximum errors reach 4 µm. Whereas table offsets of 80 µm and 120 µm respectively cause maximum absolute values of 7 µm and 13 µm. In all the three cases the measurement errors dispersion increased with increasing sphere center-to-center distance.

Sphere diameters were also affected by the rotary table shifts experimentally investigated. In this case, for a 40 µm offset sphere diameters present maximum errors of 8 µm. Increasing the offset the maximum errors also increase and reach respectively 23 µm and 60 µm for a 80 µm and 120 µm offset.

For an offset of 40 µm form errors reach 46 µm. With a 80 µm offset maximum form errors of 90 µm are present, whereas 178 µm of maximum form error were obtained for a 120 µm offset.

Chapter 5

CT helical scanning for coordinate metrology

In this chapter, the use of an innovative and high potential alternative scanning method in CT metrology, CT helical scanning, is investigated. CT helical scanning, in fact, can provide several advantages compared to traditional circular trajectories; however, at the state of the art it is still not widely exploited for industrial metrology applications. This chapter focuses on the study and determination of the metrological performance and the measurement errors that affect CT helical scans. First, an overview of helical scanning principles and advantages is given in section 5.2. In section 5.3 the inherent limits of traditional circular scanning trajectories are experimentally studied and demonstrated by mean of a specifically designed experimental investigation using different cone-angles. Section 5.4 deals with the experimental determination of the metrological performances and measurement errors in CT helical scanning and the investigation of the sensitivity of measurement results to the main helical scanning parameters. Finally, an optimization of helical scanning parameters is provided in order to enhance CT measurement accuracy. The work presented in this chapter was carried out in collaboration with North Star Imaging Inc.

5.1. Introduction

With the advent of X-ray CT in the field of industrial metrology as an innovative and powerful non-contact measuring technique providing valuable alternatives to classical (i.e. tactile and optical) coordinate measuring machines (CMMs) [1,2,43], a wide variety of new and traditional measurement tasks have become possible on a multitude of industrial applications. As discussed in chapter 2 in fact, CT technology enables to perform unique analyses on components with many different applications in a variety of markets. One of the key aspects of the use of X-ray computed tomography for coordinate metrology in fact are the new possibilities that this technology has made available, mainly in combination with the new industrial trends such as the production of complex objects with additive manufacturing (AM) technologies [45]. In relation to the wide variety of components and measurement tasks that the modern industry requires for, it is extremely important to investigate all the potentialities of X-ray computed tomography for coordinate metrology and to overcome the current limits of the technology.

Besides the conventional 3D CT technique using circular scanning trajectories other alternative CT scanning methods exist as described in [2]. However, at the state art, although the benefits they might provide, many of these methods are not fully exploited in industry because of their additional complexity. One innovative and extremely powerful alternative scanning method is the use of helical scanning trajectories for coordinate metrology [106,107]. Despite its known application in the medical field [10,12], helical scanning is rarely used in industrial settings specifically in the field of metrology. Its potential in industry however, is of high relevance. For many industrial applications, indeed, (e.g. automotive, aerospace markets) scanning of long objects exceeding the dimensions of the detector is usually required, while providing accurate measurements [106]. Furthermore, in many cases, high scan resolution is required even for big components in order to analyze specific details. This is typically problematic with conventional cone-beam circular trajectories. Traditional circular scans moreover, are always affected by the cone-beam artifact which is inherent in the conventional circular scanning method and contributes to degrade image quality [11]. Helical scanning thus is an extremely powerful solution which enhances the flexibility of the system and makes possible to scan components that do not fit into a single detector [2,106,107]. Also, when using suitable parameters, it enables obtaining strong improvements on image quality, and significant reductions of the cone-beam artifact. On the other side, the further complexity of the technology introduces additional error sources for metrological applications. It is clear therefore that X-ray CT helical scanning is an advanced technology that enables solving a huge variety of industrial problems and goes beyond the limits of traditional circular scanning trajectories. For this reason, assessing the measurement errors of CT systems using the principle of helical scanning, and determine the metrological performances of this advanced technology have become of crucial importance for its application for coordinate metrology [106].

As discussed in section 3.3 at the state of the art [62], there are no internationally accepted standards for performance verification of CT systems. ISO TC 213 WG 10 is currently working on ISO 10360-11 which is at the draft stage. Up to now, the reference has been provided by the German guideline VDI/VDE 2630-1.3 [65]. In strict accordance with the ISO 10360 series for CMMs [53], the document prescribes to calculate the metrological characteristics length measurement errors (*E*) and/or sphere distance errors *SD*, and probing errors of size and form (respectively *PS* and *PF*) for testing the 3D global and local error behavior of the overall CT system. The procedures proposed are valid for systems relying on the axial CT principles, therefore also for helical scanning trajectories [106].

At the state of the art, the use of helical scanning for industrial metrology has not been fully studied yet, and just a few studies are available which are reported in the following. In [108] the authors compare probing errors for circular and helical scanning by mean of simulations tools. A simulated workpiece consisting on six spheres positioned in different regions of the simulated detector was used for the analysis. Simulated results prove significantly lower *PF* for helical scanning, however no consideration are provided for length measurement errors or sphere distance errors and no real data are acquired to validate the simulation. No information is also given on the influence of helical scanning parameters. In [109] exact helical cone-beam reconstruction using Katsevich filtered back projection is implemented. A $(10\ \text{mm})^3$ titanium alloy cube featuring 25 spherical calottes is scanned. Simulated results are compared with real data, however in this case helical scans show the highest form errors in contrast with simulated data.

The aim of this chapter is to investigate the metrological performances of CT helical scanning for coordinate metrology, and in particular to study the main influence quantities that affect CT helical scanning and to determine its measurement errors. CT helical scanning measurement errors are also compared to traditional circular scans, the limits of which are experimentally shown and analyzed. The investigation of CT helical scanning metrological performances and the analyses of the measurement errors caused by the main influence quantities are an essential requirement for the use of CT systems using helical scanning principles as coordinate measuring systems (CMSs), and a detailed description still lacks in the literature. Additionally, the chapter focuses on the optimization of the main helical scanning parameters in order to enhance CT measurement accuracy.

The chapter is mainly divided in three sections. Section 5.2 gives a detailed overview of helical scanning principles and the advantages it provides for industrial applications. In section 5.3 the inherent limits of traditional circular scanning trajectories are experimentally studied and demonstrated by mean of a specifically designed experimental investigation using different cone-angles. Section 5.4 deals with the experimental determination of measurement errors in CT helical scanning, specifically the study of the metrological performances and the determination and quantification of the errors caused by the most relevant helical scanning parameters. A design of experiments is also performed in order to investigate the sensitivity of measurement results to the main helical scanning parameters. The obtained results are also compared to traditional circular scanning trajectories. An optimization of helical scanning parameters is also provided in order to enhance CT measurement accuracy.

5.2. CT Helical scanning technique

5.2.1. Helical scanning measuring principles

Industrial cone-beam CT systems using the principle of helical scanning also consists of the three main CT systems components that characterize the systems relying on traditional circular scanning trajectories, i.e. the X-ray source, the rotary table and the detector. In the case of helical trajectories however, additional movements of these components are required. Helical scanning principle in fact consists of a different scanning strategy in which the rotation of the object is simultaneously performed with a translational movement along the rotation axis, as schematically shown in Figure 5.1.

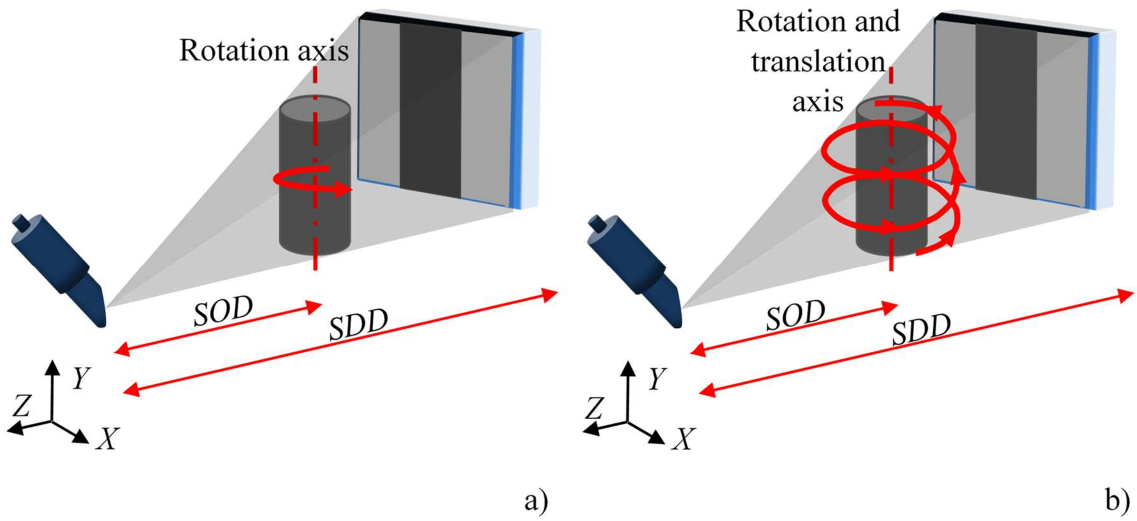

Figure 5.1: Schematic representation of scanning geometries for a) cone-beam CT with circular trajectories, b) cone-beam CT with helical trajectory.

The translational movement along the vertical axis (*Y* axis) can be obtained by moving the manipulator along the vertical direction, or with a combined movement of source and detector. Regardless how the movement is obtained, the travelling path of a point on the sample, viewed by a fixed point on the detector, describes a helix [106,107]. After the X-ray projections are acquired according to the above mentioned principles, they are then reconstructed into a single CT volume enabling therefore all the metrological analyses described in chapter 2. Although the global CT process chain is still the same than for circular trajectories and comprises the phase of X-ray projections acquisition, reconstruction, and e.g. dimensional analyses on the obtained CT volume, the presence of the additional translational movement differentiate CT helical scanning and conventional cone-beam circular scans. Due to the different trajectories, additional scan parameters are present for helical trajectories, and are presented in the following.

As described above, the use of helical trajectories always comprises a translational movement along the rotation axis direction, that in the case of the most common industrial CT system set-up given in Figure 5.1 is along the vertical direction. The amount of travel in the vertical direction (see Figure 5.2), depends on the height of the sample, and therefore on the movement required in order to acquire the complete CT volume of the entire component.

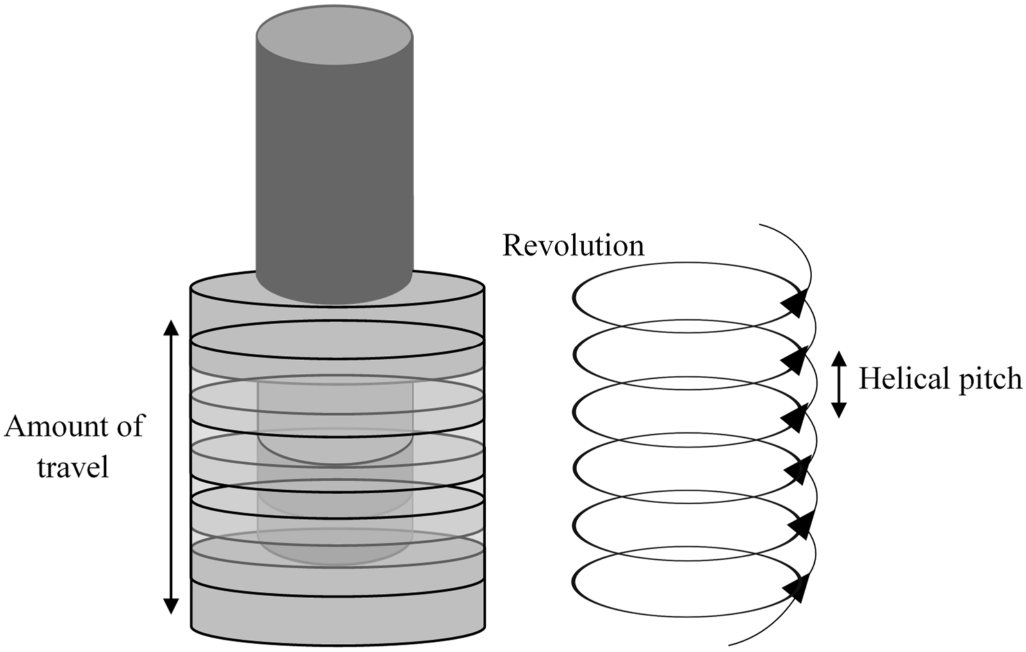

Figure 5.2: Schematic description of the main helical scanning parameters.

During its translational movement along the entire amount of travel, the sample is also contemporarily rotated. The number of revolutions describes the number of times the sample is rotated. Finally, another relevant parameter related to the ones previously introduced is the helical pitch which describes the vertical travel per revolution.
It comes that at the end of a helical scan the sample will have moved of a quantity equal to the total amount of travel in the rotation axis direction. The vertical distance the sample will move for each revolution will be given by the helical pitch.

5.2.2. Comparison between helical and circular scanning trajectories

As introduced before helical scanning trajectories enable to obtain several advantages compared to traditional circular scanning trajectories. In particular, the benefits helical scans provide are extremely important for industrial metrology purposes. In fact, helical scans not only provide a substantial improvement on image quality when using suitable scanning parameters, but also make possible to solve measuring tasks that cannot be performed with conventional circular scanning trajectories. The advantages provided by helical scanning are presented and discussed in the following.

Analysis on long objects exceeding the dimension of the detector

Often a variety of industrial applications demands for quality control on elongated objects that exceed the vertical dimension (the height) of the detector and thus cannot be completely scanned in one single time. This is the case of components for example in the aerospace and automotive industry, for which dimensional measurement tasks and other kinds of non-destructive analyses (e.g. porosity analysis) are required while having accurate measurements [106].

When using conventional circular cone-beam scans the limit is given by the height of the sample, which if exceeds the dimension of the detector in the vertical direction cannot be scanned in one single time. In this case multiple circular CT scans can be acquired on different regions of the sample and investigated separately, however many times the features of interest must be contained in the same CT volume in order to perform the required measurements according for example to the datum given in the technical drawing. In other cases, the CT volumes obtained from different CT circular scans performed on the different zones of the sample can be aligned in the post-processing phase in order to create a single CT volume. This process however is highly dependent on the alignment procedures, and many times in industrial components good reference elements are not available in each of the zones of the sample in order to perform an accurate and precise alignment of different CT scans.

When using helical scanning trajectories instead no constraints are present in the rotation axis direction. In fact, thanks to the translational movement along the vertical axis of Figure 5.1 it is possible to scan the entire component of interest even if it exceeds the dimension of the detector, and then reconstruct its 3D model. The only constraint is given by the dimensions of the cabinet in the case of closed systems, in fact the scanned components must fit into the cabinet.

Helical scanning therefore strongly enhances the flexibility of the system and enables to perform measurements that otherwise would not be possible with traditional circular scans.

Enhancement of scan resolution

A consequence of the possibility to scan components that do not fit vertically into a single detector, is that the CT scan resolution can be enhanced when using helical trajectories. This is shown in Figure 5.3.

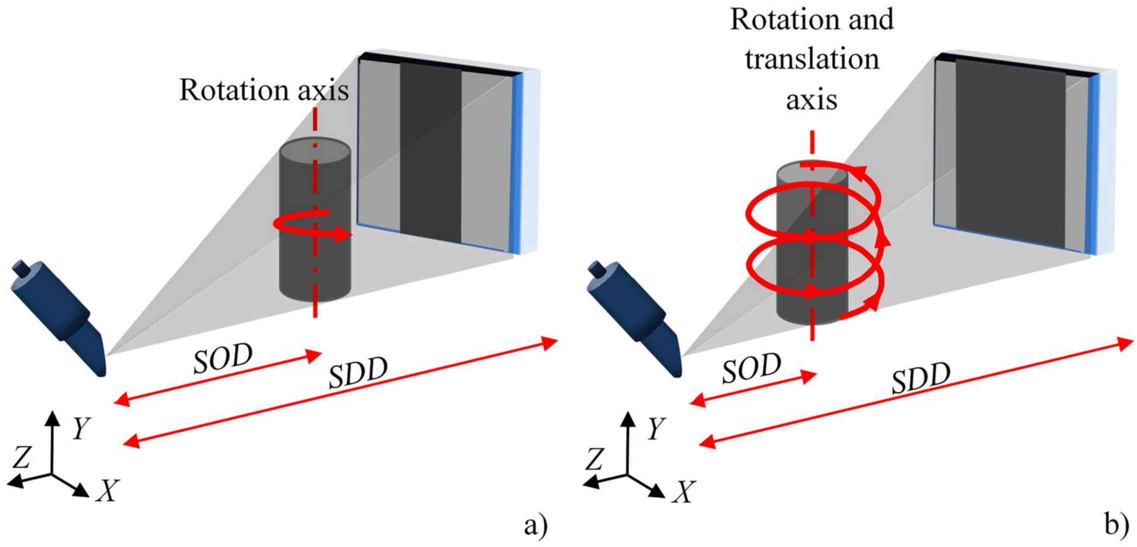

Figure 5.3: Schematic representation of the enhancement of scan resolution that can be obtained when using helical scanning trajectories. a) scan resolution obtained with conventional circular scans, b) improved scan resolution of helical scans.

As visible in Figure 5.3 b), in the case of helical scans, the source-to-object distance *SOD* can be decreased till when the horizontal dimensions of the sample fit in the field of view of the detector. This enables to have a higher magnification and therefore a smaller voxel size which means a better resolution compared to the voxel size that could be obtained when using circular trajectories (see Figure 5.3 a)). All of this without the need to perform multiple CT scans or to cut the part. It comes that helical scanning does not only provide extremely relevant advantages just for big components that due to their dimensions cannot be scanned with conventional circular cone-beam trajectories, but also for smaller components that require high resolution scans. This is the case for example of micro components, the dimensions of which would not be critical for performing a traditional CT scan but that, due to the high resolution CT scans requirements in order to analyze specific details, cannot be scanned in one single cone-beam circular CT scan entirely. Helical scanning therefore it is not only beneficial for performing scans on big components but also when extremely high resolution is required together with the scanning of the entire object.

<u>*Reduction of cone-beam artifact*</u>

One of the most relevant advantages that helical scans provide is the possibility to significantly reduce and theoretically eliminate the cone-beam artifact that it is always present in circular scanning trajectories.

One of the most popular reconstruction algorithms for circular trajectories is the Feldkamp-Davis-Kress (FDK) algorithm [9]. Although being based on an approximate formula and not on theoretical exact reconstruction, the FDK algorithm is one of the most widely implemented algorithms for 3D direct reconstruction [11]. This is mainly because of its relative simplicity in implementation, its efficiency in computation and speed of reconstruction and for it similarity to the well-known and widely implemented filtered backprojection (FBP) for fan-beam systems. Moreover, for reasonable cone-angles the FDK is capable of producing reconstructions not significantly inferior to those of slice-by-slice reconstructions using parallel or fan-beam data [9]. The FDK algorithm in fact is effective in combating some of the effects caused by the cone-beam artifacts [11]. It was demonstrated in [9] that the FDK gives the correct result for the intensity integrated along the axial direction. This means that density is conserved along lines parallel to the axis of rotation. From this property, it comes that the principal effect that is expected is blurring in the axial direction [9].

This concept is resumed in the so called completeness condition for exact reconstruction, also known as Tuy and Smith sufficiency condition which requires that there exists at least one cone-beam source point in every plane intersecting the object [110, 111]. This condition is not satisfied in circular cone-beam CT. Therefore, shading and streaking artifacts i.e. the cone-beam artifact (or Feldkamp artifact) caused mainly by incomplete sampling due to the lack of information in the Fourier spectrum [12] occur while moving away from the central plane of the detector and increase with the cone-angle.

In particular Figure 5.4 reports the regions were a lack of information in the Fourier spectrum is registered.

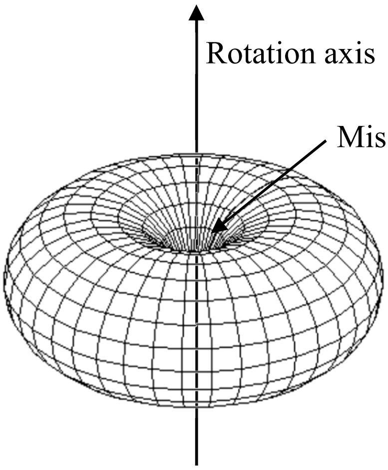

Figure 5.4: Outside the torus the Fourier spectrum lacks of information. Adapted from [108].

The presence of the cone-beam artifact in the axial direction is not dependent on the amount of data and would resist even increasing the number of projections [9].
An example of cone-beam artifacts in circular scanning trajectories is given in Figure 5.5.

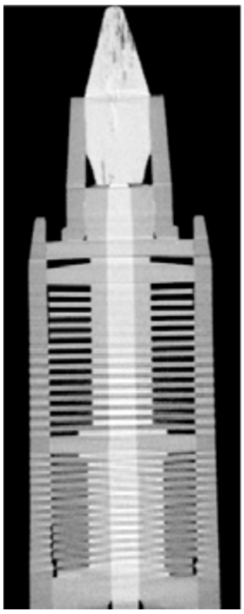

Figure 5.5: Example of cone-beam artifact in circular scanning trajectories. As visible in the upper and lower part of the image severe cone-beam artifacts are present on flat surfaces [112].

Although the presence of cone-beam artifacts varies with the shape and density of the objects the following considerations are valid. The greatest errors might be expected with flat surfaces positioned perpendicularly to the rotation axis, i.e. lying parallel to the central plane of the detector and far away from it. The reconstruction of such an object will be smeared in the vertical direction and for a given source-to-object distance *SOD* the artifacts will increase with increasing object distance from the central plane [9,11].
Moreover, the bigger is the cone-angle (Figure 5.6), and the closer the object is to the detector edges, the stronger will be the cone-beam artifact effects. Bigger cone-angles are obtained for smaller source-to-detector distances *SDD*, whereas the higher the

magnification will be, and therefore the smaller the voxel size, the closer the sample will be to the detector edges (see Figure 5.6).

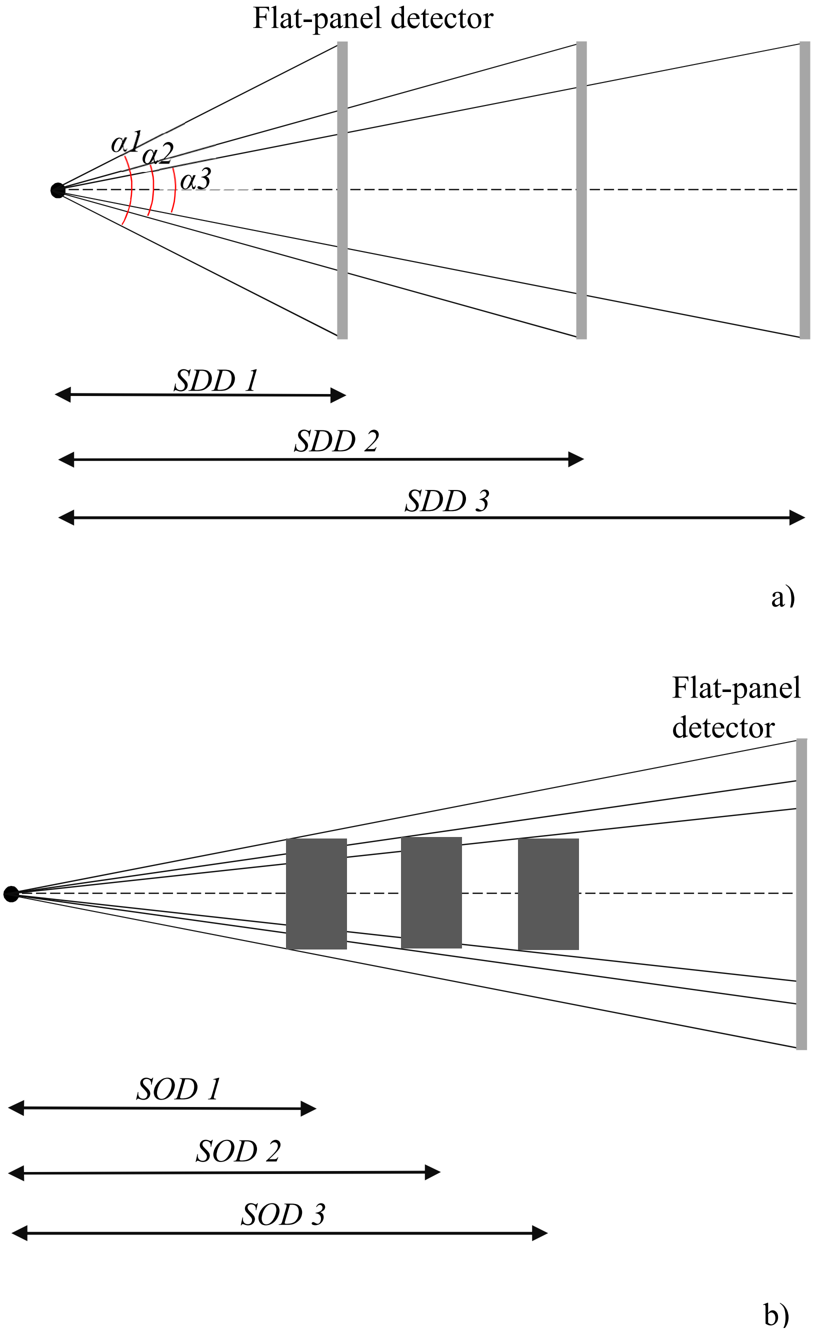

Figure 5.6: Effect of cone-angle and object magnification on cone-beam artifact. a) effect of increasing SDD, α1, α2 and α3 describe the different cone-angles b) effect of magnification for a fixed SDD.

Of course good practice guidelines can be adopted in order to reduce the effects of cone-beam artifacts in circular scans, such as using long *SDD*, positioning flat surfaces in a tilted orientation and never perpendicular to the rotation axis, avoid performing scans with the component too close to the edges of the detector etc. However, as discussed above in circular scans the cone-beam artifact will always be present and its effect can just be reduced.

When using helical trajectories instead, with an appropriate helical pitch, these artifacts can be considerably reduced [108,112], and in principle they can be completely eliminated since the completeness conditions for exact reconstruction can be met. Figure 5.7 reports the section of the same component that has been scanned with circular (Figure 5.5) and helical scanning trajectories (Figure 5.7).

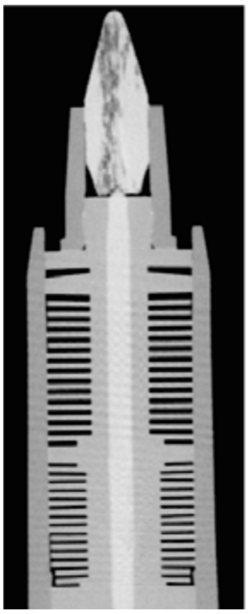

Figure 5.7: Example of enhanced image quality obtained when using helical scanning trajectories [112].

From Figure 5.7 it is visible how strong improvements on image quality can be obtained when using helical trajectories with respect to what is shown in Figure 5.5. This obtained enhancement on image quality is extremely relevant for coordinate metrology purposes because it enables to achieve more accurate and reliable measurements, to decrease and to have more consistent determinations of the measurement uncertainty which is essential for traceability establishment, but it is of major importance also for non-destructive testing where often the presence of artifacts does not enable to see or masks some internal defects, voids, cracks etc.

<u>*Improvement of CT scanning parameters*</u>

The possibility to significantly reduce the cone-beam artifacts has also some positive benefits on the selection of the CT scanning parameters. In fact, often when using circular cone-beam scanning trajectories due to the need to reduce the cone-beam artifacts effects the sample is positioned with a tilted orientation to avoid having surfaces lying perpendicular to the rotation axis and the *SOD* and thus the voxel size (assuming a fixed *SDD*) is chosen so that to avoid the feature of interest being at the extreme zones of the detector vertically where the effects of this artifact are stronger. Many times this causes the voxel size to be bigger than the one actually needed to scan the entire sample. When using helical scans instead thanks to the possibility to considerably reduce the cone-beam artifacts there is no constraint in the voxel size (in order to reduce the effects of the cone-beam artifact) which can be significantly decreased and thus a better resolution can be obtained.

When dealing with systems with a variable *SDD* moreover the use of helical trajectories enables to significantly decrease the source-to-detector distance which causes the cone-angle to increase. This would cause serious artifacts for conventional circular scans since, as discussed before, the bigger the cone-angle the bigger the effects of the cone-beam artifacts. The reduction of *SDD* that is possible for helical scans has several benefits. With a shorter *SDD* a higher penetration of material can be obtained making possible to achieve a good penetration also for components for which the X-ray penetration in not enough when using much longer *SDD*. When the X-ray penetration is enough instead for both longer and shorter *SDD*s, the higher penetration of material enables also to decrease the scanning power with respect to scans performed with longer *SDD*s. This means that also the focal spot dimensions and possible focal spot drifts can be reduced with clear benefits for measurement accuracy.

Also, if the interest is in a reduction of scanning time, with shorter *SDD*s it is possible to decrease the exposure time which causes a reduction of the scan time.

5.3. Experimental investigation on the effects of the cone-angle on the measurement accuracy of circular scanning trajectories

In this section the influence of the cone-angle on the measurement accuracy of CT measurements performed using conventional circular scanning trajectories is investigated. As reported in section 2.1 the cone-beam artifact is always present in circular scanning trajectories. One of the most widely implemented reconstruction algorithms for cone-beam circular trajectories is the FDK algorithm. However, for cone-beam circular trajectories the so called completeness condition for exact reconstruction, also known as Tuy and Smith sufficiency condition which requires that there exists at least one cone-beam source point in every plane intersecting the object is not satisfied. This causes the presence of shading and streaking artifacts i.e. the cone-beam artifact (or Feldkamp artifact) mainly because of the incomplete sampling due to the lack of information in the Fourier spectrum that occurs while moving away from the central plane of the detector and increase with cone-beam angle.

It industrial practice, most of the systems rely on cone-beam circular scanning principles. Especially, when dealing with metrological purposes most of the times traditional circular scans are used. It comes that it is necessary to quantify the influence of the cone-beam artifacts on CT measurements performed using traditional circular cone-beam scanning trajectories, and to map the dependence of the measurement errors produced by those artifacts with the cone-angle of the X-ray beam. This section will focus on the determination of the errors caused by the cone-beam artifact and on the study of the dependence of such error with the cone-beam angle. The obtained results demonstrate the inherent limits of traditional cone-beam circular trajectories.

5.3.1. Experimental set-up

In order to investigate the measurement errors caused by cone-beam artifacts and to study the dependence of such errors with the cone-angle, an experimental campaign was designed and performed. A tactile CMM calibrated ball bar consisting of 15 equally spaced ceramic spheres glued on a carbon-fiber reinforced rod was used for the experimental investigation (see Figure 5.8). The ball bar was provided by North Star Imaging Inc. The ball bar featured sphere nominal diameters equal to 1.59 mm and sphere center-to-center distances ranging from nominally 5 mm to 70 mm. The ball bar therefore, enables the measurement of 105 sphere center-to-center distances, 15 sphere diameters and 15 sphere form errors.

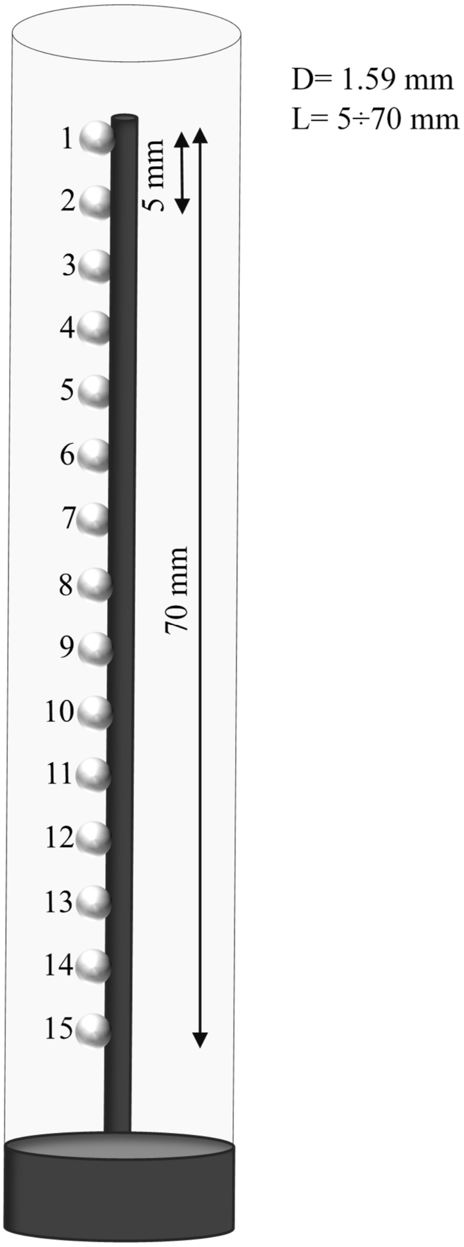

Figure 5.8:Schematic representation of the ball bar used for the experimental investigation.

The ball bar was placed in the measurement volume in the vertical direction as described in Figure 5.9 and sphere number 8, located in the middle of the rod, was manually positioned on the central plane of the detector in order to have seven spheres positioned above the middle plane of the detector and seven spheres positioned below the middle plane of the detector. This guarantees a homogeneous mapping of the effects of the cone-beam artifacts, which are expected to be maximum at the top and bottom of the detector where Radon data are not known.

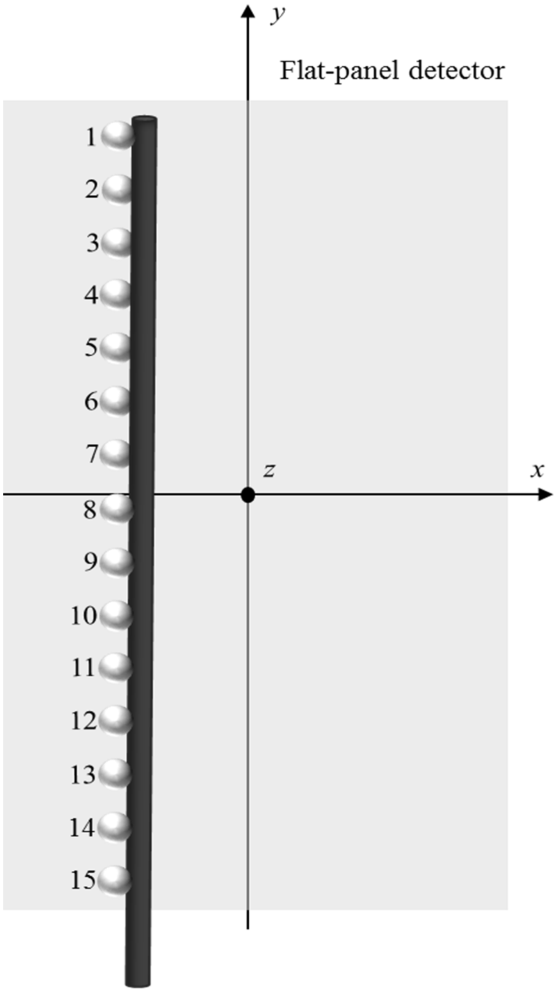

Figure 5.9: Schematic representation of the orientation and positioning of the ball bar in the measurement volume.

In order to study the influence of the cone-angle on the accuracy of CT measurements, different CT scans of the ball bar oriented and positioned according to Figure 5.9 were performed with different source-to-detector distances and thus with different cone-angles. Table 5.1 summarizes the six different CT scanning set-up used for the experimental investigation. Set-up 1 is characterized by the highest cone-angle experimentally investigated, whereas set-up 6 is characterized by the smallest cone-angle experimentally investigated.

	Set-up 1	Set-up 2	Set-up 3	Set-up 4	Set-up 5	Set-up 6
SDD	536 mm	655 mm	774 mm	893 mm	1012 mm	1300 mm
Cone-angle	25.6°	21.1°	17.9°	15.5°	13.7°	10.7°
Voxel size	0.046 mm	0.046 mm	0.046 mm	0.046 mm	0.046 mm	0.046 mm

Table 5.1: Scanning set-up used for the experimental investigation.

As it is visible, for each configuration the source-to-detector distance was changed. This allowed to investigate six different source-to-detector distances *SDD* ranging from 536 mm, the smallest *SDD* that enables to keep the whole object in the field of view, to 1300 mm the maximum *SDD* achievable with the system. Moreover, it can be seen how, the possibility to use a variable *SDD* enables to keep the same voxel size for each CT scanning set-up. This makes possible to perform CT scans with the same voxel size and thus to avoid the introduction of unwanted error sources caused by CT scans with different resolutions.

The six cone-angles depicted in Figure 5.10, and ranging from 25.6° for a *SDD* of 536 mm to 10.7° for a *SDD* of 1300 mm were used for the experimental investigation. In particular, it is visible how, when increasing the *SDD* the cone-angle decreases.

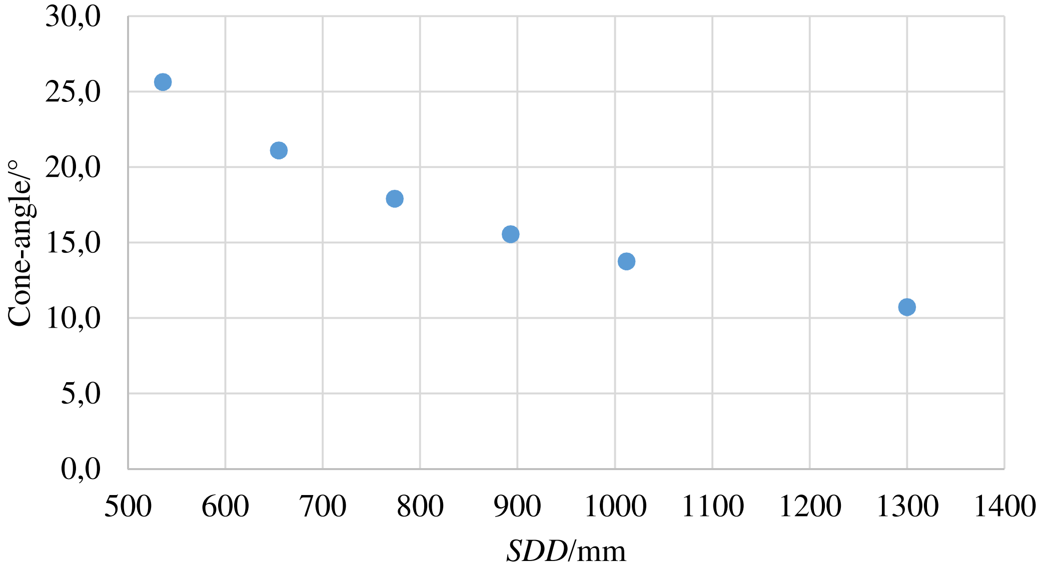

Figure 5.10: Cone-angles used for the experimental investigation.

CT scans of the ball bar were performed for the six scanning set-up reported in Table 5.1 with a NSI CXMM 50, a metrological CT system featuring a 225kV micro-focus reflection X-ray source, a 2D flat panel detector and an air-cooled cabinet.

CT scans were performed using the scanning parameters reported in Table 5.2. Due to the significantly different *SDD* used for the investigation, the scanning parameters were selected in order to keep the same voltage and current for all the six different configurations, and thus the same X-ray tube power, and adjusting the exposure time (and number of frame averaged) so that to obtain the same contrast for all CT scans.

	Set-up 1	**Set-up 2**	**Set-up 3**	**Set-up 4**	**Set-up 5**	**Set-up 6**
Voltage	110 kV	110 kV	110 kV	110 kV	110 kV	110 kV
Current	150 µA	150 µA	150 µA	150 µA	150 µA	150 µA
Exposure time	7.5 fps	5 fps	3.6 fps	2.75 fps	2.15 fps	1.25 fps
Frame averaging	7	5	4	3	2	2
Filtering	none	none	none	none	none	none
Number of projections	1500	1500	1500	1500	1500	1500

Table 5.2: Scanning parameters used for the experimental investigation.

5.3.2. Data evaluation

All CT scans were reconstructed by means of the manufacturer's reconstruction software NSI efX-ct, using a conventional FDK based algorithm. CT volumes were subsequently imported and analyzed using VGStudio MAX 2.2. The local adaptive surface determination algorithm was used for all CT scans. A region of interest of the top hemispheres was considered for performing the analysis in order to exclude the regions of the spheres that might be affected by the presence of the glue necessary to stick the spheres to the carbon-fiber reinforced rod. Sphere diameters, sphere center-to-center distances and spheres form errors were then calculated for each of the CT scans using Gaussian least-squares fitting.

Sphere distance errors, probing errors of size and probing errors of form were then computed according to VDI/VDE 2630 part 1.3 using the reference measurements collected through the CMM calibration of the ball bar.

5.3.3. Results and discussions

In this section the experimental results obtained from the CT scans performed in the six different CT scanning set-up are presented and compared to the reference tactile CMM measurements.

Before analyzing from a quantitative point of view the measurement errors caused by the presence of the cone-beam artifacts, Figure 5.11 provides a visual overview of the effects of the cone-beam artifacts on the 3D volumes of the ball bar for each of the six scanning set-up, characterized by decreasing cone-angles, experimentally investigated (for visibility reasons sphere 1 and sphere 8 are shown for each set-up).

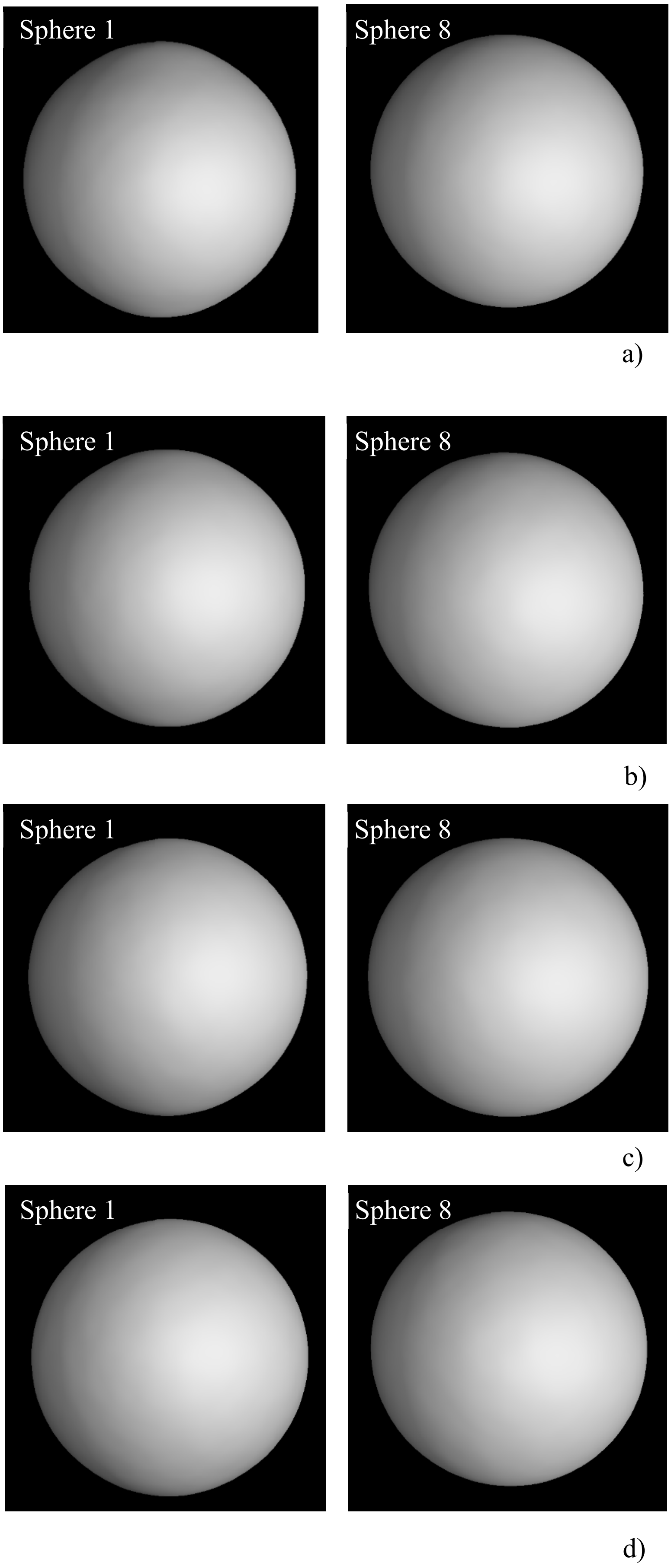
Sphere 1
Sphere 8
a)
Sphere 1
Sphere 8
b)
Sphere 1
Sphere 8
c)
Sphere 1
Sphere 8
d)

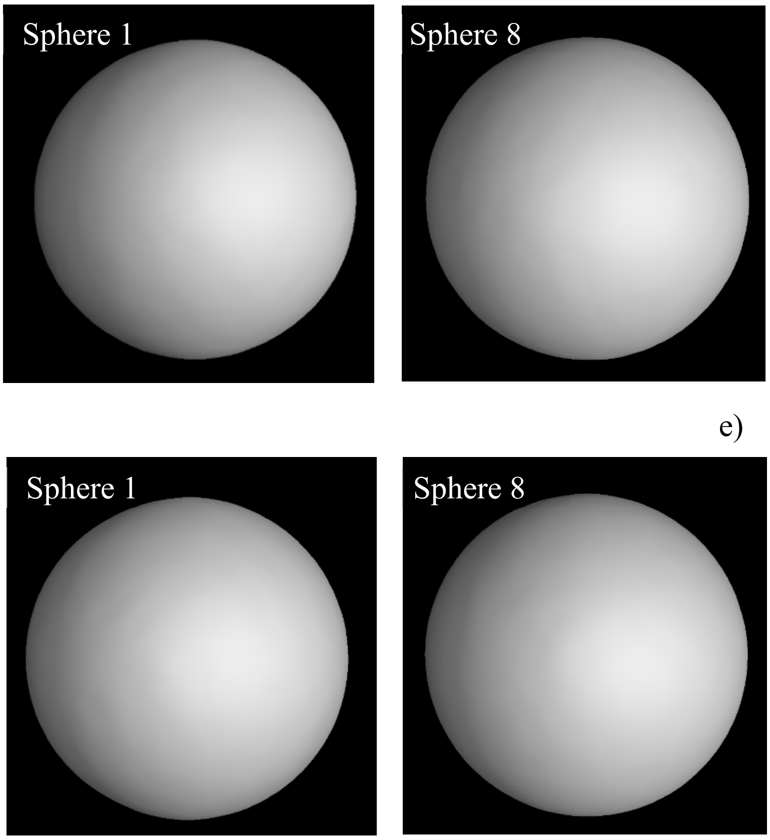

e)

f)

Figure 5.11:Visual overview of the effects of the cone-beam artifacts on the 3D model of the ball bar. For each of the six investigated scanning set-up, the effects of cone-beam artifacts on sphere 1 and sphere 8 are shown. Sphere 1 is positioned at the top of the detector whereas sphere 8 is positioned at the center of the detector. a) set-up 1, b) set-up 2, c) set-up 3, d) set-up 4, e) set-up 5, f) set-up 6.

From Figure 5.11 it is visible how the cone-beam artifacts strongly affect the image quality, in particular for the configurations characterized by the biggest cone-angles. For all the six investigated scanning set-up the spheres positioned close to the central plane of the detector are almost unaffected by the cone-beam artifacts. As described in section 5.2.2 in fact, the cone-beam artifact or Feldkamp artifact arise from the incomplete sampling due to the lack of information in the Fourier spectrum which occurs while moving away from the central plane of the detector [11]. When moving away from the central plane of the detector, the spheres of the ball bar exhibit artifacts at the poles which increase with the sphere distance from the central plane of the detector, and with the cone-angle. By comparing sphere 1, positioned at the top of the detector, for all the six investigated configurations it is clearly visible how the image quality degrades with increasing cone-angle.
It is worth noting that, due to the inherent presence of the cone-beam artifacts in cone-beam circular scanning trajectories, the cone-beam artifacts effects can be reduced but never completely eliminated.

Besides the visible effects that the cone-beam artifacts produce on image quality, when dealing with metrological applications of computed tomography it is extremely important to quantitatively determine the effects of the cone-beam artifacts on CT measurement results. The experimental results obtained for sphere center-to-center distances, sphere diameters, and sphere form errors are presented in the following.

Figure 5.12 reports the measurement results obtained for the 105 measured sphere distance errors (i.e. the sphere-center- to-center measurement errors). In the horizontal axis of the graph the nominal distance between the spheres centers is represented whereas in the vertical axis the measurement errors calculated as (CT measurements-CMM measurements) are reported.

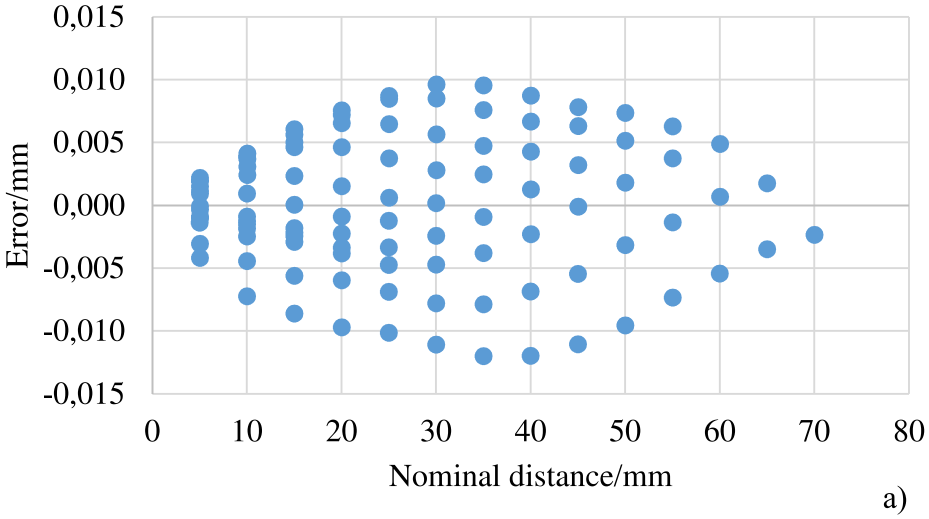

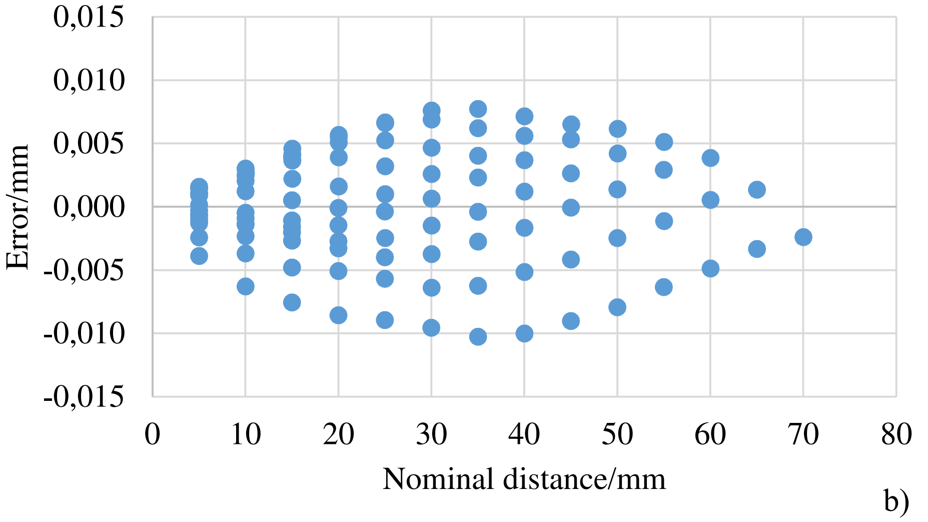

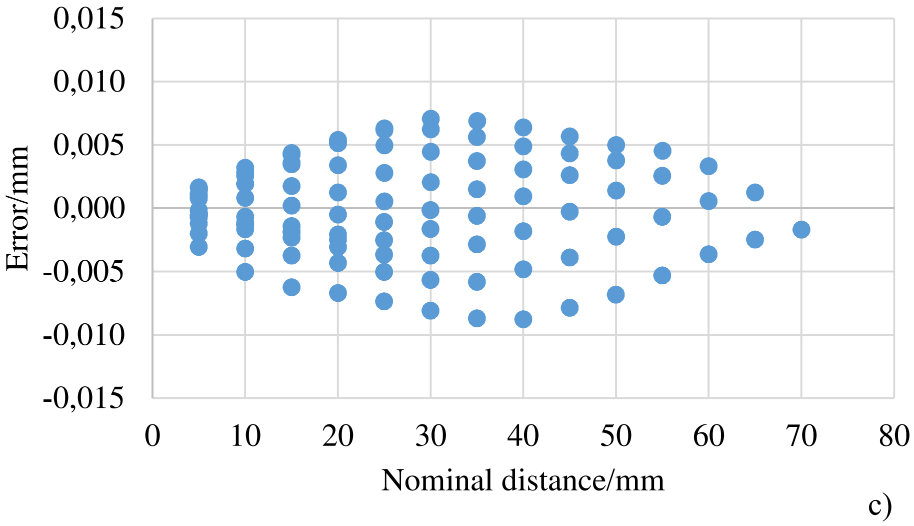
0,015
0,010
0,005
0,000
-0,005
-0,010
-0,015
Error/mm
0
10
20
30
40
50
60
70
80
Nominal distance/mm

c)

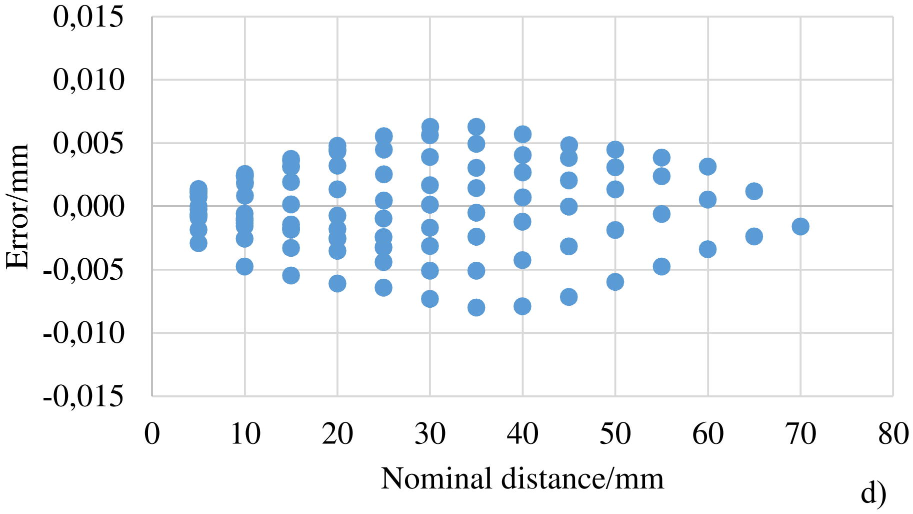
0,015
0,010
0,005
0,000
-0,005
-0,010
-0,015
Error/mm
0
10
20
30
40
50
60
70
80
Nominal distance/mm

d)

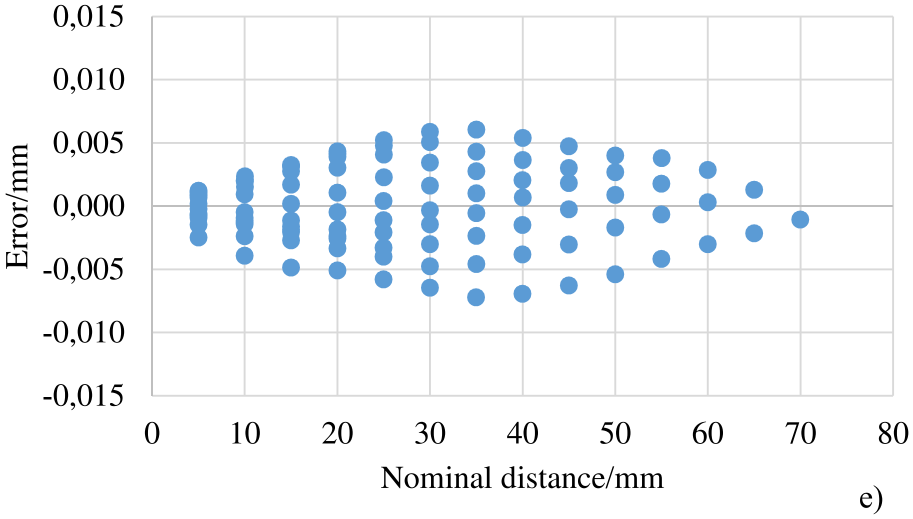
0,015
0,010
0,005
0,000
-0,005
-0,010
-0,015
Error/mm
0
10
20
30
40
50
60
70
80
Nominal distance/mm

e)

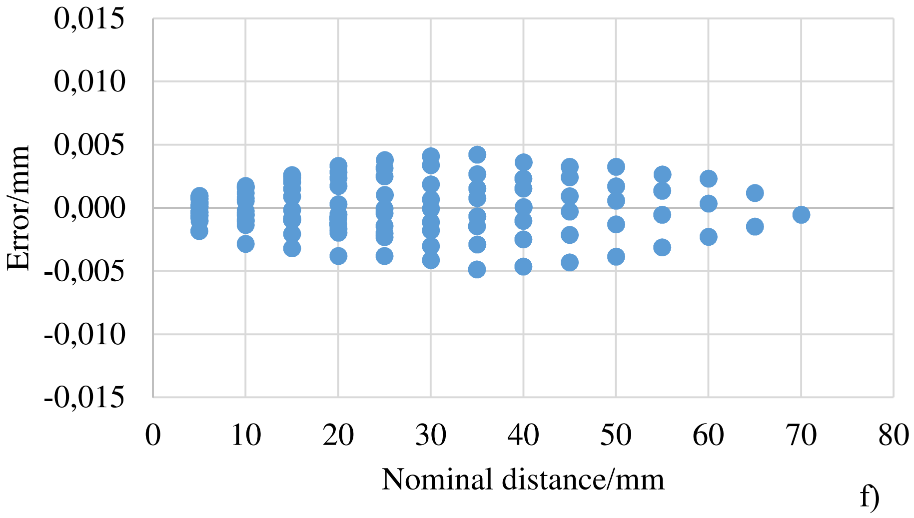

Figure 5.12: Sphere distance errors obtained for the CT scans of the ball bar performed in the six different CT scanning set-up. a) set-up 1, b) set-up 2, c) set-up 3, d) set-up 4, e) set-up 5, f) set-up 6. The horizontal axis of the graph reports the nominal distance between the sphere centers. The vertical axis gives the measurement errors calculated as (CT measurements-CMM measurements).

From the experimentally obtained results it is visible how the cone-beam artifact and cone-angle affect the center-to-center distances between the spheres. For set-up 1, characterized by a short *SDD* and a cone-angle of 25.6° the sphere distance errors reach 12 µm. With decreasing cone-angles the sphere distance errors decrease. Set-up 2,3 and 4 are characterized respectively by maximum errors of 10 µm, 9 µm, and 8 µm, whereas set-up 5 shows maximum errors of 7 µm. Set-up 6 which is characterized by the smallest cone-angle experimentally investigated and equal to 10.7° exhibits maximum errors up to 5 µm.

Figure 5.12 a) to f) also shows the particular shape that the cone-beam artifacts produce in the sphere distance errors chart. With a high cone-angle of 25.6° for example, the measurement performed between sphere 8 (nominally on the central plane of the detector) and sphere 15 (bottom of the detector) produce the highest error, while measurements performed between spheres close to the central plane of the detector (e.g. spheres 7, 8 and 9) produce smaller errors.

When using a smaller cone-angle of 10.7° this behavior is significantly reduced; also in this case the maximum errors of 5 µm are obtained when measuring distances between spheres close to central plane of the detector and spheres very close to upper or lower edges of the detector.

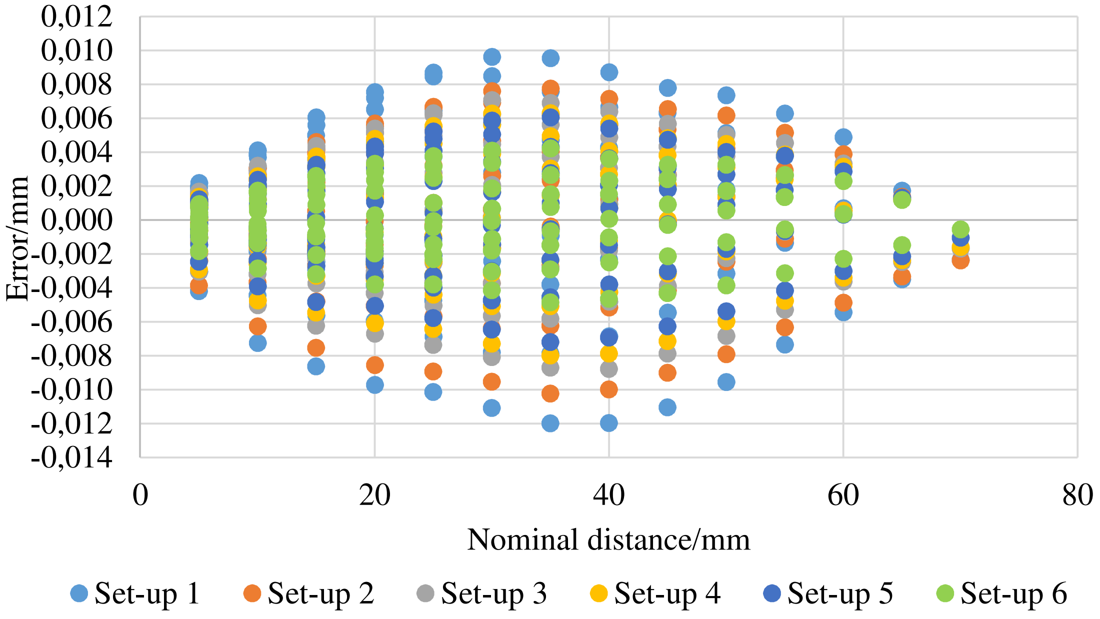

Figure 5.13: Sphere distance errors obtained for the CT scans of the ball bar performed in the six different CT scanning set-up. The horizontal axis of the graph reports the nominal distance between the sphere centers. The vertical axis gives the measurement errors calculated as (CT measurements-CMM measurements) for the six different set-up.

The effects of decreasing cone-angles on sphere distance errors is described on Figure 5.13 that summarizes the measurement results for center-to-center measurements obtained for the six investigated configurations. Figure 5.13 shows how, when decreasing the cone-angle, the sphere distance errors chart keeps the same shape (i.e. the measurements characterized by the maximum errors are the ones between the spheres positioned at the very top or very bottom of the detector and spheres positioned close to the central plane of the detector) but the measurement errors significantly decrease.

Figure 5.14 reports the measurement results obtained when measuring the probing errors of size (i.e. the sphere diameter errors).

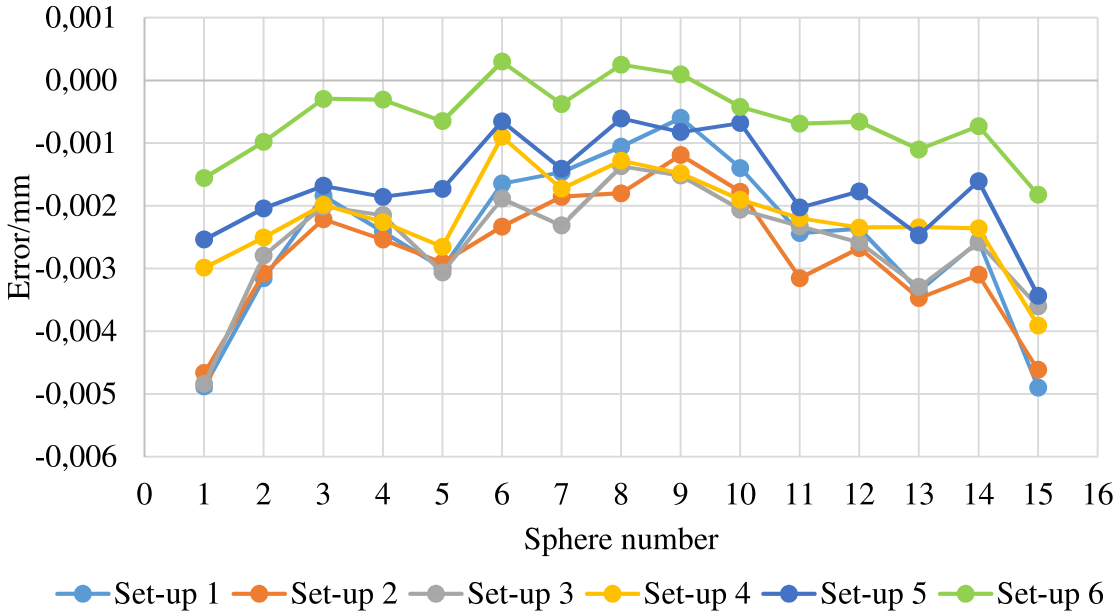

Figure 5.14: Sphere diameter errors obtained for the CT scans of the ball bar performed in the six different CT scanning set-up. In the horizontal axis of the graph the sphere number is represented, in the vertical axis the measurement errors between CT measurements and CMM measurements are reported for the six different set-up.

When using a high cone-angle of 25.6° and a short *SDD* of 536 mm, the spheres positioned at the top and bottom of the detector, namely sphere 1 and sphere 15 show the maximum diameter errors equal to 5 µm. The diameter errors decrease with decreasing sphere distance from the central plane of the detector and reach 1 µm for sphere 8 nominally positioned on the central plane of the detector. The same behavior is observed for set-up 2 and 3. Set up 4 and 5 also show a similar behavior characterized by bigger diameter errors for spheres positioned at the top and bottom of the detector however this behavior is less pronounced than for set-up 1,2 and 3, and maximum diameter errors of 4 µm and 3 µm are obtained respectively for set-up 4 and 5. Set-up 6 characterized by the smallest cone-angle experimentally investigated does not exhibit the strong trends which are present when using bigger cone-angles and presents diameter errors up to 2 µm.

The reason for the increase of the probing errors of size, when moving away from the central plane of the detector and with cone-angle is described in Figure 5.15 that shows the effect of the cone-beam artifact on the 3D volume for sphere 1 and sphere 8 for set-up 1.

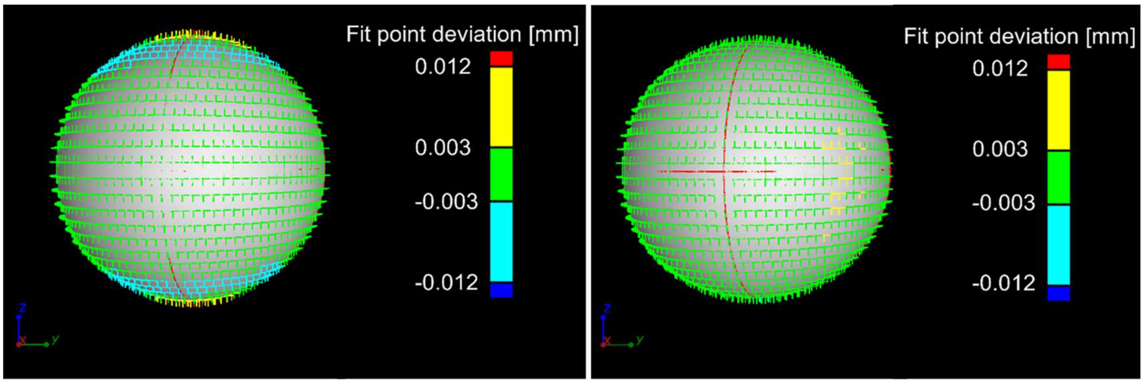

a) b)

Figure 5.15: Effect of the cone-beam artifact on the 3D model of set-up 1 for a) sphere 1 and b) sphere 8. The red lines are representative of the fitted sphere.

As visible, sphere 1 is characterized by pronounced artifacts at the poles of the sphere whereas sphere 8 does not show these significant artifacts.

Figure 5.16 reports the experimental results obtained when measuring the probing errors of form (i.e. sphere form errors) for all the spheres of the ball bar.

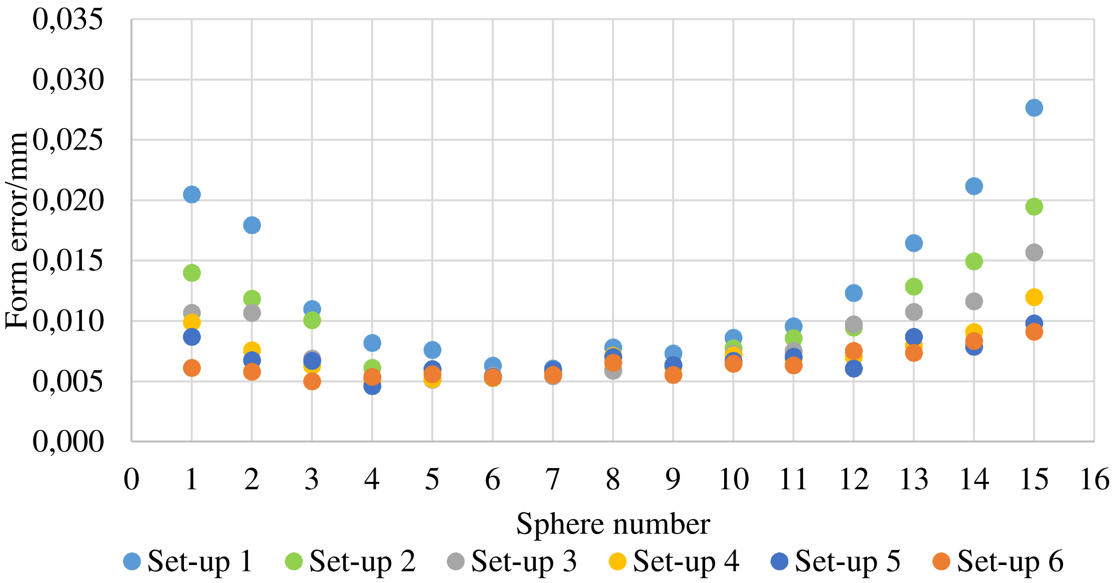

Figure 5.16: Sphere form errors obtained for the CT scans of the ball bar performed in the six different CT scanning set-up. In the horizontal axis of the graph the sphere number is represented, in the vertical axis the computed form errors are reported for the six different set-up.

From the chart it can be seen how the effects of the cone-beam artifacts are highly influencing sphere form errors and increase for spheres further away from the central plane of the detector and with cone-angle. With a high cone-angle of 25.6° form errors reach a maximum value of 28 µm for sphere 15 positioned at the bottom of the detector. Sphere 1 positioned at the top of the detector shows a form error of 21 µm. This difference is attributed to the manual centering of sphere 8 of the ball bar on the central plane of the detector. The measurement results in fact show that probing errors of form are highly sensitive to the influence of cone-beam artifacts and just a slight difference in the positioning of the spheres that should occupy symmetrical positions vertically with respect to the central plane of the detector (e.g. sphere 1 and 15, sphere 2 and 14, etc.) can cause the difference on probing errors of form visible in the chart. The cone-beam artifact effects on form measurements strongly decrease with decreasing cone-angle. When using a 10.7° cone-angle the maximum form error reach 9 µm for sphere 15 at the bottom of the detector, whereas spheres close to the central plane of the detector show form errors smaller than 7 µm.

The effects of cone-beam artifacts on probing errors of form can have a significant influence when performing point-to-point bi-directional measurements. As discussed in section 3.4 when testing the metrological performance of CT systems, the length measurement errors (*E*) are defined as bi-directional measurements. When dealing with samples composed of several combinations of spheres (e.g. ball bar, ball plates, etc.), and thus when measuring sphere distance errors (*SD*) the VDI/VDE 2630-1.3 guideline suggests two methods in order to obtain measurement errors comparable with the bi-directional measurements obtained with the *E* determination. One of these methods prescribes to add the probing errors of forms (and size) to the sphere distance errors. It is thus clear that if the probing errors of form are of significant relevance also the resulting length measurement errors will increase. In general, significant cone-beam artifacts will affect all the bi-directional point to point measurements that involve the selection of fit points on the regions where the artifacts occur. Thus cone-beam artifacts not only have an impact on image quality but as discussed above can significantly affect also the metrological performance of a CT system.

5.3.4. Conclusions

The presence of the cone-beam artifact (or Feldkamp artifact) is an inherent limit of conventional circular trajectories, which besides its effects on image quality causes significant measurement errors when dealing with metrological applications. By performing an experimental investigation using a tactile CMM calibrated ball bar featuring 15 equally spaced ceramic spheres that homogeneously covered the detector surface vertically, the effects of cone-beam artifacts on CT measurements have been investigated for varying cone-angles ranging from 25.6° to 10.7° and for different spheres positions vertically on the detector. The experimental results showed that the probing error of form is the metrological characteristic which is the most highly influenced by the presence of cone-beam artifacts. Cone-beam artifacts increase with the cone-angle and with the sphere distance from the central plane of the detector. For the scanning set-up with a cone-angle of 25.6° maximum form errors reach 28 µm for sphere 15 positioned at the bottom of the detector. When using a smaller cone-angle of 10.7° the maximum form error decrease to 7 µm and the strong trends present when using high cone-angles and showing sphere form errors significantly increasing with the sphere distance from the central plane of the detector are significantly reduced. This suggests to always optimize the scanning parameters in such a way to avoid, as much as possible, to use high cone-angles (and thus the use of short *SDD*) and to avoid positioning the feature to be measured at the top/bottom of the detector especially when the interest is on form measurements since it was shown that they are strongly affected by cone-beam artifacts. However, it was demonstrated that also probing errors of size and sphere center-to-center distances are affected by cone-beam artifacts. With a cone-angle of 25.6° maximum errors of 5 µm and 12 µm were obtained respectively for probing errors of size and sphere distance errors. In particular sphere distance errors exhibit a specific behavior caused by the presence of cone-beam artifacts because of which the distances that involve spheres at top/bottom of the detector and spheres close to the central plane of the detector present the highest errors. In circular cone-beam CT the cone-beam artifact is unavoidable (with exception of the central plane of the detector) and its effects can be significantly reduced using smaller cone-angles and avoiding positioning the feature to be measured perpendicularly to the rotation axis and close to the edges of the detector, but they cannot be completely eliminated.

5.4. Determination of measurement errors on CT helical scanning for coordinate metrology

As experimentally demonstrated in section 5.3 conventional cone-beam circular scanning trajectories present inherent limits which however are unavoidable and produce measurement errors on CT measurements. From here the need to investigate the metrological performances of different CT scanning trajectories in order to advance CT capabilities for industrial metrology. Cone-beam helical scanning is an alternative scanning method that, at the state art, is not fully exploited in industry because of its additional complexity. Helical scanning enables to obtain several advantages compared to traditional circular scanning trajectories as discussed in section 5.2.2. It does not only provide a substantial improvement on image quality when using suitable scanning parameters, but also makes possible to solve measuring tasks that cannot be performed with conventional circular scanning trajectories.

In this section the measurement errors in CT helical scanning are experimentally investigated, in particular the metrological performances and the errors caused by the most relevant helical scanning parameters are determined and compared to traditional circular scanning trajectories [106, 107]. The sensitivity of CT measurement results to the main helical scanning parameters is also analyzed. Finally, an optimization of helical scanning parameters is provided in order to enhance CT measurement accuracy [113].

5.4.1. Experimental investigation

The reference object used for performing the experimental investigations is shown in Figure 5.17 and was provided by North Star Imaging Inc. It consists of a ball bar with six equally spaced ruby spheres with nominal diameter equal to 3.18 mm glued on a carbon-fiber reinforced frame tilted 45°. The object allows measuring 15 sphere center-to-center distances ranging nominally from 10 to 50 mm.

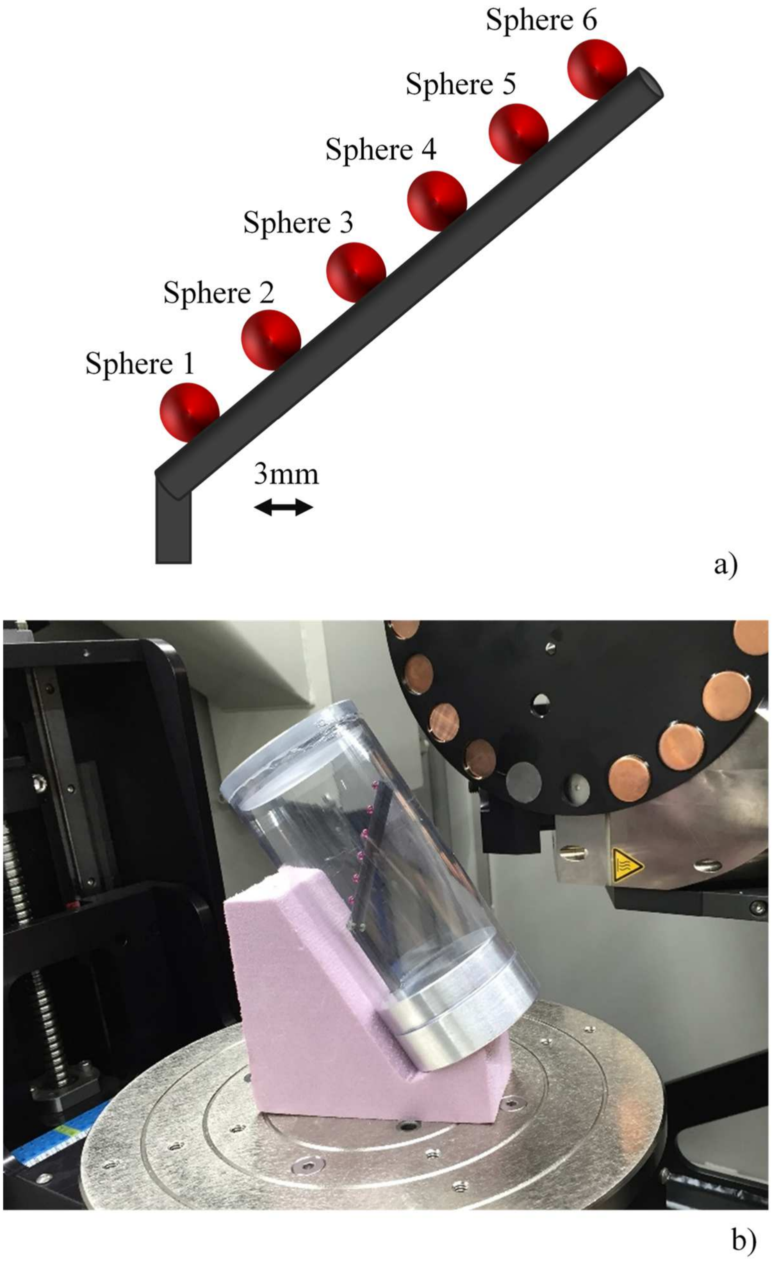

Figure 5.17: a) Schematic representation of the calibrated ball bar used for experimental investigation. b) Position and orientation of the ball bar in the measuring volume [106].

Reference measurements of the object were acquired by means of a tactile CMM equipped with a scanning probe head. Reference values of center-to-center distances between spheres, sphere diameters and form measurements were obtained through repeated CMM measurements. The reference measurements were acquired by TEC Eurolab S.r.l (Italy).

The workpiece was placed inside the measuring volume as described in Figure 5.17 b). Scanning the object in the nominally vertical orientation allows to fully take into account the cone-beam artifact.

CT scans of the ball bar were performed with a NSI CXMM metrological CT system with temperature controlled cabinet and a 225 kV micro-focus X-ray source. Each CT scan was performed with the scan parameters reported in Table 5.3, as a good compromise between scanning time and scan quality.

Voltage	110 kV
Current	180 μA
Exposure time	5fps
Frame averaging	5 fpp
Filtering	0.127 mm Cu
Voxel size	33.6 μm
SDD	536 mm
Cone-angle	25.6°
Detector pixel size	127 μm

Table 5.3: main scanning parameters used for the experimental investigation.

The reference object was scanned with both circular and helical scan trajectories. Three repeated CT scans were performed with conventional scanning mode according to the parameters of Table 5.3 and acquiring 1080 projections. As reported in Table 5.3 a very short *SDD* and thus a large cone-angle of 25.6° were used for the experimental investigations in order to compare conventional circular trajectories and helical trajectories in the most critical scanning set-up.

In order to investigate the influence of the main helical scanning parameters on the metrological performances for CT helical scanning and the effects of their interaction the Design of Experiment (DoE) was applied. The DoE is a known approach that allows considering simultaneously the influence of individual factors and their interactions on a response variable, in this case the metrological characteristics of interest (i.e. the sphere distance errors, the probing errors of size and the probing errors of form). Two relevant factors for helical scanning trajectories, influencing image quality and scanning time, were taken into account: the helical pitch (see section 5.2.1) and the number of projections. For each factor, three levels were considered: low, medium and high. This enabled to investigate the sensitivity of measurement results to the amplitude of each factor [106,113]. Each level was chosen based on a preliminary investigation and in such a way that they homogenously covered the range that is used in real practice. This resulted in a 3^2 factorial design for a total of 9 different scanning set-up. The scanning parameters used for the DoE are reported in Table 5.4.

Scan number	#1	#2	#3
Helical pitch	13.974 mm	13.974 mm	13.974 mm
N of projections	1080	2500	4000

Scan number	#4	#5	#6
Helical pitch	5.588 mm	5.588 mm	5.588 mm
N of projections	1080	2500	4000

Scan number	#7	#8	#9
Helical pitch	3.104 mm	3.104 mm	3.104 mm
N of projections	1080	2500	4000

Table 5.4:Factors and levels used in the design of experiments for helical scanning mode.

Each scan was performed with a randomized order. All CT scans, both circular and helical, were performed in step-wise mode.

5.4.2. Data evaluation

All CT data were reconstructed using NSI efX-ct reconstruction software. A standard FDK algorithm was used for reconstructing the circular scans. The helical scans were reconstructed with an FDK-based algorithm adapted for helical trajectories. No beam-hardening correction was applied. CT volumes were subsequently imported and analyzed by mean of VGStudio MAX 2.2. A local adaptive surface determination was used for all CT scans.

For each sphere a region of interest, consisting of the top hemisphere, was taken into account. This allows removing the part of spheres glued to the rod, which could lead to inaccuracies in measurements, and at the same time to take into account the cone-beam artifact at both poles of the sphere with the configuration of Figure 5.17.

Gaussian least-squares fitting was used for spheres evaluation. Sphere distance errors and probing errors of size and form were calculated according to VDI/VDE 2630 part 1.3.

5.4.3. Results and discussions

In this section the experimental results obtained from CT circular and helical scans are analyzed and compared. The first part of the section focuses on the metrological performance for CT helical scanning and the comparison between helical and circular CT scans, whereas in the second part of the section the influence of the main helical scan parameters on CT measurement errors and their optimization is addressed.

As it was demonstrated in section 5.3 the probing errors of form are the metrological characteristic which is the most influenced by the presence of cone-beam artifacts when using conventional cone-beam circular trajectories. Figure 5.18 reports the probing errors of form obtained from the experimental investigations for each of the six spheres of the ball bar. The results of the DoE for helical scans, and of circular scans are represented and compared.

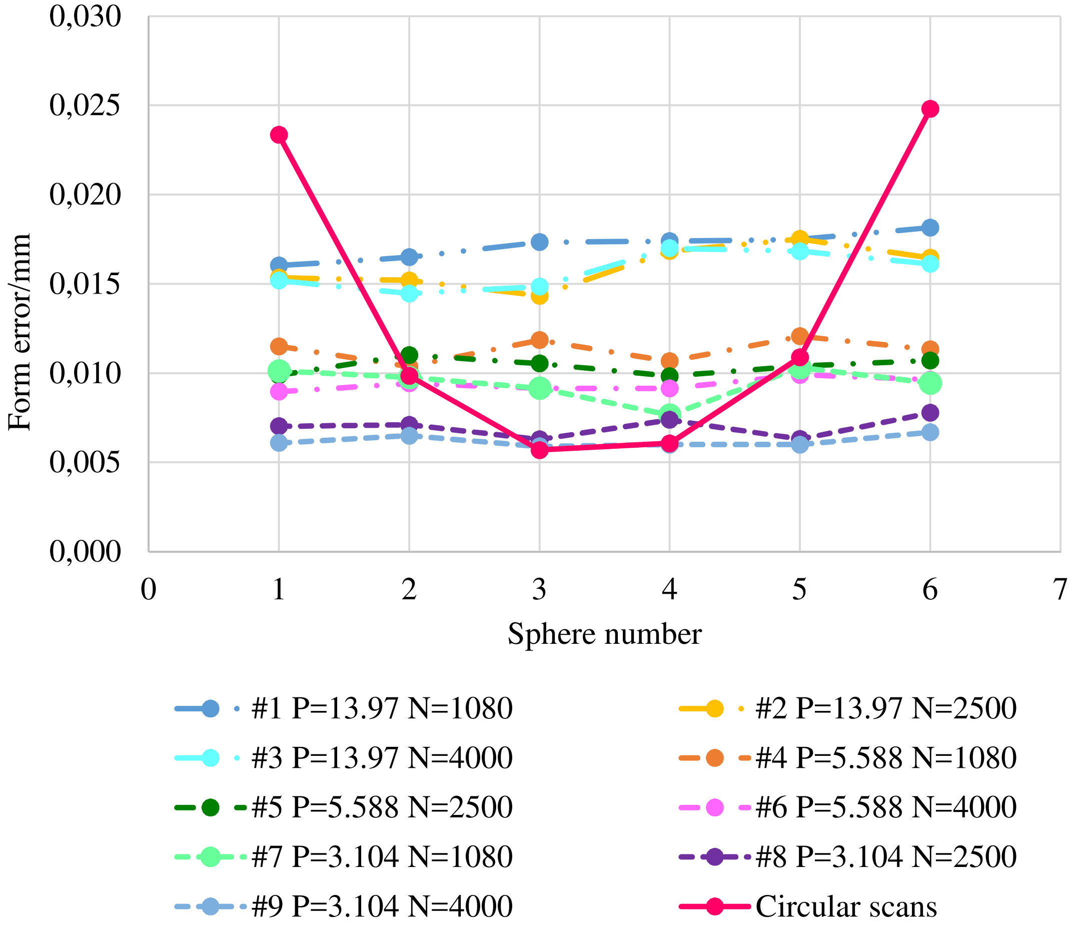

Figure 5.18: Measured probing errors of form for circular and helical scans. In the horizontal axis of the diagram the sphere number is represented, whereas in the vertical axis the computed form errors are reported for the nine CT helical scans set-up and for the traditional circular scans. In the legend of the graph, P stands for helical pitch and N for number of projections [106].

From Figure 5.18 it is evident how, for circular scan trajectories, the probing errors of form computed for the spheres at top and bottom of the detector (respectively sphere 6 and sphere 1) are highly influenced by the presence of the cone-beam artifact and due to the chosen configuration (*SDD* = 536 mm) they reach 25 µm. For spheres closer to the mid plane of the detector (sphere 3 and 4), *PF* are significantly smaller and go down to 6 µm. In circular scan trajectories therefore *PF* are not uniformly distributed, and the influence of the cone-beam artifact depends on the distance from the mid plane of the detector, and on the cone-angle (and magnification). *PF* for helical scans, instead, show a homogeneous distribution along the whole detector, regardless the used helical pitch and number of projections. For all nine helical scans set-up the trend for *PF* is almost a horizontal line. Moreover, for all the nine different helical scanning set-up analyzed and reported in Table 5.4 the maximum *PF* are smaller than the maximum *PF* obtained when using circular scanning trajectories with exactly the same scanning parameters (i.e. *SOD*, *SDD*, X-ray source settings and filtering). This demonstrates the high benefits that helical scanning provides in terms of measuring form errors regardless of the positioning of the feature of interest on the detector. With exactly the same scanning configuration in fact *PF* are reduced from 25 µm (for circular scans with high cone-angle) to 6 µm when using helical scanning. Moreover, in the latter case, uniform probing errors of form can be obtained for all spheres, even for those at bottom and top of the detector [106].

Figure 5.18 shows also the influence of helical pitch and number of projections on *PF*. Depending on the selected helical pitch, the probing errors of form range from 6 µm to 18 µm (respectively for the smallest and the highest helical pitch). With a helical pitch of 13.974 mm, which is more than four times the diameter of the spheres, probing errors of form are on average ca. 17 µm. With a smaller helical pitch of 5.588 mm *PF* are significantly lower reaching 9 µm. The smallest helical pitch of 3.104 mm provides the best results. In this case *PF* is comparable with the ones obtained with circular scans for sphere 3 and 4. In this case however, the probing error does not depend on the sphere position on the detector [106].

The number of projections seems to have a lower effect compared to the helical pitch. For all the three chosen helical pitch, increasing the number of projections decreases the probing errors of form.

Figure 5.19 shows the volumetric model of sphere 6 (the one positioned at the top of the detector) obtained respectively for helical scan set-up 9, namely the set-up with the smallest helical pitch and the highest number of projection, and the conventional circular scanning trajectories. As visible with the use of helical trajectories the cone-beam artifacts disappear in the case of the helical scan reported, whereas the circular scan is characterized by severe artifacts for spheres increasingly further away from the central plane of the detector.

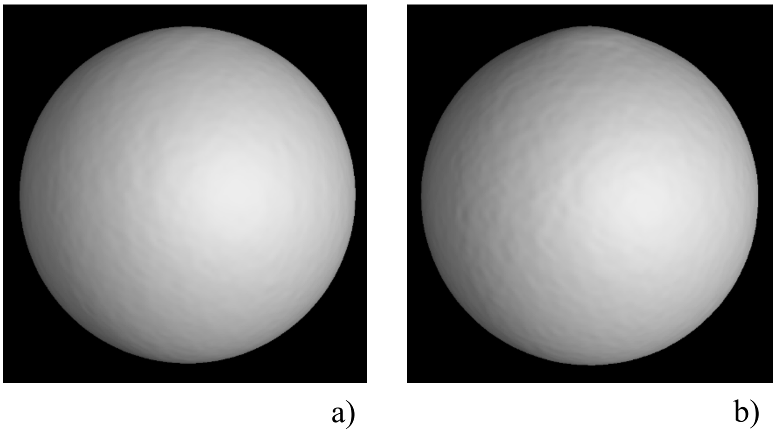
a) b)

Figure 5.19: Comparison of the 3D volumes of sphere 6, obtained for a) helical scanning set-up 9 and b) the conventional cone-beam circular trajectories.

The significant enhancement that helical scanning provides is extremely important also when dealing with bi-directional measurements. As discussed in section 5.3.3 bi-directional measurements can be significantly affected by the presence of cone-beam artifacts. In the case of two points bi-directional measurements on the zones where the cone-beam artifacts are located the bi-directional measurements will be significantly affected by measurement errors. The cone-beam artifact as demonstrated in section 5.3.3

has significant effects on probing errors of form when using cone-beam circular scanning trajectories, this causes the increase of length measurement errors obtained when adding the probing errors (of form and size) to the sphere distance errors. It comes that the benefits that helical trajectories provide can enable significant improvements on CT systems metrological performance.

Figure 5.20 presents the dependency of the measured probing errors of form and the factors helical pitch and number of projections. For each of the nine scanning set-up, the average value of the measured *PF* for the six spheres is computed. Figure 5.20 shows how the helical pitch has the highest influence on *PF*. By decreasing the helical pitch to a value close to the dimension of the characteristic to be inspected, the probing errors of form improve significantly. The number of projections has a smaller influence on the measured probing errors of form. By increasing the number of projections, *PF* improve.

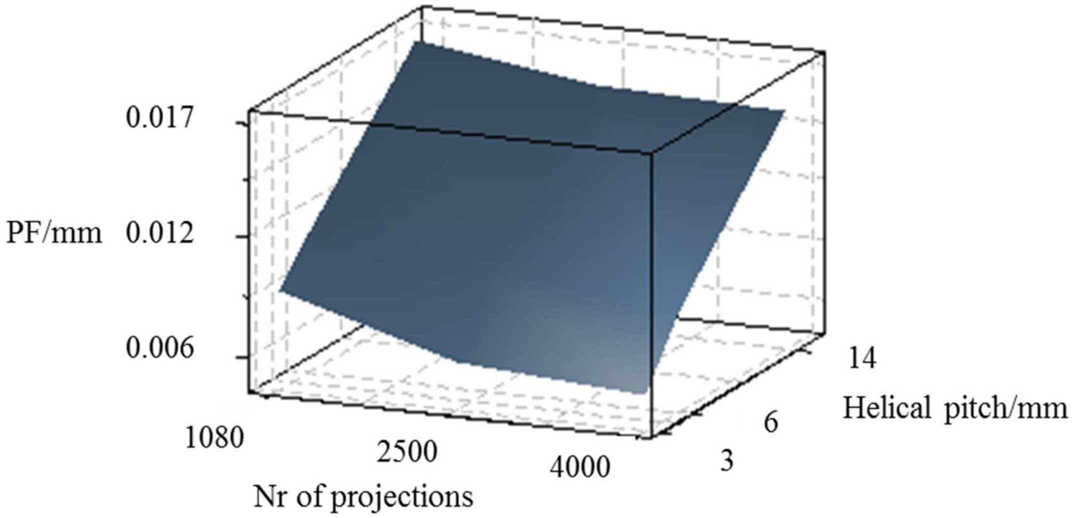

Figure 5.20: 3-D plot of measured probing errors of form, and factors considered in the design of experiments for helical scans [106].

Figure 5.21 and Figure 5.22 represent respectively the average probing errors of size and average sphere center-to-center measurement errors for the nine helical scans set-up investigated. For each of the nine scanning set-up, the average value of the measured *PS* for the six spheres, and the 15 center-to-center measurements are computed. Average probing errors of size are always smaller than 2 µm, average sphere distance errors are also always smaller than ca. 2 µm.

In Figure 5.21 the influence of the factors helical pitch and number of projections on the measured probing error of size is also described.

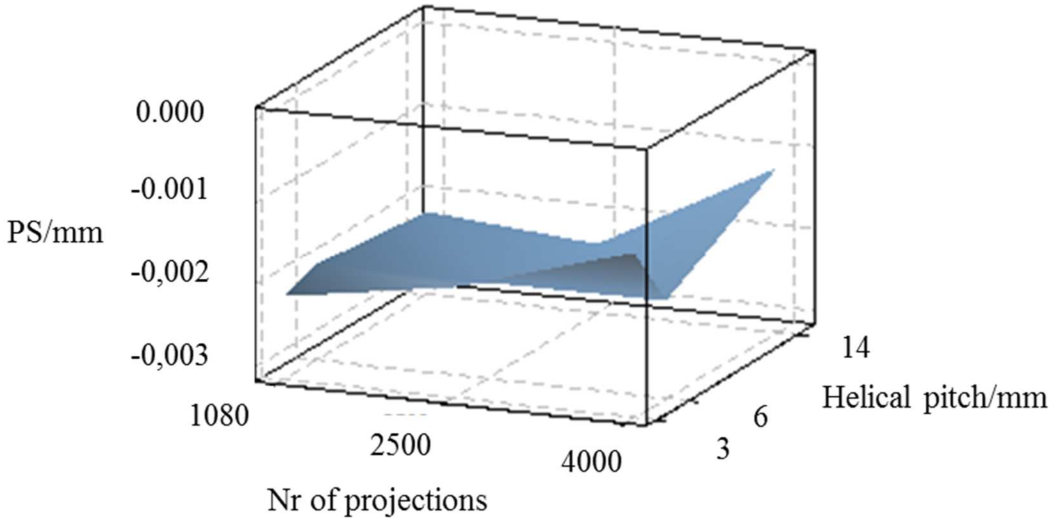

Figure 5.21: 3-D plot of the relationship between PS and helical pitch and number of projections [106].

In Figure 5.21, the 3D plot assumes the shape of a horizontal plane. This means that the helical pitch and number of projections are not significantly influencing the measured *PS*.

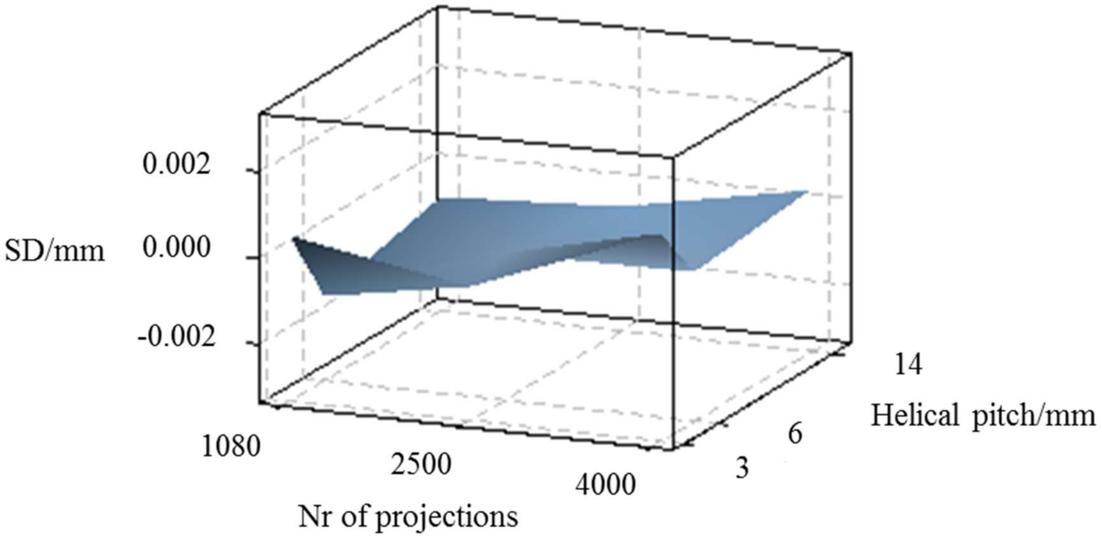

Figure 5.22: 3-D plot of the relationship between length measurement errors and helical pitch and number of projections [106].

Also for sphere center-to-center measurements the 3D plot (Figure 5.22) assumes the shape of a horizontal plane meaning that the helical pitch and number of projections, with the three levels considered in this study, are not influencing the calculated sphere distance errors.

5.4.4. Optimization of helical scanning parameters for accurate coordinate metrology

As demonstrated with the obtained experimental results helical scanning enables several advantages for metrological applications compared to traditional cone-beam circular scans, providing significant enhancements on image quality and decreased measurement errors, especially when dealing with form measurements. Moreover, helical scanning allows also for an improvement on the scanning parameters compared to traditional circular trajectories. It was experimentally demonstrated in fact, that helical scans provide lower measurement errors than conventional cone-beam circular trajectories when dealing with high cone-beam angles and short source-to-detector distances *SDD*s. However, when dealing with CT helical trajectories it has been shown that additional scanning parameters influence the measurement results. In particular, it was experimentally found that the parameters helical pitch and number of projections significantly affect the probing errors of form. It is therefore necessary to select the correct scanning parameters in order to fully exploit CT helical scanning potentials.

In the following, an optimization for helical scanning parameters in order to obtain accurate CT measurements is provided.

As described in Figure 5.18 for all the 9 helical scanning set-up, the trend for *PF* is almost a horizontal line meaning that *PF* are always homogenously distributed along the whole detector regardless of the used helical pitch and number of projections. However, as discussed, the helical pitch and number of projections affect the accuracy of CT helical scans. Specifically, it decreases with increasing helical pitch and decreasing number of projections.

Figure 5.23 describes from a quantitative point of view the effects of the helical pitch on the measured *PF*.

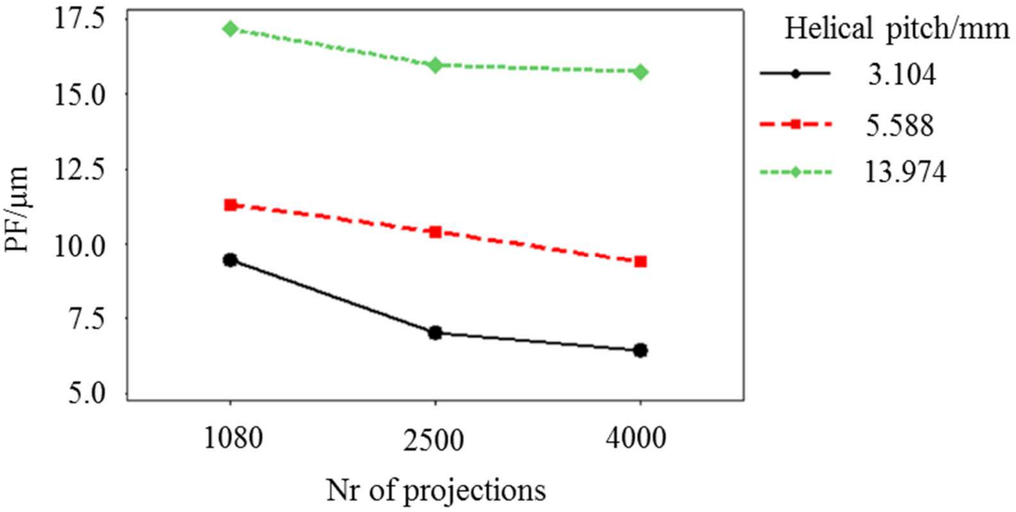

Figure 5.23: Influence of helical pitch on measured PF for helical scans [113].

Each point of the graph represents the average *PF* calculated from the six spheres of the ball bar. With a helical pitch of 13.974 mm, more than 4 times the diameter of the spheres, average probing errors of form range between 17 µm to 16 µm depending on the number of projections. With a smaller helical pitch of 5.588 mm, *PF* are significantly lower ranging from 11 µm with 1080 projections to 9 µm with 4000 projections. The smallest helical pitch of 3.104 mm provides the best results and range from ca. 9.5 µm to 6 µm respectively when using 1080 and 4000 projections. In this latter case, *PF* is comparable with the one obtained with circular scans for spheres in the middle plane of the detector, but for helical scans the probing error does not depend on the sphere position on the detector.

In Figure 5.24, the dependency of measured *PF* and number of projections is reported. Each point of the graph represents the average *PF* calculated from the six spheres of the ball bar.

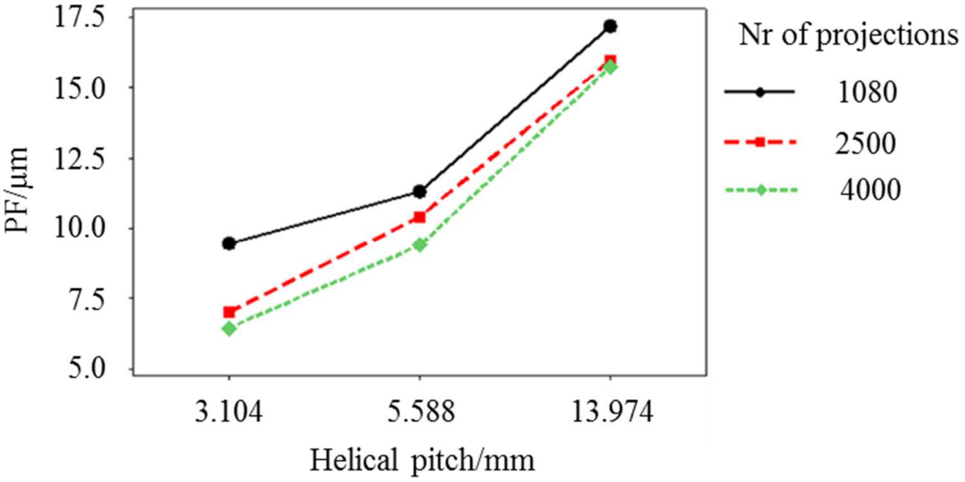

Figure 5.24: Influence on number of projections on measured PF for helical scans [113].

The number of projections has a lower effect compared to the helical pitch. This is visible by noticing that the black, red, and green dataset describing the experimental results show much less variability then in Figure 5.23. For all the three chosen helical pitches, when increasing the number of projections *PF* decreases. This effect is more significant when using a smaller pitch, which means an increased number of revolutions, and therefore a smaller number of projections per revolution (with fixed number of projections). Specifically, the strongest effects of a decreased number of projections occur for set-up 7 of helical scans, characterized by a helical pitch of 3.104 mm and 1080 projections. Nevertheless, the *PF* obtained for set-up 7 are comparable to the ones obtained for set-up 5 characterized by a 5.588 helical pitch and 2500 projections. Also, comparing the values obtained using a 13.974 mm pitch and 4000 projections, and those using a 5.588 mm pitch and 1080 projections, differences around 4 µm are obtained. Scanning times in the latter case are significantly reduced. The use of a small helical pitch therefore, is more effective in reducing the probing errors of form than the number of projections. Using a high number of projections and a high helical pitch is not sufficient for reducing the probing errors of form. The experimental results therefore suggest that it in order to achieve a good compromise between scanning time and measurement accuracy it is effective to optimize the scanning parameters in a way to decrease the helical pitch (which increases the scanning time) to a value similar to the dimension of the characteristic to be inspected, and to decrease the number of projections (which decreases scanning time) to a suitable value for the given helical pitch, avoiding undersampling. This gives a good compromise between the accuracy and scanning time [113].

5.4.5. Conclusions

In this chapter, the use of CT helical scanning for coordinate metrology was studied. CT helical scanning in fact is an alternative scanning method that, when using suitable scanning parameters can provide significant advantages compared to traditional circular scanning trajectories. Despite its well-known use in the medical field, its use is under-utilized in industrial practice, specifically for industrial metrology purposes. This is mainly because of the additional complexity that this kind of technology requires. An experimental investigation using a tactile CMM calibrated ball bar consisting on six equally spaced ruby spheres was designed and performed in order to investigate the metrological performances of CT helical scanning and compare them to the ones of conventional cone-beam circular trajectories. For the purpose of the study, a short source-to-detector-distance and a high cone-angle of 25.6° were investigated in order to study the measurement accuracy of both technologies in the most critical situation. The Design of Experiments (DoE) method was also applied in order to investigate the influence of the main helical scanning parameters on the metrological characteristics sphere distance errors *SD*, probing errors of size *PS* and probing errors of form *PF*. The use of helical trajectories in fact, implies also the presence of additional scanning parameters that influence the accuracy of CT measurements. Nine helical scanning set-up characterized by three different helical pitch (3.104 mm, 5.588mm and 13.974 mm) and three different number of projections (1080, 2500 and 4000 projections) were thus investigated by performing repeated CT scans. The experimental results proved that helical scanning can perform better than conventional circular scanning. Strong improvements can be obtained not only on image quality but also on measurement accuracy especially when dealing with form measurements.

The use of helical scanning trajectories reduces significantly the measured probing errors of form. With exactly the same scanning configuration, *PF* are reduced from 25 µm (for circular scans with high cone-angle) to 6 µm when using helical scanning. Moreover, for all the nine investigated scanning set-up, *PF* are not dependent on the location of the sphere from the mid plane of the detector and uniform probing errors of form can be obtained for all spheres, even for those at top and bottom of the detector. When using the smallest helical pitch experimentally investigated, average *PF* equal to 6 µm are present whereas they increase to average values of 17 µm when using a helical pitch of 13.974 mm. The helical pitch has a strong influence on the measured *PF,* when decreasing the helical pitch the probing errors of form decrease. The influence of the number of projections is less pronounced than the one of the helical pitch, increasing the number of projections decreases the probing errors of form. The experimental results proved that by using a helical pitch of the same dimensions of the characteristics to be inspected, a significant enhancement of helical scanning accuracy is achieved. In particular, the use of a small helical pitch is more effective in reducing the probing errors of form than the number of projections. Using a high number of projections and a high helical pitch is not sufficient for reducing the probing errors of form. In order to achieve a good compromise between measurement accuracy and scanning time, it is therefore suggested to decrease the helical pitch (which increases the scanning time) to a value similar to the dimension of the characteristic to be inspected, and to decrease the number of projections (which decreases scanning time) to a suitable value for the given helical pitch, avoiding undersampling.

Probing errors of size and sphere distance errors were also calculated. Experimental results show no significant influence of the parameters helical pitch and number of projections for the experimentally tested conditions.

The experimental investigations therefore prove that helical scanning, with appropriate scan parameters, can perform even better than traditional circular scans with a strong improvement on image quality and measurement accuracy. This leads to strong benefits on several industrial applications, from non-destructive testing where image quality is important for the visual detection of crack, and defects, to metrological application where high measurement accuracy is needed. Moreover, besides the improvements on measurement accuracy and image quality, helical scans provide several other relevant benefits such as the possibility to scan elongated objects in one single scan, and the enhancement of scan resolution (thanks to the possible reduction of the source-to-object distance). These proven advantages confirm the high importance and potentialities of helical scanning for metrological application.

Chapter 6

Effects of surface roughness on X-ray CT dimensional measurements

In this chapter, the influence of surface roughness on CT dimensional measurements is investigated. Surface roughness is an important influence quantity, the study of which is fundamental for CT measurement uncertainty determination and thus for traceability establishment and for CT measurement accuracy enhancement. Every industrial component in fact is characterized by a specific surface roughness that is linked to its functional behavior. The understanding of the effects of surface roughness on CT dimensional measurements, therefore, is necessary for using CT systems in coordinate metrology. The chapter is mainly divided into five parts. Section 6.1 and 6.2 respectively provide a short introduction and a brief overview of CT and tactile CMM measuring principles. Section 6.3 reports the experimental studies performed on specifically designed reference objects developed in order to investigate the influence of surface roughness on CT dimensional measurements on samples characterized by periodic roughness profiles. Then, section 6.4 reports the design concepts and the implementation of the developed simulation analyses, and the obtained measurement results which also compared to the experimental analyses. Finally, section 6.5 provides the conclusions on the effects of surface roughness on CT dimensional measurements on periodic roughness profiles.

6.1. Introduction

Over the last years, X-ray computed tomography has been increasingly used as an advanced dimensional measuring technique. Its application for dimensional quality control purposes involves a wide variety of applications and industrial sectors of modern industry. In fact, thanks to the unique advantages that CT provides compared to traditional measuring techniques, dimensional analysis in a non-contact and non-destructive way are enabled, especially on difficult to access geometries, including internal features on a wide variety of components.

CT dimensional quality control is performed on several stages of the different products cycles, from the design stage, in order to optimize product development, to the end-life of products, e.g. to analyze the causes of failures.

Thanks to CT application in all of these different phases and in extremely different sectors and markets, it comes that the variety of products that undergo CT dimensional quality control is extremely wide and presents different designs, features, properties and functions. Moreover, depending on the application each part is characterized by specific tolerances.

In particular, each surface of every industrial component is characterized by a specific surface texture, obtained by one or a sequence of manufacturing processes each of them giving a peculiar surface topography. Surface topography is extremely important for industrial parts because it is connected to the functional behavior of the component. For this reason, industrial components are characterized by a wide variety of surface roughness and surface finishing, depending on which are their functions.

The components that are CT scanned thus, are characterized by extremely different surface topographies and surface roughness which often can be very high. This is the case for example of castings and additive manufacturing (AM) parts. In particular CT and AM are strictly connected. In fact, while AM technologies enable to produce high-complex internal and external geometries, CT makes possible to analyze in a non-destructive way these components that often are impossible to analyze with conventional measurement techniques. Due to inherent characteristics of AM techniques, AM components are often characterized by high surface roughness that can reach several tens of microns.

As described in chapter 3, the accuracy of CT dimensional measurements is affected by multiple error sources [63,82,114], one of them being the surface roughness of the scanned parts. In particular, parts with highly rough surfaces – e.g. castings and additive manufactured (AM) parts – can cause significant deviations between CT and tactile dimensional measurements, due to the different surface filtering characteristics of the two measuring methods [115].

Surface roughness moreover, can cause a considerable increase of uncertainty especially for parts characterized by high surface roughness [82,114]. The determination of roughness effects on CT dimensional measurements, therefore, is crucial for CT applications. Determining the influence of surface roughness on CT dimensional measurements in fact, is necessary for CT measurement uncertainty determination which is an essential requirement to obtain CT measurement traceability. Moreover, the knowledge of roughness specific effects on CT measurements enables to enhance CT measurement accuracy.

At the state of the art, there are no internationally accepted standards for CT performance verification and measurement uncertainty determination. As described in section 3.3 the German guidelines VDI/VDE 2630-1.3 [65] and VDI/VDE 2630-2.1 [66] are available. While VDI/VDE 2630-1.3 covers the performance verification of CMMs with CT sensors, and it is not specifically intended to address surface roughness effects on CT measurements, VDI/VDE 2630-2.1 describes the determination of the uncertainty of CT measurements. In particular, the approach there described is based on the experimental uncertainty determination approach outlined in ISO 15530-3 [89] for coordinate measuring machines (CMMs) which can be adapted also to CT, as proposed in several previous works [48,82,88,91,116]. According to the method specified in ISO 15530-3, the uncertainty component associated with the influence of the workpiece (e.g. surface roughness), namely u_w, contributes to the expanded uncertainty. It comes that roughness effects on CT dimensional measurements must be quantified and taken into account for measurement uncertainty determination.

Schmitt and Niggemann [82], assessed the uncertainty of CT dimensional measurements for a sandblasted aluminum workpiece with roughness value *Rz* in the range of 6 µm. There, the authors proposed to estimate surface roughness effects on the basis of averaged *Rz* (maximum peak to valley height of the profile in the sampling length) measurements and assuming that the surface lies half within the part material. A rectangular distribution was assumed and an uncertainty contribution of 0.6/2 times the mean *Rz* was calculated. Bartscher et al. [91] stated that an uncertainty contribution in the order of *Rz*/2 can be considered as an upper limit, and estimated effects of less than a quarter of *Rz* for a workpiece with *Rz* up to 134 µm. Boeckmans et al. [117] and Salzinger et al. [115] reported that deviations between CT and tactile dimensional measurements are presents.

In this chapter, the influence of surface roughness on CT dimensional measurements on periodic roughness profiles is investigated. The aim of the work is to study the nature, quantify and model the effects of surface roughness on CT dimensional measurements, and to determine the measurement errors due to surface roughness, with respect to traditional tactile CMM measurements that are often used as reference measurements in industrial practice, and correlate them with surface roughness parameters. In particular, since the effects of surface roughness for tactile measurements have already been studied [118], this work focuses on the effects for CT measurements, considering the deviations from tactile measured points that ideally lie only on the peaks of the measured surface. The influence of surface roughness on CT dimensional measurements is investigated considering the combined effects of surface morphology and surface filtering characteristics of CT measurements. In fact, as described above CT scanned workpieces are characterized by a wide variety of surface topographies and surface roughness, and are typically analyzed with different CT scans resolutions depending on their size and on the requirements of the measurement tasks to be performed. This contributes to further complicate the determination of surface roughness effects which thus depend on several variables. The modelling of roughness effects on CT dimensional measurements for different surface topographies and roughness, and for various CT scans resolution enables for a knowledge-based roughness error correction which is extremely beneficial for industrial applications, to enhance CT measurement accuracy and for CT measurement uncertainty establishment, a crucial step towards CT measurement traceability. The possibility to correct for surface roughness effects is shown and discussed, and measurement uncertainty is calculated according to the experimental approach derived from ISO 15530-3.

Section 6.2 provides an overview of the main concepts of surface texture and definitions, as well as on the comparison between CT and tactile CMM data. Section 6.3 and 6.4 deal respectively with the experimental and simulation analyses carried out to investigate surface roughness effects on CT dimensional measurements performed on periodic roughness profiles.

6.2. Deviations between CT and tactile CMM measurements due to surface roughness

6.2.1. Surface texture and definitions

Real surfaces are not perfect and present some irregularities or errors. Ideal surfaces in fact, are just theoretical and perfect surfaces that exist on the technical drawings and with boundaries the nominal dimensions of the workpiece. In real practice however, errors occur and deviations between real and ideal surfaces exists. These errors can be grouped in two categories, macro-geometrical errors (i.e. form and position errors) or micro-geometrical errors (e.g. surface waviness and roughness).

Surface texture is described by the repetitive or random deviations, caused by these micro-geometrical errors, from the ideal surface. The texture of a surface is obtained as a consequence of one or a sequence of manufacturing processes. Thus the surface texture properties depend on the specific production process and process parameters and are strictly related to the function of industrial components. Sequences of different manufacturing processes in fact are typically performed in order to confer to the surface the desired surface finishing which is proper for the functional behavior of the industrial part.

In relation to the errors that can affect a surface, when dealing with surface texture measurements filters are used to separate form, waviness and roughness. Specifically, waviness refers to the long wavelength components while roughness refers to the short wavelength and high frequency components. Figure 6.1 describes the separation of the surface components by mean of their different wavelengths.

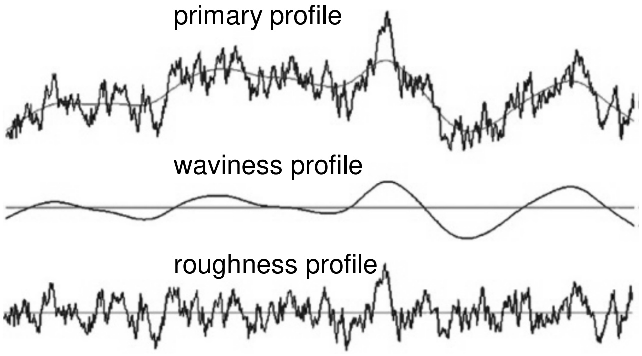

Figure 6.1: Description of surface components separation by mean of their different wavelengths [101].

Three filters (see Figure 6.2) with different cut-offs are typically used in order to distinguish between the surface long and short wavelength components.

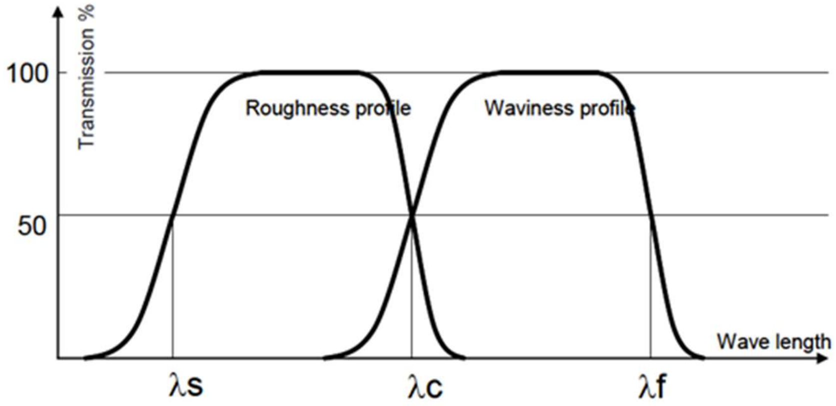

Figure 6.2: Separation of surface components with different wavelengths. Surface roughness is characterized by short wavelength and high frequencies components [119].

λ_f is used to separate waviness and longer wavelength components, λ_c separates waviness and roughness components. Finally, λ_s is used to cut-off components with wavelengths shorter than surface roughness.

In the following the focus is on surface roughness, and surface roughness parameters and definitions that are used throughout the following of the chapter and are essential to investigate the effects of surface roughness on CT measurements. All the following definitions are provided with reference to the roughness profile, i.e. after form removal and after suppressing the waviness components (long wavelength components).

Surface texture parameters are used to give the surface texture a quantitative value, and can be divided into amplitude parameters and spacing parameters (and hybrid parameters). Here in the following the surface texture parameters of interest for this work are described according to ISO 4287: Geometrical Product Specifications (GPS), Surface texture: Profile method – Terms, definitions and surface texture parameters [120].

Amplitude parameters

Maximum profile peak height, *Rp*
The *Rp* parameter is defined as the largest profile peak height within the sampling length.

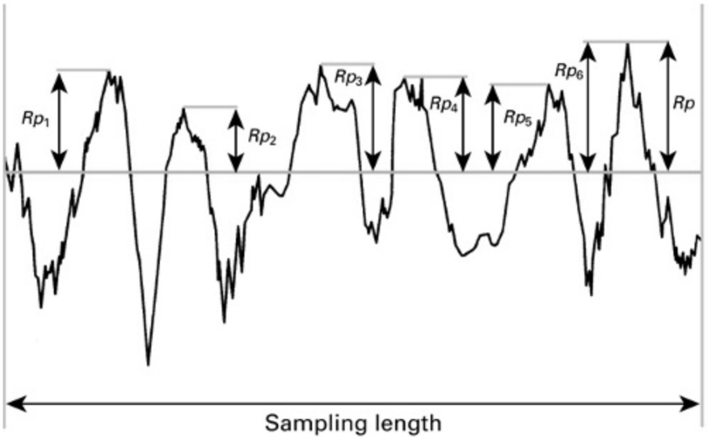

Figure 6.3: Definition of the Rp roughness parameter [101].

Maximum profile valley depth, *Rv*

The *Rv* parameter is described as the largest profile valley depth within the sampling length.

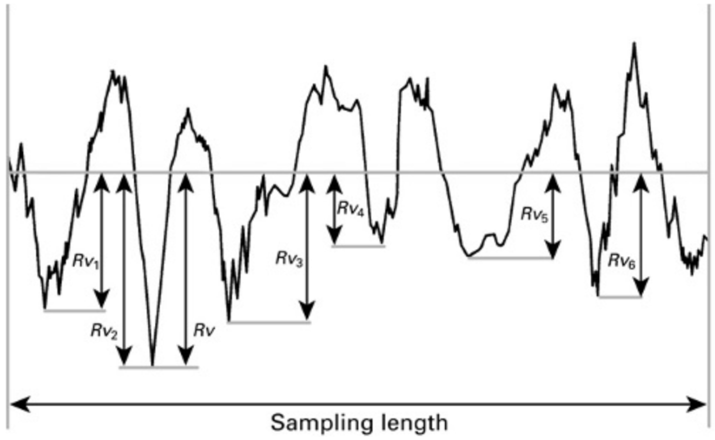

Figure 6.4: Definition of the Rv roughness parameter [101].

Maximum height of the profile, *Rz*

The *Rz* parameter is given by the sum of the *Rp* and *Rv* parameters within the sampling length.

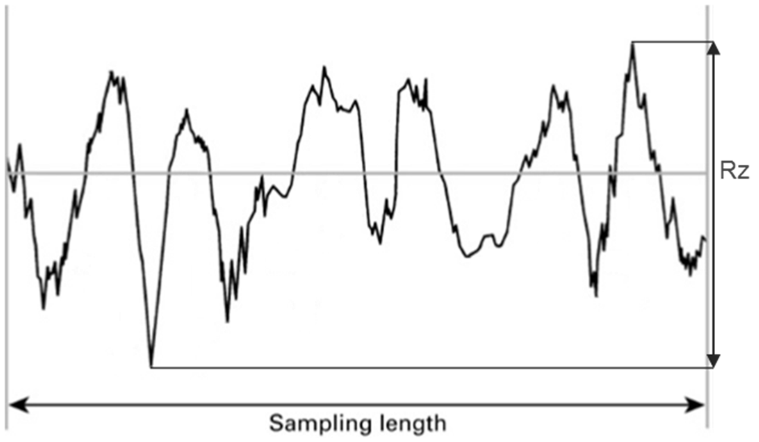

Figure 6.5: Definition of the Rz roughness parameter. Adapted from [101].

Mean deviation of the profile, *Ra*

The *Ra* parameter is defined as the arithmetic mean of the absolute ordinate values within the sampling length. Figure 6.6 provides the graphical derivation of the *Ra* parameter.

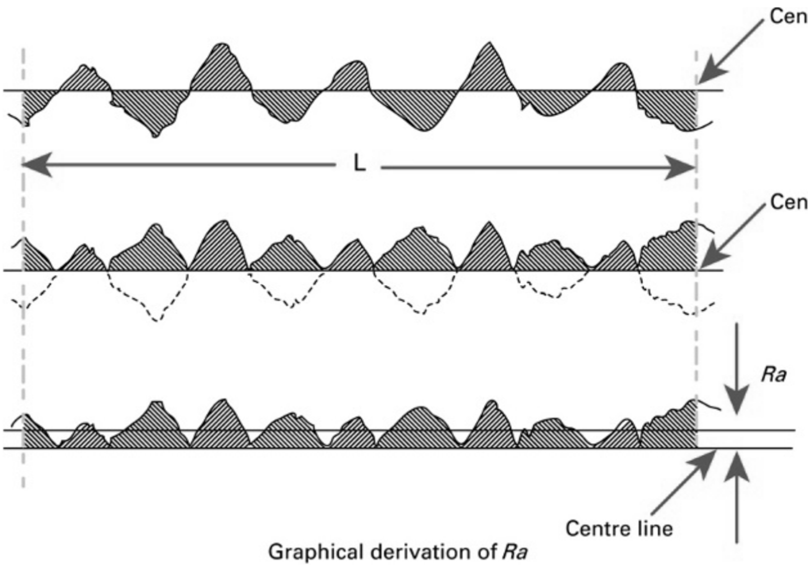

Figure 6.6: Definition of the Ra roughness parameter [101].

<u>*Spacing parameters*</u>

Mean width of the profile elements, *RSm*

RSm describes the mean value of the profile elements widths within the sampling length. A profile element width *Xs* is defined as the length on the mean line section containing a profile peak and adjacent valley.

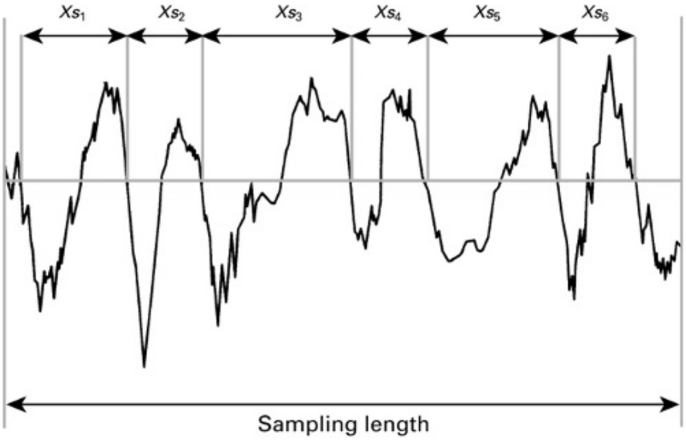

Figure 6.7: Definition of the RSm roughness parameter [101].

However, amplitude and spacing parameters are not sufficient to uniquely describe the surface texture and its properties. In fact, parameters like *Ra*, *Rz*, *RSm* etc. do not give any information about the shape of a surface. This is represented in Figure 6.8 were three different surfaces characterized by the same period, *Ra* and *Rz* parameters are reported.

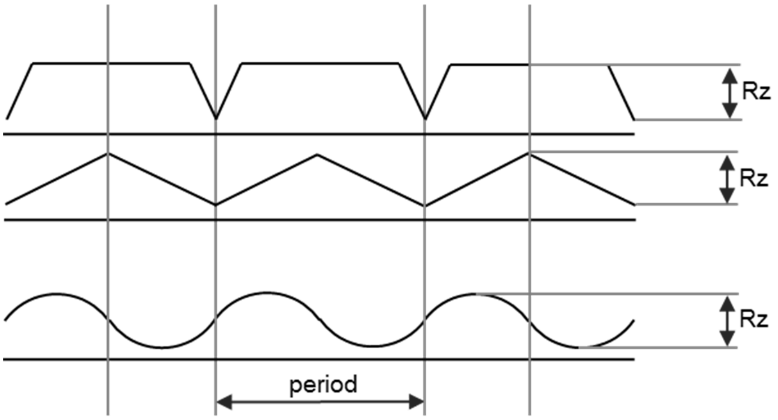

Figure 6.8: Representation of three different surfaces characterized by the same Ra, Rz and period but with extremely different shapes.

As visible from Figure 6.8 the three surfaces represented are characterized by extremely different shapes, and thus will have different functional behaviors.

In order to describe the shape and the material distribution of a surface the profile parameters described so far are not enough.

For this purpose, the Material ratio curve, also known as Abbot-Firestone curve provides substantial additional information on a surface.

Material ratio curve or Abbot-Firestone curve

The Abbot-Firestone curve represents the material ratio of the profile as a function of level, as reported in Figure 6.9.

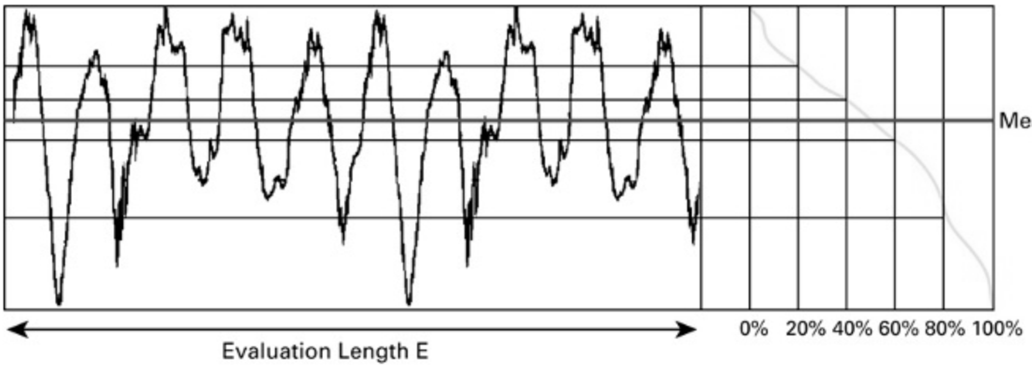

Figure 6.9: Abbot-Firestone curve [101].

The material ratio is given by the ratio of the bearing length to the evaluation length and it is expressed as a percentage. The bearing length is defined as the sum of the section lengths, at a certain level on the profile, obtained intersecting the profile with a drawn line parallel to the mean line. The bearing length and thus the material ratio are 0% when the line intersects the profile at the highest peak, and 100% when the line intersects the profile at the deepest valley.

For its definition thus, the material ratio curve describes the way in which the bearing length varies with the considered level (i.e. height) of the profile. This enables to distinguish the different shapes of the profiles. The Abbot-Firestone curve thus will be used in the following of this chapter in order to characterize the different surfaces investigated.

6.2.2. Comparison between CT and tactile CMM measuring principles

While dealing with the application of computed tomography for dimensional metrology, tactile CMM measurements are often used as reference values and compared to CT measurements [47]. In fact, due to the well-established knowledge and the presence of internationally accepted standards for CMMs performance verification [53] and determination of measurement uncertainty [89], tactile CMMs can provide traceable measurements and several methods exist for accuracy enhancement [46]. However, the different measuring principles on which tactile CMMs and CT systems rely on cannot be neglected. Due to the different acquisition principle, surface roughness may produce significant deviations between tactile CMM and CT measurement results.

Tactile CMMs acquire points by means of the mechanical contact between the probe stylus tip and the surface of the workpiece under investigation as reported in Figure 6.10. Probing points can be acquired by different strategies (e.g. point by point or in scanning mode), with a point density which depends on user settings.

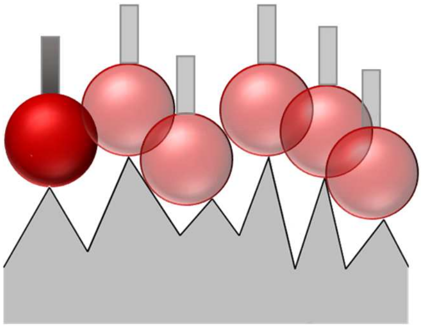

Figure 6.10: Tactile CMMs measuring principles. Measurement points are acquired by mean of the mechanical contact between the probe tip and the surface of the work piece.

On the other hand, CT is an imaging technique and its measuring principle is based on the attenuation of X-rays. A 3D voxel model is reconstructed from the recorded X-ray projections, and a grey value is attributed to each voxel depending on the X-ray absorption coefficient of the material and the path followed by the X-rays, as schematically described in Figure 6.11.

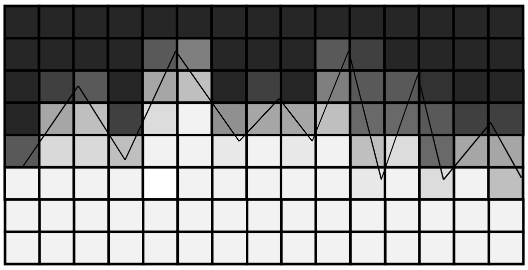

Figure 6.11:X-ray CT measuring principle.

For tactile CMMs measurement thus, due to the finite dimensions of the probe, the probe itself produces a mechanical low-pass filtering on the surface of the component, which causes the high frequencies components (e.g. surface roughness) to be cut. The mechanical filtering effect increases with the size of the probe. This means that, the acquired probing points that are used by the CMM evaluation software to compute the geometrical elements of interest (e.g. cylinders, circles, spheres, etc.) cannot reach the valleys of the profile. For tactile measurements, therefore, the acquired profile is shifted towards roughness peaks.

Computed tomography, instead, makes use of a voxel-based spatial discretization. In this case, when using a sufficiently small voxel size compared to the measured surface roughness, as well as a small focal spot size, CT takes into account also smaller wavelengths. When performing dimensional measurements on the CT volume, therefore, the fit points used for the evaluation of the geometrical elements can be distributed on the whole profile and thus allowing to virtually probe also points on the valleys of the profile. Surface roughness, therefore, may produce significant deviations between tactile CMM and CT dimensional measurements.

6.3. Experimental investigation on the effects of surface roughness on CT dimensional measurements

In this section, the experimental campaigns designed and conducted in order to determine the influence of surface roughness on CT dimensional measurements is presented.

6.3.1. Design and production of dedicated test objects

In order to investigate the influence of surface roughness on CT dimensional measurements on periodic surfaces a set of dedicated test objects was specifically designed and manufactured. As discussed in section 6.1 the aim of the work is to study and quantify the effects of surface roughness on CT dimensional measurements for different surface morphologies, surface finishing, and voxel sizes and to correlate these effects to the surface roughness parameters of the scanned part. In section 6.2.1 it was described how the roughness parameters (e.g. *Rz*, *RSm*, etc.) can provide a quantitative value to describe the surface finishing of a component however they do not give any information on the shape of the surface under investigation. The Abbot-Firestone curve instead provides the additional information to describe the shape and bearing properties of a surface.

For the experimental investigations, different samples were manufactured using two very different production processes, i.e. Fused Deposition Modelling (FDM) and turning, and a combination of these technologies. These processes were chosen in order to obtain samples characterized by significantly different roughness profiles, surface finishing and material distributions, for experimentally investigating the influence of different surface topographies.

In the following, the dedicated test objects designed and manufactured for the experimental investigations are presented and described.

Fused Deposition Modeling Test object

Fused Deposition Modeling (FDM) is an additive manufacturing technique that enables the production of components layer by layer by the extrusion of a heated filament. The FDM process basically consists of a preparation phase in which the user imports on the 3D printer software the CAD model (an STL model) of the part. Subsequently the STL model is processed in order to define the orientation of the object, which also defines the direction of the layers deposition, to determine the slices and the path for the extrusion of the filament, and the zones of the sample which require the use of some supporting material, which will be removed after production. After this preparation phase the production takes place and the material (polymer or metal) is heated and extruded from a nozzle which moves according to the path previously determined and deposits the material in order to form the part.

The FDM technique was selected for the production of the sample as it enables to obtain periodic surfaces characterized by high surface roughness and with high bearing curves i.e. the material is more distributed on the peaks. Ideally in fact, as described in Figure 6.12, the theoretical FDM profile is composed of semi-circumferences with period equal to the diameter of the wire used for the production.

Figure 6.12: Theoretical FDM profile. Ideally a periodic profile is generated with period equal to the diameter D of the extruded wire.

As visible in Figure 6.12, the material is more distributed on the peaks, whereas narrow and sharp valleys are present. The FDM process leads to high surface roughness due to its inherent principles. It was thus purposefully selected in order to study the influence of surface roughness on CT measurements where surface roughness is a predominant influence quantity. From preliminary investigations conducted on various test samples experimentally produced it was observed that with the FDM technology it is also possible to obtain surface roughness in the order of $Rz>100$ µm.

In this work, a Stratasys Dimension 1200es, see Figure 6.13, was used for the manufacturing. This 3D printer is capable of manufacturing samples with maximum dimensions of 254 mm x 254 mm x 305 mm by using a thermoplastic wire made of ABS plus.

Figure 6.13: Stratasys Dimension 1200es used for the experimental investigation.

The cylindrical test object reported in Figure 6.14 was thus produced by using a thermoplastic ABS plus wire with a nominal diameter of 0.330 mm.

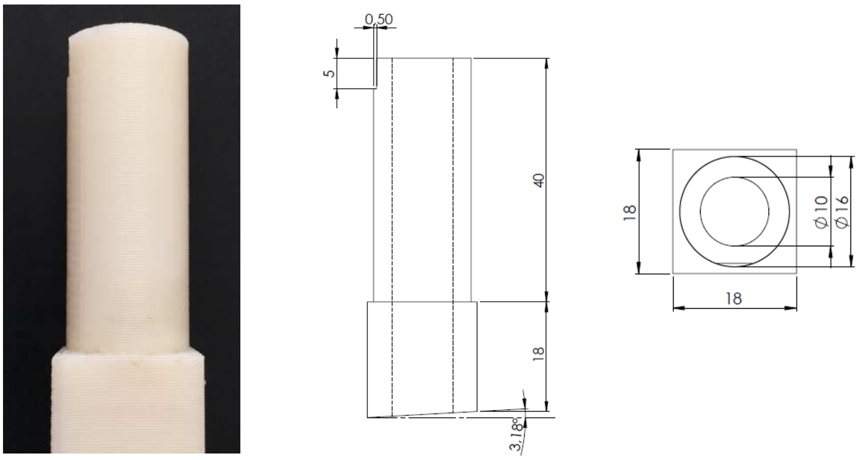

a) b)

Figure 6.14: Test object designed and manufactured for the experimental investigation. a) image of the test object after production and removal of supporting materials, b) technical drawing of the test object with nominal dimensions.

As visible from Figure 6.14 the geometry of the produced test object consists of a hollow cylindrical body with a cubical structure at the bottom, and with the production layers oriented perpendicularly to the axis of the cylinder. The design considerations that led to the development and production of the object of Figure 6.14 are described in the following. The production of a hollow cylindrical sample was chosen for its simple geometry which enables at the same time to measure geometrical characteristics such as diameters of cylinders and to guarantee the access to internal and external geometries if properly dimensioned. The aim of the study, in fact, is to determine the effects of surface roughness on CT dimensional measurements; therefore, it is essential that the test object presents consistent geometrical characteristics to be measured with CT and tactile CMM techniques. Moreover, in order to characterize its surface morphology, the test object also requires to be measured by a roughness profiler, therefore it is essential that all the geometries and surfaces of interest are accessible. It was decided to produce the sample in the vertical direction (i.e. with layers deposited one on each other vertically) in order to properly investigate the effects of surface roughness on CT dimensional measurements of diameters.

In order to guarantee an easy fixturing of the object a cubical zone was also designed specifically for the fixturing. The inferior base of this cubical structure was also inclined by an angle α in order to facilitate the positioning during CT scans. As described in section 5.2.2 in fact, planar surfaces oriented perpendicularly to the rotation axis suffer from cone-beam artifacts. In order to reduce the presence of these artifacts planar surfaces should be positioned in an inclined orientation.

As discussed before, one of the aim of the work is to investigate the influence of the voxel size on the effects caused by surface roughness on CT dimensional measurements. The dimensions of the object were thus designed by taking into account the dimensional constraints given by the geometrical magnification and consequently the voxel sizes wanted to achieve with the CT system used for the experimental investigations, this information is provided in section 6.3.2. Moreover, besides the constraints given to achieve the voxel sizes of interest, external and internal diameters of the cylinder were chosen in such a way to guarantee a sufficient thickness of material. A proper dimensioning in fact is necessary for a good optimization of CT scanning parameters and CMM measurement procedures. ABS in fact is a low density material that can be penetrated by X-rays of relatively low power. The thickness of the hollow cylinder was therefore dimensioned in order to have a good contrast and avoid the use of extremely long exposure times (which increase the scanning time) but at the same time in order to avoid having too thick sections that would require the use of higher X-ray powers that increase the focal spot size.

After the production of the test object, CMM reference measurements and tactile roughness measurements were performed.

CMM measurements were performed in a laboratory temperature controlled environment at 20 °C. The workpiece was let stabilize in order to achieve the thermal stability. The temperature of the workpiece was kept under control during the CMM measurement process by mean of thermocouples. Repeated CMM measurements were performed with a tactile CMM, Zeiss Prismo Vast with MPE of length: $2 + L/300$ mm, where L is the length in mm. Circular probing paths, orthogonal to the sample axis, and at different heights of the sample were acquired in scanning mode both on external and internal regions of the workpiece.

Tactile roughness measurements were acquired with a Zeiss TSK Surfcom 1400. Roughness measurements, perpendicular to the sample layers, were performed using cut-off filters according to ISO 4288 [121]. Repeated measurements were collected on different zones of the workpiece, both on internal and external regions in order to well characterize the sample surface. Average Rp values of 37 µm and Rz values of 119 µm were obtained for the external surface and average values of Rp values of 38 µm and Rz values of 121 µm were obtained for the internal surface.

Turned Test object

In order to investigate the influence of surface roughness on a completely different surface morphology than the one generated by the FDM process, the sample described in Figure 6.15 was produced by turning, using a CNC lathe.

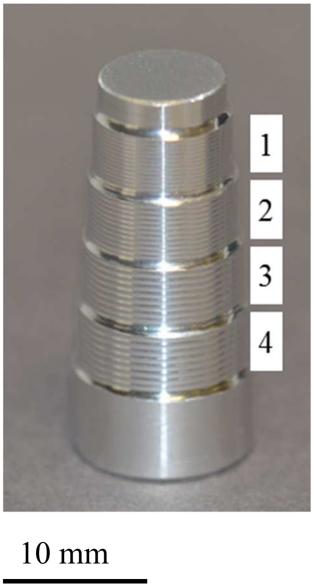

Figure 6.15: Turned sample produced for the experimental investigations.

The sample is made of aluminum, which is relatively easy to penetrate with X-rays and features four different sections characterized by different roughness parameters. Each section was produced with different diameters ranging nominally from 9.9 mm on section 1 to 12.4 mm on section 4 (see Table 6.1) in order to easily identify each section and to optimize the turning procedure.

Each zone was machined using the same tool radius but with different feed rates, in order to obtain different roughness parameters for each zone (surface roughness increases from zone 1 to zone 4). This allows studying the influence of the amplitude of roughness parameters with respect to CT surface filtering characteristics. The dimensions of the workpiece were designed, as described for the FDM sample, taking into account the dimensional constraints given by the magnification, and thus the voxel sizes chosen for the experimental CT scans, and in order to use a low X-ray scanning power to minimize the focal spot dimensions. In the case of the turned object, however, also the vertical dimensions were designed in order to include all the sections of the sample in the field of view for all CT scanning configurations.

After production, the workpiece was measured with the tactile CMM Zeiss Prismo Vast. After the achievement of thermal stability in a temperature controlled environment at 20 °C, repeated CMM measurements were performed acquiring circular probing paths in scanning mode, orthogonal to the sample axis, for each section of the sample.

Surface topography was measured with the optical profiler Sensofar Plu Neox. Roughness measurements were performed using cut-off filters according to ISO 4288. Repeated measurements were collected for each of the four zones on different regions, in order to well characterize the sample surface. The average *Rz* and *Rp* values are reported for each section in Table 6.1.

	Diameter/mm	***Rz***/µm	***Rp***/µm
Section 1	9.9	17	11
Section 2	10.7	25	16
Section 3	11.6	45	29
Section 4	12.4	51	33

Table 6.1: Nominal diameters, and average values of the experimentally measured Rz and Rp parameters.

Figure 6.16 shows one of the datasets of the experimentally measured topographies for each section.

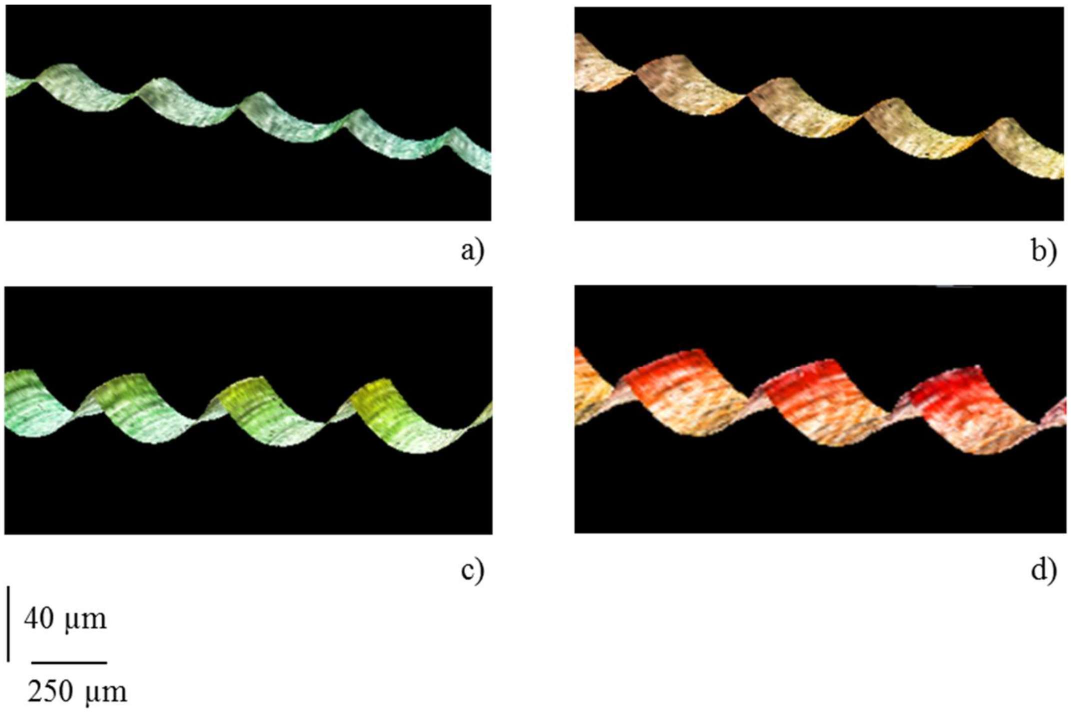

Figure 6.16: Example topographies from one of the datasets of the experimentally measured surfaces on the different sections of the workpiece. a) Section 1, b) Section 2, c) Section 3, d) Section 4.

As visible also from Figure 6.16, the surface roughness increases from section 1 to section 4 of the sample, and the material distribution is similar for all the four sections of the cylinder. Compared to the FDM sample of Figure 6.14 it is visible how the sample obtained by turning presents a completely different material distribution, and thus bearing curves. The material in fact is much more distributed on the valleys rather than on the peaks. Moreover, due to the inherent characteristics of the manufacturing process also the surface roughness in terms of *Rz* is smaller in the case of the turned object.

FDM + Turning test object

Besides the two previously described samples, a third sample reported in Figure 6.17 was produced by coupling the two above mentioned manufacturing processes, i.e. Fused Deposition Modeling and turning.

Figure 6.17: Test object manufactured by coupling FDM and turning.

First a sample with the same characteristics of the FDM sample described before was produced with the same process parameters, after that the external surface of the sample was turned with a conventional lathe. The external surface before and after the machining process is shown in Figure 6.18.

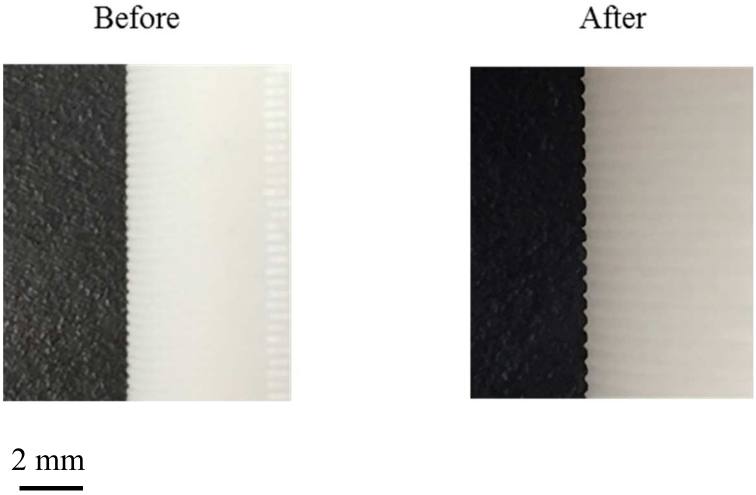

Figure 6.18: External surface of the sample. a) with the original FDM finishing before the machining process, b) after the machining process.

The turning parameters were determined so that to achieve a high surface roughness (*Rz* equal to 124 μm).
The manufacturing of this sample was designed in order to produce a sample made from the same material of the FDM sample, but characterized with a significantly different bearing curve and material distribution. In this way, it is possible to compare the effects of surface roughness on two samples characterized by the same dimensions and material, and similar *Rz* roughness parameter, but with completely different material distributions.
Tactile CMM measurements of the sample were performed in a laboratory temperature controlled environment at 20 °C. The sample was let stabilize in order to achieve the thermal stability; then, repeated CMM measurements were performed with a tactile CMM, Zeiss Prismo Vast with MPE of length: 2 + *L*/300 mm, where *L* is the length in mm. Circular probing paths, orthogonal to the sample axis, and at different heights of the sample were acquired in scanning mode.
Tactile roughness measurements were acquired with a Zeiss TSK Surfcom 1400. Roughness measurements, perpendicular to the sample layers, were performed using cut-off filters according to ISO 4288. Repeated measurements were collected on different zones of the workpiece, in order to well characterize the sample surface. Average values of *Rp* = 96 μm and *Rz* = 124 μm were measured.

6.3.2. Experimental CT scans set-up

CT scans with different voxel sizes were performed for each of the samples described in section 6.3.1 in order to investigate the effects of surface roughness on CT dimensional measurements on different surface morphologies taking into account CT surface filtering characteristics.
In order to correlate the effects of surface roughness on CT dimensional measurements to the surface roughness parameters and to investigate how the various surface morphologies and surface roughness are taken into account with varying voxel size, the following voxel sizes were chosen in such a way that for each sample:

- One or more CT scans are characterized by a voxel size smaller than the measured *Rz* parameter of the sample;
- One or more CT scans are characterized by a voxel size ca. of the same order of magnitude of the measured *Rz* parameter of the sample;
- One or more voxel sizes are characterized by a voxel size bigger than the measured *Rz* parameter of the sample.

The *voxel size/Rz* ratio was chosen as criterion to determine the voxel size for the experimental investigations because, as reported in section 6.2.1, *Rz* describes the maximum peak-to-valley height of the profile in the sampling length and therefore characterizes the roughness profile amplitude. Using the *voxel size/Rz* ratio enables to study how the surface roughness is taken into account when the voxel completely contains, locally, the roughness profile amplitude (i.e. voxel size bigger than *Rz*), when the roughness profile is just contained locally by the voxel (i.e. voxel size ~ *Rz)*, and when the voxel is so small that peaks and valleys of the profile are described by several sets of voxels (i.e. voxel size smaller than *Rz*).

Following these considerations, using the experimentally measured *Rz* values for the three samples, the voxel sizes reported in Table 6.2 were experimentally investigated for the FDM sample, turned sample, and FDM+turning sample.

	Voxel size 1	**Voxel size 2**	**Voxel size 3**	**Voxel size 4**
FDM	19 µm	50 µm	100 µm	125 µm
Turned	17 µm	50 µm	91 µm	125 µm
FDM+turning	19 µm	50 µm	100 µm	125 µm

Table 6.2: Voxel sizes experimentally investigated for the FDM sample, turned sample and FDM+turning sample.

Four voxel sizes were chosen for each sample. As introduced before, the dimensions of the samples were designed in order to have the entire sample in the field of view for all the chosen voxel sizes. For all the three samples, voxel size 1 i.e. the smallest voxel size investigated was the smallest voxel size that enabled to have the entire sample in the field of view and placed in the CT measuring volume in the tilted orientation, so that to avoid the presence of cone-beam artifacts affecting the upper plane of the cylinders. Voxel size 4 was the maximum voxel size achievable with the CT system used for the experimental investigation. Voxel size 2 and 3 were selected in order to be ca. of the same order of magnitude respectively of *Rz*/2 and *Rz* for the FDM and turned FDM sample and at the same time in order to homogenously map the various magnifications. For the turned sample voxel size 2 and 3 were determined in such a way to homogenously investigate the various *Rz* parameters present in the various sections of the turned sample and the various magnifications.

All CT scans were performed with the metrological CT system Nikon MCT 225 featuring a temperature controlled cabinet and micro-focus X-ray source. For each of the voxel sizes reported in Table 6.2 and for each sample, 3 repeated CT scans were performed. A total of 36 CT scans were thus performed.
For all CT scans, the test objects were placed inside the CT volume in the tilted orientation as shown in Figure 6.19.

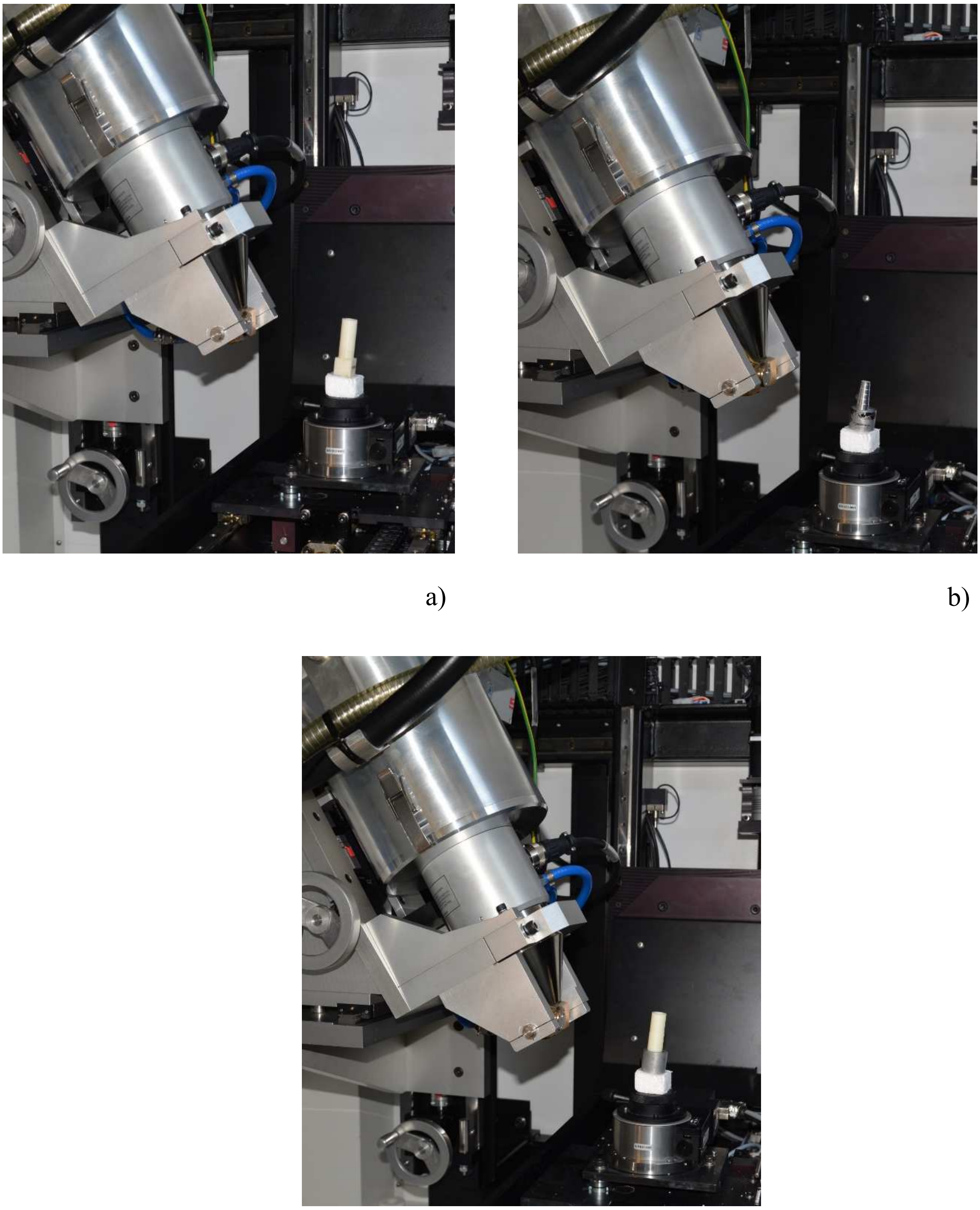

a)

b)

c)

Figure 6.19: Orientation of the object in the CT measuring volume. a) FDM test object, b) turned test object, c) turned FDM test object.

In all cases, before the scanning processes, the samples were let stabilize in the temperature controlled cabinet at 20° C for several hours in order to achieve stability after fixturing and to achieve the thermal stability.

CT scans of the FDM sample and the turned FDM sample were performed with the scanning parameters reported in Table 6.3.

Voltage	80 kV
Current	75 µA
Exposure time	4 s
Filtering	No
Nr. projection	1500
Detector pixel size	200 µm

Table 6.3: Scanning parameters used for the experimental investigations for the FDM test object and turned FDM test object.

The same scanning parameters were used for both sample, because they are characterized by the same material and dimensions and in order to compare the results for samples scanned with the same scanning conditions. As visible, a low scanning power was used for the CT scans in order to keep the X-ray focal spot size and drift at minimum.

Table 6.4 reports the scanning parameters used for the turned aluminum sample.

Voltage	175 kV
Current	45 µA
Exposure time	1.415 s
Filtering	0.25 mm Cu
Nr. projection	1500
Detector pixel size	200 µm

Table 6.4: Scanning parameters used for the turned aluminum sample.

Also in this case the X-rays power was kept at minimum in order to minimize focal spot effects.

During all CT scans, temperature was kept under control by means of thermocouples embedded into the CT system. No significant deviations from the reference metrological temperature were found: the temperature was observed to be constant at 20°C ± 0.1°C.

6.3.3. Data evaluation

After the CT volume reconstruction, all CT scans were imported and analyzed by mean of VGStudio MAX 3.0. The local adaptive surface determination algorithm was used for the CT surface determination step for all the scans performed. After that, for each of the three samples, the corresponding alignment used for acquiring the CMM measurements was reproduced in the CT datasets.

As described before, during the CMM measurements acquisition step, for each of the three samples circular probing paths orthogonal to the samples axes were acquired in scanning mode at different *z* coordinates (in each of the three reference systems used *z* is the axis nominally parallel to the cylinder axis). The measurands of interest for each sample are thus circles diameters at different heights. For the turned and turned FDM samples the circular probing paths were acquired only on the outer surfaces of the cylinders, whereas for the FDM sample circular probing paths were acquired on both the outer and inner surfaces of the hollow cylinder. The acquisition of probing paths at the same z coordinate on inner and outer surfaces for the FDM sample enables to compare the effects caused by surface roughness on inner and outer geometrical characteristics. Gaussian least-squares fitting was used for the diameters evaluation.

In the CT datasets each diameter was evaluated by fitting a cylinder with a height corresponding to the period of the profile, (e.g. 0.33 mm for the FDM sample). Fitting a cylinder instead of a circle was necessary to simulate the same probing areas interested by CMM measurements. Moreover, often, fitting circles on CT data is not the most consistent approach. Circles in fact might be too sensitive to the presence of noisy data in the particular section or to the presence of localized artifacts or outliers. Fitting a cylinder instead enables to average and/or cancel out these effects. Also in this case Gaussian least-squares fitting was used for the diameters evaluation.
A high density of fitting points with a spacing grid of 1 µm was used for the CT analyses of each cylinder. This guarantees that all the fitting points are well distributed on the whole roughness profile. Figure 6.20 shows the fit points distributions for some of the measurands of the three samples experimentally analyzed. For a better visibility only one of the edges of the cylindrical sections are reported for each sample. The red lines visible in the image are representative of the fitted cylinders.

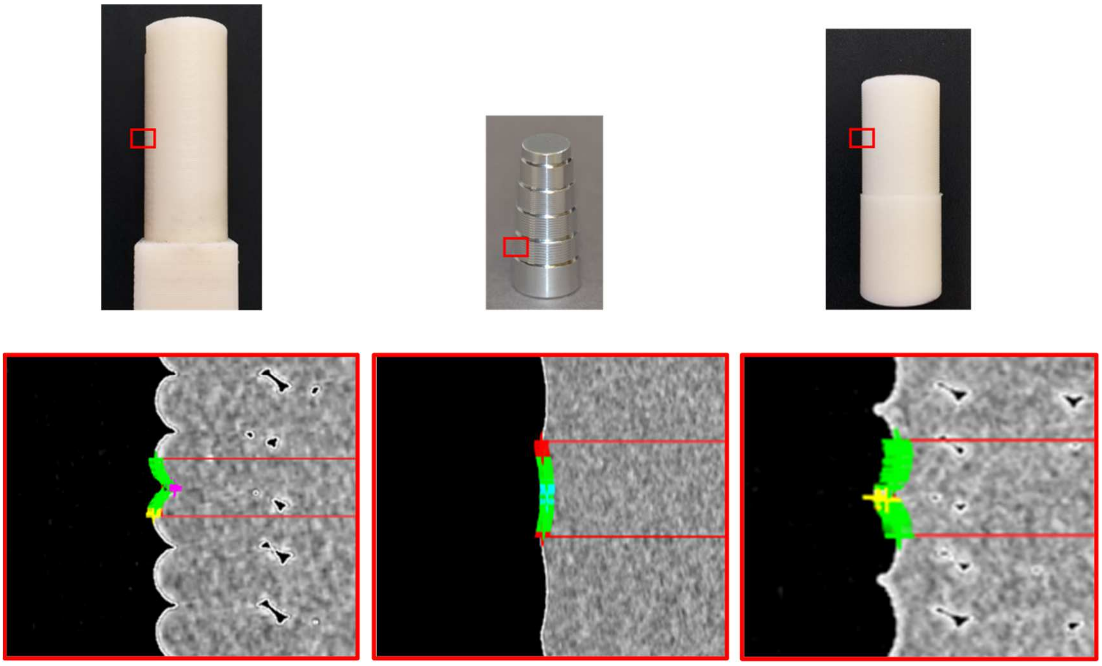

a) b) c)

Figure 6.20: Fit points distributions for some of the measurands of a) FDM sample, b) turned sample, c) FDM+turning sample.

6.3.4. Experimental results

In order to investigate the influence of surface roughness on CT dimensional measurements, the volumetric models obtained from the CT scans of the experimentally manufactured dedicated test objects featuring various surface morphologies and roughness parameters and scanned at different voxels sizes are provided in the following. Figure 6.21 reports the 3D volumes obtained from the CT scans of the FDM sample at 19 µm, 50 µm, 100 µm and 125 µm voxel sizes.

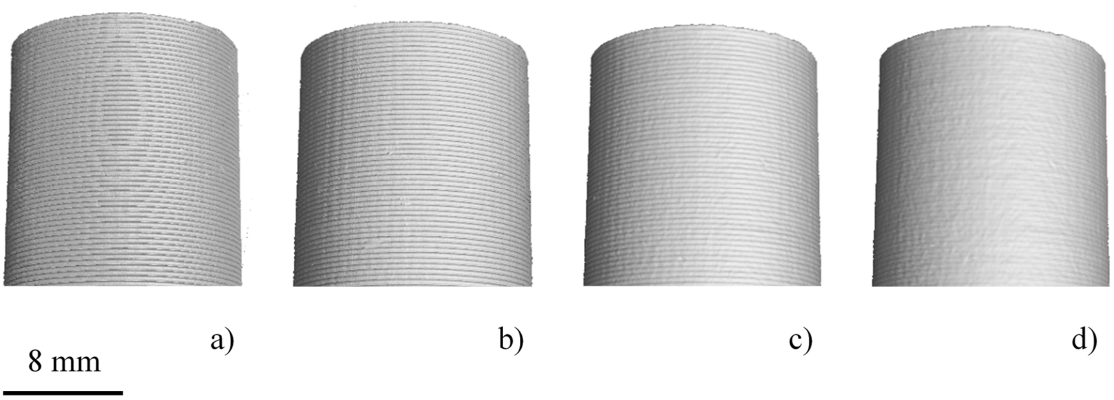

Figure 6.21: Volumetric models of the FDM sample obtained from the CT scans at different voxel sizes: a) 19 µm voxel size, b) 50 µm voxel size, c) 100 µm voxel size, d) 125 µm voxel size.

By comparing the 3D models obtained with the different voxel sizes it is well visible how, with an increasing voxel size, the CT surface is progressively smoothed and loses the details characterizing peaks and valleys. This is also visible in Figure 6.22, which shows the volumetric models of the turned sample featuring four sections characterized by different surface roughness properties.

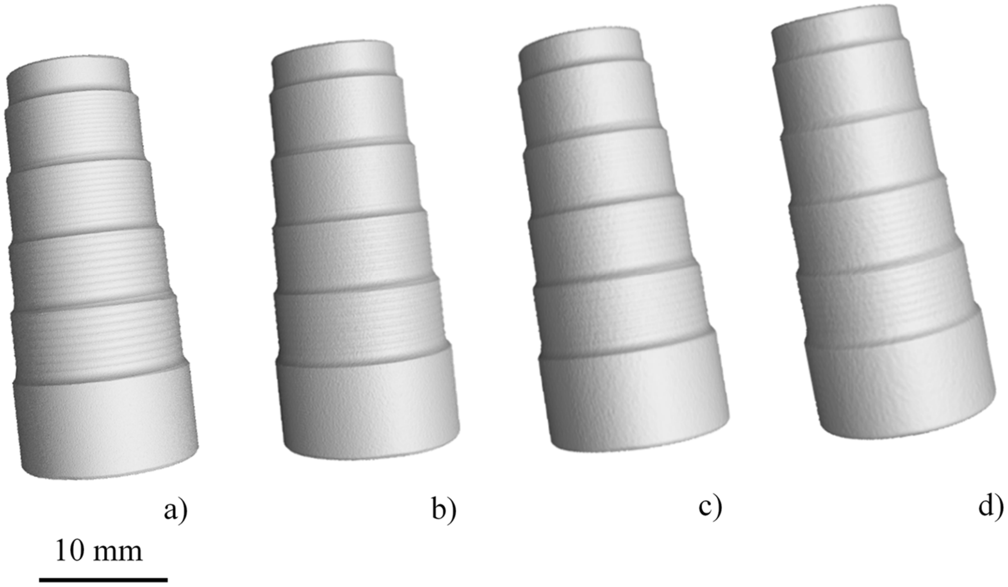

Figure 6.22: Volumetric models of the turned sample obtained from the CT scans at different voxel sizes: a) 17 µm voxel size, b) 50 µm voxel size, c) 91 µm voxel size, d) 125 µm voxel size.

Thanks to the different sections with different roughness parameters that characterize the turned sample and the different voxel sizes considered it is possible to compare the effects of the same voxel size on the different sections of the cylinder characterized by different roughness parameters, and to compare how the surface description of the same section varies with varying voxel sizes. For example, by analyzing section 1 it is visible how with an increasing voxel size, the surface details progressively diminish and the lays of the turning process are not visible anymore.
In Figure 6.23, the 3D models of the turned FDM sample are presented. Also here it can be noted how the CT surface quality degrades with an increasing voxel size.

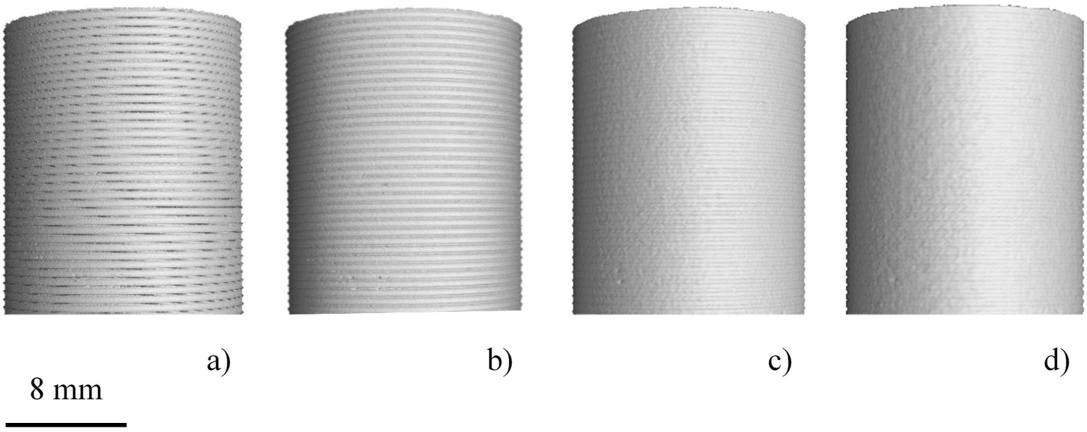

Figure 6.23: 3D models of the turned FDM sample obtained from the CT scans at different voxel sizes: a) 19 μm voxel size, b) 50 μm voxel size, c) 100 μm voxel size, d) 125 μm voxel size.

The experimentally performed CT scans show that CT operates a surface filtering on the actual surface. In particular, CT surface filtering is a low-pass filtering, which filters out higher frequency components. In the 3D reconstructed volumes of the CT scans experimentally performed, both peaks and valleys of the roughness profiles are filtered with increasing voxel size. The scans experimentally performed therefore show, that the voxel sizes have a significant effect on the description of the surface morphology.

In order to quantify and investigate how surface roughness influences CT dimensional measurements with respect to tactile CMM measurements acquired on the peaks of the roughness profiles, for each of the samples produced for the experimental campaigns (i.e. the FDM sample, the turned sample and the turned FDM sample) the CT measured least-squares diameters are compared to the reference least-squares diameters. For each measurand the deviation is calculated as the difference between CT measured least-squares diameters and reference least-squares diameter measurements.

Figure 6. 24 reports the deviations experimentally obtained for the least-squares diameter measurements performed on the outer surface of the FDM sample for all the voxel sizes investigated. The horizontal axis of the graph represents the measurand number (i.e. the different diameters measured at different heights of the sample, see section 6.3.3), whereas in the vertical axis the deviations between CT measurements and reference

measurements are reported. Each of the columns of the chart represents the average of the measurement results obtained from the 3 repeated CT scans for each configuration.

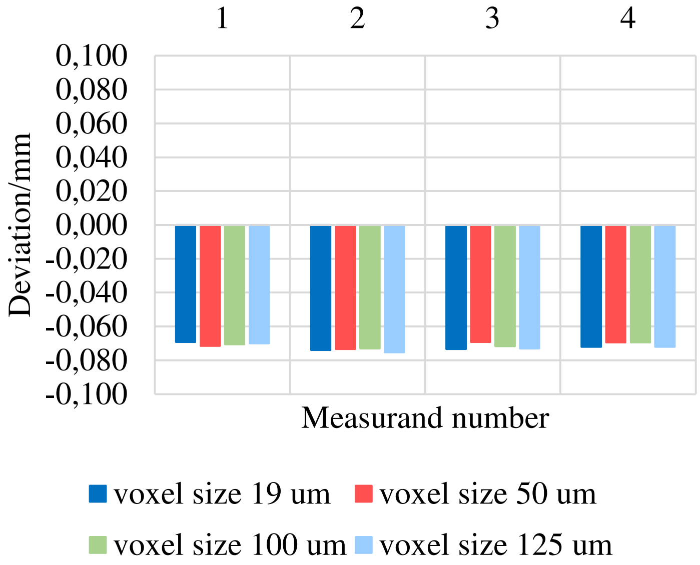

Figure 6.24: Deviations between CT measurements and reference measurements performed on the outer surface of the FDM sample. In the horizontal axis the different measurands investigated are represented whereas in the vertical axis the deviations calculated as (CT measured values - Reference values) are reported. The different colors represent the different voxel sizes investigated.

From Figure 6.24 it is immediately visible how for all the measurands and for all the different voxel sizes investigated the deviations between CT measurements and reference measurements present negative values. Negative deviations mean that CT measurements are always smaller than the reference measurements. In particular, these negative deviations do not show significant differences for the different measurands and for the voxel sizes investigated. Average deviations of -0.072 mm are present.

By analyzing Figure 6.25, which represents the measurement results obtained for the least-squares diameter measurements on the inner surface of the FDM sample at corresponding heights of the least-squares diameters on the outer surface presented in Figure 6.24, it is visible how the inner diameter measurements present the same behavior of the outer diameters reported in Figure 6.24 but with the opposite sign.

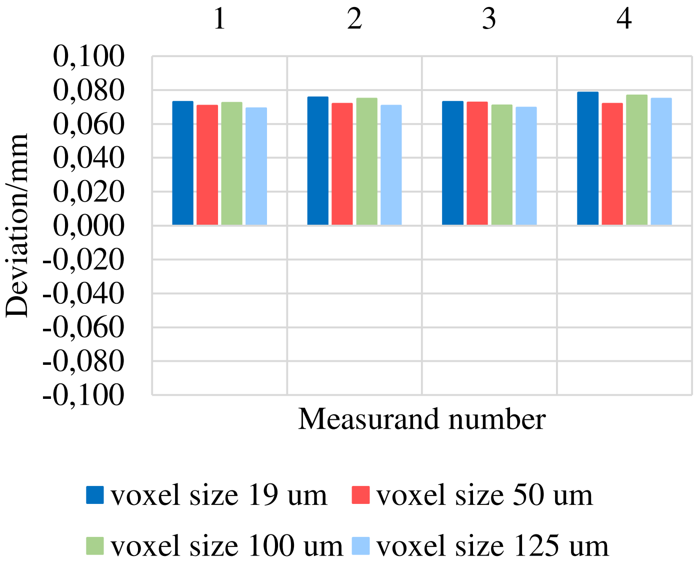

Figure 6.25: Deviations between CT measurements and reference measurements performed on the inner surface of the FDM sample. In the horizontal axis the different measurands investigated are represented whereas in the vertical axis the deviations calculated as (CT measured values-Reference values) are reported. The different colors represent the different voxel sizes investigated.

In this case, the inner diameters measured by CT present positive deviations with respect to the reference measurements meaning that CT inner diameter measurements are always bigger than the reference measurements. It is visible also in this case how similar deviations are present for all the measurands investigated and for all the voxel sizes experimentally studied, which on average are equal to 0.073 mm.

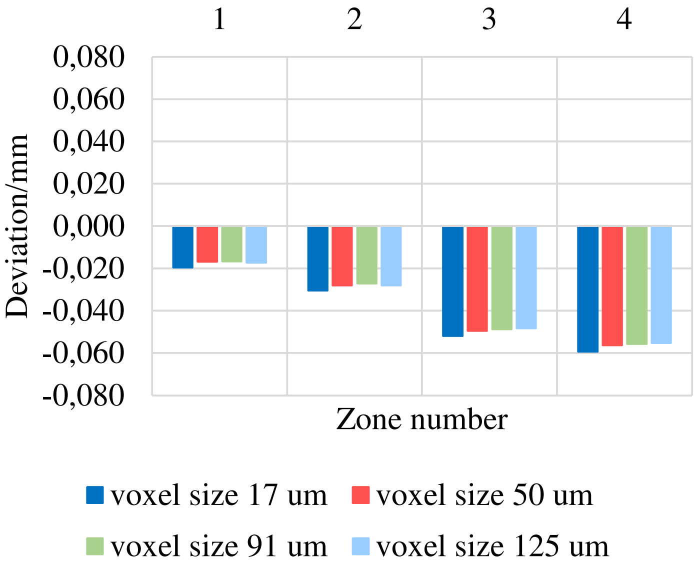

Figure 6.26: Deviations between CT measurements and reference measurements performed on the turned sample. In the horizontal axis the different zones of the sample, characterized by surface roughness increasing from zone 1 to 4 are represented whereas in the vertical axis the deviations calculated as (CT measured values-Reference values) are reported. The different colors represent the different voxel sizes investigated.

Figure 6.26 reports the experimental results obtained from the repeated CT scans of the turned sample for each of the four different voxel sizes investigated. Each of the columns of the chart represents the average of the measurements results obtained from the 3 repeated CT scans for each configuration.
Also in this case CT measurements show negative deviations with respect to the acquired reference measurements. By analyzing the deviations obtained for the four zones characterized by different surface roughness parameters and with an increasing surface roughness from zone 1 to 4, it can be noted how the deviations increase with increasing surface roughness. In particular, average deviations of -0.018 mm, -0.028 mm, -0.050 mm, -0.057 mm were found respectively for zone 1, zone 2, zone 3 and zone 4.

Figure 6.27 reports the measurement results obtained for the turned FDM sample least-squares diameter measurements. Each of the columns of the chart represents the average of the measurements results obtained from the 3 repeated CT scans for each configuration.

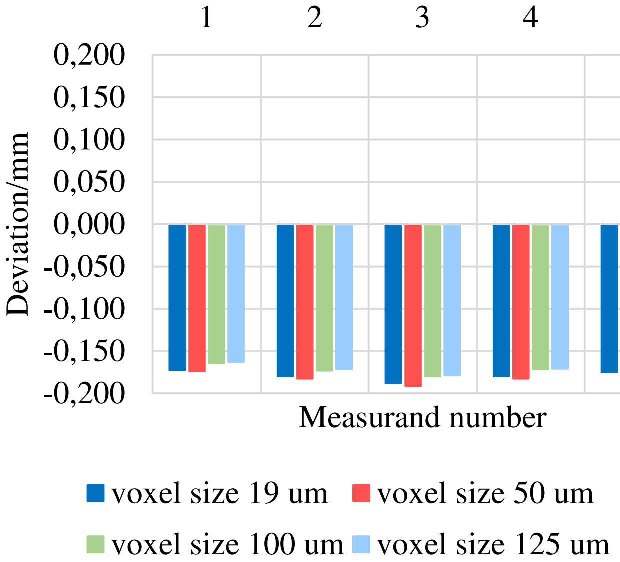

Figure 6.27: Deviations between CT measurements and reference measurements performed on turned FDM sample. In the horizontal axis the different measurand numbers are represented whereas in the vertical axis the deviations calculated as (CT measured values-Reference values) are reported. The different colors represent the different voxel sizes investigated.

CT measured least-squares diameters are always smaller than reference measurements and, as it happened for the FDM sample, characterized by the same material (ABS plus) but completely different surface morphology, and scanned with the same scanning parameters, the deviations experimentally found are present for all the measurands analyzed and for all the voxel sizes investigated. In this case, average deviations of -0.175 mm are present.

By analyzing the measurement results reported from Figure 6.24 to Figure 6.27 it can be concluded that the particular behaviors experimentally found for all the measurements performed on the three samples specifically manufactured, i.e. the FDM sample, the turned sample and the turned FDM sample, are caused by surface roughness. Specifically, the experimentally obtained results demonstrate that surface roughness produces a systematic error between CT and tactile CMM measurements. The experimentally measured least-squares diameters on the outer surfaces of the cylinders are always smaller than the corresponding CMM reference values, while least-squares diameters on the inner surfaces are always bigger than CMM values. This systematic difference is caused by the different measuring principles on which tactile CMMs and CT rely on. The experimental results also show how the existing systematic error caused by surface roughness can be related to the surface roughness of the scanned workpiece. In fact, it was observed that the absolute value of the systematic error varies with the surface roughness of the object and the bigger is the surface roughness the bigger is the bias *b* between CT and CMM measurements.

In particular, the experimental results demonstrate how the bias *b* between CT and tactile CMM measurements is related to the *Rp* parameter of the roughness profile [122]. This is visible in Figure 6.28, which reports the experimentally obtained measurement results for least-squares diameter measurements performed on the outer surfaces of the cylinders for all the samples and for all the voxel sizes investigated. Each point of the graph represents the average measurements obtained from the three repeated CT scans performed for each voxel size.

In the vertical axis of the graph, the ratios between the deviations *b* (calculated as CT measurements minus reference measurements) and the *Rp* values are plotted, whereas in the horizontal axis the ratios between the voxel sizes and *Rz* parameters are plotted.

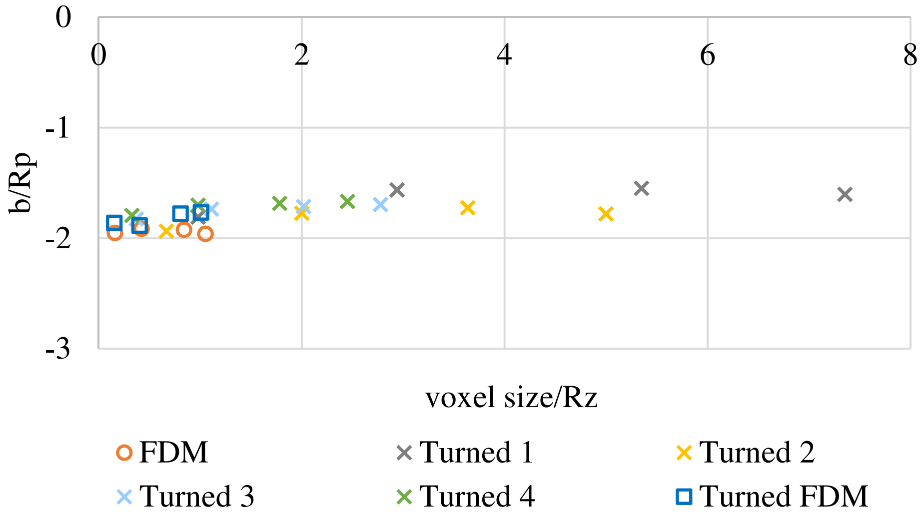

Figure 6.28: Results obtained from the experimental investigations. Diameter measurements of the FDM sample are represented as circles, diameter measurements obtained for the different zones (characterized by increasing roughness) of the turned sample are represented as crosses of different colors, and diameter measurements of the turned FDM sample are represented as squares.

These two a-dimensional ratios were selected because they allow comparing different profiles characterized by different roughness parameters and scanned with different voxel sizes.

Figure 6.28 shows how for the experimentally investigated roughness profiles the surface roughness causes a bias with respect to the reference measurements, of approximately two times the *Rp* value of the scanned workpiece [122]. The same results were found for

least-squares diameter measurements performed on the inner cylindrical surface of the FDM sample; however, in this case the bias presents the opposite sign.
Moreover, the average deviations experimentally obtained are constant with the different voxel sizes used in this work (up to 125 µm). In fact, it can be seen how varying the voxel size (i.e. *voxel size/Rz* ratio) for the given measurands, the average *b/Rp* values are still close to 2*Rp*.

Additional investigations were also conducted on another turned aluminum cylinder characterized by a lower surface roughness compared to those reported in Figure 6.28, with an *Rp* value of 2 µm. A higher dispersion of *b/Rp* values was found in this case. This can be explained because in this case the surface roughness is not the predominant influence quantity among those that usually occur in CT measurements of parts with reduced surface roughness. While parts with high surface roughness produce higher values of *b* (resulting in systematic errors that should be corrected as it will be discussed in section 6.3.7), for parts with small surface roughness the systematic effect is more difficult to be identified and, therefore, in this case the influence of surface roughness on CT measurements could be considered in the measurement uncertainty (e.g. using the methods proposed in references [82] and [91]).

The effect of surface roughness in these experimental campaigns was investigated by performing diameters measurements on cylindrical parts. However, it could be generalized also for other types of measurements (e.g. position of flat surfaces) by considering an offset equal to *Rp* of the CT least-squares surface from the reference surface measured on the peaks.

6.3.5. Influence of surface morphology and voxel size on CT dimensional measurements

Figure 6.28 describes how the systematic error caused by surface roughness between CT least-squares diameters and reference tactile CMM least-squares diameters is on average equal to 2*Rp*. However, Figure 6.28 gives also another important information. In fact, thanks to the *b/Rp* ratio and *voxel/Rz* ratio it is possible to compare completely different surfaces scanned with various voxel sizes. The experimental results show how the investigated surface morphologies do not affect the systematic error caused by surface roughness between CT and CMM measured least-squares diameters. In fact, as described before the FDM sample, the turned sample, and turned FDM sample present completely different material distributions. While the FDM sample is characterized by the material more distributed on the peaks, the turned sample and turned FDM sample are characterized by much more material on the valleys rather than on the peaks. In particular, the turned FDM sample present sharp and narrow peaks. In all of these cases, as visible in Figure 6.28 the *b/Rp* ratios are close to 2*Rp*. Also the voxel size, was not found to significantly impact on the average deviations between CT measured least-squares diameters and reference measurements.
This is also visible in Figure 6.29, which reports a detail of the edge profile of a CT section of the FDM sample. In Figure 6.29, the different white lines represent the edge profile

(obtained after the surface determination) of the same CT section but obtained from the different CT scans performed with different voxel sizes. After having performed the alignment of all CT volumes according to the alignment used during CMM measurements, and after having performed the surface determination step it was thus possible to obtain Figure 6.29 (in the figure the contrast has been stretched in order to have a black and withe image for better visibility).

Figure 6.29: Detail of a CT section of the FDM sample. The same surface profile obtained from the CT scans performed with the four different voxel sizes is represented, after the surface determination step and alignment of the CT volumes.

It can be noted how, when varying the voxel size, the surface profile is affect by the surface filtering due to the CT structural resolution, which causes the peaks and valleys to be progressively smoothed with increasing voxel size. Globally, however, the surface filtering caused by CT does not affect CT least-squares diameters evaluations.

Figure 6.30, 6.31 and 6.32 report respectively the central sections of the FDM sample, turned sample and turned FDM sample for all the different voxel sizes investigated. In all the cases the same detail of cylinder edge profile is shown for the various voxel sizes.

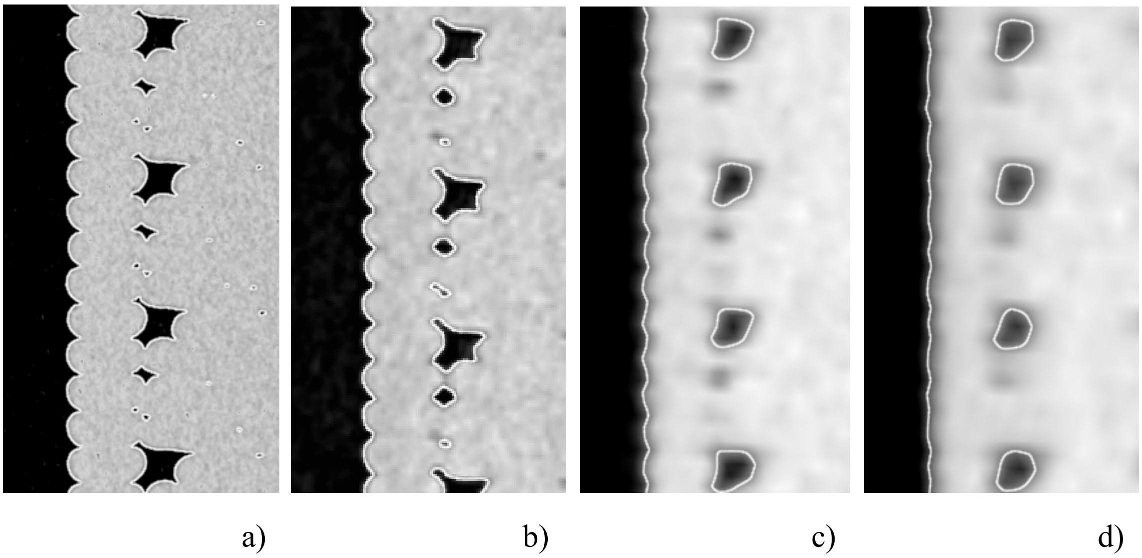

Figure 6. 30: Details of the central sections of the FDM cylinder experimentally scanned. a) 19 µm voxel size, b) 50 µm voxel size, c) 100 µm voxel size, d) 125 µm voxel size.

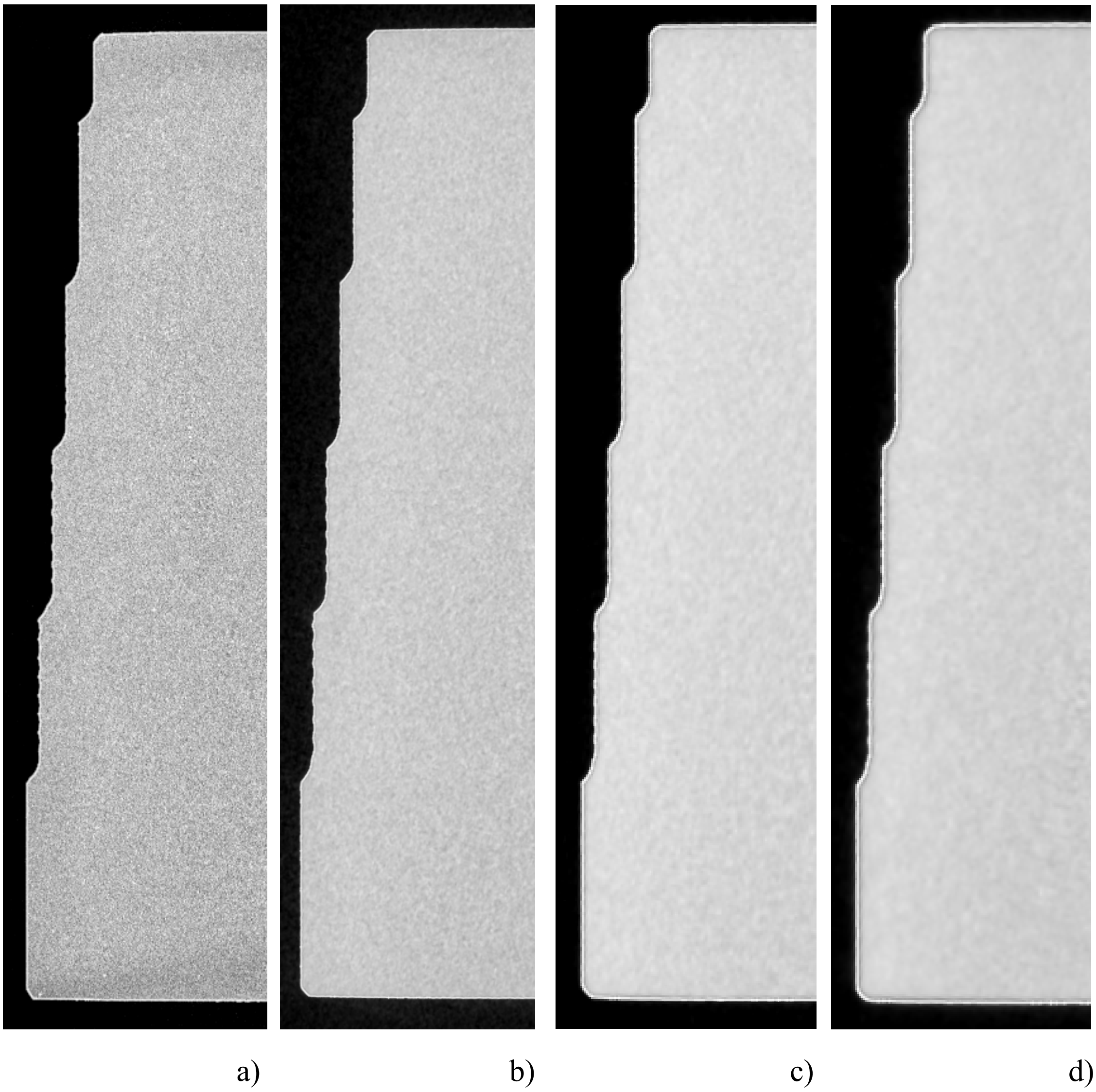

Figure 6. 31: Details of the central sections of the turned cylinder experimentally scanned. a) 17 µm voxel size, b) 50 µm voxel size, c) 91 µm voxel size, d) 125 µm voxel size.

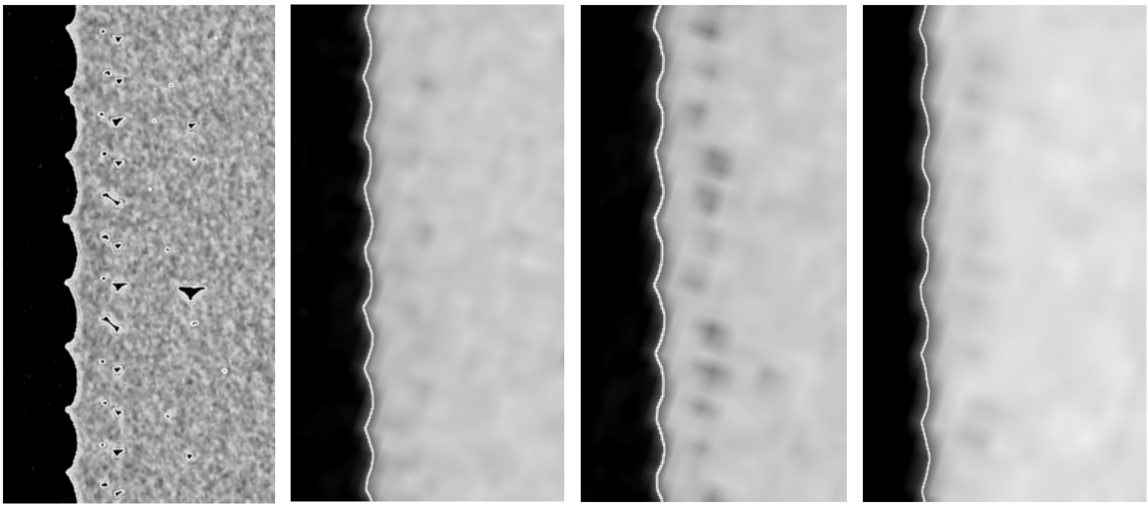

a) b) c) d)

Figure 6.32: Details of the central sections of the turned FDM cylinder experimentally scanned. a) 19 µm voxel size, b) 50 µm voxel size, c) 100 µm voxel size, d) 125 µm voxel size.

From Figure 6.30 it is visible how the valleys of the FDM sample are significantly affected by the voxel size dimensions. In fact, in the case of the FDM sample the valleys are much sharper and narrower than the peaks which instead are characterized by a significant amount of material.

In the case of the turned sample (Figure 6.31), contrarily to what happened for the FDM sample, the description of the peaks of the turned test object is more affected by the voxel size than the description of the valleys. In fact, due to the different manufacturing process which requires a removal of material, the material distribution is opposite to the one of the FDM sample, and the valleys present a bigger amount of material whereas the peaks are sharper and characterized by a smaller material distribution.

When analyzing the turned FDM sample, see Figure 6.32, it is possible to directly compare the volumetric models of the FDM turned sample to the volumetric models obtained from the CT scans on the FDM sample which is characterized by the same dimensions, same material, similar *Rz* value but completely different and opposite surface morphologies. In the case of the turned FDM sample, the peaks are mostly affected by the degrading CT scans resolution. The voxels in fact contain grey value information which are used by the surface determination algorithm in order to determine the CT surface of the object, however, the grey value of each voxel provides an average information on the content of material on each voxel but not how this material is distributed. Therefore, sharp peaks or valleys on average have smaller percentages of material on the voxel, and this affect the surface determination. The sharper is the peak/valley the more this effect will be pronounced.

The experimental results show how the surface filtering caused by CT structural resolution does not affect least-squares measurements which present an average offset equal to *Rp* of the CT least-squares surface from the reference surface measured on the peaks.

6.3.6. Influence of post processing parameters on CT measurements on rough surfaces

In order to investigate the influence of post processing parameters on CT measurements performed on rough surfaces different sets of fit points spacing grids were used for the least-squares diameter measurements evaluations.

The spacing grid describes the fit points spacing that is used in the fitting point process on the CT volume. This parameter was selected for the analysis as from preliminary investigations performed in order to optimize the post-processing parameters used in the previous sections, it was found to be influencing the measurement results. Besides this parameter, it is also extremely important to optimize the other parameters of the software used for the analysis, independently of the particular software, in such a way that the fit points are not discarded in specific regions of the sample.

These considerations are highly relevant when dealing with rough surfaces, in this case in fact in order to well describe the roughness profile captured by CT after the surface determination step it is necessary that the fitting points are well distributed on the surface. If this does not happen, some parts of the profile might not be sampled in the point fitting process even though CT is capable of detecting them. The extreme consequence of this leads to aliasing effects. This is valid in general for all operations in which a signal, is not sampled in the appropriate way. In CT measurement of rough surfaces this might lead to strong effects on least-squares measurements. For example, if the fit point spacing grid is too big it might be the case that CT least-squares diameter measurements of e.g. a FDM part characterized by high surface roughness are highly overestimated/underestimated if the points used for the fitting operations are sampled just on the peaks/valleys.

Figure 6.33 describes the effect of different spacing grids on least-squares diameter measurements performed on the CT volume of the FDM sample scanned with a voxel size of 19 µm. In order to compare the measurement results obtained with the optimized spacing grid of 1 µm used in the previous sections, the deviations between CT least-squares diameters obtained with the new spacing grids and CT least-squares diameters obtained with the 1 µm spacing grid are reported in the vertical axis of the graph. The horizontal axis of the graph reports the measurand numbers (i.e. in this case the least-squares diameters calculated on the outer cylindrical surface at different heights of the FDM sample).

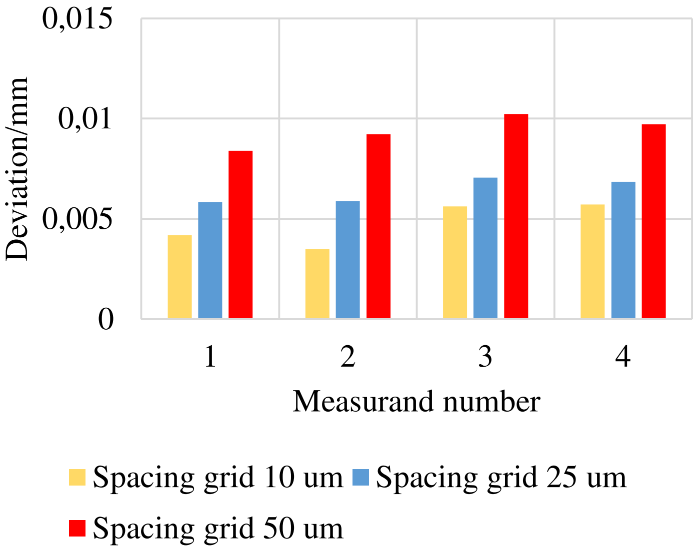

Figure 6.33: Effect of the amplitude of the fit points spacing grid on CT least-squares diameters measurements.

The graph shows that, the spacing grid influences CT dimensional measurements on rough surfaces. In particular, for the FDM sample, with increasing spacing grid the CT measured least-squares diameters become bigger than the CT least-squares diameters calculated with a spacing grid of 1 µm. The 50 µm spacing grid provides the bigger diameters which differ up to 10 µm from the CT diameters calculated with a spacing grid of 1 µm. In the case of the FDM sample in fact, when increasing the spacing grid, the probability of detecting points on the peaks of the roughness profile increases and this causes a shift of the least-squares diameter towards the peaks of the profile and thus closer to CMM measurements acquired on the peaks of the profile.

Therefore, it is strongly suggested when analyzing samples characterized by high surface roughness to always optimize the parameters of the post-processing software used for the analysis, in such a way that the CT detected surface is well sampled and characterized. On the contrary if the post processing parameters are not well optimized additional measurement errors will be caused in the post-processing phase.

6.3.7. Correction of systematic errors due to surface roughness and CT measurement uncertainty determination

In this section, the possibility to correct the systematic errors due to roughness is discussed. For this purpose, other two additional repeated CT scans on the FDM sample with a voxel size of 19 µm were performed (for a total of 5 repeated CT scans) in order to calculate CT measurement uncertainty.

Although the deviations between CT and CMM measurement results are due to the different acquisition principles of the two measuring techniques, and therefore cannot be attributed only to CT, CMM measurements are currently considered as reference when compared to CT measurements. For this reason, in the following, CMM measurements are used as reference and, consequently, systematic errors due to surface roughness are intentionally attributed to CT [123]. Therefore, in the following, the reference diameter is defined as the diameter measurable by CMM. This approach is useful especially in relation to industrial measurements, where CMMs are currently used to determine reference results to be compared with CT results.

According to the GUM [28]), systematic errors shall always be corrected for, and not considered in the uncertainty budget. However, for practical reasons, sometimes the bias is accounted for in the uncertainty budget. This was for example the approach suggested in the first version of ISO 15530-3 (ISO/TS 15530-3:2004 [124], which was then slightly changed in ISO/DIS 15530-3:2009 [125] that is the document cited in [82]). In the current version (ISO 15530-3:2011 [89]), instead, the bias is not added to the uncertainty but is corrected for, in accordance to the GUM. The two different approaches for uncertainty evaluation (ISO 15530-3:2011 and ISO/DIS 15530-3:2009) are compared in the following.

In the new approach described in ISO 15530-3:2011, the expanded measurement uncertainty U is determined by a series of repeated measurements, by Equation (6.1):

$$U = k \cdot \sqrt{u_{cal}^2 + u_p^2 + u_w^2 + u_b^2} \tag{6.1}$$

where k is the coverage factor, u_{cal} is the calibration uncertainty of the calibrated workpiece, u_p the uncertainty of measurement procedure, u_w the uncertainty associated with the influence of the workpiece (e.g. surface roughness, material and manufacturing variations, etc.), and u_b the uncertainty of the systematic error. According to this approach, the bias contribution b is not added to the expanded measurement uncertainty U.

Vice versa, in the old approach described in ISO/DIS 15530-3:2009, the bias is accounted for directly in the uncertainty budget. According to ISO/DIS 15530-3:2009 (which was the approach used also in [82]), the uncertainty is determined by Equation (6.2):

$$U = k \cdot \sqrt{u_{cal}^2 + u_p^2 + u_w^2 + b^2} \tag{6.2}$$

where the bias contribution b is taken into account directly for determining the expanded measurement uncertainty U. This approach was used for example by Schmitt and Niggemann in [82]. There the uncertainty component due to surface roughness is assigned a rectangular distribution with limits ±Rz/2, and then added to the uncertainty associated with the influence of the workpiece (u_w) which then contributes to the overall uncertainty (U) of CT measurements. The case study investigated in [82] is a workpiece with an average Rz of 6.82 µm, and CT scanned with a voxel size of 145 µm. In that case, therefore, the roughness uncertainty component was not large, and the application of the ISO/DIS 15530-3:2009 approach was possible without major consequences for the overall CT measurement uncertainty evaluation. However, when applying this approach also for parts characterized by high surface roughness, the u_w component could reach very high values and become the predominant component in the uncertainty budget, leading to a considerable overestimation of measurement uncertainty. This is the case for parts characterized by high surface roughness such as additive manufactured parts [123].

Therefore, especially in this case, it is recommended to always correct for the systematic errors due to surface roughness, in accordance to GUM and to ISO 15530-3:2011.

Figure 6.34 shows the results obtained from the 5 repeated measurements of the FDM sample.

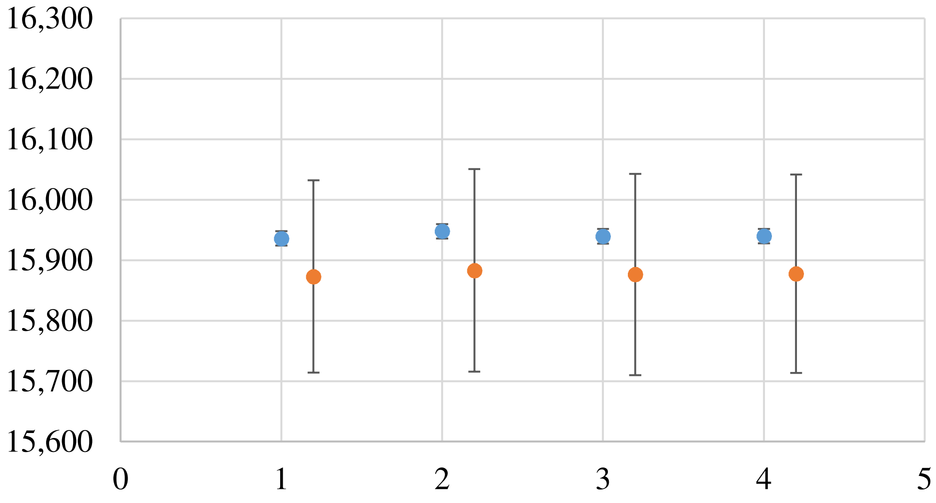

Figure 6. 34: Uncertainties of CT measurements for least-squares diameters of the FDM sample calculated according to the approach inspired by ISO/DIS 15530-3:2009. Blue dots and the corresponding error bars represent tactile CMM measurements and calibration uncertainties, orange dots and the corresponding error bars represent CT measurements and CT measurement uncertainties.

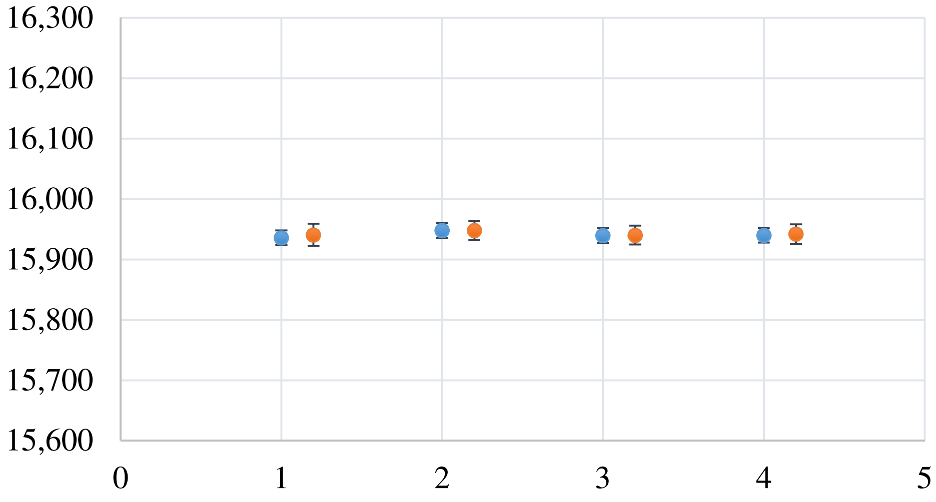

Figure 6.35: Uncertainties of CT measurements for least-squares diameters of the FDM sample calculated according to the approach inspired by ISO 15530-3:2011. Blue dots and the corresponding error bars represent tactile CMM measurements and calibration uncertainties, orange dots and the corresponding error bars represent corrected CT measurements and CT measurement uncertainties.

In Figure 6.34, CT values are represented with the measurement uncertainty calculated according to the approach suggested in [82] (according to ISO/DIS 15530-3:2009). In this case, no correction of systematic errors is applied, the bias b is added to the CT uncertainty budget, and a rectangular distribution is assigned to the uncertainty component coming from surface roughness u_w as proposed in [82]. In this case, the bias *b* is the predominant contribution and produces a large overestimation of CT measurement uncertainty, which is on average 164 µm in Figure 6.32. When ISO 15530-3:2011 is applied (Figure 6.35), and systematic errors due to surface roughness are corrected, a significant decrease of CT measurement uncertainty is obtained, as visible by comparing Figure 6.35 to Figure 6.34.

6.4. Simulation analyses on the influence of surface roughness on CT dimensional measurements

The design concepts of the numerical simulation campaigns, the implementation and the obtained results are presented in the following. The numerical simulations were performed in collaboration with the metrology group of the University of Padova [122].

6.4.1. Materials and methods

In addition to the experimental investigations, numerical simulation analyses of CT images were performed. Simulations, in fact, are a powerful tool that enables to further extend the experimental studies considering a wider set of roughness profiles and different voxel sizes. In real practice in fact, due to several constraints, it is possible to manufacture a finite number of test samples characterized by different periodic surfaces. Physical constraints due to the manufacturing processes and process parameters, in fact, exist: for example, thinking to an ideally triangular periodic profile it is extremely difficult to produce a sharp enough tool to manufacture it. Moreover, time and cost constraints exist, for both the manufacturing phase of the samples, and for their measurement process. Producing different surfaces in fact requires different tools, manufacturing processes and thus machines, which of course are available to a reasonable extent. While dealing with CT measurements moreover, especially time constraints are of significant importance. As described in section 2.4 CT scanning times vary depending on the sample properties (material composition and geometrical properties) and the measurement tasks to be performed and required accuracy. For all these reasons it is therefore possible to manufacture and measure only a selected and finite number of test objects experimentally.

On the other hand, although with simplifications, simulations allow for a theoretically unlimited number of analyses on a wide variety of surfaces. In this case, no physical production of test objects is required, and scanning time is replaced by the computation time. It is worth noting that also when using simulation the computation time can be significant but that depends on a variety of factors such as the simulation software used, the simulation parameters, simplifications adopted, measurement tasks etc. Simulation also provides other benefits: it enables to isolate different influence quantities by acting on the simulation software parameters and to know a-priori the reference dimensions of the simulated test objects, which coincide with the nominal dimensions.

For all these reasons, different sets of simulation analyses were designed and implemented.

Scorpius XLab (Fraunhofer EZRT, Germany) was used for performing simulated CT scans. In addition, to allow a high number of analyses, numerical simulations were also implemented in Matlab. In particular, a set of 16 bit grey scale images were generated for simulating CT bi-dimensional sections of cylinders, each featuring a specific roughness profile. This enabled to further extend the study with significant reduction of the required simulation time with respect to 3D simulations performed using Scorpius XLab [122]. Further details on the simulated bi-dimensional sections are given in the following.

6.4.2. Simulation campaign

6.4.2.1. Description of the simulation analyses

As presented in section 2.4.2 the CT reconstructed volume is composed of voxels, where the voxels are the 3D dimensional entities whose name describes the concept of "volumetric pixels". Each voxel is characterized by one singular gray value obtained, after the processing of all acquired radiographic projections, as the average X-ray density of the corresponding area (see section 2.4.2).
Thinking for simplicity to a section of a reconstructed CT volume of a given object, and reasoning on the voxel grid, the resulting bi-dimensional image that describes the section will be composed of the 2D sections of the voxels (in case of cubical and isotropic voxels the 2D sections are squares) with each voxel characterized by a particular gray value (see Figure 6.34).

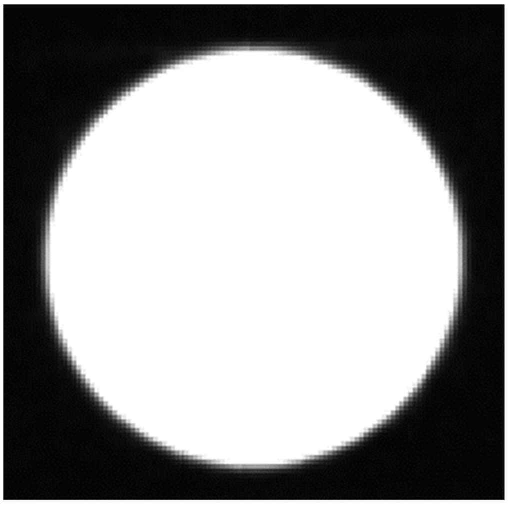

Figure 6.36: 2D section of a reconstructed CT volume of a sphere. Each voxel is characterized by one singular grey value.

The bi-dimensional image of Figure 6.36, thus, is a bi-dimensional matrix of pixels, characterized by a number of rows and columns equal to the number of voxels contained in the horizontal and vertical dimensions of the section considered, with each element (pixel) of the matrix characterized by a given grey level. For 16 bit detectors the gray level is expressed as a number that can range between 0 and 65535 gray levels (2^{16}).

In this resulting image, some of the voxels will be completely covered by the material of the object, some of them will be completely covered by the background for example air, and some others will be covered just by a certain percentage of material.
These concepts are represented in Figure 6.37 which describes what in computed tomography is called the “partial volume effect”.

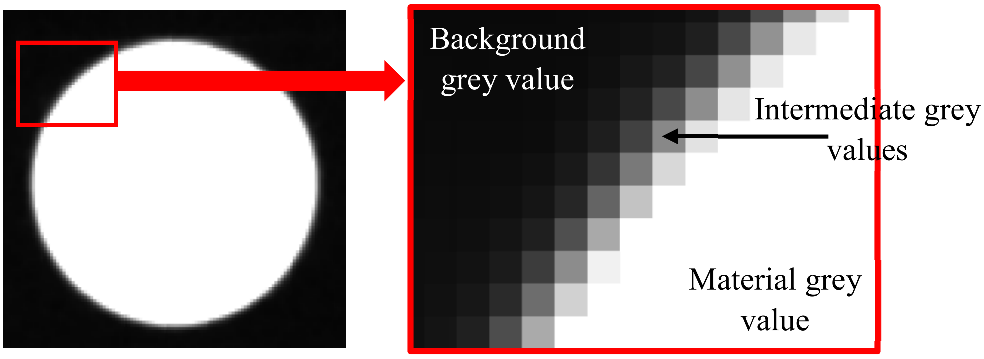

Figure 6.37: Schematic representation of the partial volume effect. Voxels that only partially contains the object material have an intermediate grey value which depends on the amount of material contained in the voxel.

The voxels just partially covered by the material of the object are the voxels which are located on the proximity of the actual surface of the object. For this reason, these voxels have intermediate grey values. In fact, as visible in Figure 2.9 in Section 2.4.3 the histogram describing the gray values present in a CT volume is composed by several gray levels with intermediate values ranging between the background and the object material. In Figure 6.37 it is visible how the region where the actual object surface is located is the one of the voxels characterized by intermediate grey levels. Surface roughness effects on CT measurements therefore are to be searched in that regions.

Taking into account the previous concepts and considerations, a Matlab routine was developed for the simulations campaign in order to generate sets of 16 bit grey scale images representing CT bi-dimensional sections of cylinders characterized by different roughness profiles [122]. An example of bi-dimensional image representing an ideal section of a cylinder with FDM roughness profiles is reported in Figure 6.38.

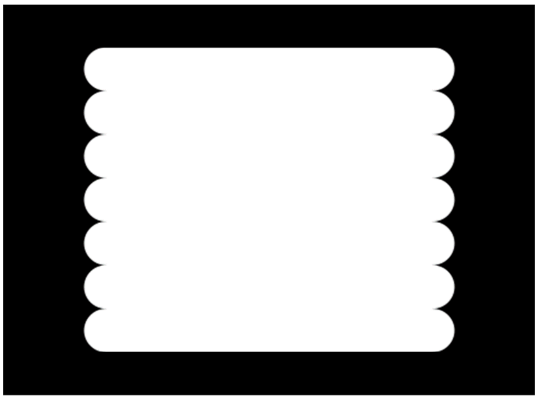

Figure 6.38: Example of a bi-dimensional image representing an ideal section of a cylinder with FDM roughness profiles.

It was chosen to simulate cylindrical sections in order to compare the results with the experimental analyses reported in section 6.3 which were performed on cylindrical samples. Moreover, it was decided to simulate bi-dimensional images for significantly reducing the computation time and thus enabling the possibility to simulate a wide variety of profiles as it will be described later in this section.

As described before, because the interest is on surface roughness effects, the simulated CT bi-dimensional sections of the cylinders are characterized by different roughness profiles. The workflow for producing the simulated images is explained in the following. First the analytical profiles were obtained, i.e. the profiles generated by mean of proper mathematical functions. For example, in the case of turned profiles the mathematical function control parameters were *Rz* and the tool radius. Being based on the analytical description each profile is thus characterized by an ideal shape. After the analytical profiles generation, a reference grey scale image was created for each of the different profiles. Starting from these reference grey scale images, each profile was imaged with different voxel sizes (described in the following) by applying an under-sampling technique making use of the percentage of material contained in each voxel.

In order to take into account the partial volume effect described before, a strategy was developed. In fact, the same roughness profile could be imaged differently depending on the coordinates of its points inside the voxel grid. For example, this is visible in Figure 6.39 for an ideal turned profile.

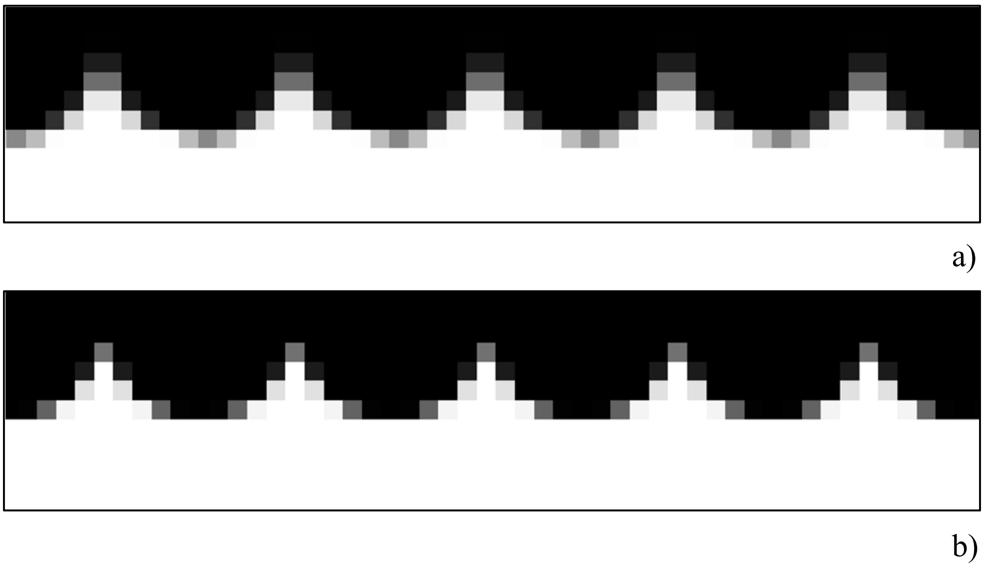

Figure 6.39: Effects of two different positionings a) and b) in the voxel grid for an ideal turned profile. Depending on the profile position on the voxel grid, and therefore on the amount of material contained on the voxels, the profiles are imaged in a different way.

As visible, different positions of roughness peaks (for turned profiles) or valleys (for FDM profiles) can cause different descriptions of the profile. To take this effect into account, different positions of the profile inside the voxel grid were considered for each investigated roughness profile. In particular, 81 different positions were considered for each profile, obtained as a combination of 9 different positions of the profile in both *x* and *y* directions.

6.4.2.2. Definition of surface morphologies and roughness parameters

In order to investigate the combined effects of surface morphology and voxel size dimensions on CT dimensional measurements performed on periodic roughness profiles a wide set of the grey scale images described above was produced with various roughness profiles and voxel sizes.

As reported in section 6.2.1 the shape and material distribution of a profile can be described by the Material Ratio curve, also known as Abbot-Firestone curve. Following the same considerations that led to the development and manufacturing of the FDM test object and turned samples described in section 6.3, also in this case FDM type roughness profiles and turned roughness profiles were considered. In fact, as described in section 6.3 FDM roughness profiles and turned roughness profiles are characterized by completely different material distributions and thus Abbot-Firestone curves. In fact, while FDM profiles present narrow and sharp valleys with respect to the smoother peaks, turned profiles are characterized, depending on process parameters, by narrower and sharper peaks and smoother valleys.

In particular, FDM type roughness profiles and turned roughness profiles within the two extreme cases defined by an ideal turned profile composed of semi-circumferences and its exact opposite i.e. an ideal FDM profile (see Figure 6.12) were considered for the simulation analyses. Figure 6.40 reports the most significantly different Abbot-Firestone curves of the simulated profiles. The curves are represented as normalized in the vertical axis with respect to the *Rz* parameter in order to compare the material distributions of profiles with different *Rz* values.

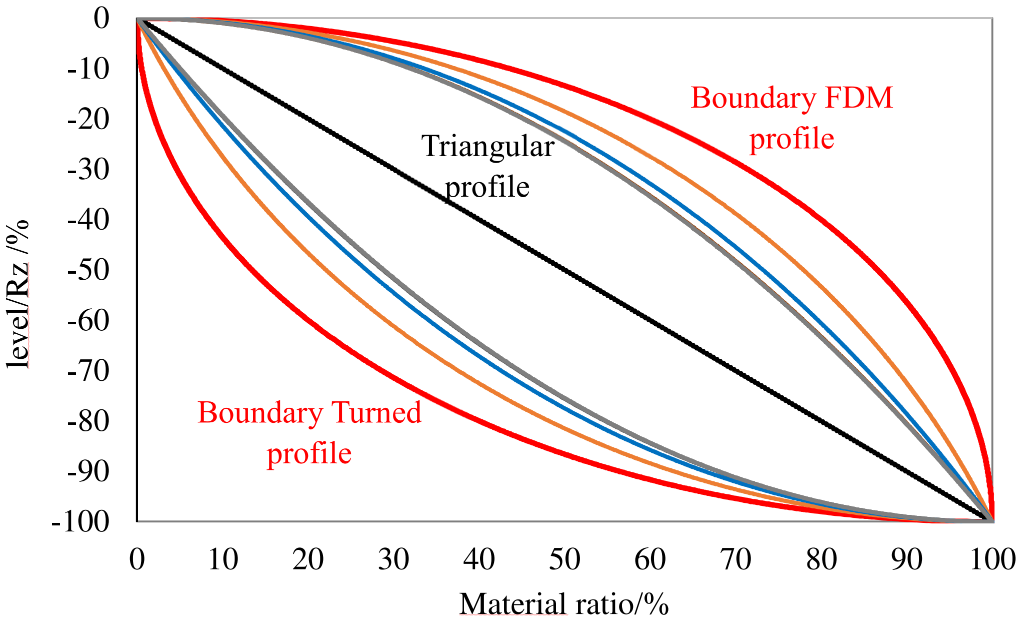

Figure 6.40: Normalized Abbot-Firestone curves of part of the profiles used for the simulation analyses. The red convex and concave curves represent respectively the ideal turned and FDM profiles composed of perfect semi-circumferences. The profiles in between these two curves present intermediate characteristics.

The ideal triangular profile which is characterized by a straight Abbot-Firestone curve (Figure 6.40) was also considered in order to study the effects of surface roughness on a surface characterized by properties in between the two extreme cases of Figure 6.40.

The FDM type and turned roughness profiles considered in the simulations campaign were generated in order to have specific *Rz* values and *RSm* values. The specific *Rz* and *RSm* were chosen so that to obtain roughness profiles with similar roughness parameters and material distribution properties to the experimentally investigated ones and in order to have a good mapping of substantially different surfaces. Profiles characterized by the same material distribution but different *Rz* and *RSm* values were also investigated in order to confirm the results for profiles that maintain the same shape but are just "scaled".
Table 6.5 summarizes the ranges of *Rz* and *RSm* parameters used for the simulated roughness profiles.

	Nr. of profiles	***Rz*/µm**	***RSm*/µm**
Turned	11	[20, 125]	[135, 556]
FDM	11	[20, 125]	[135, 556]
Triangular	1	125	250

Table 6.5: Ranges of Rz and RSm roughness parameters used for the simulation of roughness profiles [122].

As visible from Figure 6.40, the Abbot-Firestone curves of the roughness profiles investigated and thus the material distribution properties vary with varying profile. In particular, with reference to the turned roughness profiles, they can be characterized by completely different peaks morphologies, although maintaining the classical turned roughness profile shape. Figure 6.41 provides a visual overview of the ideal turned roughness profiles considered.

Rz=20 µm
RSm=136 µm

Rz=20 µm
RSm=249 µm

Rz=50 µm
RSm=400 µm

Rz=50 µm
RSm=556 µm

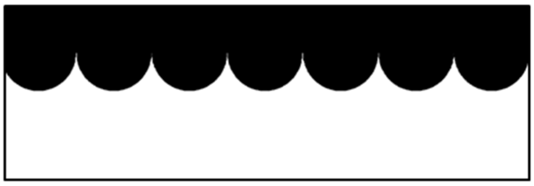

Rz=75 µm
RSm=150 µm

Rz=75 µm
Rsm=229 µm

Rz=75 µm
RSm=466 µm

Rz=100 µm
RSm=200 µm

Rz=100 µm
Rsm=245 µm

Rz=100 µm
Rsm=529 µm

Rz=125 µm
RSm=250 µm

Figure 6.41: Ideal turned roughness profiles. Although the profiles present the classical turning finishing, they can be characterized by completely different peaks morphologies.

Different turning parameters, cause significant differences in the material distribution on the peaks. The ratio *RSm/Rz* was used in the design phase of the simulation campaign in order to obtain a good mapping of different surfaces. In fact, it expresses the proportion of how much the profile elements are spaced with respect to their height. For a given family of profiles, the bigger is the ratio, i.e. the bigger is *RSm* with respect to *Rz*, the smoother is the profile.

The sections featuring the FDM type, turned and triangular roughness profiles described above were imaged with 20 different voxel sizes (from 1 µm up to a maximum of 3*Rz*), obtaining 20 images with different resolutions for each profile. The simulated voxel sizes were correlated to the *Rz* parameters following the same considerations described in section 6.3 for the experimental investigations. Maximum voxel sizes up to 3*Rz* were chosen in order to investigate the effects of voxel sizes definitely bigger than the *Rz* parameters. Thus a number of 1620 images for each of the 23 profiles was obtained leading to a total number of 37260 images. It is therefore evident how it is not possible to experimentally obtain such a high number of datasets and how the developed simulation campaign enables to investigate a significant number of different cases.

6.4.3. Data evaluation

After all the 37260 images were generated, they were processed using a subpixel edge detection algorithm implemented in Matlab [126].
After the edge detection, from the extracted profiles, the least-squares diameters were evaluated for each of the 37260 images using Matlab.

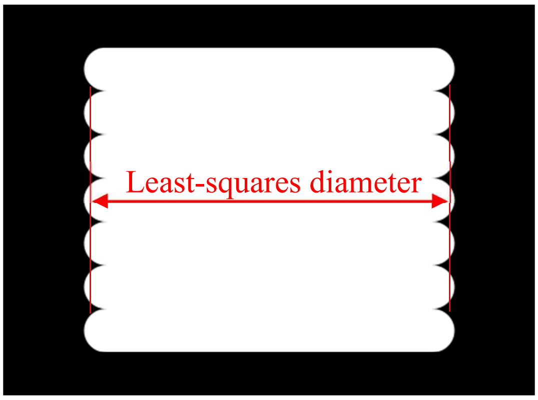

Figure 6.42: Schematic representation of an ideal FDM section with the measurands of interest for the simulation investigation.

As it was done for the experimental analysis in section 6.3 the "CT simulated" diameters obtained with the process described before were compared with reference measurements. The reference diameters used in this case are, for each of the sections featuring the profiles of Table 6.5, the diameters computed from the corresponding analytical profiles using only the extreme peak points in order to reproduce ideal CMM measurements probing only the peaks of the profiles.

6.4.4. Simulated results

In the following sections, the main results obtained from the simulations campaign are presented and discussed.

6.4.4.1. Effects of surface morphology and voxel size on least-squares diameters

As it was described in section 6.3 for the experimental investigations, also in this case the same graph of Figure 6.28 is built in order to analyze the measured least-squares diameters for the simulated images, and it is reported in Figure 6.43.

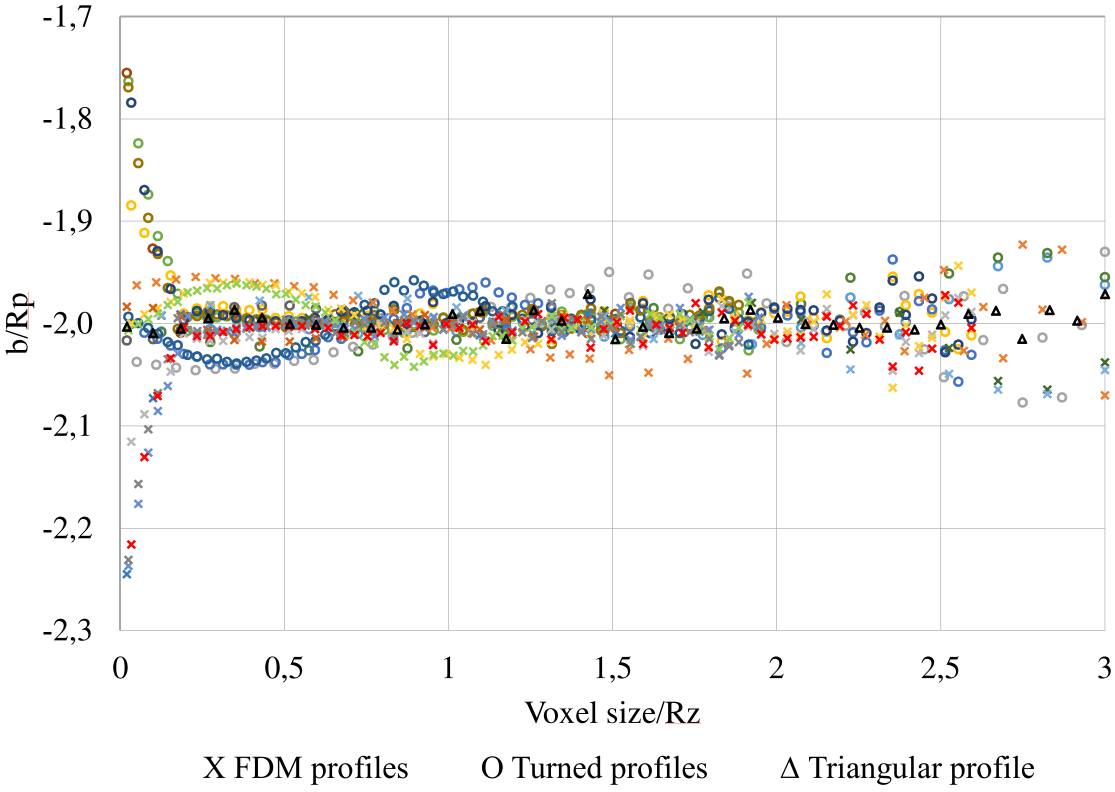

Figure 6.43: Measurement results obtained for least-squares diameter measurements from the numerical simulations. Each point in the graph represents the mean value calculated from 81 images simulated in order to take into account the partial volume effect. FDM type profiles are represented as crosses, turned profiles as circles, and triangular profiles as triangles. Different colors represent different surface profiles [122].

The ratios *b/Rp* (vertical axis of the graph) and *voxel size/Rz (*horizontal axis of the graph*)* were used for analyzing the results in order to compare different profiles with various characteristics. In this case however, *b* expresses the deviation calculated as the difference between the measured least-squares diameters from the simulated CT images and the reference diameters computed, for each profile, using only the extreme peak points from the analytical profile in order to reproduce ideal CMM measurement probing only the peaks of the profile.

FDM type profiles are represented with crosses whereas turned profiles and the triangular profile are represented respectively with circles and a triangle. The different colors represent profiles with different characteristics (e.g. different *Rz* and *RSm* values). Each point represented in the graph is obtained as the average of 81 images, simulated in order to take into account the partial volume effect as described in section 6.4.2.1.

As visible, the simulation results show that the mean deviations between least-squares diameters and reference diameters are constantly around 2*Rp* on average and do not present a dependency from the profile roughness characteristics. In fact, the profiles reported in Figure 6.41 are characterized by completely different material distributions (i.e. FDM type, turned and triangular) and different roughness parameters (e.g. *Rp*, *Rz* and *RSm*). In particular, simulation results are in between *b/Rp*=1.9 and *b/Rp*=2.1.

From Figure 6.43 it is visible however how, for specific profiles, for *voxel size/Rz* ratios smaller than 0.2, the results obtained from the profiles characterized by the steepest peaks or valleys (i.e. the FDM and turned profiles with smaller *RSm/Rz* ratio) present larger deviations which exceed the range between 1.9 and 2.1 times the *b/Rp* ratio. This behavior was found to be caused by the edge detection algorithm. In proximity of the very sharp peaks or valleys that characterize the FDM and turned profiles with smaller *RSm/Rz* ratios considered in the simulation analysis, for example the ideal FDM and turned profiles characterized by perfect semi-circumferences, the algorithm generates a distortion of the extracted edge surface. Due to this a too high number of fitting points for the least-squares diameter measurements are selected around these peaks or valleys, causing the observed deviations [122].

When using large voxel sizes the expected standard deviations increase; for example, when using the subpixel edge location algorithm based on partial area effect, standard deviations were found to be within 3% of the voxel size.

Besides the previously reported considerations on least-squares diameter measurements performed on profiles with different Abbot-Firestone curves, the simulation results show also how, profiles with the same material distributions but different roughness parameters, i.e. profiles that are just scaled in dimensions, lead to exactly overlapping measurement results.

Comparing the simulation results reported in Figure 6.43 to the experimental results described in Figure 6.28, it can be seen how the obtained results are in good agreement.

The simulation analyses here presented therefore show how, when measuring least-squares diameters on CT simulated sections, the least-squares diameters, on average present *2Rp* deviations from the reference diameter measurements acquired on the peaks of the profile. Simulation results show that the mean deviations of 2*Rp* take place independently from the profile roughness characteristics.

6.4.4.2. Surface roughness effects on maximum and minimum diameters

Although it was shown that the surface morphology does not significantly affect the least-squares diameter measurements on the CT simulated sections, it is worth analyzing visually what happens when imaging different profiles with various voxel sizes. In section 6.3 it has been already shown experimentally how CT surface filtering characteristics affect the roughness profile description and how this description is highly dependent also on the profile morphology. As discussed in fact, CT technique is affected by the partial volume effect, because of which the voxels in proximity of the actual surface are characterized by intermediate grey values which depend on the percentage of material contained in the voxels. In fact, as discussed above voxels contain grey value information which are used by the surface determination algorithm in order to determine the CT surface of the object. However, the grey value of each voxel provides an average information on the content of material on each voxel but not how this material is distributed. In the surface determination step, by mean of specific algorithms, typically with sub-voxels accuracy, the object surface is located making use of the grey level information. It comes that roughness profiles with extremely sharp peaks (or valleys) will be characterized by lower material percentages on the peaks (or valleys) with respect to profiles characterized by very rounded peaks (or valleys). This affects the roughness profile description.

Figure 6.44 reports examples of some of the images of the ideal turned profile (characterized by perfect semi-circumferences and *Rz*= 125 µm and *RSm*= 250 µm) and of the turned profile (characterized by *Rz*= 50 µm and *RSm*= 556 µm) simulated with different voxel sizes. For each profile, the images provided are shown with the same displacement (see section 6.4.2.1). The comparison between these two profiles is provided because, although being both turned profiles they present significantly different material distribution properties. While the first one is characterized by a low *RSm*/*Rz* ratio and present extremely sharp peaks, the second one is characterized by a high *RSm*/*Rz* ratio and the material distributed on the peaks is more than in the previous case (i.e. the peaks are less sharp).

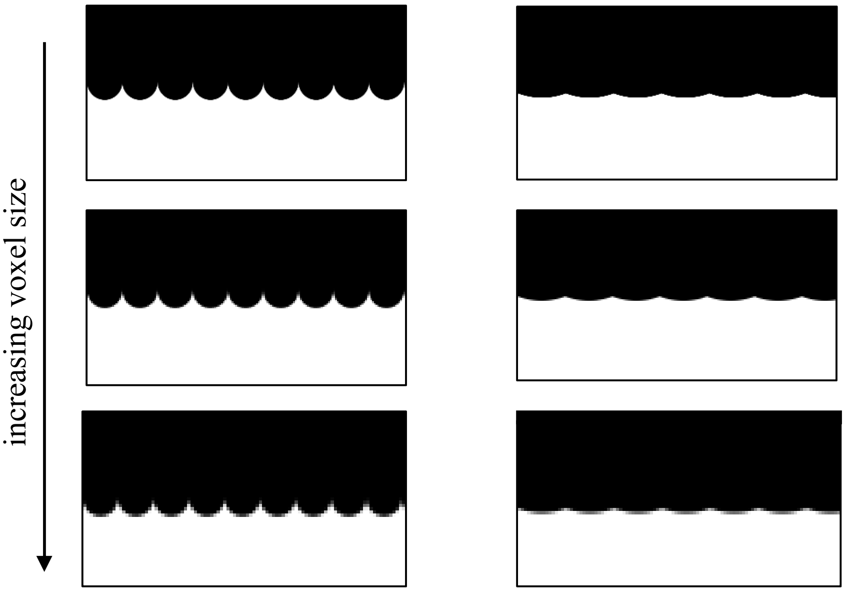

Figure 6.44: Images of the ideal turned profile composed of semi-circumferences and characterized by Rz=125µm and RSm=250µm and of the turned profile characterized by Rz=50 µm and RSm=556 µm. The profile with Rz=125µm and RSm=250µm is shown on the left hand side of the image, whereas the profile of Rz=50 µm and RSm=556 µm is shown on the right side of the image.

As visible from Figure 6.44 when increasing the voxel size both profiles are imaged in a different way. The filtering effects caused by the voxel size and its interaction with the particular surface morphology affect the maximum and minimum diameter measurements.

Figure 6.45 reports the maximum and minimum diameter measurements obtained for the two profiles represented in Figure 6.44. Each point of the graph represents the average of 81 different images obtained with different displacements of the profile inside the voxel grid in order to take into account the partial volume effect.

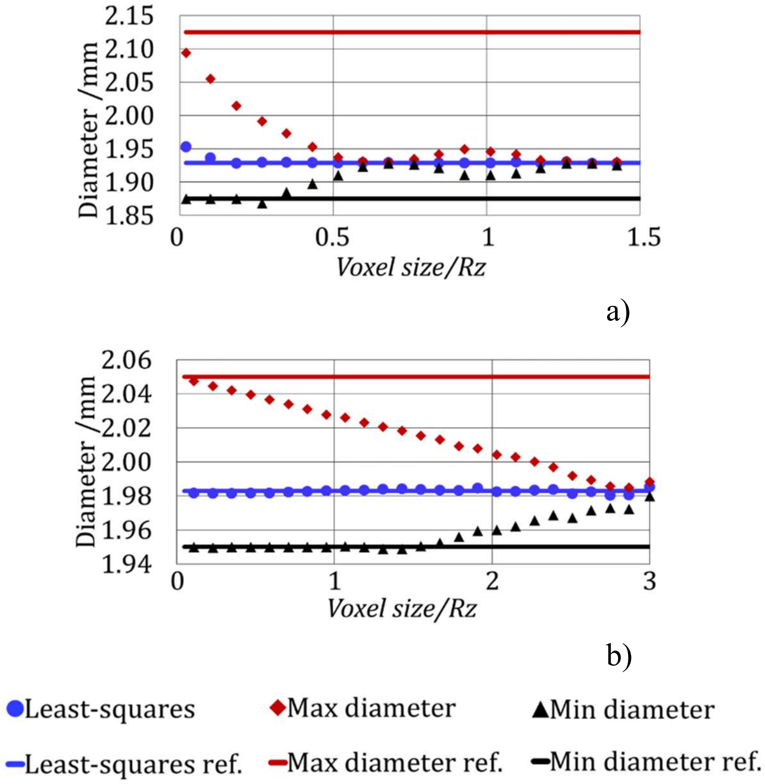

Figure 6.45: Maximum and minimum diameter measurements obtained for different voxel sizes for a) ideal turned profile composed of semi-circumferences and characterized by Rz=125µm and RSm=250µm, b) a turned profile characterized by Rz=50 µm and RSm=556 µm [122].

From Figure 6.45 a) it can be noted how maximum and minimum diameters are significantly affected by the voxel size. As described in section 6.3 for the experimental results, with increasing voxel size CT filters out the higher frequencies, and the profiles appear to be smoothen. This reflects also on the maximum and minimum diameter measurements.

Figure 6.45 a) shows how in the case of an ideal turned profile characterized by semi-circumferences the maximum diameter is highly affected by the voxel size dimensions. In particular, with increasing voxel size the maximum diameter rapidly decreases because the sharp roughness peaks are filtered out, and it tends to converge to the measured least-square diameter. The minimum diameter instead presents two different behaviors. In a first small region of the chart, characterized by small voxel sizes, the minimum diameter remains constant. When the voxel size increases, due to the voxel dimensions, the valleys are also filtered by the voxel size and the minimum diameter starts increasing and tends to the measured least-square diameter. Figure 6.45 b) reports the measurement results obtained for maximum and minimum diameters in the case of the turned profile characterized by *Rz*=50 µm and *RSm*=556 µm. Also in this case it is visible how the maximum and minimum diameters are affected by the voxel size dimensions. Comparing the results of Figure 6.45 a) and b) it is also visible the effect of the surface morphology on maximum and minimum diameters measurements. In Figure 6.45 b) in fact, the maximum diameter presents a less rapid decrease with respect to Figure 6.45 a) and tends to converge to the least-squares diameter for bigger voxel sizes. This is because the profile of Figure 6.45 b) is characterized by a different material distribution and features less sharp peaks than the ones of the ideal turned profile composed of semi-circumferences. For this reason, the surface filtering operated by the voxel size is different with respect to the one of Figure 6.45 a). When analyzing the minimum diameters as well the profile of Figure 6.45 b) presents a less rapid increase and the initial region were the minimum diameter remains almost constant is bigger than in the case of the ideal turned profile composed of semi-circumferences. This is because for the profile characterized by Rz=50 µm and RSm=556 µm the valleys are much wider. This is also visible from Figure 6.44. For this reason, the minimum diameter tends to converge to the least-squares diameter for bigger voxel sizes.

From these charts it is evident therefore that maximum and minimum diameters are significantly affected by the voxel size due to the surface filtering it produces. Moreover, the surface filtering is different depending on the particular surface morphology. For given turned or FDM type profiles, the bigger it the RSm/Rz ratio, the smaller is the filtering produced by the voxel size. This is because CT technology is based on the attenuation of the X-rays and the way in which a profile is described depends on the voxels grey values and thus the percentage of material contained in each voxel. Profiles characterized by extremely sharp peaks or valleys therefore will be more problematic because the narrow and sharp peaks and valleys occupy a small part of the voxel even though the voxel size is really small. For this reason, the sharp peaks and valleys will be subject to a higher surface filtering.

This filtering is mainly caused by the voxel size dimensions, however also other factors that occur in real measurements such as the blurring caused by the focal spot dimensions can contribute to this filtering. For example, when the unsharpness caused by the finite focal spot dimensions [1] is of the same order of magnitude or bigger than the voxel size, the focal spot effects on the CT surface filtering characteristics become relevant. When analyzing the CT surface filtering characteristics, the surface determination algorithm is of high importance. In the surface determination phase in fact, the grey level information contained in the voxels are converted into point coordinates information of the points belonging to the object. Depending on the type of algorithm used therefore the voxel grey levels can be treated differently. In particular algorithms characterized by a voxel accuracy will produce higher deviations with respect to algorithms characterized by a sub-voxel accuracy. Maximum and minimum diameters therefore will be significantly influenced by the surface determination algorithm.

6.5. Conclusions

In this chapter the influence of surface roughness on CT dimensional measurements on periodic roughness profiles has been investigated by mean of experimental and simulation analyses.

For the experimental investigation three dedicated cylindrical test objects were specifically designed and manufactured by mean of two different manufacturing processes, FDM and turning and a combination of them. The use of these production processes enabled to obtained samples characterized by significantly different material distributions: i.e. the FDM sample is characterized by a high amount of material on the peaks and narrower and sharper valleys, whereas the turned samples are characterized by much less material distributed on the peaks which are much sharper and narrow then the FDM peaks. The influence of surface roughness on CT least-squares diameter measurements was thus studied by performing repeated CT scans of the various samples at different voxels sizes. The voxel sizes were chosen based on the *Rz* parameter of the scanned workpieces in order to perform CT scans with a voxel size smaller than *Rz*, of the same order of magnitude of *Rz* and bigger then *Rz*. Additional voxel sizes were also investigated in order to have a good mapping of the voxel size effect.

The experimental results show how CT measured least-squares diameters on the outer surfaces of the samples are always smaller than reference measurements, whereas CT measured least-squares diameters on the inner surfaces of the FDM sample (which was purposefully produced with a hollow cylindrical geometry) are always bigger than reference measurements. Moreover, this difference was found to be for all the investigated measurands of approximately 2*Rp* on average. Surface roughness therefore produces a systematic error between CT measurements and reference measurements acquired on the peaks of the roughness profile the reason of which is identified to be the different measuring principles on which CT and tactile CMMs rely on. The systematic error caused by surface roughness was confirmed for the different voxel sizes investigated and up to 125 µm used in this work. It was also experimentally demonstrated how, although the 2*Rp* systematic error is present for all the voxel sizes investigated in this work, the various samples are affected by a surface filtering due to the voxel size dimensions. In particular, this surface filtering is a low pass filtering which cut off high frequency components. The bigger is the voxel size and in general the worst is the CT structural resolution the bigger is the surface filtering that occurs. Peaks and valley moreover are filtered in a different way depending on the particular surface morphology. Additional investigations were also conducted in order to investigate the influence of post-processing parameters on CT dimensional measurements. When dealing with highly rough surfaces it is fundamental that the point fitted in the CT volume are well distributed on the whole roughness profile detected by CT. Software parameters therefore need to be optimized in order to do not discard points on specific regions of the profile. The spacing grid of the fit points was found to affect CT least-squares diameter measurements. When the spacing grid is to big additional measurement errors occurs. It is therefore necessary to always optimize the post-processing parameters depending on the specific characteristic of the workpiece under investigation.

The knowledge of the effects caused by surface roughness on CT dimensional measurement on periodic roughness profiles is also important for CT measurement uncertainty determination. One of the methods which is typically used to determine CT measurement uncertainty is based on the ones described in ISO 15530-3 for CMMs. Previous work in literature suggested to treat surface roughness effect as an uncertainty component and add it to the uncertainty budget determined according to ISO 15530-3. However, when dealing with high surface roughness this approach leads to a high overestimation of measurement uncertainty. It was experimentally demonstrated how the correction of roughness systematic errors, in accordance to the GUM which prescribes to correct known systematic errors, leads to a strong decrease of CT measurement uncertainty.

Simulated analyses were performed with a Matlab routine in order to extend the study on a set of simulated CT sections (2D images) of cylinders in accordance to the experimental analyses, reproducing a high number of different roughness profiles (e.g. FDM, turned, triangular). Each profile was imaged at various voxel sizes and considering several different positions inside the pixel grid to take into account the partial volume effect which affects CT measurements. Simulation results also show that the mean deviations between least-squares diameters and reference diameters of $2Rp$ take place independently from the profile roughness characteristics. However, when using large voxel sizes, the expected standard deviations increase; for example, when using the subpixel edge location algorithm based on partial area effect, standard deviations were found to be within 3% of the voxel size.

The effect of surface roughness in this work was investigated by performing diameter measurements on cylindrical parts. However, it could be generalized also for other types of measurements (e.g. position of flat surfaces) by considering an offset equal to Rp of the CT least-squares surface from the reference surface measured on the peaks.

It was also shown that the CT surface filtering that occurs when varying the voxel size, has a significant effect on maximum and minimum diameters evaluated from the CT simulated images. The combined effect of profile morphology and voxel size is significantly stronger in this case of maximum and minimum diameter measurements than for least-squares diameters, and produces larger deviations for steeper peaks/valleys.

Chapter 7

Conclusions

The research presented throughout this PhD thesis focused on the study of measurement traceability, and the accuracy enhancement in industrial computed tomography for coordinate metrology. X-ray CT in fact, in the recent years has demonstrated to provide unique advantages in the field of coordinate metrology, enabling the possibility to perform a wide variety of measurement tasks that often are not possible with conventional measuring systems such as tactile and optical CMMs. This is possible thanks to CT working principle which allows for the acquisition of a 3D model of the scanned object containing dense volumetric data. For example, one significant advantage that CT provides is the ability to perform dimensional and geometrical measurements of inner features non accessible by tactile and optical CMMs, without any need to cut or destroy the component. The use of X-ray CT systems as non-contact coordinate measuring systems therefore has opened new horizons in the field of industrial metrology and manufacturing engineering. In order to use CT systems as coordinate measuring systems capable of providing accurate and reliable measurements however CT measurement traceability has to be established and the accuracy of CT measurements has to be studied. One fundamental requirement in order to enable traceable and accurate measurements with CT is the identification, understanding and study of the influence factors affecting CT measurements and the determination of the measurement errors they produce as well as the sensitivity of CT measurement results to the specific error sources. The determination of the effects and measurement errors caused by the influence quantities affecting CT measurements is fundamental for determining CT task specific measurement uncertainty which is necessary in order to obtain CT measurements traceability, and in order to enhance CT measurement accuracy by properly correcting for these errors or optimizing CT scanning measurement procedures. Moreover, the accuracy of CT measurements can be enhanced also by considering new scanning technologies in the field of CT dimensional metrology such as helical scanning trajectories. In this case however, new influence factors will be present and need to be analyzed.

This PhD thesis is divided mainly into four parts, related to the above mentioned research needs, the main conclusions of which are presented in the following.

In the first part of the thesis (chapter 1-chapter 3), an overview of the role of industrial computed tomography in the coordinate metrology field is provided together with the description of X-ray CT working principle and CT measurement chain. The main applications and advantages that CT provides with respect to classical CMMs are presented and discussed.

The concepts of metrological traceability and accuracy, and the role of traceability in dimensional metrology are discussed. Specifically, in chapter 3 the state of the art in the international framework for the standardization of CT in the field of dimensional metrology is reviewed and discussed. The procedures and methods for metrological performance verification, and measurement uncertainty determination are analyzed. The influence factors affecting CT measurement chain are discussed and grouped into categories. The needs in order to establish CT measurement traceability and enhance the accuracy of CT measurements are studied and a discussion is provided.

The CT system geometrical errors are, among the influence factors affecting CT measurement chain, of primary importance and thus were studied and analyzed in the second part of the thesis (chapter 4). As for classical CMMs and most precision measuring instruments the design of a CT system involves the assembly of several components; the physical structure of a CT system itself is a source of measurement uncertainty. In a CT system the most important components are the X-ray source, the rotary table and the detector. These components need to be carefully aligned to obtain accurate measurements. The system geometry provides the necessary information to fully describe the geometry of data acquisition and performing the tomographic reconstruction on which all the dimensional analyses are based. Thus an error in the CT system geometry used for reconstruction affects all the subsequent steps in the measurement chain.

In chapter 4 the CT system geometrical errors are first analyzed and studied in detail from a theoretical point of view making use also of the literature of classical CMMs, and the possible geometrical errors affecting a CT system are described and reviewed. Then three different experimental campaigns specifically designed and involving the use of tactile CMM calibrated reference objects are presented together with a detailed description and discussion of the obtained measurement results. The work was performed in collaboration with North Star Imaging Inc. In the first of the experimental campaigns the effects of the detector angular misalignments, namely detector pitch, yaw and roll, on measurements performed in the vertical direction were studied by mean of a calibrated ball bar featuring 7 equally spaced spheres. These misalignments were physically induced on a flat-panel detector, and different amplitudes of misalignment (i.e. 0.5°, 1°, 1.5°) were induced for detector pitch, yaw and roll for a total of 9 misaligned configurations. The obtained measurement results enable to identify the characteristic symmetric measurement errors produced by detector pitch on sphere-center-to-center distances and sphere diameter measurements performed on a ball bar oriented in the vertical direction.

In particular, in the experimentally tested conditions it was found that distances between spheres positioned above the central plane of the detector and distances between spheres positioned at symmetrically opposite position below the central plane of the detector present equal and opposite errors. The lengths which comprise points symmetric about the central horizontal axis of the detector are characterized by a smaller error because they have opposite errors that cancel out.

While it was found that the primary effect of the investigated detector pitch is on sphere center-to-center measurements and diameter measurements, detector yaw affects mainly form measurements. Detector roll instead produces a high distortion of the CT volume which is extremely significant already with a 0.5° misalignment. The results obtained showed a dependency of the measurement error on the amplitude of the misalignment and suggested also a dependency with the measurement direction and object positioning on the measurement volume. For this reason, a second experimental campaign was designed using a calibrated ball plate featuring 25 ruby spheres. Detector pitch, yaw, and roll were mechanically induced on a flat-panel detector, and 3 amplitudes of misalignment (0.5°, 1°, 1.5°) were considered for each of the misalignments. Each scan was repeated 3 times for a total of 27 scans and 9 misaligned configurations. The obtained measurement results enable to quantitatively determine identify and map the dependency of the measurement errors, in presence of the different misalignments, with the measurement direction and object positioning in the measurement volume. In particular, the considered detector pitch about the central horizontal axis of the detector was found to produce symmetric errors in the vertical measurement direction and scaling errors in the horizontal direction. In the experimentally tested conditions, the 50 vertical center-to-center distance measurements performed on the ball plate (i.e. measurements between spheres belonging to the same column) exhibit a specific trend about the central horizontal axis of the detector, and this behavior does not vary with the detector columns, i.e. the horizontal position of the column does not affect the measurement errors. The 50 horizontal measurements, i.e. measurements between spheres belonging to the same row, are affected by scaling errors which increase with increasing vertical distance of the rows from the central plane of the detector (and with increasing amplitude of the misalignment). These scaling errors are caused by the magnification errors which are responsible of the symmetric behavior found for the vertical measurements. The magnification errors increase by vertically moving away from the central plane of the detector and are generated due to the induced detector pitch. Sphere center-to-center distances and diameter measurements are thus significantly affected by detector pitch, and the errors increase with the amplitude of the misalignments and vertical distance from the center of the detector, and in the case of horizontal center-to-center measurements with the measured distance. Form errors instead were found not to be affected by the detector pitch investigated up to 1.5°. Detector yaw was found to influence the image quality of the CT scans and mainly the form errors. Also in this case the form errors increase with the amplitude of the misalignment. Specifically form errors increase with increasing horizontal distance of the spheres from the center of the detector. Detector roll produces the highest errors among the detector misalignments experimentally tested, and causes strong distortions on the CT volume. For detector roll, diameter errors and form errors were found to increase with the radial distance from the center of the detector.

In order to compare the effects of misalignments on the different components of a CT system, rotary table misalignments were studied. In particular, rotary table horizontal shifts were mechanically induced in the rotary table, and the calibrated ball plate was CT scanned. Three different amplitudes of horizontal shifts were considered ranging from 40 µm to 120 µm. The measurement errors on sphere center-to-center measurements, diameter measurements and form measurements were determined. The experimental results showed how this kind of rotary table misalignment strongly affects image quality causing blurry edges in all the spheres of the plate. This blurring increases with the amplitude of the misalignment. In particular diameter errors and form errors are mostly affected by this misalignment.

Thanks to the studies performed the measurement errors caused by each specific geometrical misalignment were determined and characterized. The detailed comprehension and quantification of the effects of geometrical misalignments is an essential step to achieve the development of calibration procedures for CT systems and to obtain traceable CT measurements which is the final aim of CT metrology. Knowing which effects are produced by each misalignment, and which is the sensitivity of CT measurements to the particular misalignment enables also to enhance CT measurement accuracy.

The measurement errors affecting CT measurements are also caused by other influencing factors such as the cone-beam artifacts which inherently characterize CT cone-beam circular trajectories. The third part of this PhD thesis concerns the investigation of the metrological performances of CT helical scanning for coordinate metrology, and in particular the study of the main influence quantities that affect CT helical scanning and the determination of its measurement errors. CT helical scanning measurement errors are also compared to traditional circular scans, the limits of which are experimentally shown and analyzed. The work was carried out in collaboration with North Star Imaging Inc.

CT helical scanning is an alternative scanning method that, when using suitable scanning parameters can provide significant advantages compared to traditional circular scanning trajectories. These advantages include the ability of scanning long objects exceeding the dimensions of the detector in one single scan, the enhancement of scan resolution, the possibility to eliminate the cone-beam artifacts and to improve CT scanning parameters. Despite its well-known use in the medical field, the use of CT helical scanning is under-utilized in industrial practice, specifically for industrial metrology purposes. This is mainly because of the additional complexity that this kind of technology requires. The investigation of CT helical scanning metrological performances and the analyses of the measurement errors caused by the main influence quantities are an essential requirement for the use of CT systems using helical scanning principles as coordinate measuring systems (CMSs), and a detailed description still lacks in the literature.

In the first part of chapter 5, a detailed overview of helical scanning principles is presented and the advantages that helical scanning provides for industrial metrology applications are studied and discussed.

The measurement errors caused by cone-beam artifacts for conventional cone-beam circular trajectories were studied and determined by performing an experimental investigation using a tactile CMM calibrated ball bar featuring 15 equally spaced ceramic spheres that homogeneously covered the detector surface vertically. Different cone-angles ranging from 25.6° to 10.7° were experimentally studied in order to quantitatively determine the effects of cone-beam artifacts on CT measurements. The probing error of form was found to be the metrological characteristic which is the most highly influenced by the presence of cone-beam artifacts. The bigger is the cone-angle and the bigger is the distance from the central plane of the detector the higher the measured probing errors of form. Sphere center-to-center measurements and diameter measurements were also found to be affected by the cone-beam artifacts. In particular sphere center-to-center measurements are characterized by a specific trend which is caused by the cone-beam artifacts. The distances between spheres positioned further away from the central plane of the detector and spheres close to the central plane of the detector present the biggest errors. Also for diameter measurements and sphere center-to-center measurements the cone-beam artifact effects increase with the cone-angle.

The metrological performances of CT helical scanning were experimentally investigated and compared to the ones of conventional cone-beam circular trajectories. A calibrated ball bar was used for the experimental investigation. The use of helical trajectories causes the presence of additional scanning parameters that influence the accuracy of CT measurements. A DoE was performed in order to investigate the influence of the main helical scanning parameters on the metrological characteristics sphere distance errors *SD*, probing errors of size *PS* and probing errors of form *PF*. Nine helical scanning set-up characterized by three different helical pitch and three different number of projections were investigated by performing repeated CT scans. The experimental results proved that the use of helical scanning trajectories can reduce significantly the measured probing errors of form. Moreover, for all the nine investigated scanning set-up, the probing errors of form are not dependent on the location of the sphere from the mid plane of the detector and uniform probing errors of form can be obtained for all spheres, even for those at top and bottom of the detector. The helical pitch was found to have a strong influence on the measured *PF*. When decreasing the helical pitch, the *PF* decreases. The influence of the number of projections is less pronounced than the one of the helical pitch, increasing the number of projections decreases the probing errors of form. The experimental results proved that by using a helical pitch of the same dimensions of the characteristics to be inspected a significant enhancement of helical scanning accuracy is achieved. Probing errors of size and sphere distance errors were also calculated. Experimental results show no significant influence of the parameters helical pitch and number of projections for the experimentally tested conditions.

The experimental investigations conducted prove that helical scanning, with appropriate scan parameters, can perform even better than traditional circular scans with a strong improvement on image quality and measurement accuracy. This leads to strong benefits on several industrial metrology applications.

Due to the wide application of CT in several industrial markets, extremely different components undergo dimensional quality control by CT. The scanned components are often characterized by high surface roughness. This is for example the case of workpieces produced by the newly developed additive manufacturing technologies. In chapter 6 of this thesis the measurement errors due to surface roughness on CT dimensional measurements on periodic roughness profiles were determined by mean of experimental and simulation analyses. Surface roughness effects were studied taking into account the combined effects of surface morphology and CT surface filtering characteristics.

First the different measuring principles of CT and conventional tactile CMMs are reviewed and compared. Then a study was performed in order to design and develop the experimental and simulation analyses by using the concepts of surface roughness characterization and studying them in relation to CT dimensional measurements.

For the experimental investigations three dedicated cylindrical test objects were specifically designed and manufactured by mean of two different manufacturing processes, FDM and turning and a combination of them in order to obtain samples characterized by significantly different material distributions. CMM measurements of least-squares diameters were performed for all the three samples. The influence of surface roughness on CT least-squares diameter measurements was investigated by performing repeated CT scans of the various samples at different voxels sizes. The experimental results show how CT measured least-squares diameters on the outer surfaces of the samples are always smaller than reference measurements, whereas CT measured least-squares diameters on the inner surfaces of the FDM sample (which was purposefully produced with a hollow cylindrical geometry) are always bigger than reference measurements. By studying the obtained results in relation to the roughness parameters of the investigated samples it was determined that the difference between the CT measured least-squares diameters and the reference diameters is related to the *Rp* surface roughness parameter and, for all the investigated measurands of all samples, differences of ca. 2*Rp* are present on average. Surface roughness therefore produces a systematic error between CT measurements and reference measurements acquired on the peaks of the roughness profile the reason of which is identified to be the different measuring principles on which CT and tactile CMMs rely on. The systematic error caused by surface roughness was confirmed for the different voxel sizes investigated and up to 125 µm used in this work. It was also experimentally demonstrated how, although the 2*Rp* systematic error is present for all the voxel sizes investigated in this work, the various samples are affected by a surface filtering due to the voxel size dimensions. In particular, this surface filtering is a low pass filtering which cuts off high frequency components. The bigger is the voxel size and in general the worst is the CT structural resolution the bigger is the surface filtering that occurs. Peaks and valleys moreover are filtered in a different way depending on the particular surface morphology. Additional investigations were also conducted in order to investigate the influence of post-processing parameters on CT dimensional measurements. When dealing with highly rough surfaces it is fundamental that the point fitted in the CT volume are well distributed on the whole roughness profile detected by CT. The spacing grid of the fit points was found to affect CT least-squares diameter measurements. It is therefore necessary to always optimize the post-processing parameters depending on the specific characteristics of the workpiece under investigation. It is also demonstrated how, the knowledge of the effects caused by surface roughness on CT dimensional measurements on periodic roughness profiles is important for CT measurement uncertainty determination. Previous works in literature suggested to treat surface roughness effect as an uncertainty component and add it to the uncertainty budget determined according to ISO 15530-3. However, it is demonstrated in this work how when dealing with high surface roughness this approach leads to a high overestimation of measurement uncertainty. It is experimentally shown how the correction of roughness systematic errors, in accordance to the GUM, leads to a strong decrease of CT measurement uncertainty and to the enhancement of CT measurement accuracy.

Simulated analyses were also performed with a Matlab routine in order to analyze a set of simulated CT sections (2D images) of cylinders in accordance to the experimental analyses, reproducing a high number of different roughness profiles (e.g. FDM, turned, triangular). Each profile was imaged at various voxel sizes and considering several different positions inside the pixel grid to take into account the partial volume effect which affects CT measurements. Simulation results also showed that the mean deviations between CT simulated least-squares diameters and reference diameters of 2*Rp* take place independently from the profile roughness characteristics.

It was also shown that the CT surface filtering that occurs when varying the voxel size, has a significant effect on maximum and minimum diameters evaluated from the CT simulated images. The combined effect of profile morphology and voxel size is significantly stronger in this case of maximum and minimum diameter measurements than for least-squares diameters, and produces larger deviations for steeper peaks and valleys.

The effects of surface roughness which in this thesis were investigated by performing diameter measurements on cylindrical parts, can be generalized also for other types of measurements (for example position of flat surfaces) by considering an offset equal to *Rp* of the CT least-squares surface from the reference surface measured on the peaks.

In this chapter therefore it was proven how the understanding, determination and modeling of the measurement errors caused by specific influence quantities is a fundamental step in order to obtain CT measurement traceability and to enhance CT measurement accuracy.

References

[1] Kruth JP, Bartscher M, Carmignato S, Schmitt R, Chiffre L De, Weckenmann A. Computed tomography for dimensional metrology. CIRP Annals – Manufacturing Technology, 2011;60(2):821–42. doi:10.1016/j.cirp.2011.05.006.

[2] De Chiffre L, Carmignato S, Kruth JP, Schmitt R, Weckenmann A. Industrial applications of computed tomography. CIRP Annals – Manufacturing Technology, 2014;63(2):655–77. doi:10.1016/j.cirp.2014.05.011.

[3] Müller P. (2012) Coordinate Metrology by Traceable Computed Tomography. PhD Thesis. Technical University of Denmark.

[4] Thompson A, Leach R. (2018) Introduction to Industrial X-ray Computed Tomography. In: Carmignato S., Dewulf W., Leach R. (eds) Industrial X-Ray Computed Tomography. Springer, Cham

[5] Hermanek P, Rathore JS, Aloisi V, Carmignato S. (2018) Principles of X-ray Computed Tomography. In: Carmignato S., Dewulf W., Leach R. (eds) Industrial X-Ray Computed Tomography. Springer, Cham

[6] Buratti A, Bredemann J, Pavan M, Schmitt R, Carmignato S. (2018) Applications of CT for Dimensional Metrology. In: Carmignato S., Dewulf W., Leach R. (eds) Industrial X-Ray Computed Tomography. Springer, Cham

[7] ISO 9001:2015. Quality management systems – Requirements. International Organization for Standardisation.

[8] ISO 14253-1:2017. Geometrical product specifications (GPS) – Inspection by measurement of workpieces and measuring equipment – Part 1: Decision rules for verifying conformity or nonconformity with specifications. International Organization for Standardisation.

[9] Feldkamp LA. Practical cone-beam algorithm. Journal of the Optical society of America A, 1984;1(6): 612–9. https://doi.org/10.1364/JOSAA.1.000612.

[10] Buzug TM (2008). Computed tomography: from photon statistics to modern cone-beam CT. Springer Science & Business Media.

[11] Hsieh J. A practical cone beam artifact correction algorithm. Nuclear Science Symposium Conference Record, 2000 IEEE;2:15/71–15/74. doi 10.1109/NSSMIC.2000.950053.

[12] Hsieh J (2003). Computed tomography: principles, design, artifacts, and recent advances (Vol. 114). SPIE press.

[13] Aloisi V, Carmignato S, Schlecht J, Ferley E. Investigation on metrological performances in CT helical scanning for dimensional quality control. In Proceedings of 6th Conference on Industrial Computed Tomography (iCT), 2016.

[14] Sun W, Brown SB, Leach RK. An overview of industrial X-ray computed tomography. NPL, 2012.

[15] Carmignato S, Dreossi D, Mancini L, Marinello F, Tromba G, SavioE. Testing of x-ray microtomography systems using a traceable geometrical standard. Measurement Science and Technology, 2009;20(8): 084021. doi:10.1088/0957-0233/20/8/084021.

[16] Stock SR. Recent advances in X-ray microtomography applied to materials. International Materials Reviews, 2008;53(3):129–81. doi:10.1179/174328008X277803.

[17] Banhart J (2008). Advanced tomographic methods in materials research and engineering (Vol. 66). Oxford University Press.

[18] ISO 15708–1:2002. Non-destructive testing–Radiation methods–Computed tomography –Part 1: Principles. International Organization for Standardization.

[19] Cierniak R (2011). X-Ray computed tomography in biomedical engineering. Springer, London

[20] Cantatore A, Müller P (2011). Introduction to computed tomography. DTU Mechanical Engineering.

[21] Christoph R, Neumann HJ (2011). X-ray Tomography in Industrial Metrology Precise , Economical and Universal. Verlag Moderne Industrie.

[22] Hiller J, Reindl LM. A computer simulation platform for the estimation of measurement uncertainties in dimensional X-ray computed tomography. Measurement, 2012;45(8):2166–82. doi:10.1016/j.measurement.2012.05.030.

[23] Hiller J, Maisl M, Reindl LM. Physical characterization and performance evaluation of an x-ray micro-computed tomography system for dimensional metrology applications. Measurement Science and Technology, 2012;23(8):085404. doi:10.1088/0957-0233/23/8/085404.

[24] Weiß D, Lonardoni R, Deffner A, Kuhn C. Geometric image distortion in flat-panel X-ray detectors and its influence on the accuracy of CT-based dimensional measurements. In Proceedings of iCT conference, 2012.

[25] Aloisi V, Carmignato S, Schlecht J, Ferley E, (2017). Investigation on the effects of X-ray CT system geometrical misalignments on dimensional measurement errors. In Proceedings of 7th Conference on Industrial Computed Tomography (iCT), 2017.

[26] Ferrucci M, Leach R K, Giusca C, Carmignato S, Dewulf W. Towards geometrical calibration of x-ray computed tomography systems—a review. Measurement Science and Technology, 2015;26(9), 092003.

[27] Stolfi A, De Chiffre L, Kasperl S. (2018) Error Sources. In: Carmignato S., Dewulf W., Leach R. (eds) Industrial X-Ray Computed Tomography. Springer, Cham

[28] JCGM 100 (2008). Evaluation of measurement data - Guide to the expression of uncertainty in measurement. Joint Committee for Guides in Metrology.

[29] Weckenmann A, Krämer P. Assessment of measurement uncertainty caused in the preparation of measurements using computed tomography. In Proceedings of the XIX IMEKO World Congress, Fundamental and Applied Metrology, Portugal, 2009:1888–92.

[30] Welkenhuyzen F, Kiekens K, Pierlet M, Dewulf W, Bleys P, Voet A. Industrial Computer Tomography for Dimensional Metrology : Overview of Influence Factors and Improvement Strategies. In Proceedings of the 4th international conference on optical measurement techniques for structures and systems: Optimess2009, 2009:401–10.

[31] Angel J, Chiffre L De, Kruth JP, Tan Y, Dewulf W. Performance evaluation of CT measurements made on step gauges using statistical methodologies. CIRP Journal of Manufacturing Science and Technology, 2015;11:68–72.

doi:10.1016/j.cirpj.2015.08.002.

[32] Weiß D, Shi Q, Kuhn C, Zeiss C, Gmbh IMT. Measuring the 3D resolution of a micro-focus X-ray CT setup. In Proceedings of iCT conference, 2012.

[33] Dewulf W, Tan Y, Kiekens K. Sense and non-sense of beam hardening correction in CT metrology. CIRP Annals – Manufacturing Technology 2012;61(1):495–8. doi:10.1016/j.cirp.2012.03.013.

[34] Tan Y, Kiekens K, Welkenhuyzen F, Angel J, Chiffre L De. Simulation-aided investigation of beam hardening induced errors in CT dimensional metrology. Measurement Science and Technology, 2014;25(6):064014. doi:10.1088/0957-0233/25/6/064014.

[35] Kiekens K, Welkenhuyzen F, Tan Y, Bleys P, Voet A, Kruth JP, Dewulf W. A test object with parallel grooves for calibration and accuracy assessment of industrial computed tomography (CT) metrology. Measurement Science and Technology, 2011;22(11), 115502. doi: https://doi.org/10.1088/0957-0233/22/11/115502

[36] Ontiveros S, Carmignato S, Yagüe-Fabra JA. Fundamental correction strategies for accuracy improvement of dimensional measurements obtained from a conventional micro-CT cone beam machine. CIRP Journal of Manufacturing Science and Technology, 2013;6(2):143–8. doi:10.1016/j.cirpj.2013.02.007.

[37] Yagüe-Fabra JA, Ontiveros S, Jiménez R, Chitchian S, Tosello G, Carmignato S. A 3D edge detection technique for surface extraction in computed tomography for dimensional metrology applications. CIRP Annals – Manufacturing Technology, 2013;62(1):531–4. doi: https://doi.org/10.1016/j.cirp.2013.03.016.

[38] Ontiveros S, Yagüe-Fabra JA, Jiménez R, Tosello G, Gasparin S, Pierobon A, Carmignato S, Hansen HN. Dimensional measurement of micro-moulded parts by computed tomography. Measurement Science and Technology, 2012;23(12):125401. https://doi.org/10.1088/0957-0233/23/12/125401.

[39] Christof Reinhart. Industrial CT & Precision. Conference in "Application of CT Scanning in Industry" at Danish Technological Institute, 2011.

[40] Heinzl C, Kastner J, Gröller E. Surface Extraction from Multi-Material Components for Metrology using Dual Energy CT. IEEE transactions on visualization and computer graphics, 2007;13(6). doi: 10.1109/TVCG.2007.70598.

[41] Heinzl C, Kastner J, Georgi B, Lettenbauer H. Comparison of surface detection methods to evaluate cone beam computed tomography data for three dimensional metrology. In Proceedings of International symposium on digital industrial radiology and computed tomography (DIR), 2007.

[42] Müller P, Cantatore A, Andreasen JL, Hiller J. Computed tomography as a tool for tolerance verification of industrial parts. Procedia CIRP, 2013;10:125–32. doi:10.1016/j.procir.2013.08.022.

[43] Bartscher M, Neuschaefer-Rube U, Wäldele F. Computed Tomography – A Highly potential Tool for Industrial Quality Control and Production near Measurements. VDI BERICHTE, 2004:477-482.

[44] Carmignato S. Computed tomography as a promising solution for industrial quality control and inspection of castings. Metallurgical Science and Tecnology, 2013;30(1).

[45] Thompson A, Maskery I, Leach RK. X-ray computed tomography for additive

manufacturing : a review. Measurement Science and Technology, 2016;27(7): 072001. doi:10.1088/0957-0233/27/7/072001.

[46] Trapet E, Savio E, Chiffre L De, Unimetrik SA. New advances in traceability of CMMs for almost the entire range of industrial dimensional metrology needs. CIRP Annals-Manufacturing Technology, 2004;53(1):433-8. doi: https://doi.org/10.1016/S0007-8506(07)60733-1.

[47] Carmignato S. Accuracy of industrial computed tomography measurements: Experimental results from an international comparison. CIRP Annals – Manufacturing Technology, 2012;61(1):491–4. doi:10.1016/j.cirp.2012.03.021.

[48] Bartscher M, Neukamm M, Hilpert U, Neuschaefer-Rube U, Härtig F, Kniel K, Ehrig K, Staude A, Goebbels J. Achieving traceability of industrial computed tomography. Key engineering materials, 2010;437:79-83. doi: 10.4028/www.scientific.net/KEM.437.79.

[49] JCGM 200 (2012). International vocabulary of metrology – Basic and general concepts and associated terms (VIM) 3rd edition. Joint Committee for Guides in Metrology.

[50] EA-4 / 02 M : 2013. Evaluation of the Uncertainty of Measurement In Calibration.

[51] ISO/IEC 17025:2005. General requirements for the competence of testing and calibration laboratories. International Organization for Standardisation.

[52] Ferrucci M. (2018) Towards Traceability of CT Dimensional Measurements. In: Carmignato S., Dewulf W., Leach R. (eds) Industrial X-Ray Computed Tomography. Springer, Cham

[53] ISO 10360-1:2000. Geometrical Product Specifications (GPS) – Acceptance and reverification tests for coordinate measuring machines (CMM) – Part 1: Vocabulary. International Organization for Standardisation.

[54] Bartscher M, Neuschaefer-Rube U, Illemann J, Borges de Oliveira F, Stolfi A, Carmignato S. (2018) Qualification and Testing of CT Systems. In: Carmignato S., Dewulf W., Leach R. (eds) Industrial X-Ray Computed Tomography. Springer, Cham

[55] BS EN 16016-1:2011. Non destructive testing — Radiation methods — Computed tomography Part 1 : Terminology.

[56] ASTM E1441 – 11. Standard Guide for Computed Tomography (CT) Imaging. American Society for Testing and Materials.

[57] ASTM E1570 – 11. Standard Practice for Computed Tomographic (CT) Examination. American Society for Testing and Materials.

[58] ASTM E1672 – 12 Standard Guide for Computed Tomography (CT) System Selection. American Society for Testing and Materials.

[59] ASTM E1695 – 95(2013). Standard Test Method for Measurement of Computed Tomography (CT) System Performance. American Society for Testing and Materials.

[60] ASTM E1935 – 97(2013). Standard Test Method for Calibrating and Measuring CT Density. American Society for Testing and Materials.

[61] Bartscher M, Illemann J, Neuschaefer-rube U. Evaluation ISO test survey on material influence in dimensional computed tomography. Case Studies in Nondestructive Testing and Evaluation, 2016;6:79–92. doi:10.1016/j.csndt.2016.04.001.

[62] Bartscher M, Sato O, Frank H, Neuschaefer-Rube U. Current state of standardization in the field of dimensional computed tomography. Measurement Science and Technology, 2014;25(6):064013. doi:10.1088/0957-0233/25/6/064013.

[63] VDI/VDE 2630-1.2 (2010). Computed tomography in dimensional measurement – Influencing variables on measurement results and recommendations for computed tomography dimensional measurements. VDI, Dusseldorf.

[64] VDI/VDE 2630-1.1 (2016). Computed tomography in dimensional measurement – Fundamentals and definitions. VDI, Dusseldorf.

[65] VDI/VDE 2630-1.3 (2011). Computed tomography in dimensional measurement – Guideline for the application of DIN EN ISO 10360 for Coordinate Measurement Machines with CT sensors. VDI, Dusseldorf.

[66] VDI/VDE 2630-2.1 (2015). Computed tomography in dimensional measurement – Determination of the uncertainty of measurement and the test process suitability of coordinate measurement systems with CT sensors. VDI, Dusseldorf.

[67] Stolfi A, De Chiffre L. Interlaboratory comparison of a physical and a virtual assembly measured by CT. Precision Engineering, 2017. doi:10.1016/j.precisioneng.2017.08.018.

[68] Wilhelm RG, Hocken R, Schwenke H. Task specific uncertainty in coordinate measurement. CIRP Annals – Manufacturing Technology, 2001;50(2): 553-563. doi: https://doi.org/10.1016/S0007-8506(07)62995-3.

[69] Hansen HN, Chiffre L De. An industrial comparison of coordinate measuring machines in Scandinavia with focus on uncertainty statements. Precision engineering, 1999; 23(3):185-195. doi: https://doi.org/10.1016/S0141-6359(99)00009-4.

[70] ISO 10360-2:2009. Geometrical product specifications (GPS) – Acceptance and reverification tests for coordinate measuring machines (CMM) – Part 2: CMMs used for measuring linear dimensions. International Organization for Standardisation.

[71] ISO 10360-5:2010. Geometrical product specifications (GPS) – Acceptance and reverification tests for coordinate measuring machines (CMM) – Part 5: CMMs using single and multiple stylus contacting probing systems. International Organization for Standardisation.

[72] Zanini F, Balcon M, Carmignato S, 2014. ISO TC 213 WG 10 experimental study on material influence in dimensional computed tomography-Report of tests performed at University of Padova.

[73] Hermanek P, Oliveira FB De, Carmignato S, Bartscher M. Experimental investigation of new multi-material gap reference standard for testing computed tomography systems. In Proceeding of 7th Conference on Industrial Computed Tomography (iCT), 2017.

[74] ISO/TS 23165:2006. Geometrical product specifications (GPS) – Guidelines for the evaluation of coordinate measuring machine (CMM) test uncertainty. International Organization for Standardisation.

[75] Illemann J, Bartscher M, Jusko O, Härtig F, Neuschaefer-Rube U, Wendt K. Procedure and reference standard to determine the structural resolution in coordinate metrology. Measurement Science and Technology, 2014;25(6):064015.

doi:10.1088/0957-0233/25/6/064015.

[76] Carmignato S, Pierobon A, Rampazzo P, Parisatto M, Savio E. CT for Industrial Metrology – Accuracy and Structural Resolution of CT Dimensional Measurements. In Proceeding of Conference on Industrial Computed Tomography (iCT), 2012.

[77] Bartscher M, Bremer H, Birth T, Staude A, Ehrig K. The resolution of dimensional CT − an edge-based analysis. In Proceeding of Conference on Industrial Computed Tomography (iCT), 2012.

[78] Zanini F, Carmignato S. Experimental investigations on the structural resolution in metrological computed tomography. In Proceeding of 7th Conference on Industrial Computed Tomography (iCT), 2017.

[79] Arenhart FA, Baldo CR, Fernandes TL, Donatelli GD. Experimental Investigation of the Influencing Factors on the Structural Resolution for Dimensional Measurements with CT Systems. In Proceeding of 6th Conference on Industrial Computed Tomography (iCT), 2016.

[80] Zanini F, Carmignato S. Two-spheres method for evaluating the metrological structural resolution in dimensional computed tomography. Measurement Science and Technology, 2017;28(11), 114002.

[81] Dewulf W, Kiekens K, Tan Y, Welkenhuyzen F, Kruth J. Uncertainty determination and quantification for dimensional measurements with industrial computed tomography. CIRP Annals – Manufacturing Technology, 2013;62(1):535–8. doi:10.1016/j.cirp.2013.03.017.

[82] Schmitt R, Niggemann C. Uncertainty in measurement for x-ray-computed tomography using calibrated work pieces. Measurement Science and Technology, 2010;21(5);054008. doi:10.1088/0957-0233/21/5/054008.

[83] Bartscher M, Hilpert U, Fiedler D. Determination of the Measurement Uncertainty of Computed Tomography Measurements Using a Cylinder Head as an Example. Technisches Messen, 2008;75(3):178–86. doi:10.1524/teme.2008.0822.

[84] Wenig P, Engineering E. Examination of the Measurement Uncertainty on Dimensional Measurements by X-ray Computed Tomography. In Proceedings of 9th European Conference on Non-Destructive Testing (ECNDT), 2006.

[85] JCGM 101 : 2008. Evaluation of measurement data – Supplement 1 to the “ Guide to the expression of uncertainty in measurement ” – Propagation of distributions using a Monte Carlo method.

[86] Trenk M, Franke M, Schwenke H. The “ Virtual CMM ” a software tool for uncertainty evaluation – practical application in an accredited calibration lab. In Proceedngs of ASPE: Uncertainty Analysis in Measurement and Design, 2004.

[87] Nardelli VC, Donatelli GD, Arenhart FA, Porath MC. Uncertainty evaluation of computed tomography measurements using multiple calibrated workpieces. II CIMMEC, 2011.

[88] Müller P, Hiller J, Dai Y, Andreasen JL, Hansen HN, De Chiffre L. Estimation of measurement uncertainties in X-ray computed tomography metrology using the substitution method. CIRP Journal of Manufacturing Science and Technology, 2014;7(3), 222–32. doi:10.1016/j.cirpj.2014.04.002.

[89] ISO 15530-3:2011. Geometrical product specifications (GPS) – Coordinate measuring machines (CMM): Technique for determining the uncertainty of

measurement – Part 3: Use of calibrated workpieces or measurement standards. International Organization for Standardisation.

[90] Bartscher M, Hilpert U, Goebbels J, Weidemann G. Enhancement and proof of accuracy of industrial computed tomography (CT) measurements. CIRP Annals – Manufacturing Technology, 2007;56(1): 495–8. doi:10.1016/j.cirp.2007.05.118.

[91] Bartscher M, Neukamm M, Koch M, Neuschaefer-Rube U, Staude A, Goebbels J, Ehrig K, Kuhn C, Deffner A, Knoch A. Performance assessment of geometry measurements with micro-CT using a dismountable work-piece-near reference standard. In Proceedings of 10th European Conference on Non-Destructive testing, 2010.

[92] Kumar J, Attridge A, Wood PKC, Williams MA. Analysis of the effect of cone-beam geometry and test object configuration on the measurement accuracy of a computed tomography scanner used for dimensional measurement. Measurement Science and Technology, 2011;22(3):035105. doi:10.1088/0957-0233/22/3/035105.

[93] Ferrucci M, Ametova E, Carmignato S, Dewulf W. Evaluating the effects of detector angular misalignments on simulated computed tomography data. Precision Engineering, 2016;45:230–241.

[94] Aloisi V, Carmignato S, Schlecht J, Ferley E, Savio E. Experimental investigation on the influence of detector misalignment on X-ray CT measurement accuracy. In Proceedings of Euspen's 17th International Conference and Exhibition, 2017:375 376, ISBN: 978-0-9957751-0-7.

[95] Müller P, Hiller J, Cantatore A, De Chiffre L. Investigation of measuring strategies in computed tomography. Proceedings of the International Conference on New technologies in manufacturing (NEWTECH), 2011:31–42, ISBN 978-80-214-4267-2.

[96] Muller P, Hiller J, Dai Y, Andreasen JL, Hansen HN, De Chiffre L. Quantitative analysis of scaling error compensation methods in dimensional X-ray computed tomography. CIRP Journal of Manufacturing Science and Technology, 2015;10: 68–76. doi:10.1016/j.cirpj.2015.04.004.

[97] Lifton JJ, Malcolm AA, Mcbride JW, Cross KJ. The Application of Voxel Size Correction in X-ray Computed Tomography for Dimensional Metrology. In Proceedings of Singapore international NDT conference & exhibition, 2013.

[98] Schwenke H, Knapp W, Haitjema H, Weckenmann A, Schmitt R, Delbressine F. Geometric error measurement and compensation of machines – An update. CIRP Annals – Manufacturing Technology, 2008;57(2):660–75. doi:10.1016/j.cirp.2008.09.008.

[99] Sartori S, Zhang GX. Geometric error measurement and compensation of machines. CIRP Annals – Manufacturing Technology, 1995;44(2): 599–609.

[100] Sun Y, Hou Y, Zhao F, Hu J. A Calibration Method for Misaligned Scanner Geometry in Cone-beam Computed Tomography. Ndt & E International, 2006;39(6), 499–513.

[101] Leach RK, (2014). Fundamental principles of engineering nanometrology. Elsevier.

[102] Hocken RJ, Pereira PH (Eds.), (2016). Coordinate measuring machines and systems. CRC Press.

[103] Yang K, Kwan AL, Miller DF, Boone JM, Yang K. A geometric calibration method for cone beam CT systems. Medical physics, 2006;33(6):1695–1706. doi:10.1118/1.2198187.

[104] Strubel G, Clackdoyle R, Mennessier C, Noo F. Analytic Calibration of Cone-Beam Scanners. In Nuclear Science Symposium Conference Record, IEEE, 2005;5:2731–5.

[105] VGStudio MAX user manual, Volume Graphics, Heidelberg.

[106] Aloisi V, Carmignato S, Schlecht J, Ferley E. Investigation on metrological performances in CT helical scanning for dimensional quality control. In Proceedings of 6th Conference on Industrial Computed Tomography (iCT), 2016.

[107] Aloisi V, Carmignato S, Schlecht J, Ferley E. Computed tomography helical scanning for dimensional metrology: evaluation of measurement errors. Materials Evaluation, 2016:74(7):1055-1059. ISSN: 00255327.

[108] Hiller J, Kasperl S, Schön T, Schröpfer S, Weiss D. Comparison of Probing Error in Dimensional Measurement by Means of 3D Computed Tomography with Circular and Helical Sampling. In Proceedings of 2nd International Symposium on NDT in Aerospace, 2010.

[109] Muders J, Hesser J, Lachner A, Reinhart C. Accuracy Evaluation and Exploration of Measurement Uncertainty for Exact Helical Cone Beam Reconstruction Using Katsevich Filtered Backprojection in Comparison to Circular Feldkamp Reconstruction with Respect to Industrial CT Metrology. In Proceedings of International Symposium on Digital Industrial Radiology and Computed Tomography, 2010.

[110] Smith BD. Image reconstruction from cone-beam projections: necessary and sufficient conditions and reconstruction methods. IEEE transactions on medical imaging, 1985;4(1):14–25. doi:10.1109/TMI.1985.4307689.

[111] Wang G, Lin TH, Cheng PC. Error analysis on a generalized Feldkamp's cone-beam computed tomography algorithm. Scanning, 1995;17(6):361–370.

[112] Franz M, Funk C, Hiller J, Kasperl S, Krumm M, Schröpfer S, Ezrt F. Reliability of Dimensional Measurements by Computed Tomography for Industrial Applications. In 4th European–American Workshop on Reliability of NDE, 2009.

[113] Aloisi V, Carmignato S, Schlecht J, Ferley E, Savio E. Investigation on scan parameters for accurate dimensional measurements by CT helical scanning. In Proceedings of Euspen 16th International Conference & Exhibition, 2016:557-558, ISBN: 978-0-9566790-8-6, Nottingham (UK), 30 May-3 June.

[114] Fiedler D, Bartscher M, Hilpert U. Dimensionelle Messabweichungen eine industriellen 2D-Computertomographen: Einfluss der Werkstü ckrauheit. In Proccedings of DGZfP, German Society of NDT – 2004.

[115] Salzinger M, Hornberger P, Hiller J. Analysis and comparison of the surface filtering characteristics of computed tomography and tactile measurements. In Proceedings of 6th Conference on Industrial Computed Tomography (iCT), 2016.

[116] Carmignato S, Savio E. Traceable volume measurements using coordinate measuring systems. CIRP Annals – Manufacturing Technology, 2011;60(1):519–522. doi:10.1016/j.cirp.2011.03.061.

[117] Boeckmans B, Tan Y, Welkenhuyzen F, Guo YS, Dewulf W, Kruth JP. Roughness offset differences between contact and non-contact measurements. In Proceedings

of Euspen's 15th International Conference and Exhibition, 2015:189–90. ISBN 14: 978-0-9566790-7-9.

[118] Weckenmann A, Estler T, Peggs G, McMurtry D. Probing systems in dimensional metrology. CIRP Annals – Manufacturing Technology, 2004;53(2):657–684. doi: https://doi.org/10.1016/S0007-8506(07)60034-1.

[119] De Chiffre L (2011). Geometrical Metrology and Machine Testing – Textbook. DTU Mechanical Engineering, ISBN 978-87-7078-155-8.

[120] ISO 4287:1997. Geometrical Product Specifications (GPS) – Surface texture: Profile method – Terms, definitions and surface texture parameters. International Organization for Standardization.

[121] ISO 4288:1996. Geometrical Product Specifications (GPS) – Surface texture: Profile method – Rules and procedures for the assessment of surface texture. International Organization for Standardization.

[122] Carmignato S, Aloisi V, Medeossi F, Zanini F, Savio E. Influence of surface roughness on computed tomography dimensional measurements. CIRP Annals – Manufacturing Technology, 2017;66(1):499-502. doi: https://doi.org/10.1016/j.cirp.2017.04.067.

[123] Aloisi V, Carmignato S. Influence of surface roughness on X-ray computed tomography dimensional measurements of additive manufactured parts. Case Studies in Non Destructive Testing and Evaluation, 2016;6:104-110. doi: 10.1016/j.csndt.2016.05.005.

[124] ISO/TS 15530-3:2004. Geometrical Product Specifications (GPS) – Coordinate measuring machines (CMM): Technique for determining the uncertainty of measurement – Part 3: Use of calibrated workpieces or standards. International Organization for Standardization.

[125] ISO/DIS 15530-3:2009. Geometrical Product Specifications (GPS) – Coordinate measuring machines (CMM): Technique for determining the uncertainty of measurement – Part 3: Use of calibrated workpieces or standards. International Organization for Standardization.

[126] Trujillo-pino A, Krissian K, Alemán-flores M, Santana-Cedrés D. Accurate subpixel edge location based on partial area effect. Image and Vision Computing, 2013;31:72–90. doi:10.1016/j.imavis.2012.10.005.

Publications

[1] **Aloisi V**, Carmignato S, Savio E. Effect of surface roughness on uncertainty of X-ray CT dimensional measurements of additive manufactured parts. In Proceedings of Euspen 15th International Conference & Exhibition, 2015:187-188, ISBN: 978-0-9566790-7-9, Leuven (Belgium), 1-6 June.

[2] **Aloisi V**, Carmignato S (2015). Investigation on the effects of surface roughness on X-ray CT dimensional measurements. Abstract published in Proceedings of International Symposium on Digital Industrial Radiology and Computed Tomography (DIR), 2015, Ghent (Belgium), 22-25 June 2015.

[3] **Aloisi V**, Carmignato S, Schlecht J, Ferley E. Investigation on metrological performances in CT helical scanning for dimensional quality control. In Proceedings of 6th Conference on Industrial Computed Tomography (iCT), 2016, Wels (Austria), 9-12 February.

[4] **Aloisi V**, Carmignato S. Influence of surface roughness on X-ray computed tomography dimensional measurements of additive manufactured parts. Case Studies in Non Destructive Testing and Evaluation, 2016;6:104-110. doi: 10.1016/j.csndt.2016.05.005.

[5] **Aloisi V**, Carmignato S, Schlecht J, Ferley E, Savio E. Investigation on scan parameters for accurate dimensional measurements by CT helical scanning. In Proceedings of Euspen 16th International Conference & Exhibition, 2016:557-558, ISBN: 978-0-9566790-8-6, Nottingham (UK), 30 May-3 June.

[6] **Aloisi V**, Carmignato S, Schlecht J, Ferley E. Computed tomography helical scanning for dimensional metrology: evaluation of measurement errors. Materials Evaluation, 2016:74(7):1055-1059. ISSN: 00255327.

[7] Piasentini F, Scanavini A, Carmignato S, **Aloisi V**, Rigodanza M. Evaluating the use of industrial X-ray CT for the reverse engineering of bowed stringed instruments. In Proceedings of 3rd Annual Conference COST FP1302 WoodMusICK: Making wooden musical instruments: an integration of different forms of knowledge, 2016, ISBN: 978-84-945603-3-0, Barcelona (Spain), 7-9 September. doi: http://dx.doi.org/10.3926/wm2016.

[8] Carmignato S, **Aloisi V**, Medeossi F, Zanini F, Savio E. Influence of surface roughness on computed tomography dimensional measurements. CIRP Annals – Manufacturing Technology, 2017;66(1):499-502. doi: https://doi.org/10.1016/j.cirp.2017.04.067.

[9] **Aloisi V**, Carmignato S, Schlecht J, Ferley E, (2017). Investigation on the effects of X-ray CT system geometrical misalignments on dimensional measurement errors. In Proceedings of 7th Conference on Industrial Computed Tomography (iCT), 2017. Leuven (Belgium) 7-9 February.

[10] **Aloisi V**, Carmignato S, Schlecht J, Ferley E, Savio E. Experimental investigation on the influence of detector misalignment on X-ray CT measurement accuracy. In Proceedings of Euspen's 17th International Conference and Exhibition, 2017:375-376, ISBN: 978-0-9957751-0-7, Hannover (Germany), 29 May-2 June.

[11] Hermanek P, Rathore J, **<u>Aloisi V</u>**, Carmignato, S. (2018). Principles of X-ray Computed Tomography. In: Carmignato S., Dewulf W., Leach R. (eds) Industrial X-Ray Computed Tomography. Springer, Cham.